Alma Mater Studiorum - Università di Bologna

DOTTORATO DI RICERCA IN

AUTOMOTIVE PER UNA MOBILITÀ INTELLIGENTE

Ciclo 35

Settore Concorsuale: 09/C1 - MACCHINE E SISTEMI PER L'ENERGIA E L'AMBIENTE

Settore Scientifico Disciplinare: ING-IND/08 - MACCHINE A FLUIDO

PERFORMANCE ASSESSMENT OF VEHICULAR CONNECTIVITY IN HYBRID ELECTRIC VEHICLES FOR FUEL AND EMISSIONS REDUCTION

Presentata da: Lorenzo Brunelli

Coordinatore Dottorato	**Supervisore**
Nicolò Cavina	Nicolò Cavina

Esame finale anno 2023

To my family.

Not all those who wander are lost.

[J.R.R. Tolkien]

Abstract

In the last decades, urbanization led to an increasing number of vehicles on the roads, resulting in more polluted air and more congested urban centers. As a countermeasure, the national agencies have started to introduce stricter regulations in terms of pollutant emissions per driven kilometers alongside more demanding type approval procedures. Thus, manufacturers are responding with innovative solutions such as more efficient conventional engines and the introduction of Hybrid Electric Vehicles (HEVs), which have proven to be a sustainable alternative to the conventional powertrain. In this framework, there is also the need to re-organize the management of urban mobility to optimize traffic flows to decrease congestion. The most frequently applied measures are urban centers with increasing traffic limitations, regarding both the conventional vehicles (Low-Emission Zone – LEZ) and the non-conventional vehicles (Zero-Emission Zone – ZEZ). Moreover, innovative technologies are being implemented both on the vehicle and the infrastructure, such as wireless communication, cloud computing, and innovative sensors. These technologies are generally indicated as vehicle-to-vehicle (V2V), vehicle-to-infrastructure (V2I), and vehicle-to-network (V2N) communication. Together with the latest Advanced Driver-Assistance Systems (ADAS), these technologies allow calculating an *electronic horizon* (shortly known as eHorizon) which represents a virtual reconstruction of the trip ahead for a planned route. It is conventionally divided into "short horizon", regarding information about nearby vehicles and traffic lights, and the "long horizon", which includes information about the selected route, the slope, and the speed limits.

In this regard, this dissertation aims to demonstrate the advantages of such information to manage the energy flow and the pollutant emissions more efficiently and sustainably, comparing the results with the noteworthy works presented in the literature review in Chapter 2.

Firstly, since the more the control function becomes complex the more its testing and validation are demanding, Chapter 3 presents an innovative and universal simulation environment supported by Vehicle-to-Everything (V2x) connectivity that has been set up with a focus on safety, reliability, and reproducibility. More in detail, it consists of a Hardware-in-the-Loop (HiL) system enhanced with vehicular connectivity to test a supervisory controller (Hybrid Control Unit) where the predictive functions will be implemented. In addition to all the advantages of a conventional HiL layout, it can exchange real data with cloud service providers and nearby devices.

Furthermore, to handle the over-the-air interfaces between the powertrain controllers, the cellular network, and the Intelligent Transportation Systems (ITS-G5), a custom Telecommunication Control Unit (TeCU) with proprietary functionalities has been developed and implemented in the HiL. Moreover, a Human-Machine Interface (HMI), based on a tablet running an Android-based Navigator App, has been introduced to allow the driver to set the desired destination and to visualize the suggested route based on actual traffic conditions. Then, the navigation and connectivity data have been used in Chapter 4 and Chapter 5 to develop energy management strategies. In particular, focusing on the changes in urban mobility, several metropolitan cities have introduced Zero-Emissions Zones where the use of the Internal Combustion Engine is forbidden to reduce localized pollutants emissions. This is particularly problematic for Plug-in Hybrid Electric Vehicles, which usually work in charge depleting mode. So, the risk of not having enough energy stored to carry out the driving mission and then paying a fee is substantial. Thus, this dissertation presents a viable solution by exploiting vehicular connectivity to retrieve navigation data of the urban event along a selected route. The battery energy needed, in the form of a minimum State of Charge (SoC), is calculated by a Speed Profile Prediction algorithm and a Backward Vehicle Model. That value is then fed to both a Rule-Based Strategy, developed specifically for this application, and an Adaptive Equivalent Consumption Minimization Strategy (A-ECMS). The effectiveness of this approach has been tested with the Connected Hardware-in-the-Loop (C-HiL) on a driving cycle measured on-road, stimulating the predictions with multiple re-routings.

However, even if hybrid vehicles represent a key enabler to comply with the upcoming regulations, the inherently reduced engine load and the repeated engine starts and stops may reduce substantially the temperature of the exhaust after-treatment system (EATS), leading to relevant issues related to pollutant emission control. In this context, electrically heated catalysts (EHCs) represent a promising solution to ensure high pollutant conversion efficiency without affecting engine efficiency and performance. Chapter 7, Chapter 8, and Chapter 9 aim at studying the advantages provided by introducing a predictive EHC control function for a light-duty Diesel plug-in hybrid electric vehicle (PHEV) equipped with a Euro 7-oriented EATS. Based on the knowledge of future driving scenarios provided by vehicular connectivity, engine first start can be predicted and therefore an EATS pre-heating phase can be planned. For this purpose, a representative 0-D model has been considered to define the most convenient pre-heating strategy and different real driving scenarios have been simulated to test the proposed EHC predictive control strategy. Moreover, this would allow complying with the scenarios introduced by the Euro 7 regulation proposal, while enabling the adoption of a simplified EATS architecture resulting in reduced manufacturing costs.

All the activities presented in this doctoral dissertation have been carried out at the *Green Mobility Research Lab* (GMRL), a research center resulting from the partnership between the University of Bologna and FEV Italia s.r.l., which represents the industrial partner of the research project.

Keywords

hybrid electric vehicles (HEVs) · Software-in-the-Loop (SiL) · Hardware-in-the-Loop (HiL) · vehicle-to-everything (V2X) · zero-emission zone (ZEZ) · predictive functions · energy management · emissions management · electrically heated catalyst

Contents

List of figures

List of tables

Nomenclature

Acronyms

4WD	Four-Wheel Driving
CO_2	Carbon dioxide
CO	Carbon monoxide
NH_3	Ammonia
NMHC	Non-methane hydrocarbons
NO_2	Nitrogen dioxide
Nox	Nitrogen oxides
A-ECMS	Adaptive ECMS
A-RBS	Adaptive RBS
ADAS	Advanced Driver-Assistance Systems
ADASIS	Advanced Driver Assistant Systems Interface Specifications
AER	All-Electric Range
AMT	Automated Manual Transmission
BEV	Battery Electric Vehicle
BMEP	Brake Mean Effective Pressure
BMS	Battery Management System
BSFC	Brake Specific Fuel Consumption [g/kWh]
BSG	Belt-driven Starter Generator
$BSNO_x$	Brake Specific NO_x [g/kWh]
BVM	Backward Vehicle Model
C-HiL	Connected Hardware-in-the-Loop
C-RBS	Combined RBS
CAV	Connected Automated Vehicles
CB	Charge Blended
CD	Charge Depleting
CG	Central gateway
CI	Charge Increasing
CS	Charge Sustaining

DCT	Dual-Clutch Transmission
DOC	Diesel Oxidation Catalyst
DoE	Design of Experiments
DP	Dynamic Programming
DPF	Diesel Particulate Filter
EATS	Exhaust After-Treatment Systems
EATS	Exhaust After-treatment System
EC	European Commission
ECMS	Equivalent Consumption Minimization Strategy
ECPMS	Equivalent Consumption and Pollutant Minimization Strategy
ECU	Electronic / Engine Control Unit
EECMS	Equivalent Emissions and Consumption Minimization Strategy
EGR	Exhaust Gas Recirculation
EHC	Electrically heated catalyst
EM	Electric Motor
EMS	Energy Management Strategies
EO	Engine Out
EPA	Environmental Protection Agency
FC	Fuel Consumption
FFT	Fast Fourier Transform
GHG	Greenhouse gas
HC	Unburned hydrocarbons
HCU	Hybrid Control Unit
HD	Hybridization Degree
HEV	Hybrid Electric Vehicles
HiL	Hardware-in-the-Loop
HMI	Human-Machine Interface
HV	High-Voltage
ICE	Internal Combustion Engines
ISG	Integrated Starter Generator
ITS	Intelligent Transport Systems
KPI	Key Performance Indicators
LCV	Light Commercial Vehicle
LEZ	Low-Emission Zone
LNT	Lean NOx-trap
LP EGR	Low Pressure EGR
LPS	Load-Point Shift
LTM-SCR	Low Thermal Mass SCR
LV	Low-Voltage

MAE	Mean Absolute Error
MiL	Model-in-the-Loop
MPC	Model Predictive Control
MSP	Map Service Provider
NEDC	New European Driving Cycle
OBU	On-Board Unit
OCV	Open-circuit Voltage
OEM	Original Equipment Manufacturers
OVC	Off-Vehicle Charging
PEMS	Portable Emission Measuring Systems
PF / S	Predictive Functions / Strategy
PHEV	Plug-in Hybrid Electric Vehicle
PM	Particulate matter
PMP	Pontryagin's Minimum Principle
PN	Particulate number
RBS	Rule-Based Strategy
RDE	Real Driving Emissions
REESS	Rechargeable Electric Energy Storage System
RSU	Road-Side Unit
SCR	Selective Catalytic Reduction
SDPF	SCR-coated Diesel Particulate Filter
SiL	Software-in-the-Loop
SoC	State of Charge
SPP	Speed Profile Prediction
TAT	Turnaround time [ms]
TCU	Transmission Control Unit
TeCU	Telecommunication Control Unit
THC	Total hydrocarbons
TO	Tailpipe Out
TWC	Three-Way Catalyst
UF	Utility Factors
V2I	Vehicle-to-Infrastructure
V2N	Vehicle-to-Network
V2P	Vehicle-to-Pedestrian
V2V	Vehicle-to-Vehicle
WLTC	Worldwide harmonized Light vehicles Test Cycle
WLTP	Worldwide harmonized Light vehicles Test Procedure
ZEZ	Zero-Emission Zone

Roman symbols

$a(\cdot)$	Adaptive term of the equivalence factor [-]
A_0	Amplitude at f = 0 m^{-1} [m]
A_r	Amplitude of the r-th harmonic of the noise-related MAS [km/h]
$a_{acc,max}$,$a_{dec,max}$	Maximum vehicle acceleration / deceleration [m/s^2]
a_{acc},a_{dec}	Vehicle acceleration and deceleration [m/s^2]
$A_{c,r}$	Amplitude related to the traffic code c and range r [m]
A_{cond}	Contact area of the brick [m^2]
A_{ext},A_{int}	External and internal brick surface [m^2]
$A_{n,r,j}$	Amplitude related to the j-th speed signal [m]
$\mathrm{CO_2}$	$\mathrm{CO_2}$ production [g/km]
$\mathrm{C_1}(\cdot)$	Capacitance of the RC circuit [F]
c_c	Coolant specific heat capacity [J/(kg $\cdot$ K)]
$C_n(\cdot)$	Battery nominal capacity [Ah]
c_p	Specific heat capacity (at constant pressure) [J/(kg·K)]
c_s	Corrective factor for close segments [-]
$CO_{2,c}$	Corrected $\mathrm{CO_2}$ production [g/km]
CW_c	Traffic code weight [-]
d	Predicted speed profile discretization step [m]
	Diameter of the cross-section of the brick [m]
$d(\cdot)$	Traveled distance [km]
d_0	Travelled distance when the prediction occurs [m]
d_i,d_f	Initial/final distance delimiting CB mode [km]
$d_{i,Z}$,$d_{f,Z}$	Initial/final distance delimiting the ZEZ [km]
d_Z	ZEZ length [km]
ΔE_{pre}	Additional energy required for the pre-heating [J]
$E_{I_p^+}$,$E_{I_r^+}$	Predicted and measured energy related to positive inertia [Wh]
$E_{I_p^-}$,$E_{I_r^-}$	Predicted and measured energy related to negative inertia [Wh]
E_{RL_p},E_{RL_r}	Predicted and measured energy related to the road load [Wh]
$F(\cdot)$	Force [N]
F_0,F_1,F_2	Coast-down parameters [N], [N/(km/h)], [N/(km/h)^2]
f_r	Frequency of the r-th harmonic of the noise-related MAS [1/m]
$F_r(\cdot)$	Force acting on the wheels [N]
	Rolling friction force [N]
$F_a(\cdot)$	Aerodynamic friction force [N]
$f_{c,r}$	Frequency related to the traffic code c and range r [m^{-1}]
$F_{cd}(\cdot)$	Total resistance curve calculated with the coast-down test [Nm]
$F_g(\cdot)$	Gravitational force [N]

$F_{I^+}(\cdot)$,$F_{I^-}(\cdot)$	Positive/negative inertial force [N]
$F_{mot}(\cdot)$	Propulsion force for vehicle traction [N]
$f_{n,r,j}$	Frequency related to the traffic code c and range r [m^{-1}]
$F_{res}(\cdot)$	Resistant force acting on the vehicle [N]
$F_{RL}(\cdot)$	Road load [N]
$F_r(\cdot)$	Rolling friction force [N]
g	Gravitational acceleration [m/s^2]
h_a	Convective heat transfer coefficient of the environmental air [W/(K·m^2)]
h_c	Convective heat transfer coefficient of the battery coolant [W/(K·m^2)]
h_{ext},h_{int}	External and internal convective heat transfer coefficient [W/(m^{2}K)]
h_{fast},h_{std},h_{slow}	Enthalpy of the fast, standard, and slow SCR reactions respectively [J/mol]
$I_b(\cdot)$	Battery current [A]
$J(x_0,u)$,$J(x_0,u^*)$	Admissible/minimum cost for the optimal problem
k	Discrete time index (or stage)
$k_a(\cdot)$	Adaptive factor [-]
k_d	Minimum number of sub-segments to create an acceleration-deceleration maneuver
k_p	Penalty factor [-]
k_{CO_2}	CO$_2$ conversion factor [g$_{CO_2}$/l$_{fuel}$]
k_{acc},k_{dec}	Reductive factor of the vehicle maximum acceleration/deceleration [-]
k_{FC},k_{NOx},k_{T3}	DoE parameters [-]
l	Length of the brick [m]
l_j	Measured speed segmentation [m]
$\dot{m}_c(\cdot)$	Battery coolant mass flow rate [kg/s]
$\dot{m}_{f,b}(\cdot)$	Virtual fuel mass flow rate associated to battery usage [kg/s]
$\dot{m}_{f,eq}(\cdot)$	Equivalent fuel mass flow rate [kg/s]
$\dot{m}_f(\cdot)$	Fuel mass flow rate [kg/s]
m_s	Mass of the considered solid material [kg]
$m_{f,c}(\cdot)$	Corrected fuel consumption [kg]
M_X	Molar mass of the species X [g/mol]
m_X^{in},m_X^{out},	Mass of the species X [g]
MAS	Vehicle maximum allowable speed [km/h]
MAS_n	Noise-related MAS [km/h]
MAS_t	Traffic related MAS [km/h]
N	Number of sub-segments of the speed profile prediction [-]
	Number of iterations of the backward vehicle model [-]
n	Polynomial coefficient of the penalty function
$n(\cdot)$	Engine revolution speed [rpm]
n_c	Number of close segments [-]

n_p	Number of cells strings [-]
N_r	Number of points within range r [-]
N_s	Number of segments [-]
n_s	Number of series-connected cells [-]
n_v	Maximum number of elements of output vector
n_{fast},n_{std},n_{slow}	Moles involved in the fast, standard, and slow SCR reactions respectively [mol]
n_X	Moles of the species X [mol]
Nu	Nusselt number [-]
Nu_t	Corrected Nusselt nuber [-]
$P(\cdot)$	Power [W]
$p(\cdot)$	Penalty term of the equivalence factor [-]
$P_b(\cdot)$	Battery net power output [W]
P_{aux}	Auxiliary power [W]
$P_{b,loss}(\cdot)$	Battery power losses [W]
$P_{el}(\cdot)$	Electrical power [W]
$P_{EM}(\cdot)$	Required power to electric motors [W]
$P_{mech}(\cdot)$	Mechanical net power at the crankshaft [W]
	Mechanical power [W]
P_{pre}	Power required for the pre-heating [W]
$\dot{Q}_{air}(\cdot)$	Thermal power related to the air-battery convective heat exchange [W]
$\dot{Q}_{cool}(\cdot)$	Cooling heat rate due to battery-coolant convective heat exchange [W]
$\dot{Q}_{exo}(\cdot)$	Heat transfer related to the NOx reduction [W]
$\dot{Q}^{conv}_{ext,i}(\cdot)$,$\dot{Q}^{conv}_{int,i}(\cdot)$	External and internal convection heat exchange for the i-th brick [W]
$\dot{Q}^{cond}_{i}(\cdot)$	Conduction heat exchange for the i-th brick [W]
$\dot{Q}^{cond}_{i}(\cdot)$	Total heat exchange for the i-th brick [W]
$\dot{Q}^{rad}_{i}(\cdot)$	Radiation heat exchange for the i-th brick [W]
Q_{lhv}	Fuel lower heating value [J/kg]
R	Number of dominant harmonics of the noise-related MAS [-]
$R_0(\cdot)$	Ohmic resistance [Ω]
$R_1(\cdot)$	Resistance of the RC circuit [Ω]
r_w	Wheel radius [m]
Re	Reynolds number [-]
$s(\cdot)$	Equivalence factor [-]
S_a	Surface of the air-battery convective heat transfer [m^2]
S_c	Surface of the battery-coolant convective heat transfer [m^2]
sfc_{eq}	Virtual specific fuel consumption [kg/kJ]
$\bar{T}_{s,i}(\cdot)$,$\bar{T}_{g,i}(\cdot)$	Solid and gas average temperature [°C]
$\Delta T_{ml,c}(\cdot)$	Logarithmic mean temperature difference [°C]

Δt_{pre}	Time required for the pre-heating [s]
t	Time [s]
$T(\cdot)$	Torque [Nm]
	Temperature [°C]
$T_i(\cdot)$	Initial temperature [°C]
t_i, t_f	Initial/final time instant delimiting CB mode [s]
$T_r(\cdot)$	Torque request at the wheels [Nm]
t_s	Computational time step [s]
$t_u(\cdot)$	Update time [s]
T_{amb}	Ambient temperature [°C]
$T_{c,in}, T_{c,out}$	Input / output coolant temperature [°C]
T_{cold}, T_{warm}	Temperature thresholds for engine maps [°C]
$T_{EM}(\cdot)$	Electric machines torque [Nm]
$T_{g,0,i}(\cdot), T_{s,0,i}(\cdot)$	Initial temperatures of the gas and of the solid material respectively [°C]
$T_{g,out,i}(\cdot)$	Gas temperature at the brick outlet [°C]
$t_{i,Z}, t_{f,Z}$	ZEZ entrance/exit time instant [s]
$T_{ICE}(\cdot)$	Internal combustion engine torque [Nm]
$T_{LPS}(\cdot)$	Torque required for the load-point shift [Nm]
T_{min}, T_{max}	Minimum/maximum torque in CS mode [Nm]
$T_{req}(\cdot)$	Torque requested by the driver for traction [Nm]
$T_{s,fin,i}(\cdot)$	Final temperature of the i-th solid brick [°C]
$T_{trm,in}(\cdot)$	Total requested torque upstream of the transmission [Nm]
$T_w(\cdot)$	Driver torque request at the wheels [Nm]
$\mathbf{u}$	Control variables vector
$\mathbf{v}$	Predicted vehicle speed profile [km/h]
$V(\cdot)$	Voltage [V]
$v(\cdot)$	Vehicle longitudinal speed [km/h]
$V_0(\cdot)$	Voltage drop related to the ohmic resistance [V]
$V_1(\cdot)$	Voltage drop related to the RC circuit [V]
$V_b(\cdot)$	Battery voltage [V]
$V_{b,int}$	Internal battery voltage [V]
v_{lim}	Road segment's legal speed limit [km/h]
v_{min}, v_{max}	Minimum/maximum speed in CS mode [Nm]
$V_{OC}(\cdot)$	Open circuit voltage [V]
$v_{p,i}, v_{r_i}$	Predicted and measured speed at point i [km/h]
w_{warm}, w_{cold}	Weighting factors for engine maps [-]
$\mathbf{x}$	State variables vector

Greek symbols

$\alpha(\cdot)$	Angle of slope [rad]
$\alpha_{\%}(\cdot)$	Percentage road slope [%]
$\boldsymbol{\alpha}_{\%}$	Predicted road slope profile [%]
β	NO_2/NOx mass ratio [-]
ϵ	Emissivity [-]
ϵ_s	Gas heat transfer effectiveness in space [-]
ϵ_t	Solid heat transfer effectiveness in time [-]
$\bar{\eta}_{EM}$	Electric motors average efficiency [-]
$\bar{\eta}_{ICE}$	Engine average efficiency [-]
$\bar{\eta}_{ISG}$	ISG average efficiency [-]
η	Efficiency [-]
η_c	Coulombic efficiency [-]
η_{DCDC}	DCDC efficiency [-]
λ_g,λ_s	Thermal conductivity of the gas and the solid [W/(m·K)]
$\boldsymbol{\xi}$	Vector of the predicted battery SoC [-]
$\Delta\xi_t$	Target SoC tolerance [-]
$\Delta\xi_Z$	Net SoC for ZEZ in eDrive [-]
$\xi(\cdot)$	Battery state of charge [-]
ξ_i	Initial SoC [-]
ξ_1	SoC value at the first iteration within the BVM [-]
ξ_f	Final SoC [-]
$\xi_{i,Z}$,$\xi_{f,Z}$	SoC at ZEZ entrance/exit [-]
$\xi_{min,b}$,$\xi_{max,b}$	Minimum/maximum SoC in CS mode [-]
$\xi_{r,f}$	Final value of the reference SoC (at ZEZ entrance) [-]
$\xi_r(\cdot)$	Reference SoC [-]
ξ_s	Safety SoC margin for target SoC evaluation [-]
ξ_t	Target SoC at ZEZ entrance [-]
ρ_c	Battery coolant density [kg/m^3]
ρ_f	Fuel density [kg/l]
σ	Stefan-Boltzmann constant [W/(m^2K^4)]
τ	Time constant of the vehicle acceleration transient [s]
	Total transmission ration [-]
$\Psi(\cdot)$	Global boundary conditions
$\omega(\cdot)$	Engine revolution speed [rad/s]

Notation

$a(\cdot)$,$A(\cdot)$	functions
$\mathbf{a}$,$\mathbf{A}$	vector or matrix
$[\mathbf{a}]_i$	element i of the vector $\mathbf{a}$

Chapter 1

Introduction

In this chapter, an overview of the current automotive background is given in order to practically comprehend the reasons and motivations lying behind the research project and how the global regulatory targets and customer demand are driving the automotive industry to improve vehicle efficiency. In particular, the current and upcoming European regulations in terms of CO_2 and pollutant emissions are presented alongside their measurement and test procedures. Finally, the state-of-the-art of exhaust after-treatment systems and the electric hybridization of the vehicles are presented as valid solutions to address the air pollution related to the transportation sector.

1.1 Motivation

The last decades of the twentieth century have been characterized by an exponential trend of industrialization and consequently a growth in greenhouse gas (GHG) emissions, such as carbon dioxide (CO_2). This is heavily conditioning one of the most demanding challenges of present times: global warming. Moreover, the increasing rate of urbanization led to a massive migration of people from the rural areas to the urban centers as shown in Fig. 1.1. In [1], it is reported that, in 2016, 4 billion people lived in urban areas and this number is projected to increase to 7 billion by 2050 [2].

One of the direct consequences is the worsening of urban mobility and air quality. In fact, 21% of the CO_2 emitted comes from the transportation sector [3], especially near the city centers. As an example, in Fig. 1.2 the concentration in ppm of nitrogen dioxide (NO_2) is represented, thus it is possible to see that the higher concentration corresponds to the urban areas (the red dots on the map). This trend forced the national governments and local administrations to introduce countermeasures such as more demanding vehicle approval procedures and traffic limitations.

In particular, the European Commission (EC) sets the limit of 95 [g/km] of CO_2 for 2021 and 80 [g/km] for 2025. Moreover, the EC replaces the New European Driving Cycle (NEDC) with the Worldwide harmonized Light vehicles Test Procedure (WLTP) to better match the laboratory

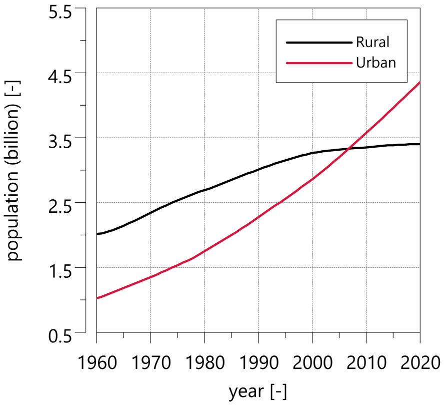

Figure 1.1: Trend of the population living in urban and rural areas [2]

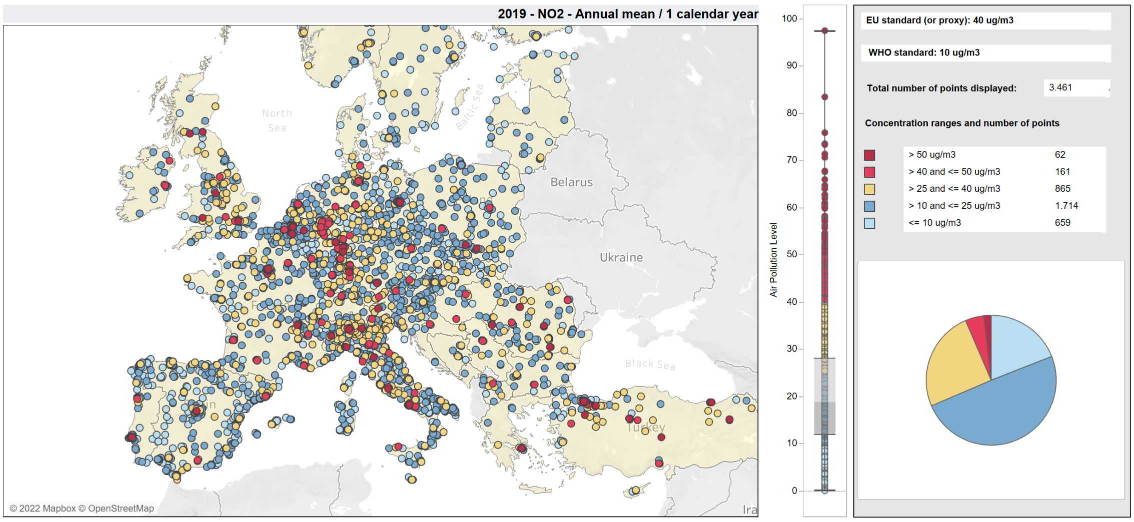

Figure 1.2: NO_2 concentration in Europe [4]

estimates of fuel consumption and emissions with the measures of an on-road driving condition. In fact, the difference between in-use and type-approval fuel consumption has been evaluated to be around 11% [5]. Then, in 2017 it introduced the Real Driving Emissions (RDE) testing procedure in addition to laboratory tests. In the RDE test, a car is driven on public roads and over a wide range of different conditions which are designed to be more representative of driving conditions normally encountered on European roads [6]. On-board emissions measuring is performed by means of Portable Emission Measuring Systems (PEMS) that provide a complete real-time monitoring of the key pollutants emitted by the vehicle. On the other hand, the local administrations introduce measures to optimize the traffic flows and to avoid localized pollution, often related to the urban areas. One of the more common actions is to increase traffic limitations, regarding both the conventional vehicles (Low-Emission Zone – LEZ) and the non-conventional vehicles (Zero-Emission Zone – ZEZ) [7].

In response to this trend, the Original Equipment Manufacturers (OEM) developed innovative solutions such as more efficient conventional internal combustion engines (ICE), effective Exhaust After-Treatment Systems (EATS), and more complex but efficient powertrains such as Hybrid Electric Vehicles (HEVs). In fact, if the electric energy used for propulsion can be derived from renewable energy sources, this vehicle technology is a promising way to reduce global warming. As a consequence, the penetration of HEVs in the automotive market is supposed to increase in the next decades [8], with 48% of the total volume of passenger cars represented by hybrid vehicles in 2030 [9]. Alongside the improvements in the propulsion system, the OEMs also developed dedicated EATS for the abatement of each regulated pollutant, such as the Three-Way Catalyst (TWC) for conventional gasoline engines, the Diesel Oxidation Catalyst (DOC), the Diesel Particulate Filter (DPF) and the Selective Catalytic Reduction (SCR) for diesel engines.

Moreover, technological advancement allowed innovations to be implemented both on the vehicle and on the infrastructure, such as wireless communication, cloud computing, innovative sensors, and artificial intelligence functions (such as computer vision). These technologies result in Vehicle-to-Vehicle (V2V), Vehicle-to-Infrastructure (V2I), and Vehicle-to-Network (V2N) communication. Together with the latest Advanced Driver-Assistance Systems (ADAS), these technologies allow calculating an electronic horizon (shortly known as eHorizon) which represents a virtual reconstruction of the planned route. It is conventionally divided into *short horizon*, which comprehends information about nearby vehicles and traffic lights, and the *long horizon*, which includes information about the selected route, the slope, and the speed limits.

In light of the considerations above, HEVs and vehicular connectivity could represent a valid solution for addressing not only the CO_2 but even the pollutant emissions. This possibility has been addressed and further investigated during this research activity by focusing on the reduction of urban air pollution. In particular, predictive energy and emissions management strategies for HEVs have been developed on the basis of navigation data retrieved via long-range connectivity. With this aim, an advanced connected Hardware-in-the-Loop (HiL) system has been set up to effectively test the control strategies in a simulation environment with the real control unit and real-time, up-to-date route information.

1.2 Type-approval regulations

As mentioned before, this work focuses on the reduction of CO_2 and pollutant emissions produced by HEVs using them as parameters for the performance evaluation of the control strategies under test. Hence, a brief introduction to the related in-force regulations is provided in this section. For the sake of brevity, only the European laws for passenger cars will be discussed in detail, firstly the ones related to greenhouse gases (GHG) and then the ones concerning criteria pollutants.

1.2.1 Greenhouse gases

In 2017, The EC introduced the law EU2017/R1151 [10] that regulates greenhouse gases produced by light- and heavy-duty vehicles by means of the WLTP. The latter was intended to harmonize test procedures worldwide, thus a cycle representing typical driving characteristics around the world has been developed. This is referred to as the World Harmonized Light-duty Vehicle Test Cycle (WLTC), depicted in Fig. 1.3 as it was designed using a large number of real-world drives gathered from around the world to better represent everyday driving profiles. The real-world driving data used as input for this development came from five different regions: the European Union plus Switzerland, the United States, India, Korea, and Japan. More in detail, the WLTC is divided into four parts with different average speeds: *low*, *medium*, *high*, and *extra high*, which are listed in Tab. 1.1.

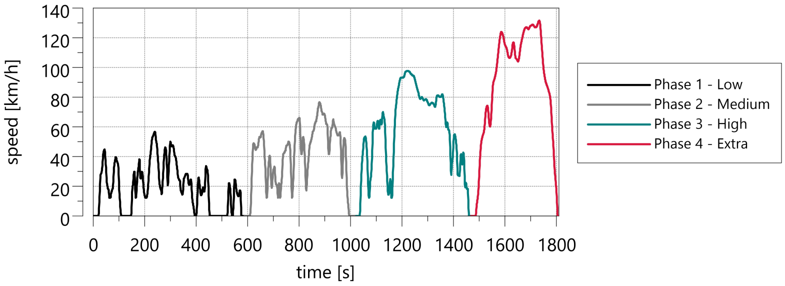

Figure 1.3: The WLTP test cycle

Table 1.1: WLTC test section specifications for class 3 vehicle [10]

	Units	Low	Medium	High	Extra high	Total
Distance	m	3095	4756	7162	8254	23266
Duration	s	589	433	455	323	1800
Idle time	%	26	11.1	6.8	2.2	-
Maximum speed	km/h	56.5	76.6	97.4	131.3	-
Average speed	km/h	25.7	44.5	60.8	94	-

The regulation also defines a specific procedure, summarized in Fig. 1.4, for vehicles propelled by more than one power source, such as the Off Vehicle Charging (OCV) HEVs, also known as Plug-in HEV (PHEV). In fact, the electrical energy consumption must be properly converted into equivalent fuel consumption. With this aim, after initial preconditioning, the vehicle performs consecutive driving cycles in Charge Depleting (CD) mode, using the electrical power as a preferential source until the battery is completely discharged. Then, the vehicle performs another WLTC, but without charging the battery at the beginning, hence in Charge Sustaining (CS) mode. Finally, the values of energy and fuel consumption are weighted to obtain the corrected value. Since this procedure will be applied in Chapter 4 and Chapter 5 to compare the different strategies, the specific tests are discussed hereafter.

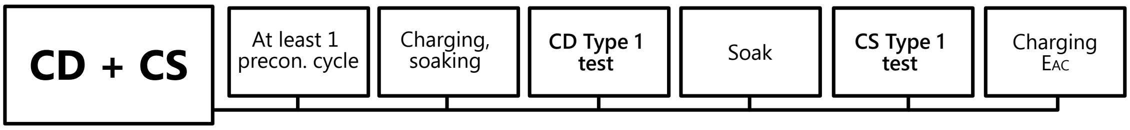

Figure 1.4: Test procedure for hybrid electric vehicles [10]

- **CD Type 1 test**: the Type 1 test shall consist of prescribed sequences of dynamometer preparation, fueling, soaking, and operating conditions. During each driven preconditioning cycle, the charging balance of the rechargeable electric energy storage system (REESS) shall be determined. Moreover, the test vehicle shall be kept in an area with ambient conditions of 23°C with a tolerance of ± 3°C. Then, the consecutive cycles are carried out, starting with a fully charged REESS and with the vehicle operated in charge-depleting operating condition, as represented in Fig. 1.5.

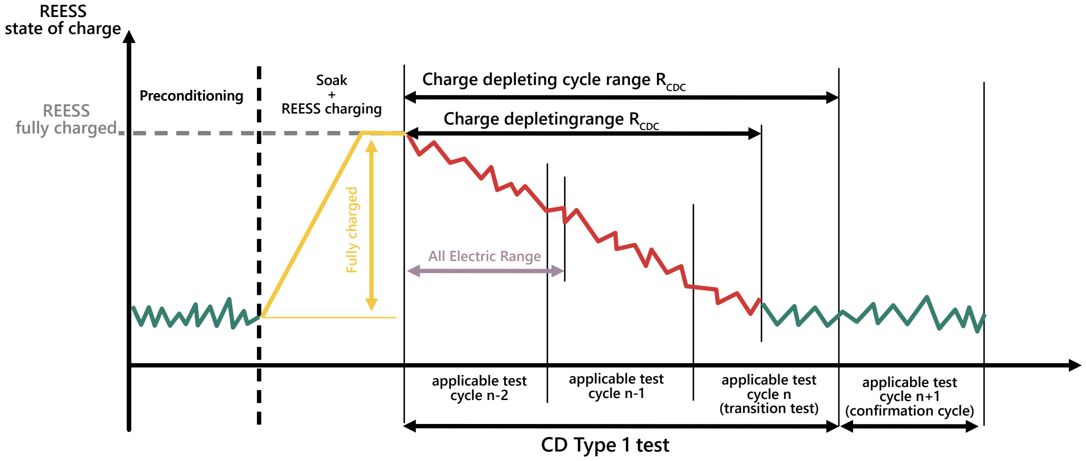

Figure 1.5: CD Type 1 test [10]

The end of the charge-depleting Type 1 test is reached when the break-off criterion, described by Eq. (1.1), is verified for the first time. The number of applicable WLTP test cycles up to and including the one where the criterion was reached is set to *n+1*. The applicable WLTP test cycle *n* is defined as the transition cycle while the *n+1* as the confirmation cycle.

$$REEC_i = \frac{|\Delta E_{REESS,i}|}{E_{cycle} \cdot \frac{1}{3600}} = \frac{\int_{t_0}^{t_{end}} U_i(t) I_i(t) dt}{\int_{t_0}^{t_{end}} F(t) d(t) dt} < 4\% \tag{1.1}$$

where:

- $REEC_i$ is the relative electrical energy change for the i-th cycle of the CD test;
- $\Delta E_{REESS,i}$ is the variation of electrical energy of the REESS during i-th cycle in Wh;
- E_{cycle} energy demand related to the complete driving cycle in Ws;
- I_i is the electric current of the REESS during the cycle i in A;
- U_i represents the voltage of the REESS during the cycle i in V;
- $d(t)$ is the traveled distance at the instant t in m;
- $F(t)$ represents the driving force at the instant t in N and that is expressed by:

$$F(t) = f_0 + f_1 \cdot v(t) + f_2 \cdot v^2 \tag{1.2}$$

where:

- f_0, f_1 and f_2 are the road load coefficients for the test vehicle under consideration in N, $\frac{N}{km/h}$ and in $\frac{N}{km/h^2}$respectively;
- $v(t)$ is the vehicle speed in km/h

Moreover, the CD Type 1 test defines the All-Electric Range (AER) as the distance driven when the first engine start occurs and it is expressed by the purple line in Fig. 1.5.

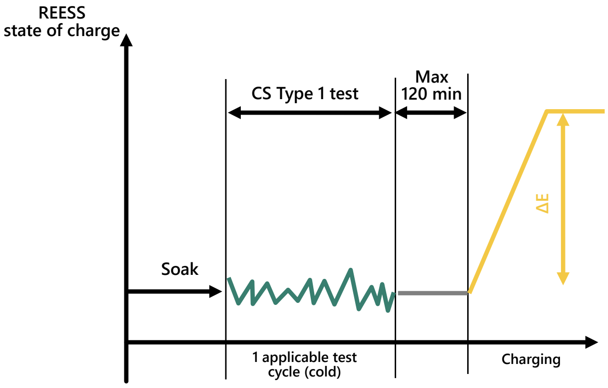

Figure 1.6: CS Type 1 test [10]

- **CS Type 1 test**: after the soaking period the procedure continues without recharging the REESS, as shown in Fig. 1.4. The test provides for a set of n CS Type 1 cycles, represented in Fig. 1.6, where the first one is called *reference cycle*. The other $n-1$ cycles have to contain at least one measurement with a negative charging balance $E_{REESS,i}$, and one measurement with a positive charging balance.

An additional correction of the measured CO_2 shall be applied if $\Delta E_{REESS,CS}$ calculated as Eq. (1.1) is negative, thus corresponding to the discharging of REESS, and the following constraint is verified:

$$c = \frac{|\Delta E_{REESS,CS}|}{E_{f,CS}} > 0.005 \tag{1.3}$$

where c is the correction criterion and $E_{f,CS}$ is the charge-sustaining energy content of the consumed fuel during the test, calculated as:

$$E_{f,CS} = 10 \cdot Q_{hv} \cdot m_{f,CS,nb} \cdot d_{CS} \tag{1.4}$$

where Q_{hv} is the heating value of the fuel (specified in [10]) in $\frac{kWh}{l}$, $m_{f,CS,nb}$ is the fuel consumed during the CS cycle in $\frac{l}{100km}$, the suffix nb stands for *not balanced* and d_{CS} is the total driven distance during the test in m. The factor 10 is only the conversion factor to Wh.

If these conditions are verified, the CO_2 must be corrected considering the electrical energy consumption for each WLTC phase (shown in Fig. 1.3) as follows:

$$m_{CO_2,p} = m_{CO_2,nb,p} + K_{CO_2} \cdot E_{CS,p} \tag{1.5}$$

where $m_{CO_2,nb,p}$ is the CO_2 emission of phase p in $\frac{g}{km}$, $E_{CS,p}$ is the electrical energy consumed in phase p of the WLTC (described in Tab. 1.1), and K_{CO_2} is the corrective factor, analytically defined by:

$$K_{CO_2} = \frac{\sum_{n=1}^{n_{CS}}((EC_{CS,n} - EC_{CS,avg}) \cdot (M_{CO_2,CS,nb,n} - M_{CO_2,CS,nb,avg}))}{\sum_{n=1}^{n_{CS}}(EC_{DC,CS,n} - EC_{DC,CS,avg})^2} \tag{1.6}$$

where:

- $EC_{CS,n}$ is the energy consumption associated with the n-th CS cycle, in kWh/km;

- $EC_{CS,avg}$ is the average energy consumption over the n CS cycles, in kWh/km;

- $m_{CO_2,CS,nb,n}$ is the net CO_2 emissions during the n-th CS test, in g_{CO_2}/km;

- $m_{CO_2,CS,nb,avg}$ is the average CO_2 emissions of the n CS test, in g_{CO_2}/km.

Consequently, the mass of CO_2 is weighted on the distance of each phase and then summed as in 1.7 both for the charge depleting and charge-sustaining test.

$$m_{CO_2,CS,w} = \frac{\sum_{i=1}^{i=4}(M_{CO_2,CS,nb,n} \cdot d_i)}{d_{tot}} \tag{1.7}$$

where d_i is the driven distance of the i-th phase in km.

Furthermore, the regulation introduces the utility factors (UF), which are ratios based on driving statistics depending on the range achieved in charge-depleting condition and they are

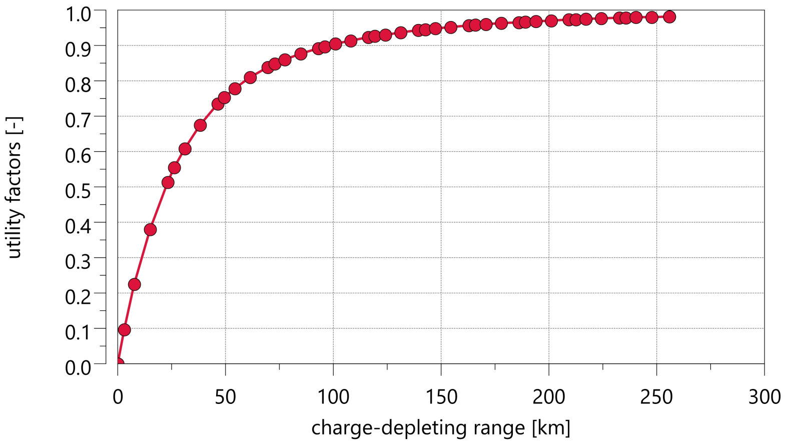

Figure 1.7: Utility factors

reported in Fig. 1.7 [10]. The UFs are used to weigh the charge-depleting and charge-sustaining exhaust emission compounds, CO_2 emissions, and fuel consumption for Off-Vehicle Charging (OVC) HEVs, as described by Eq. (1.8).

$$m_{CO_2,w} = \sum_{p=1}^{k}(UF_p \cdot m_{CO_2,CD,p}) + (1 - \sum_{p=1}^{k}(UF_p) \cdot m_{CO_2,CS,w} \tag{1.8}$$

1.2.1.1 Eco-innovation bonus

Even if the WLTC simulates the real-driving CO_2 emissions more accurately than the previous NEDC, a certain discrepancy between declared and real-world CO_2 and pollutant emissions remains [11]. On the one hand, this is related to the more dynamic and unpredictable driving behaviors [12][13] that can lead to an increase in CO_2 production by up to 95%. On the other hand, there are innovative technologies that produce real-world CO_2 savings beyond what is measured over the standardized test cycle during vehicle type approval, also referred to as eco-innovations. These were first introduced by the EU regulation 2009/R443 [14] for passenger cars and EU regulation 2011/510 for light commercial vehicles. In 2020, EU regulation 2019/631 [15] entered into force replacing the previous ones and setting new CO_2 emission targets and standards for new-registered cars and vans. Policy schemes similar to the European eco-innovation scheme can be found outside the European Union, like in USA [16] and China [17].

In an attempt to ensure that the eco-innovations provision incentivizes novel technologies, the approval procedure presented by the European Commission for eco-innovations [18] restricts which technologies are eligible, as summarized in [19]. In particular, eco-innovations:

- may not be currently mandated or part of the EC strategy to reduce CO_2 emissions from light-duty vehicles [20] (e.g., tire pressure monitoring systems, tire rolling resistance measures, gear shift indicators), and must be outside of type-approval conditions;

- must be novel and thus not have a market penetration higher than 3% in 2009;
- must contribute to the safety or performance of the vehicle, thus excluding nonessential comfort technologies like entertainment and air-conditioning systems;
- must produce measurable CO_2 savings during repeated tests, exceeding 1 g/km in a statistically significant manner.
- can be bundled in technology packages in order to meet the 1 g/km CO_2 saving threshold as long as they are functionally similar, i.e., aggregate CO_2 savings can be measured using one testing methodology.

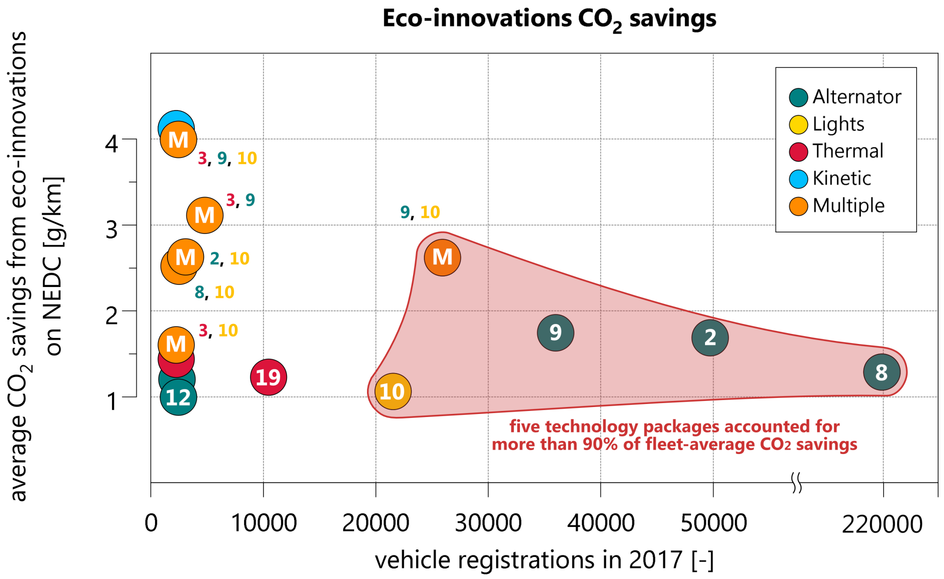

Figure 1.8: Average CO_2 savings and number of vehicles registered with each eco-innovation technology [19]

For the sake of clarity, Fig. 1.8 gives an example of the eco-innovations used in the 2017 new passenger car market in terms of average emission reduction and the number of cars equipped with it. Because some vehicles were sold with multiple eco-innovations, several markers represent combined eco-innovations. The figure shows that five eco-innovation technology packages accounted for more than 90% of fleet-average CO_2 savings, which are reported here as a reference:

- innovative alternator with high-efficiency diodes (eco-innovation 8), developed by Bosch and by far the most impactful eco-innovation. Although it had a relatively minor impact on CO_2 emissions for a single vehicle, with CO_2, it was installed in more than 200.000 new cars in 2017;

- high efficient alternator with synchronous active rectification (eco-innovation 09) also developed by Bosch;
- another highly efficient alternator (eco-innovation 2) presented by Valeo;
- lighting technologies (eco-innovation 10) by Daimler

A noteworthy technology is an adaptive state of charge control in hybrids (eco-innovation 04) developed by Bosch. In fact, the functions developed and presented in this dissertation would be left apart by the type approval regulations but may be proposed as eco-innovations technologies. Thus, the functions will not only provide more efficient energy management of the vehicle but also possibly help the OEM with CO_2 credits.

1.2.2 Criteria Pollutants

The US Environmental Protection Agency (EPA) denominates the "criteria" air pollutants because it sets standards for them based on the criteria, which are characterizations of the latest scientific information regarding their effects on health or welfare [21]. These pollutants are particulate matter, photochemical oxidants (including ozone), carbon monoxide, sulfur oxides, and nitrogen oxides. In particular:

- **Carbon monoxide (CO)**: predominantly controlled by the fuel–air mixture in the cylinder, independently of fuel type [22]. With a rich mixture, more fuel than the stoichiometric amount can react with the air in the cylinder. Therefore, not all of the fuel can be completely burned. Conversely, with lean mixture, the probability of complete combustion increases and the CO decreases. The CO formation can be described by the combustion reaction:

$$\mathrm{C}_x\mathrm{H}_y + \mathrm{zO_2} \longrightarrow \mathrm{aCO_2} + \mathrm{bCO} + \mathrm{dH_2O} \tag{1.9}$$

  where $x = a + b$, $y = 2d$, and $z = a + b/2 + d/2$.

- **Unburned hydrocarbons (HC)**: primarily formed from the hydrocarbons-based present in the fuel that partially reacts, recombines, or remains unburnt. Even the partial oxidation and evaporation of the lubricant oil could generate a small amount of HC.
- **Nitrogen oxides (NO_x)**: they include both nitrogen monoxide (NO), which is predominant during combustion [23], and nitrogen dioxide (NO_2) species. Their formation was described by the well-known Zel'dovich mechanism, further extended by Lavoie [24], and comprises three reactions for near-stoichiometric fuel–air mixtures:

$$\mathrm{N_2} + \mathrm{O} \leftrightarrow \mathrm{NO} + \mathrm{N} \tag{1.10}$$

$$\mathrm{N} + \mathrm{O_2} \leftrightarrow \mathrm{NO} + \mathrm{H} \tag{1.11}$$

$$N + OH \leftrightarrow NO + O \tag{1.12}$$

On the other hand, NO_2 is formed by NO being further oxidized following the forward reaction:

$$NO + O \leftrightarrow NO_2 \tag{1.13}$$

- **Particulate matter (PM) and number (PN)**: generally formed in the rich regions of the combustion chamber, at temperatures around 1400°C and pressures of 100 bar. The particulate matter or "soot" are also grouped with respect to the diameter, while also the number of particles is regulated.

Due to their inherent harmfulness to human beings, and the increasing number of passenger cars and transportation vehicles on the roads, in Europe the criteria pollutants have been regulated since the 1990s by means of the Euro emission standards [25], setting more stringent limits. The Fig. 1.9 shows the emissions limits trend for Diesel passenger cars from the Euro 3 (2000) to the actual in-force regulation Euro 6 (2015), where for example the NO_x limit is decreased by 84%.

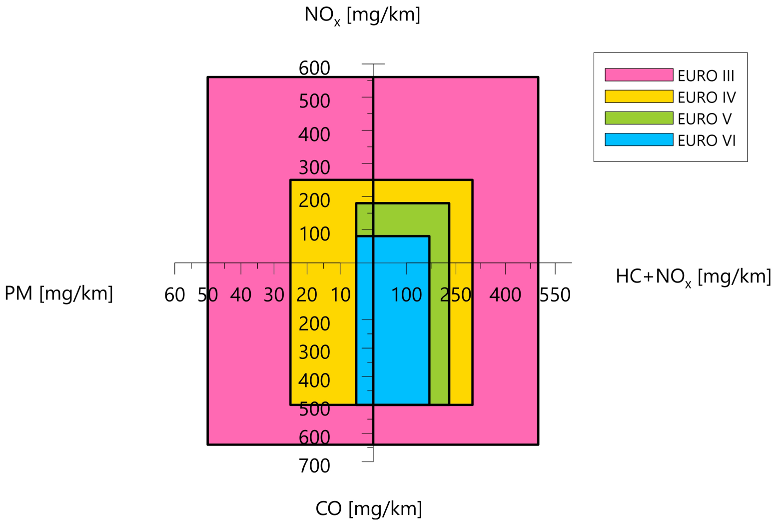

Figure 1.9: Diesel passenger cars EU regulations limits trend from Euro 3 to Euro 6

For a matter of completeness, the not-to-exceed limits introduced by the in-force regulation EU2012/R459 [26] are reported in Tab. 1.2, both for gasoline and diesel passenger cars, since the limits will be used in Chapter 9 to assess the performance of the developed strategies. In Tab. 1.2 THC are the total hydrocarbons, NMHC are the non-methane hydrocarbons, PM and PN are the particulate matter and number respectively.

In order to further reduce emissions on the road to climate neutrality, the EC is planning to introduce more demanding limits with the upcoming Euro 7 regulation, which should come into

Table 1.2: Euro 6 criteria pollutants limits [26] compared with the two Euro 7 scenarios introduced in [27]

		Euro 6		Euro 7	
		PI	CI	Scenario A	Scenario B
CO	mg/km	1000	500	300	100
THC	mg/km	100	-	*tbd*	*tbd*
NMHC	mg/km	68	-	*tbd*	*tbd*
NO_x	mg/km	60	80	30	10
THC + NO_x	mg/km	-	170	-	-
PM	mg/km	4.5	4.5	*tbd*	*tbd*
PN	n/km	6×10^{11}	6×10^{11}	1×10^{11}	6×10^{11}
CH4	mg/km	-	-	10	5
N2O	mg/km	-	-	10	5
NH3	mg/km	-	-	5	2

force between 2025 and 2027. According to the first draft proposed in [27], the Euro 7 regulation would require that the emission limits, besides being lower than Euro 6 ones, are enforced in nearly any possible operating condition. Focusing on pollutant emissions limits, two different scenarios have been proposed within the current draft, referred to as Scenario A and the more demanding Scenario B. The criteria pollutants limits are reported in Tab. 1.2, where the reduction of 90% of NO_x emissions and the introduction of new regulated species are observed. NO_x emissions control will become critical considering this challenging limit and the new testing conditions which will increase the impact of cold start phases on the whole driving cycle. Therefore, car manufacturers would be required to adopt extremely advanced after-treatment technologies to fulfill such demanding emission standards, leading to increased manufacturing costs [28].

1.2.2.1 Real-driving emissions

Initially, EU regulators were using the NEDC to certify exhaust emissions of cars and light commercial vehicles in an easy, repeatable, and reproducible manner. The test is performed at the chassis dynamometer in a vehicle-emissions laboratory under well-defined temperature and humidity ambient conditions. Nevertheless, modern vehicles complete the NEDC using a modest share of available engine power and covering a limited portion of possible real-world operating conditions. In fact, the researchers reported growing discrepancies between laboratory and on-road emissions from 9% in 2009 to a peak of 42% in 2015 [29], especially for nitrogen oxide (NO_x) emissions [30]. To overcome this problem, in 2017 the European Council introduced the WLTP for the type approval, as already explained in Chapter 1.2.1. In addition to the WLTP laboratory tests, the Real-Driving Emissions (RDE) test cycle, represented in Fig. 1.10, has been adopted. This four-part package regulation was introduced over the course of three years between September 2017 and September 2020 for the type approval of light-duty vehicles in the EU. The RDE test uses a portable emissions measurement system (PEMS) to measure the gaseous emissions, emitted during the road driving test. Pollutant limits are only defined for NO_x and PN according to the Euro 6 limits expressed in Tab. 1.2 multiplied by a conformity factor. This allows vehicles to be measured with higher pollutant levels during an RDE test than the Euro 6 standard by including the measurement uncertainty of PEMS.

During an RDE cycle, a car is driven on public roads over a wide range of different conditions, so it's easy to understand how it can differ from a laboratory test. The vehicle must follow a speed profile that has to satisfy a series of requisites defined by the R1151 regulation, Annex IIIA [10]. These are related to maximum/minimum accelerations, average speeds (for all the phases), time share, altitude, and three different zones, and are summarized in Tab. 1.3 and Tab. 1.4.

Table 1.3: Distance and speed specifications for each urban, rural, and motorway part of the RDE test

Trip specifications		**Provision set in the legal text**
Total trip duration		Between 90 and 120 min
Distance	Urban	> 16 km
	Rural	> 16 km
	Highway	> 16 km
Trip composition	Urban	29% to 44% of the distance
	Rural	23% to 43% of the distance
	Highway	23% to 43% of the distance
Average speeds	Urban	15 to 40 km/h
	Rural	Between 60 km/h and 90 km/h
	Highway	> 90 km/h (> 100 km/h for at least 5 min)

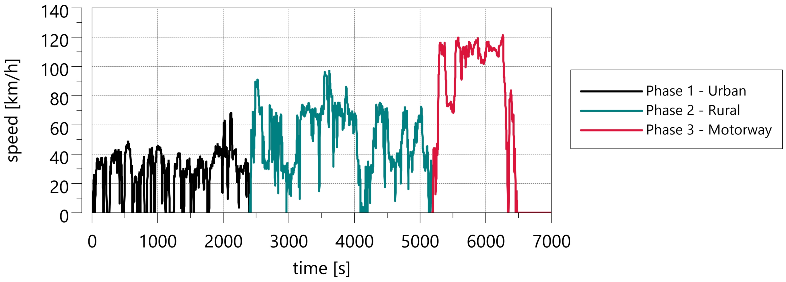

Figure 1.10: Example of a Real-Driving Emissions driving cycle with a focus on each phase

To be valid, each section of an RDE trip (urban, rural, and motorway) must be below the line in Fig. 1.11 showing speed multiplied by acceleration ($v * a$) and above the line showing relative positive acceleration (RPA). As clearly explained in [6], three possible RDE trips are plotted to illustrate how dynamic boundary conditions work. In this case, only Trip 1 is valid, while Trip 2 would be too aggressive in urban driving and Trip 3 too passive on both rural and motorway sections.

Table 1.4: Boundary conditions for RDE test [6]

Parameter		**Provision set in the legal text**
Payload		≤ 90% of maximum vehicle weight
Altitude	Moderate	0 to 700 m
	Extended	Between 700 and 1300 m
Altitude difference		No more than a 100-m-altitude difference between start and finish
Cumulative altitude gain		1200 m/100 km
Ambient temperature	Moderate	0°C to 30°C
	Extended	From –7°C to 0°C and 30°C to 35°C
Stop percentage		Between 6% and 30% of urban time
Maximum speed		145 km/h (160 km/h for 3% of motorway driving time)
Dynamic boundary conditions (see Fig. 1.11)	Maximum metric	95th percentile of $v * a$
	Minimum metric	RPA (relative positive acceleration)
Use of auxiliary systems		Free to use as in real life (operation not recorded)

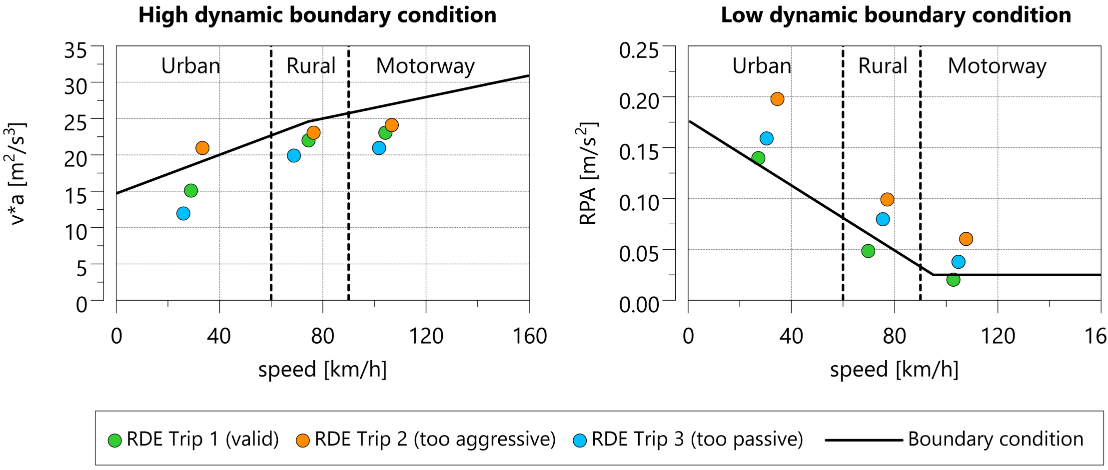

Figure 1.11: Dynamic boundary conditions with three illustrative RDE trips. [6]

Despite the in-force RDE trip definition is moving closer to the real-world driving operation, [27] highlights that there are several maneuvers not covered properly. Euro 7 proposal defines a more stringent real-driving procedure with the aim to clear the gap between the type-approval tests and the real world. In particular, vehicle laboratory testing would be maintained only for CO_2 and pollutants that cannot be measured with PEMS, while a wider range of ambient temperatures and altitudes would be investigated during the road tests. Moreover, there would be no substantial limitations on the driving cycles to be considered for the vehicle type approval procedure, meaning that any driving cycle longer than 5 km and any possible performed maneuver will be considered valid for the test, since no more speed, acceleration, and road grade limitations are provided.

The differences between the in-force RDE type approval procedure and the RDE proposed by Euro 7 are summarized in Tab. 1.5.

Table 1.5: Comparison of testing methods on RDE cycles according to in-force regulation and the Euro 7 proposal

Parameter	Euro 6	Euro 7
Ambient temperature	Moderate: 0 ÷ 30°C Extended: -7 ÷ 35°C	-10 ÷ 40°C -
Average Speed	Urban: 15-40 km/h	-
Altitude	Moderate: 0 – 700m Extended: 700 – 1300m	- -
$a * v$ [95th]*	Limits defined in [31]	-
Positive elevation	Total: <1200 [m/100km] Urban: <1200 [m/100km]	- -
Trip distance	Urban/Rural/Motorway >16 km each	> 5 km

1.3 Advanced powertrains

As a response to the stringent regulations presented above, the OEMs boost research and development to define more efficient and clean solutions [32]. In the following paragraphs, the more relevant components, architecture, and technologies will be briefly discussed, starting from the countermeasures to abate criteria pollutants, then analyzing the different hybrid powertrain typologies developed so far to reduce CO_2 emissions, and finally presenting the innovative technologies introduced to make the vehicles as sustainable and safe as possible.

1.3.1 Exhaust after-treatment systems

Exhaust after-treatment systems (EATS) for internal combustion engines have been in development for over 60 years, with the first publication being presented in 1957 by Cannon et al.[33] of Ford and in 1959 by Nebel and Bishop [34] of General Motors. As noted by [35], the researchers have found ways to improve the efficiency and efficacy of catalytic converters which translates into lower component and operating costs for the EATS overall. Due to the inherent nature of the several criteria pollutants introduced in 1.2.2, the EATS require specialized components to ensure the highest conversion efficiency possible, leading to complex layouts such as the one shown in

Fig. 1.12. Moreover, the criteria pollutants formation heavily depends on the different kinds of the engine (e.g., spark ignition, compression ignition), the fuel composition, and the mixture formation. Therefore, in the following paragraphs, an overview of the commonly adopted components is given for each pollutant species.

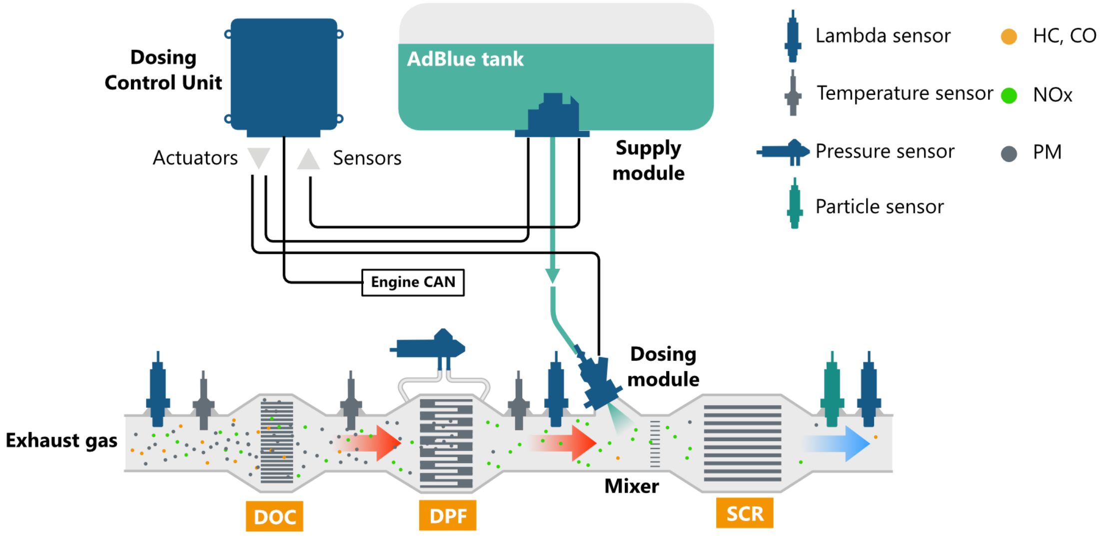

Figure 1.12: Example of a diesel EATS compliant with Euro 6 [36]

1.3.1.1 CO and HC oxidation

- **Oxidation catalysts**: they were developed by Engelhard Corporation in 1973 [37] to lower the emissions of carbon monoxide (CO) and hydrocarbons (HC) in the exhaust from gasoline spark ignition (SI) engines, and installed in Light Commercial Vehicle (LCV) from model year 1975. The oxidation catalyst was introduced in response to the 1970 Clean Air Act, resulting in an emissions reduction of 95% in the following decade [38]. The oxidation catalyst assumed a more important role in emissions abatement with the arrival of compression ignition (CI) engines, where it became known as the diesel oxidation catalyst (DOC), as shown in Fig. 1.12. The performance of the DOC especially depends on the operating temperature, on the precious metal catalyst used, and the washcoat that supports it. In fact, it has an operating temperature range (250-600°C [39]) outside of which its activity can fall off severely. For catalysts in general, the activity within the catalytic converter is commonly assessed by the light-off temperature, which corresponds to the reaching of 50% conversion, T_{50}. Focusing on the oxidation reactions, within the DOC the pollutant emissions are oxidized as follows:

$$C_xH_y + (2\,x + {}^1\!/\!_2 y)O_2 \rightarrow xCO_2 + {}^1\!/\!_2 yH_2O \tag{1.14}$$

$$2\,CO + O_2 \rightarrow {}_2CO_2 \tag{1.15}$$

where the HCs are oxidized to form CO_2 and water vapor as shown in Eq. (1.14) using a generic HC compound (C_xH_y), and CO is oxidized to CO_2 following Eq. (1.15), completing the combustion of the fuel-derived emissions species. Both reactions are exothermic, thus it can be used alongside a late injection of fuel to heat up the downstream components and trigger particulate filter regeneration. Moreover, the oxidation catalyst can also significantly influence the ratio of the nitrogen oxide (NO_x species in the exhaust gas, as nitric oxide (NO) can be oxidized to nitrogen dioxide (NO_2) or vice versa as expressed by Eq. (1.16):

$$2\,NO + O_2 = 2\,NO_2 \tag{1.16}$$

influencing also the performance of the downstream abatement systems, which will be presented in the next paragraph.

- **Three-way catalyst (TWC)**: they became predominant as a response to the regulations regarding NO_x, developed by adding the reduction of NO_x (expressed in Eq. (1.17)) as the "third-way" to the original oxidation catalyst. Thanks to the implementation of the three-way catalyst (TWC), the exhaust emissions from light-duty vehicles with SI engines have been drastically reduced by up to 95% with respect to the 1970s [38].

$$2\,NO = N_2 + O_2 \tag{1.17}$$

The conversion efficiency of the TWC, depicted in Fig. 1.13, is strongly affected by λ, that is the ratio between the current air-fuel ratio (AFR) and the stoichiometric value for the given fuel. In fact, if the engine operates in lean conditions ($\lambda > 1$), the exhaust gas is in a net oxidizing condition favoring the abatement of HC and CO, while penalizing the reduction of NO_x. Conversely, if the engine works rich ($\lambda > 1$). Thus, the SI engines are operated near the stoichiometric AFR ($\lambda = 1$) thanks to a closed-loop control to ensure that the TWC facilitates the three key redox reactions for criteria pollutant abatement, which is represented by the gray area in Fig. 1.13. Moreover, TWCs are designed to store (and subsequently release) excess oxygen, thus allowing a more efficient reduction of NO_x, and oxidation of HCs and COs, if the AFR is forced to oscillate around stoichiometry by the Engine Control Unit.

1.3.1.2 NOx reduction

- **Lean NO_x-trap (LNT)**: it was first presented by Johnson Matthey [40] aiming at reducing NO_x in a lean condition. In fact, it adsorbs and stores NO_x from the exhaust gases when it is in a net oxidizing state. The LNT is then regenerated by desorbing the NO_x and reducing it to

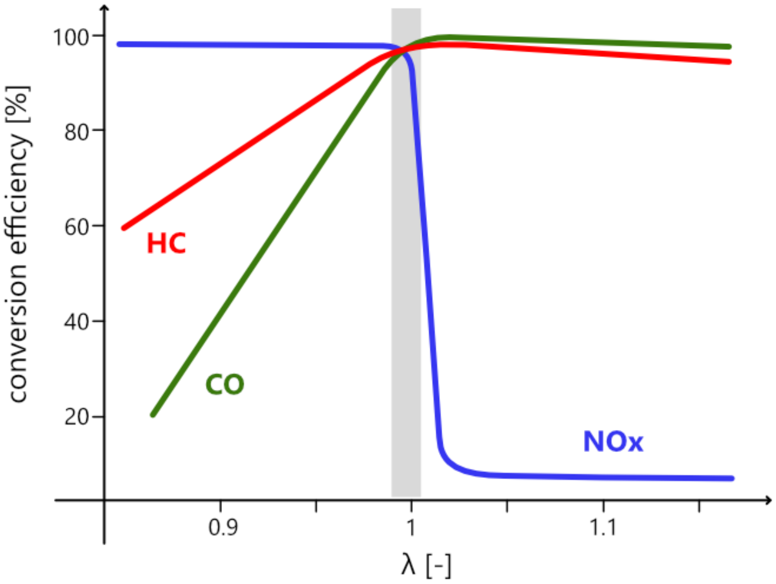

Figure 1.13: Qualitative representation of conversion efficiency of a TWC for each species

N_2 during a fuel-rich combustion mode. The reducing agents are hydrocarbons (HC), carbon monoxide (CO), and hydrogen gas (H_2) which are generated by the partial decomposition of the fuel in the engine under rich operating conditions. In their basic function, LNTs are similar to the TWC, since they use HC and CO to reduce NO_x, and NO_x and residual oxygen (O_2) to oxidize the HC and CO, but LNT perform these steps cyclically in series, instead of simultaneously [23]. Therefore, its implementation presents inherent complexity, since it requires specific control of the engine operation mode. Moreover, the most effective catalyst for LNT function is platinum (Pt), which is expensive, and the LNT requires a substantial loading of Pt for good performance through the useful life of the engine, up to two times the loading of TWC.

- **Selective Catalytic Reduction (SCR)**: introduced in the US for gas turbines in the 1990s [41], then adapted for other industrial applications, such as refineries and plants, and marine engines, all of them characterized by large displacement and quasi-steady-state operation. The first production application dates back to 2004 by Nissan [42] for heavy-duty vehicles, then broadly diffused in LCV after regulations became more demanding, as shown in Fig. 1.9. In general, the SCR system is able to selectively reduce NO_x despite the presence of O_2 by reacting with ammonia over a catalyst. Since ammonia has been declared harmful to human beings, its direct use has been ruled out. Thus, ammonia is indirectly delivered by using urea in an aqueous solution, as the ammonia source. The urea is sprayed into the exhaust pipe upstream of the SCR system as described in Fig. 1.12, where it decomposes into ammonia and CO_2 as shown by Eq. (1.18), Eq. (1.19), and Eq. (1.20). The thermolysis of the urea is limited by the temperature that must be above 200°C.

$$CO(NH_2)_{2,acq} \rightarrow CO(NH_2)_{2,gas} + nH_2O \tag{1.18}$$

$$CO(NH_2)_2 \rightarrow NH_3 + HNCO \tag{1.19}$$

$$HNCO + H_2O \rightarrow NH_3 + CO_2 \tag{1.20}$$

Consequently, the ammonia reacts with the NO_x on the catalytic sites in the SCR as described by the following chemical reactions:

$$4\,NH_3 + 4\,NO + O_2 \rightarrow 4\,N_2 + 6\,H_2O \tag{1.21}$$

$$4\,NH_3 + 4\,NO_2 \rightarrow 4\,N_2 + 6\,H_2O + O_2 \tag{1.22}$$

$$2\,NH_3 + NO + NO_2 \rightarrow 2\,N_2 + 3\,H_2O \tag{1.23}$$

Eq. (1.21) represents the standard stoichiometric SCR reaction in presence of oxygen, while by contrast Eq. (1.22) is slower and so called "slow SCR reaction". On the other hand, the Eq. (1.23), where both NO and NO_2 participate in the reaction, is considerably faster than the other two, thus, it is named "fast SCR reaction [23]. Moreover, the conversion efficiency strongly depends on the NH_3:NO_x and the NO_2:NO_x ratios, the ammonia “slip” through the system, and the production of N_2O that is a significant GHG.

1.3.1.3 Particulate matter

- **Particulate filters**: firstly introduced for CI engines, in the last years they started to be applied to SI engines, especially those with direct injection (DI) fuel systems, usually referred to as DPF for diesel, like in Fig. 1.12, and GPF for gasoline. Since the PM is not a specific chemical species but a compound of unburned additives of lubrication oil and engine debris upstream, the particulate filters perform a mechanical filtration: the exhaust flow enters through open channels, encounters the plugs on the back end, and is forced to flow through the porous walls of the ceramic substrate to be able to exit through a channel open on the downstream end, as schematically represented in Fig. 1.14. As the particulates are trapped in and on the wall, they are creating partially clogged wall pores and a surface particulate filter cake leading to an unsuitable pressure drop. As a consequence, the particulate filters required a periodical regeneration to remove the trapped particles, as already anticipated in the previous paragraphs. In general, the regeneration is done by means of oxidation reactions with oxygen or nitrogen oxides and can be active, if it is triggered periodically, or passive, if it is performed continuously. In the first case, the temperature of the exhaust has to be increased to favor the oxidation reactions, and it can be done by heating the exhaust gases or increasing the in-cylinder combustion temperature. As previously mentioned, the DOC can be used also as a gas pre-heater. In fact, with a late cycle, or post fuel injection, the fuel enters directly into the DOC that oxidizes it (with an exothermic reaction) thus triggering the regeneration. On the other hand, if passive, the NO_2 already present in the exhaust is used to oxidize the stored particulate matter without forcefully increasing the gas temperature [23].

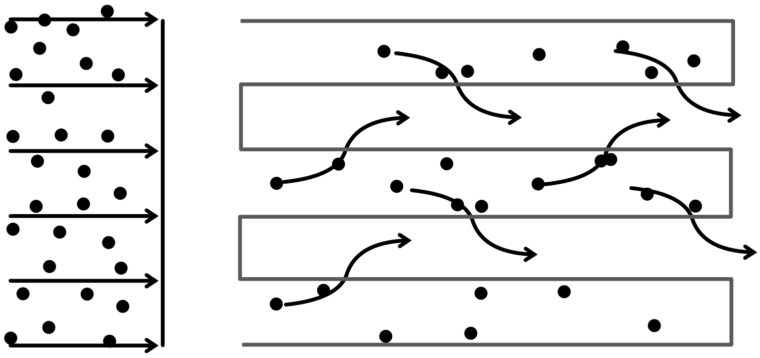

Figure 1.14: Schematic representation of the flow through the PF walls

1.3.1.4 Advanced EATS

Section 1.2 introduced the proposal of the EC in terms of future regulations, that aim at filling the gap between laboratory tests and real-world operation by lowering the criteria pollutants limits and introducing a less restricted RDE driving cycle. In this condition, even a modern vehicle with state-of-the-art EATS, like the one shown in Fig. 1.12, would not be enough. In fact, the proposed RDE cycle would increase the relevance of localized events, such as the high-power cold starts, where the EATS works in low efficient conditions. To overcome this problem, OEMs have started to develop innovative solutions to directly heat the exhaust gases without modifying the engine control strategies (e.g., late injection, early exhaust valve opening) and so avoiding a lower engine efficiency. The more promising technologies investigated so far are the implementation of an electrical heater or a diesel mini-burner.

With an electrically heated catalyst, a resistive heating element is placed in the exhaust system just upstream of the leading element of the EATS, such as the DOC. The main challenge with an electrical heater is the power required for effective heating, and the effect of that electrical power on fuel consumption. Conversely, mini-burners can provide 10-30 kW [23] of thermal power but present several challenges such as maintaining stable and clean combustion, additional fuel consumption, and a more complex layout.

1.3.2 Hybrid electric vehicles

The regulations presented in Section 1.2 put in evidence also the necessity to reduce the GHG emitted by transportation, so the OEMs needed to develop more efficient powertrains alongside the EATS presented in the previous chapter. A promising solution in terms of CO_2 reduction is the introduction of a secondary energy source, that can be of different natures (hydraulic, mechanical, electrical, etc). These innovative layouts are broadly discussed in literature in the latest years, especially analyzing the Hybrid Electric Vehicles (HEV) in terms of powertrain configuration, control strategies, and achievable benefits [43–46].

They comprehend also an electric REESS which is usually represented by a battery. The voltage and the capacity of this component are chosen on the base of the desired power output, defining the degree of electrification described by Eq. (1.24).

$$HD = \frac{P_{S,max}}{P_{S,max} + P_{ICE,max}} \tag{1.24}$$

where $P_{S,max}$ is the maximum power of the secondary source of energy while $P_{ICE,max}$ is the maximum power deliverable by the engine. Moreover, one or more Electric Motors (EM) are installed, as well, not only for traction purposes but even for transforming vehicle kinetic energy into electrical energy for battery recharging during deceleration phases (braking).

The advantages of HEVs consist in combining the characteristics of pure-electric and conventional vehicles, allowing to reduce the global energy consumption of the vehicle, and in particular:

- **regenerative braking**: the possibility to recover energy during braking phases instead of dissipating it using mechanical brakes;

- **load-point shift**: for a given speed, the operating point of the engine could be shifted to a higher efficient point by increasing the requested torque and using the energy in advance to recharge the battery. This functionality can be achieved with an energy management strategy of the power required by the engine;

- **downsizing**: since electric machines can provide part of the torque requested for traction, the engine displacement can be reduced;

- **zero-emission policy can be achieved**: in certain areas the use of the engine could be prohibited to maintain air pollution levels below a certain threshold. This task can be achieved by an HEV by addressing the full amount of torque requested to the electric motors.

On the base of what has been said so far, it's possible to distinguish the following typology of HEVs, also represented in Fig. 1.15:

- **Micro Hybrid** - $HD \sim 5\%$: vehicles equipped with an EM directly coupled to the engine with stop/start functionality. Most of them also have advanced energy management functions, which optimize the consumption of the low voltage (LV) battery;
- **Mild Hybrid EV (MHEV)** - $HD \sim 15\%$: these types generally use a compact electric motor (usually $< 20kW$) to provide stop/start features, extra power assistance during accelerations and regenerative braking. The battery is still LV allowing a minimum range of full-electric drive;
- **Full Hybrid Electric Vehicle (FHEV)** - $HD \sim 35\%$: the EMs and the battery increase in size, allowing an extended full-electric drive. The recharging of the battery can happen only with breaking recuperation and with the ICE; in this case, zero-emission policy can be fulfilled;
- **Plug-in HEV (PHEV)** - $HD \sim 50\%$: generally an FHEV with Off-Vehicle Charging (OVC) capability and an increased energy storage capacity. This allows the vehicle to drive in all-electric mode with a range that depends on the battery size and its mechanical layout (series or parallel) and shall be connected to the main electricity supply through a socket. As with pure electric vehicles, the total emissions saving, for example in CO_2 terms, depends on the electric energy production mix of the given country.

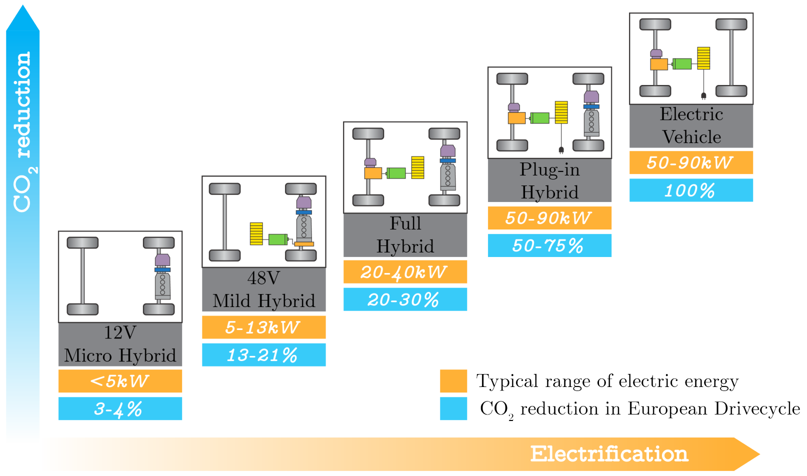

Figure 1.15: Overview of the Hybrid Electric Vehicle depending on hybridization degree and CO_2 reduction

Then, different layouts can be defined depending on how the energy flows from the energy storage (tank for ICE or battery for the EMs) to the wheels:

- **Series**: the series layout provides torque at the wheels solely by using electric motors, like electric vehicles, and the aim of ICE is to recharge the battery with the generator. The powertrain is equivalent to an EV, but since the vehicle also includes an engine, it is considered a hybrid.

  - **Parallel**: both the engine and the electric motor(s) are connected to the wheels, and their mechanical torque can be summed for propulsion. This cooperation allows to avoid engine working points where the specific fuel consumption is high.
  - **Series/parallel**: hybrid vehicles that share characteristics of both series and parallel layouts. In particular, the EM powers the vehicle from a standing start and at low speed whereas, as the speed increases, ICE and EM work together to efficiently provide the power required. As can be expected, the system is more complex featuring a *power split device* and a *generator*.

    Power split: both series and parallel working modes are applied simultaneously. This layout allows higher degrees of freedom than the parallel one and higher efficiency than the series one, but with a higher cost and complexity;

For what concern the HEVs parallel topology, several architectures are possible by varying the position of the electric machines within the driveline. As shown in Fig. 1.16, they can be defined as follow:

- **P0**: the engine is coupled to the motor through a belt, so the electric machine is called Belt-driven Starter Generator (BSG);
- **P1**: the EM is directly mounted on the crankshaft, upstream of the clutch, and it is named Integrated Starter Generator (ISG);
- **P2**: the EM is separated from the engine by a clutch, thus allowing pure electric drive;
- **P3**: the EM is mounted on the secondary shaft out of the gearbox;
- **P4**: the EM is connected to the front or rear wheels by means of a transmission ratio;

Introducing a different type of energy flow (electrical energy) in addition to the chemical one, engineers have to face new challenging problems. In fact, while the available space remains the same, the components rise in number: one or more electric motors, a bigger battery, a more powerful control unit, and the inverters have to be rationally placed inside the vehicle. Adding new components doesn't imply only a different spacing configuration but also means a more complex control at the system level.

1.3.3 Connected and autonomous vehicles

Since navigation systems are increasingly employed in the automotive sector, the available map data may not only be used for routing purposes but also to enable advanced in-vehicle applications [47]. The area of potential features reaches from headlight control up to active safety applications. With the ongoing development of navigation-based ADAS features, the interface to access the so-called ADAS Horizon is of rising importance. At this end, Advanced Driver Assistant Systems Interface Specifications (ADASIS) is an industrial platform where map providers and automotive

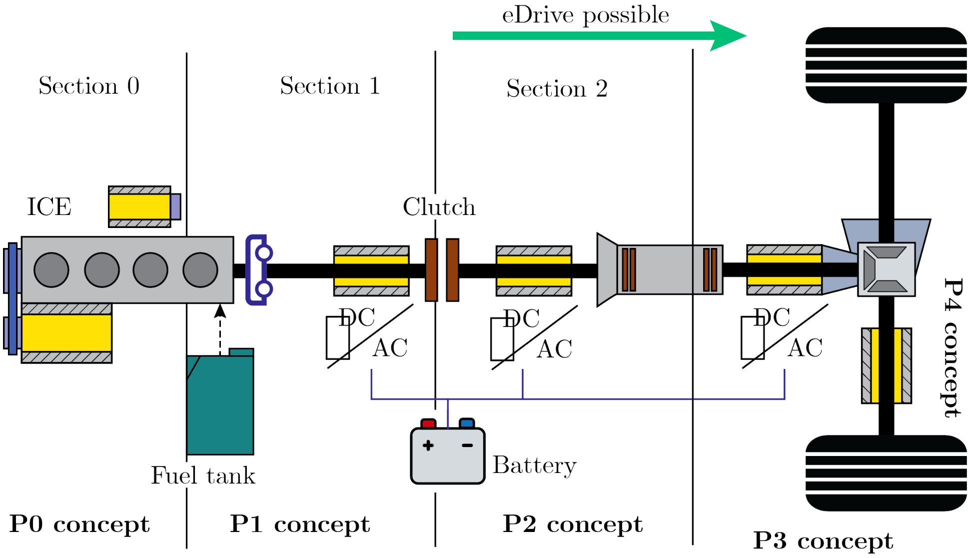

Figure 1.16: Hybrid architecture depending on EM(s) position [43]

developers work together to standardize the map data. The method of how a vehicle's control unit could be provided with the navigation data is specified as well in the ADASIS protocols [48, 49].

To enable this kind of technology, on-board vehicle sensors play a vital role in driving automation, providing the spreading concept of data fusion in order to improve navigation data availability as well as reconstruct an electronic horizon of upcoming events. In general, sensors include:

- **LIDAR (LIght Detection And Ranging)**: surveying method that measures the distance to a target by illuminating that target with pulsed laser light;
- **RADAR (RAdio Detection And Ranging)**: object-detection system that uses radio waves to determine the range, angle, or velocity of road objects;
- **Camera**: a video sensor used to analyze the environment outside and inside the vehicle.

Moreover, advancements in wireless communication technologies, sensor fusion, imaging technologies, Big Data, and analytics have created opportunities for automotive manufacturers to discover a wide range of solutions for multiple applications. Miniaturization of electronic components, advancements in navigation, and adoption of smart devices are expected to lead to advancements in the Vehicle-to-Everything (V2X) communications industry [50–54]. It is expected to show high growth potential for the development of future connected cars that will be able to interact with the surrounding environment to improve driver safety. One of the practical applications of such technologies implies reducing traffic congestion, which leads to an increase in fuel consumption and to a worsening of urban air pollution. As an additional drawback, the economic impact of traffic jam-related problems is not negligible [55], as well.

According to 3GPP [56], V2X technologies include communication between different entities and the ego-vehicle, both for safety and non-safety application. Navigation data exchange is made via different vehicular communication networks, also called nodes. Depending on the type of the node, the following classification applies:

- **Vehicle-to-Vehicle (V2V)**: the moving nodes are represented by the vehicles communicating with each other
- **Vehicle-to-Infrastructure (V2I)**: road infrastructures transmit navigation data regarding traffic lights timing, road works, traffic congestions, and so on
- **Vehicle-to-Network (V2N)**: the ego-vehicle communicates with IT networks and/or data centers
- **Vehicle-to-Pedestrian (V2P)**: vehicles connect with pedestrians or bikers on the road to prevent accidents

Chapter 2

Literature review

Chapter 1 depicted a challenging background for the automotive sector, with stricter and stricter regulations and complex powertrain layouts. In this context, vehicular connectivity and vehicle hybridization proved to be promising solutions for OEMs. Thus, this research project focuses on innovative solutions both in terms of energy management of Plug-in HEVs and emissions reduction. For this reason, a comprehensive literature review on such topics is here presented. Firstly, a broad overview of the relevant energy management strategies (EMSs) implemented and studied so far is given. Then, the more relevant studies and applications of advanced emissions reduction strategies are presented as well. Alongside their description, an analysis of the possible use of vehicular connectivity is done. Finally, a presentation of the commonly used simulation and testing environments exploiting V2x is also provided.

2.1 Energy management control strategies

In general for HEVs, and in particular for PHEVs that are capable of pure electric drive, the EMS evaluates the more efficient operating condition for the propulsion system and actuates several hybrid functions (e.g., load-point shift, regenerative breaking), as introduced in Chapter 1, by coordinating the other control units, thus the powertrain control is defined as *hierarchical*. In general, this kind of functions are deployed within a supervisory control unit, usually named Hybrid Control Unit (HCU) or Vehicle Control Unit (VCU). Focusing on a parallel hybrid, which is the one considered in this dissertation, the torque requested by the driver for traction, T_{req}, can be provided by the engine and/or by the motor(s), and so a torque-split factor, $u_s(t)$, can be introduced. So, the torque request to the engine and the electric motor(s) may respectively be defined as: $T_{ICE}(t) = (1 - u_s(t)) \cdot T_{req}(t)$ and $T_{EM}(t) = u_s(t) \cdot T_{req}(t)$. In this case, if $u_s(t) = 1$ the vehicle is driven in pure electric mode, conversely if $u_s(t) = 0$ the ICE is used as the sole energy source. The amount of power to reserve for battery recharge is one of the tasks of the EMS and it may actively be controlled by applying load-point shift to the ICE ($u_s(t) < 0$).

A first distinction can be made whether optimal control theory is adopted to define the control policy or not. As proposed in [57, 58], EMSs can be classified as:

- *heuristic*
  such strategies are based on physical considerations or intuitions and are usually developed considering maps or rules to evaluate the operative working conditions of the powertrain. Thus, there is not an explicit optimization of the power distribution;
- *sub-optimal*
  the main objective of the control algorithm is achieved by optimizing instant by instant the energy flow within the powertrain, thus minimizing a certain cost function, which could represent the energy consumption of the vehicle. Since the optimization is performed locally, namely at each calculation step of the control unit, the solution of the minimization process is inherently sub-optimal;
- *optimal*
  in this case, a global optimization is performed, meaning that the solution is the one with the best performance in terms of cost function minimization all over the possible actuation set-points. This implies the a priori knowledge of the driving cycle, with a consequent high computational load.

Since V2x technologies enhanced the possibility of retrieving navigation data and making them available on board, the prediction of future conditions of the powertrain has been investigated with the main objective of providing the supervisory controller with detailed information regarding the status of the components. In this way, the power distribution of the hybrid vehicle can be optimized while satisfying global constraints for different scenarios, such as ensuring all-electric driving in a Zero-Emission Zone.

Thus, the control strategy can be referred to as:

- *causal*
  when no prediction on the route ahead is available and then used. Then, the powertrain control is governed by a cause-effect relationship between the actuator set-points and the state variables;
- *non-causal*
  when state variables are predicted on the base of the available information of the driving mission.

Numerous investigations have been conducted on the energy management strategies [59–62] and more extensive reviews on the topic are available in literature, spanning among different characteristics such as numerical comparisons [63, 64], real-time applicability [65], and future trends for EMSs [66, 67]. In the next paragraphs, a general overview of the worth mentioning control policies is given.

2.1.1 Heuristic control strategies

As suggested by their name, heuristic energy management control strategies are based on intuitions and physical considerations to evaluate the required power distribution among the powertrain. Although a wide range of possibilities exists in choosing the vehicular parameters and the conditions to be satisfied for this task, several common design guidelines can be found.

Since HEVs have been introduced to reduce the fuel consumption and so the CO_2 production, firstly the internal combustion engine should be used in high-efficiency working conditions (for HEVs), and, in particular for PHEVs, as less as possible. Another useful guideline suggests maintaining the battery state of charge (SoC) within a certain range (for HEVs), which may correspond to the entire working range of the battery defined by the manufacturer (for PHEVs). As a result of the application of these principles, the operative mode of an HEV, without off-board charging capabilities, is typically represented by a charge-sustaining (CS) mode around a certain target value of SoC. On the other hand, for PHEVs the operative mode may result in a combination of charge-depleting (CD) and then charge-sustaining modes, since the battery can be recharged by plugging the vehicle to the grid. Therefore, the use of the electric energy stored in the REESS is always encouraged when possible because the conversion efficiency of the chemical energy of the fuel to the electrochemical one of the battery is quite low.

The aforementioned principles can be applied by means of different approaches: map-based and rule-based. The first ones are defined by multi-dimensional look-up tables usually as a function of the driver torque request, the vehicle speed, and the battery SoC. Moreover, the upper and lower thresholds can be dynamically managed by means of *fuzzy-logic* rules [68, 69]. On the other hand, rule-based strategies rely on a set of conditions defined considering vehicular parameters such as the ones above mentioned [70]. Other parameters such as the power limitations of the electric machine(s) during pure electric driving [71] can be considered for this purpose. In this case, fixed thresholds have to be established to fulfill all the conditions. Such rules can be implemented in the control policy in different ways: for example, by means of finite state machines, representing the state condition to be fulfilled for the transition from one state to another, or through hard-coded boolean conditions.

Moreover, the heuristic approach does not require to develop any optimization algorithm, which is usually more complex due to its mathematical formulation. This implies a lower computational burden required instant by instant to the supervisory controller. For those reasons, heuristic strategies, especially rule-based ones, are widely used in the automotive industry to control the energy management of the hybrid powertrain. Nevertheless, an intensive calibration campaign is needed to properly tune the look-up tables or the threshold values of such strategies. In order to speed up this process and increase the energy efficiency of the power distribution, optimal energy management strategies can be used as benchmarks [72, 73].

2.1.2 Optimal and sub-optimal control strategies

To properly understand the optimization-based control strategies, the analytical formulation of the energy management problem for HEVs is provided in this section.

Generally for HEVs, the aim of an optimal energy management strategy is to minimize the global energy consumption and so the CO_2 production, which can be represented by a mathematical function depending on actuator set-points and state variables. The latter is usually known as *cost function*, or *performance index*. In this case, the energy management strategies aim to provide a solution to this problem, which is represented by the control law that minimizes the cost function over a certain time horizon. Thus, as proposed in [64, 74], a formulation of the cost function J for HEVs including the fuel consumption can be expressed as:

$$J = \int_{t_0}^{t_f} \dot{m}_f \left(\mathbf{x}(t),\mathbf{u}(t),t\right) dt \tag{2.1}$$

where $\dot{m}_f$ is the instantaneous fuel mass flow rate, $\mathbf{x}(t)$ and $\mathbf{u}(t)$ are the vectors of the variables states of the system and the control inputs, and $[t_0,t_f]$ is the time domain in which the optimal control problem is defined. Its solution is then represented by the control policy $\mathbf{u}^*(t)$ that minimizes the performance index over the given time interval and is subjected to global boundary conditions, related to the state of the system:

$$\psi\left(x(t_f),t_f\right) = 0 \tag{2.2}$$

and local constraints, representing the admissible actuator set-points and the physical limitations of the system in terms of available torque and power, admissible speed, and SoC:

$$\begin{cases} G(\mathbf{x}(t),t) \leq 0 \\ \mathbf{u}(t) \in U(t) \end{cases} \tag{2.3}$$

The worth-mentioning optimal strategies are listed below:

- Dynamic Programming
- Pontryagin's Minimum Principle [74]
- Convex Optimization

Since this research project does not focus on optimal control development and a wider analysis has been already given by [75], only Dynamic Programming is briefly discussed in the following paragraph for a matter of completeness. The latter is an optimal, non-casual algorithm that relies on a numerical approach based on the *Principle of Optimality* proposed by the mathematician Richard E. Bellman in 1952 [76–78]. In particular, considering the powertrain as a generic dynamic system evolving over time, and assuming that all the intermediate states of this evolution are known (so a non-causal approach), the aim is to find the control policy that minimizes the given cost function. The Bellman's principle ensures that the policy related to the last part of the problem belongs to the overall optimal control policy if it is optimal by itself. Therefore, the optimization is performed in a backward-facing approach, starting from the final state to the initial one, and establishing the optimal control input at each step. In this way, it can be noticed that an a priori knowledge, or at least a prediction, of the state vector is needed. Moreover, the dynamic, multi-stage decision process strongly increases the computational load required to numerically solve the problem. For this reason, optimization-based algorithms are theoretically not implementable online. Nevertheless, since the optimality of the provided solution, they are used as benchmarks for the calibration of other energy management strategies [72].

On the other hand, sub-optimal control policies solve the optimal energy management problem defined in Eq. (2.1) by locally minimizing the cost function, which means considering a time horizon compatible with the calculation step of the supervisory controller.

The main applications of this approach are represented by

- Model Predictive Control (MPC) [79]
- Equivalent Consumption Minimization Strategy (ECMS)

Local optimization is a reliable trade-off between the real-time capability of heuristic EMSs and the optimal solution guaranteed by non-causal controllers. In particular, the ECMS has been demonstrated in [80] to be directly deducible from the optimal Pontryagin's Minimum Principle, if properly formulated. Sub-optimal strategies are inherently implementable online and do not require an intensive calibration effort. For these reasons, this kind of strategy has been chosen to be further improved with vehicular connectivity data and then deployed in the HCU. In particular, the focus is put on the ECMS, which is then briefly described hereafter.

2.1.2.1 Equivalent Consumption Minimization Strategy

The Equivalent Consumption Minimization Strategy was initially formulated by Gino Paganelli in 1999 [81] and then applied as a practical solution for the energy management problem in HEVs [82, 83].

It is based on the empirical consideration that a virtual fuel consumption can be attributed to the usage of the electric energy of the battery. Under this assumption, the cost function to be minimized can be represented by an equivalent fuel consumption that can be formulated as follows:

$$\dot{m}_{f,eq} = \dot{m}_f + \dot{m}_{f,b} \tag{2.4}$$

where

$$\dot{m}_{f,b} = s(t)\frac{P_b(t)}{Q_{lhv}} \tag{2.5}$$

In other words, the electrical energy used by the battery and the chemical energy of the fuel are correlated by an *equivalence factor* $s(t)$, shortly EF.

Other supervisory controllers perform a local minimization of an equivalent fuel consumption that considers both the real fuel consumption and the electrical power requested to the battery. Such controllers are usually considered as sub-optimal [72, 80, 84–86]. Another option is represented by optimization-based controllers, which are based on optimal control algorithms and can determine the global optimal solution for the powertrain control [58, 87, 88]. Such methodology guarantees the best energy management, but still presents issues related to online implementation, due to the high computational effort required, and the need to exactly predict future operating conditions. These energy management strategies have been deeply studied and several of them have been already deployed on board the vehicles on the market. To keep pace with the regulations trend, innovative technologies are being implemented both on the vehicle and the infrastructure, such as wireless communication, and cloud computing. Consequently, they can provide the aforementioned strategies with a forecast of the driving path ahead, resulting in more efficient energy management. Musardo et al. [89] and more recently Onori et al. [90] presented remarkable improvements to make the ECMS a real-time control strategy. In particular, in the latter work, an adaption of the equivalence factor based on a feedback from SoC has been proposed, defining the so-called Adaptive-ECMS (A-ECMS).

Several studies highlighted the benefits of future driving information for energy management strategies. An improved A-ECMS based on long-term target driving cycle recognition and short-term vehicle speed prediction is presented by Yu et al. [91]. It can optimize the equivalence factor based on mileage, SoC, long-term driving cycle, and real-time vehicle speed, resulting in a reduction of fuel consumption of 8.7%. Similarly, algorithms can determine the optimal SoC trajectory according to the traffic information, while the equivalence factor is regulated dynamically, thus enabling effective tracking of the reference SoC trajectory [92, 93]. Sun et al. [94] presented a different A-ECMS that uses a historical driving profile for equivalence factor estimation, the proposed strategy is able to foresee the change of the driving behaviors and adjust the equivalence factor more reasonably. Furthermore, Soldo et al. [95] developed a LEZ-anticipating control strategy for a PHEV bus with P2-type parallel powertrain configuration. The control strategy is based on a combined RB/ECMS, and it is superimposed by generating an optimal SoC reference trajectory aimed at enabling pure electric driving within forthcoming LEZs and minimizing the overall fuel consumption. The optimal SoC reference trajectory is generated by minimizing its length over traveled distance.

In light of this, the A-ECMS represents a good trade-off for control policy and it is suitable for implementing our predictive functions, considering both the computational power of the vehicle control unit and the results obtained so far in the literature. A general overview of the previous works performed on the topic is given in Tab. 2.1, with a focus on the improvements in ECMS on-board implementation and vehicular connectivity integration.

Table 2.1: Overview of remarkable studies on advanced energy management strategies

Authors	Application	Connectivity	Strategy	ZEZ	Results	Comments
Musardo et al. [89]	Diesel P2 PHEV	-	A-ECMS	-	FC: -18%	improvements in real-time implementation of the ECMS
Onori et al. [90]	generic HEV	-	A-ECMS	-	results closed to optimal ones	on-line adaptation of the equivalence factor with low-computational burden
Yu et al.[91]	PHEV	long- and short term connectivity	predictive A-ECMS	-	FC: -8.7%	effectiveness of driving cycle recognition and speed profile prediction in fuel consumption reduction
Lei et al. [92]	PHEV	traffic information	simplified DP and predictive A-ECMS	-	FC: -6.1%	equivalence factor adaptation based on traffic information to follow a target SoC trajectory
Chen et al. [93]	PHEV	traffic information	predictive A-ECMS	-	FC: -9.7%	
Sun et al. [94]	Power-split HEV	hystorical driving data	A-ECMS	-	FC: -3%	foresee change of the driving behaviors and adapt the equivalence factor consequently
Soldo et al. [95]	P2 PHEV Bus	long-range connectivity	RB/ECMS	LEZ	results closed to optimal ones	combined RB/ECMS strategy to anticipate LEZ to minimize FC and granting eletrci drive
This Ph.D. research	Gasoline PHEV	real-time long range vehicular connectivity	predictive A-ECMS	ZEZ	FC: -20%	fuel consumption reduction while granting enough electrical energy to perform ZEZ, implemented in the control unit

2.2 Emissions management control strategies

Emissions reduction can be achieved by acting on engine control, thus directly avoiding the production of pollutants, or on the EATS, handling the thermal management to reduce the time required to reach light-off temperature. In particular, the first approach aims at using the engine in operating points with lower emissions flow rate, trying to affect fuel consumption the least possible. On the other hand, it is possible to raise the exhaust gas temperature and so to reduce the light-off time of the EATS, increasing the conversion efficiency, as described in Section 1.3. To do so, there are two possible ways: acting directly on the engine and the combustion, or externally heating the gases through dedicated components (e.g., EHC, burner). Hence, these solutions are described in detail in the following paragraphs.

2.2.1 Engine control

For what concerns engine control to reduce emissions, different solutions have been researched during the last decades. One of the commonly employed solutions is the start of combustion delay, both for diesel and gasoline engines, which can be very effective to reduce catalyst light-off time, however it leads to significant fuel penalty, which imposes limitations on its application. Higher idle speed provides a higher exhaust gas flow rate, speeding up the catalyst heating phase; however, it is not sufficient in itself and it also implies higher fuel consumption [96]. Moreover, during idle operation, Exhaust Gas Recirculation (EGR) and Variable Valve Timing (VVT) can help the catalyst's warm-up phase, but even in this case affecting engine performance [97]. A valid alternative that can be applied to HEVs is given by the request for a higher load to the engine, using the additional power to recharge the battery.

Another promising solution is to apply the same mathematical approach presented in Section 2.1, but considering the fuel consumption and the pollutant emissions as part of the same cost function. An Equivalent Emissions and Consumption Minimization Strategy (EECMS) has been developed by Nüesch et al. [98] that tracks a specific NO_x emission limit to be respected during the real driving. Under these conditions, the strategy is developed to minimize the fuel consumption in CS mode while respecting the NO_x limits, and the results show a reduction of fuel consumption of 7%. A similar methodology has been applied by Millo et al. [99], but in this case the engine NO_x flow rate has been inserted in the cost function by means of a NO_x flow rate equivalence factor. Here, the EECMS shows a reduction of the fuel consumption of 6.1%, engine out NO_x emissions of -16.1%, and tailpipe emissions of -12.6% on the WLTC. Moreover, Tribioli et al. [100] designed a supervisory controller, based on Pontryagin's Minimum Principle, for online energy management optimization of a diesel PHEV with a parallel architecture while reducing particulate matter at the same time, reaching a decrease of -35% of PM emissions but leading to a worsening of the fuel consumption. The above-mentioned approaches can be extended also to the optimal control as done by Simon et al. [101], where a pollutant-constrained optimal energy management is derived from the Pontryagin's Minimum Principle (PMP). Then, this online approach called the

Equivalent Consumption and Pollutant Minimization Strategy (ECPMS) has been developed and tested on a Hardware-in-the-Loop test bench, proving the following emissions reduction: for CO of -3.1%, for HC of -4%, and for the NO_x of -15.9%. Conversely, a fuel consumption increase of 4.6% has been observed. Another worth mentioning study, presented by Villani et al. [102], develops a DP-based energy management strategy for the HEV with a multi-objective cost function that takes into account engine start/stops and pollutant emissions. The results show that a trade-off solution can be selected, for which the fuel consumption is near-optimal (less than 5% increase), the engine start/stops are low, and the pollutant emissions are reduced by more than 50%.

Even in this context, the availability of navigation data from the V2x communication technology can be used to better improve the powertrain and the EATS efficiencies. In particular, Kuchly et al. [103] propose an online-oriented method based on a long-term vehicle speed prediction (~20min), using cartographic information such as speed limitation, road curvature, traffic, and road signs. The Pontryagin's Maximum Principle is then applied to this speed prediction signal to convert the optimal control problem into a root-finding problem, solved using an algorithm initialized by a black-box method trained offline, allowing high computational efficiency. Here, the beneficial effects are measurable as a reduction of 1.1% of fuel consumption and of 4.4% of NO_x emissions. Furthermore, also short-range and other traffic participants can be considered as well. Moreover, Xu et al. [104] developed a traffic scenario and powertrain model in different platforms with the capability of information interchange, simulating V2I communication. With DP optimization for a single trip and different driving conditions, NO_x can be reduced by 15% while FC increases by 3%. All the previous works have been summarized and compared to the methodology presented in this dissertation in Tab. 2.2.

Table 2.2: Overview of remarkable studies on advanced fuel consumption and emissions reduction strategies

Authors	Application	EATS	Connectivity	EMS	Results	Comments
Nüesch et al. [98]	Diesel HEV	not considered	-	EECMS	FC: -7%	minimization of CO_2 while keeping engine-out NO_x below a super-imposed limit
Millo et al. [99]	Multi-purpose diesel passenger car	DOC, SDPF	-	EECMS	FC: -6%; NO_x:-12%	minimization of CO_2 and tailpipe NO_x both as terms of the cost function
Tribioli et al. [100]	Diesel PHEV	not considered	-	PMP-based	FC: slight increase; PM: -35%	minimization of CO_2 and engine-out PM emission, Euro 7 oriented
Simon et al. [101]	Gasoline HEV	TWC	-	Optimal control + EECMS	FC: 4.6%; CO: -3.1%; HC: -4%; NO_x: -15.9%	minimization of tailpipe pollutants tested on very short and limited driving cycles
Villani et al. [102]	Range-Extender Gasoline HEV	TWC	known a priori	DP-based	FC: +5%; pollutants: -50%	minimization of tailpipe pollutants for a known pick-and-delivery cycle
Kuchly et al. [103]	Diesel PHEV	not considered	road curvature, traffic, speed limitations (20-minutes)	EECMS	FC: -1.1%; NO_x: -4.4%	minimization of CO_2 and engine out NO_x
Xu et al. [104]	Diesel	LNT	V2x (simulated with CarMaker)	DP	FC: +3%; NO_x: -15%	minimization of tailpipe NO_x for a simplified vehicle model
This Ph.D. research	Diesel PHEV	EHC, DOC, LTM-SCR, SDPF, SCR	-	MBS	FC: constant; NO_x:-22% on the R1151	minimization of NO_x with a cycle-undependant model-based strategy

TWC: three-way-catalyst; LNT: lean-NO_x trap; DOC: diesel oxidation catalyst; EHC: electrically heated catalyst; SCR: selective catalyst reduction;
LTM-SCR: low thermal mass SCR; SDFP: diesel particulate filter with SCR

2.2.2 After-treatment control

As mentioned before, a substantial reduction of pollutant emissions is achieved by considering the components of the EATS, and their performance parameters. One of them is the light-off temperature which can be used as a constraint in the cost function definition for both optimal and sub-optimal control policy. To this end, Guille des Buttes et al. present in [105] a pollution-centered energy management to decrease pollutant emissions during the catalyst start-off phase without affecting fuel consumption. The strategy has been developed using three-dimensional dynamic programming with a weighted objective function and taking into account the thermal dynamics of the catalyst monolith. However, the simplified models contain few parameters and consider the internal combustion engine as a black box, omitting the influence of its control parameters (e.g. air-fuel ratio and ignition timing). Nevertheless, the reduction can vary between 8 and 33%, depending on the driving cycle, while the fuel consumption remains constant.

In addition, focusing on the highest degrees of hybridization, which means full hybrid and plug-in hybrid vehicles, the advantages and flexibility introduced by this technology are even clearer if integrated with a predictive control strategy. Such information about future driving conditions could be also employed for the management of specific EATS devices, for example by developing smart strategies to optimize particulate filter regeneration [106] or urea consumption of SCR systems [107].

More in general, the OEMs have developed and tested different solutions to reduce the emissions and increase the powertrain efficiency even considering the implementation of more advanced components, and external heaters as introduced in Section 1.3. Hassdenteufel et al. [108] presented, in collaboration with BOSCH, a demonstrator vehicle equipped with high-pressure injectors, a new cat-heating model-based strategy, 2^{nd} generation gasoline particulate filter, and two TWCs, coupled with an external burner. The results are that conventional GDI vehicles still can be a viable solution to satisfy the upcoming Euro 7 regulation. Another possible solution is represented by the e-boost, which could take over from the turbocharger during the warm-up phase, but all these solutions of course imply the installation of further powertrain components, increasing the overall cost and complexity. The problem is more evident for HEVs, where the production cost is already high, and they introduce another issue related to the EATS, which is the high-power cold start. That situation can occur when the hybrid strategy requires the engine to start at a high load operation point even if the EATS is still cold due to the previous electric driving period.

In this context, according to the state of the art, electrically heated catalysts (EHCs), employing one or more discs upstream of the catalyst that are heated by current flowing in high-resistance circuits, provide an effective solution to reduce emissions during engine cold start without affecting engine performance, since they act directly on the exhaust line [109–111].

Hamedi et al. [112] a novel EHC control strategy is investigated to increase DOC conversion efficiency minimizing EHC electric energy consumption; the results show that a reduction of more than 70% of the cumulative CO and HC emission can be reached with respect to a standard post-injection strategy. According to Gao et al. [110], the implementation of a 12V electrical heater to a standard Diesel Euro 6 EATS leads to a significant reduction of the overall pollutant emission, reaching more than 60% of cumulative NO_x emission reduction along a cold start WLTC. The CO_2 percentage penalty due to the additional EHC energy consumption is also evaluated, showing values in the range of 6-9% depending on the considered EHC control strategy. Hofstetter et al. [109] evaluated the performance in terms of CO_2 and NO_x emission of a 48V P0 Diesel hybrid equipped with an EHC, compared to those of a conventional non-hybrid vehicle. The results show that, despite the fuel consumption penalty, the NO_x level can be reduced significantly especially during city and short-distance drives, while for the same NO_x emissions level, a CO_2 saving of 7% can be achieved. The effect of the addition of an EHC on the behavior of a DOC in a hybrid RCCI truck is studied by Garcia et al. [113]; in particular, the authors show that the electrical heating helps to reduce HC and CO emissions, which is the main challenge related to high-efficiency low-temperature combustion systems, even if in some cases the EURO 6 limits are exceeded anyway. Bargman et at. [111] evaluated the effectiveness of pre-heating a PHEV's after-treatment system by means of a 48V EHC. A reduction of more than 50% of the cumulative NO_x emission related to the first engine start is observed along the considered test cycle, showing the potential of such a system in solving the issue related to ICE high-power cold start. Schallhart et al. [114] considered an innovative conductive ceramic composite material for the SCR catalyst support for a Diesel passenger vehicle; the investigated material allows direct electrical heating of the catalytic converter, thus reducing the light-off time up to one-third with respect to the base system if a pre-heating phase is considered. Also here, the potential of the introduction of an EATS pre-heating phase for reducing tailpipe pollutant emissions is highlighted, introducing also the issue of how to predict engine start.

Therefore, even if this heating method needs the installation of an additional device and the availability of a significant amount of electric energy to power it, the promising results reached in terms of reduced catalyst light-off time and improved catalyst conversion efficiencies justify further development of this technology, especially considering the current powertrain electrification trend, which makes available the electrical power needed by the EHC. The overview of the worth-mentioning works is given in Tab. 2.3 with a focus on all the innovative technologies implemented to improve the after-treatment systems management.

Table 2.3: Overview of remarkable studies on advanced EATS management strategies

Authors	Application	EATS	Connectivity	Strategy	Results	Comments
Guille Des Buttes et al. [105]	Gasoline PHEV	TWC	known a priori	light-off optimization	FC: constant; NO_x: up to -33%	pollutants reduction during the catalyst start-off phase but with very simplified model
Hopka et al. [106]	6.7L conventional diesel vehicle	DOC, SCR, DPF	long-range connectivity	smart DPF regeneration	reduced soot load and number of interrupted regenerations	real-time implementation preliminary results
Caramia et al. [107]	Diesel PHEV	DOC, DPF, SCR	known a priori	minimizing energy and urea	NO_x always below law limit	NO_x reduction by optimizing the urea consumption and limiting the ICE torque
Hassdenteufel et al. [108]	Conventional GDI vehicle	GPF, 2x TWC, external burner	-	cat-heating model-based strategy	Euro 7 limits satisfied	state-of-the-art GDI vehicles still can be a viable solution
Hamedi et al. [112]	Diesel (single cylinder)	EHC, DOC, DPF	-	RBS	CO, HC: -70%	pollutants emissions reduced during cold-start phases proved at the test bench
Gao et al. [110]	Conventional diesel vehicle	EHC, DOC, DPF, SCR	-	RBS	energy consumption: +8%; NO_x: -60%	effectiveness of EHC on reducing emissions during cold start with electrical energy consumption
Hofstetter et al. [109]	Diesel 48V P0	EHC, DOC, SDPF, SCR	-	RBS	FC: -7%; NO_x below limit	optimize the CO2 emissions while meeting NO_x limits
Garcia et al. [113]	RCCI MD diesel PHEV	EHC, DOC	-	RBS	FC: up to 5%; HC, CO under Euro 6 limits	effectiveness of EHC on advanced combustion system
Bargman et at. [111]	Gasoline PHEV	EHC, TWC	-	pre-heating TWC strategy	NMOG+NO_x: -50%	pollutant emissions reduction during first engine start in the US06 cycle
Schallhart et al. [114]	Conventional diesel vehicle	conductive ceramic composite material SCR	-	direct electrical heating of the catalytic converter	light-off reduction time reduced of 65%	application of innovative conductive materials for impreoved pre-heating phase
This Ph.D. research	Diesel P2 PHEV	EHC, DOC, LTM-SCR, SDPF, SCR	known a priori	First ICE start prediction	NO_x: up to -50%	predictive pre-heating phase to NO_x reduction to satisfy the more demanding scenario of Euro 7

2.3 Testing and validation platform

The validation and verification of connectivity-based functionalities are becoming more demanding as they must be tested in a huge number of scenarios, regarding dangerous (e.g., emergency brake) and highly unpredictable situations (e.g., Collaborative Adaptive Cruise Control and connectivity-related functions) to be declared reliable [115]. The challenge is therefore to develop a testing and validation framework that can replicate the effectiveness of road conditions and traffic scenarios. In this way, it is possible to transfer the tests from the road to the virtual simulation, saving costs and time. Following this tendency, specific commercial software were developed and made available on the market, such as PreScan and ITS Modeller presented by Tideman and van Noort in [116], whose aim is to provide the automotive industry with a tool for developing connected vehicle systems from concept to production. Always in a virtual environment, Aramrattana et al. [117] presented a simulation framework (consisting of driving, traffic, and network-simulators) for testing and evaluating Co-operative Intelligent Transport Systems (C-ITS) applications. Once the simulation of vehicles and networks in a virtual environment is established, Xu and Shen [118] improve it with optimal energy management, which is tested using the short horizon information coming from the leading vehicle in the collaborative environment. Grahle et al. [119], from Bosch, used this simulation framework to evaluate the advantages of a route preview (long horizon) in order to determine in which part of the trip it would be more convenient to regenerate the DPF. Likewise, in Ford, Hopka et al. [106] translate that example into a real prototype controller mounted on a prototype vehicle. On the other hand, the short horizon communication is not implemented in this contribution. A similar on-road test is proposed by Menarini et al. [120] where a short-range wireless communication is tested with an Intersection Collision Warning function and then verified on a real vehicle. Symmetrically, the long horizon is left apart as well as the vehicle dynamics. An evolution of that work is presented by Szendrei et al. [121] where several On-Board Units (OBU) and Road-Side Units (RSU) hardware have been connected to a microscopic traffic simulator (Simulator of Urban Mobility - SUMO) to integrate real vehicular communication devices. This research focuses on the C-ITS simulation for automated vehicles while it does not simulate the vehicles' dynamics nor the long horizon connectivity. Simulation frameworks like these are used also for Automated Vehicles functions development as shown by Gelbal et al. [122], who set up a Hardware-in-the-Loop simulator for developing automated driving algorithms. In this case, the Real-Time PC carries out the simulations of other moving vehicles while also generating traffic scenarios while the prototype control unit runs the algorithm. However, the long horizon is not simulated even in this work. A step further was made by Shao et al. [123] who developed an Engine-in-the-Loop system integrated with a real-time traffic simulator (named VISSIM), to evaluate the performance of emerging connected vehicle applications. This allows a systematic evaluation of connected vehicle mobility and energy savings, as emissions and fuel consumption can be measured precisely. Then, a real vehicle equipped with an OBU is driving along with other connected vehicles. That vehicle data is transmitted to the

HiL, which reacts consequently. There is nothing concerning the long horizon, and, besides, it has been assumed that perfect communication is available between vehicles. Finally, Kim et al. [124] focused on the development of a sustainable framework for testing control strategies for Connected Automated Vehicles (CAVs). They presented an HiL where vehicle dynamics are up to ETAS DESK-LabCar, controlled by on-board ECUs i.e., MicroAutoBox and Matrix embedded PC-Adlink. The latter oversees the communication with the OBU and the cloud, respectively through Ethernet and LTE. The environment and the perception sensors are simulated with PreScan while the micro-traffic with PTV VISSIM. Such an advanced simulation framework is very interesting, but it has been presented with a short driving routine. The overmentioned state of the art is summarized in Tab. 2.4.

Table 2.4: Overview of remarkable studies on eHorizon simulation environments

Reference	Vehicle model	Long horizon	Short horizon	Cloud computing	Use cases	Major innovations
Tideman and Van Noort [116]	No	No	Simulated	No	C-ITS	Software for designing and evaluating connected vehicle systems
Aramrattana et al. [117]	Yes	No	Simulated	No	C-ITS (CACC)[1]	Simulator to involve human driver
Xu and Shen [118]	Yes	No	Simulated	No	C-ITS (CACC)	Optimal energy management with V2V data
Grahle et al. [119]	Yes	Simulated	No	No	eHorizon functions	Demonstrates the advantages of route information in DPF regeneration
Hopka et al. [106]	Real vehicle	Yes	No	No	eHorizon functions	DPF regeneration strategy with prediction of traffic and route information on-board
Menarini et al. [120]	No	No	Yes	No	C-ITS (ICW)	HiL system for developing connectivity controllers ready for the road
Szendrei et al. [121]	No	No	Yes	No	C-ITS (dynamic rerouting)	HiL system with V2x OBU/RSU support and real C-ITS protocol stacks and APIs
Gelbal et al. [122]	Yes	No	Yes	No	CAVs algorithms	Highly realistic HiL system for connected and autonomous driving functions
Shao et al. [123]	Real vehicle	No	Yes	No	C-ITS (CACC and emissions)	Engine-in-the-Loop that replicates a real vehicle on the road
Kim et al. [124]	Yes	No	Yes	Yes	CAVs algorithms	Connected HiL for developing and testing of on-board and in-cloud automated functions
This Ph.D. research	Yes	Yes	Yes	Yes	eHorizon functions, CAVs algorithms	Modular Connected HiL for developing and testing of on-board and in-cloud predictive eHorizon functions

[1] Between parenthesis there is the specific Intelligent Traffic System analyzed in the article

2.4 Innovative contribution of the dissertation

The present dissertation is focused on exploiting vehicular connectivity to improve energy and emissions management, in order to help the OEMs comply with future regulations. Firstly, a Speed Profile Prediction (SPP) algorithm has been developed [125] and formally presented in [75] to predict an energetically equivalent velocity trace based on navigation data. The speed profile is then forwarded to the Backward Vehicle Model (BVM) described in [126], which predicts the necessary amount of electrical energy to perform the ZEZ in full electric mode. This value, expressed in terms of a target SoC, is used as input for the energy management strategies under test. Regarding the latter, since the RBS introduced in [126] is not designed to work differently from the conventional Charge-Depleting / Charge-Sustaining (CD/CS) mode, in this work an Adaptive-RBS (A-RBS) has been defined. In particular, it uses the same reference SoC used by the A-ECMS to dynamically adapt the electric drive thresholds depending on the remaining distance from the ZEZ, thus working in a Charge Blended (CB) mode. To verify the improvements with respect to the RBS in terms of CO_2 reduction, the two strategies are compared on two different RDE cycles at the Software-in-the-Loop (SiL). The results show that the A-RBS outperforms the RBS only when the initial SoC is lower than the target SoC and so the HV battery must be charged. Conversely, the RBS is still more efficient when the initial SoC is higher than the target SoC and the CD/CS mode is required. Consequently, since the aim is to design a strategy that reduces the energy consumption in all the possible scenarios, a Combined-RBS (C-RBS) is finally defined to perform CB mode or in CD/CS depending on the initial value of the SoC. Finally, the A-ECMS and the C-RBS have been tested at the C-HiL on a driving profile measured on the road during a specific time slot of the day. Differently from the one presented in [127], this simulation environment presents a layout reduced in complexity as the sole Telecommunication Control Unit (TeCU) is in charge of querying the Map Service Provider (MSP) and gatewaying the data. Moreover, a Human-Machine Interface (HMI) has been introduced to be as close to the prototype vehicle as possible. More in detail, the vehicle HMI is replicated by a tablet running an Android-based Navigator App, that allows the driver to set the desired destination and to see the suggested route based on actual traffic conditions. Meanwhile, the related navigation data are collected from the MSP and sent to the TeCU. Moreover, if the actual position of the vehicle deviates from the route proposed by the app or if the actual level of traffic changes, the app can trigger the request for a re-routing. In these cases, the navigation data are refreshed, and the prediction is performed again, evaluating the updated target SoC. Besides, the tests have been conducted starting from different initial SoC values, during the same time slot of the recorded driving profile to reduce the natural randomness of the traffic conditions as much as possible. In conclusion, the simulations highlight both the goodness of the predictions even under varying traffic conditions, and the improvements brought by the A-ECMS in terms of CO_2 reduction.

Regarding the simulation environment in which the previous strategies have been developed and tested, this work counts on a highly detailed vehicle model (validated over experimental data) supervised by the production level HCU software unlike those presented in [116, 120, 121] with complete access to the components and controllers models. The HCU is then equipped with the typical V2x communication technologies, both for the long horizon such as in [106, 119], and the short horizon such as in [120–124]. Moreover, the connection to the private server enables the testing of cloud computing and predictive maintenance functions, as in [124]. So, the proposed HiL-based validation platform results in a more modular and universal tool for testing and validating predictive eHorizon functions. On one hand, it provides higher flexibility due to the possibility to test different kinds of predictive functions (long and short horizon, predictive maintenance) and the capability of acting on each component and controller model. On the other hand, it grants higher reliability, as both the hardware and the software are the same as those implemented on the vehicle, allowing seamless functions implementation on-board once validated at the HiL. Thus, it shortens the validation process and further reduces the gap between laboratory and on-vehicle tests.

The second part of this dissertation focuses on the evaluation of emissions reduction for a high-efficiency hybrid powertrain. As a first step, an advanced hybrid RBS has been developed and calibrated using a model-based approach resulting in a cycle-independent strategy that outperforms the default one. Then, since the hybrid powertrain is coupled with an advanced EATS, together with the availability of vehicular connectivity, a predictive thermal management strategy has been developed to avoid the problem of cold-start emissions. In particular, the potential of catalyst pre-heating by means of an electrical heater in reducing the overall emissions should be further investigated as one of the most effective and feasible solutions to solve the problem of cold starts on hybrid vehicles. The key enabler for the application of an EATS pre-heating to real driving cycles is the possibility to predict the engine start: therefore, this study proposes to take advantage of the knowledge of future vehicle operating conditions to predict engine first start and plan a pre-heating based on that to prevent cold start emissions. To the knowledge of the author, the contribution of a similar EHC predictive control function based on navigation data has not been investigated yet.

2.5 Organization of the dissertation

Following this introduction to the research topics and the presented novel contributions, the organization of the dissertation is as follows:

- in Chapter 3 the powertrain modeling of the high-performance PHEV under study is briefly analyzed, since it has been already discussed in detail in [75]. Then, the Connected HiL simulation environment is presented, with a focus on the navigation data exchange and the HMI development;
- in Chapter 4 the conventional RB strategies, so the Adaptive-RBS and the Combined-RBS, are introduced and tested on different RDE driving cycles; alongside, the Adaptive-ECMS is

briefly re-called from [126] as well as the predictive functions under test;

- in Chapter 5 the A-ECMS and the C-RBS are then compared at the C-HiL, on a measured driving cycle in the Metropolitan City of Bologna, using real-time navigation data forwarded by the TeCU. Then, the predictions are analyzed in terms of energy prediction assessment while the strategies' performance is evaluated by means of a fuel consumption comparison;
- in Chapter 7 the light commercial vehicle model used for the development of predictive emissions strategy is described, with a focus on the thermal model of the after-treatment components and their conversion efficiency, alongside the hybrid strategy developed for the purpose;
- in Chapter 8 the conventional RB strategy is presented and modified into a model-based strategy, to further optimize the fuel consumption and reduce the pollutants emissions independently on the driving cycle. Finally, the predictive functions are adapted for the specific application, in particular the BVM that has to be validated again. Hence, considering the available navigation data, the predictive pre-heating strategy is presented;
- in Chapter 9 the results of Urban RDE simulations at the MiL are then individually analyzed in terms of emissions reduction. Moreover, a possible alternative layout to reduce the overall cost of the EATS is finally introduced;
- in Chapter 11 the achievements of this work are analyzed, together with the possible future works to overcome the limits of this Ph.D. research project.

Part I

Energy management strategies

Chapter 3

Simulation environment

In this chapter, the focus is on the modeling of the considered hybrid electric powertrain whose main objective is to properly represent the energy flows within the powertrain itself in order to evaluate the fuel and energy consumption. At this aim, an overview of the vehicle under test is given, alongside the respective modeling approach. Moreover, the components of the powertrain are introduced and analytically described, with particular attention to the high-voltage (HV) battery, which plays a crucial role in HEVs. However, a more detailed analysis of them can be found in [75]. Finally, an overview of the Connected Hardware-in-the-Loop simulation environment is provided, with a focus on the long-range communication protocols implementation, testing, and validation.

3.1 Vehicle under test

The vehicle under test is a high-performance prototype Plug-in Hybrid Electric Vehicle equipped with a V10 5.2 liters FSI engine able to provide 533 Nm at 6500 rpm and two electric machines mounted on the front axle (in P4 position, as shown in Fig. 1.16). The latter can guarantee the four-wheel drive (4WD) to be independent by the state of charge (SoC) of the battery, as the conventional engine can work as a range-extender. In fact, the engine is coupled with an Integrated Starter Generator (ISG, P1), capable of recharging the HV battery independently or providing a positive boost. With respect to the original prototype presented in detail in [128], here the electric axle is powered by a high-voltage battery with a 2p93s layout, able to provide 19.4 Ah of total capacity (at 1C rate and T=25°C) and 384 V nominal voltage (at SoC=50% and T=25°C). The conventional powertrain is completed with a 6-speed gearbox. Then, the propulsion system is depicted in Fig. 3.1 and the vehicle's main characteristics are listed in Tab. 3.1.

Even if it is just a technology demonstrator, the vehicle had to run several validation processes, both at a component level and as a whole vehicle. From the simulation side, the prototype is entirely modeled in MATLAB & Simulink. The components' models are described in Paragraph 3.1.2 while

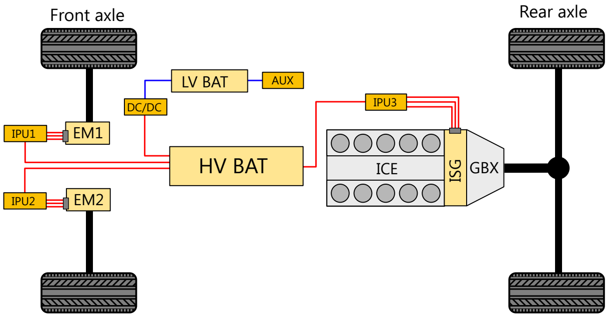

Figure 3.1: Prototype PHEV: P1P4 architecture layout

Table 3.1: Prototype PHEV: Vehicle powertrain specifications

Vehicle	Curb weight	1990 kg
	Configuration	P1P4, four-wheel drive
Engine	Type	Gasoline FSI V10
	Displacement	5.2 l
	Rated power	449 kW @ 8000 rpm
	Rated torque	533 Nm @ 6500 rpm
	Gearbox	6-AMT
Electric machines	Type	PM synchronous
	Continuous/peak power	64/140 kW
	Continuous/peak torque	145/350 Nm
	Maximum speed	8000 rpm
Battery	Type	Lithium-ion polymer
	Capacity (1C @25°C)	7.5 kWh / 19.4 Ah
	Nominal voltage	384 V

the controllers' models in Paragraph 3.1.3. All of them have been validated over experimental data and the results of the validation are shown in Paragraph 3.1.4.

3.1.1 Modeling approach for energy analysis

In order to properly conduct the energy analysis of the vehicle comprehending the developed control strategies, the *forward-backward* approach shown in Fig. 3.2 has been chosen for vehicle modeling. In this approach, the powertrain is dynamically modeled with a *forward* approach (also known as *dynamic* approach), meaning that the energy flows from the propellers to the wheels and the vehicle speed is the result of the control chain. The latter is based on a *backward* model, and so on the inverted path of the energy flow inside the vehicle, used by the driver to compute the torque set-point. On one hand, the accuracy of the speed-following control is increased due to the feedback of the effective vehicle speed, as it would happen for a realistic driver. On the other, the dynamic powertrain model ensures the power limitations of each component, introduced by the *forward-facing* energy flow. In this way, the actuators set-points evaluated by each tested strategy can be applied to the powertrain.

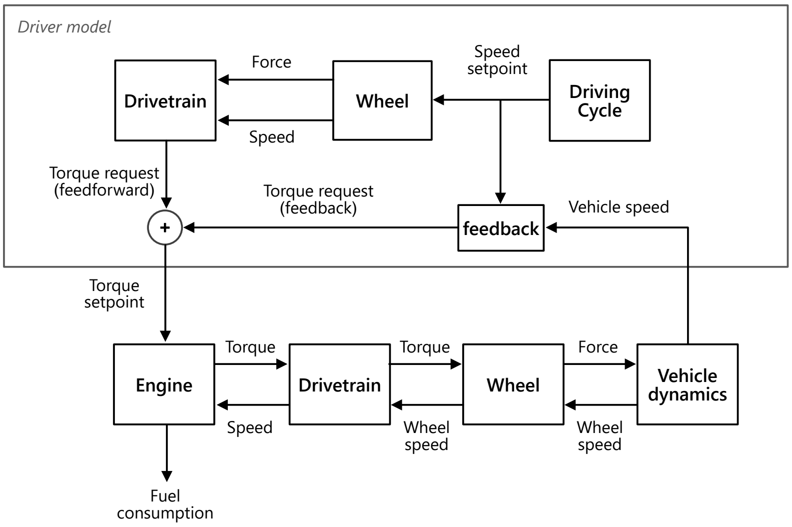

Figure 3.2: Forward-backward modeling approach based on the direction of the energy flow [74]

3.1.2 Powertrain modeling

Since the objective of the present work is the energy assessments of HEVs, the performance analyses focused on drivability (vehicle stability, handling, etc.) and comfort (noise, harshness, and vibrations) issues are neglected. For this reason, lateral and horizontal vehicle dynamics are not taken into account. Hence, considering Fig. 3.3, the fundamental equation representing the longitudinal dynamics of a vehicle in motion is the following:

$$m_v \cdot \frac{d}{dt} v(t) = F_t(t) = F_{mot}(t) - F_{res}(t) \tag{3.1}$$

where m_v, v are the mass and the speed of the vehicle, F_{mot} is the propulsion force supplied by the internal combustion engine and/or the electrical machines (P4), F_{res} is the resistant force acting on the vehicle, and F_t is the resulting traction force. The latter can be expressed as follows:

$$F_{res}(t) = F_a(t) + F_r(t) + F_g(t) \tag{3.2}$$

where F_a, F_r, and F_g are the aerodynamic friction losses, the rolling friction losses, and the gravitational force, respectively.

Another more practical solution is to consider the air and rolling friction losses together since

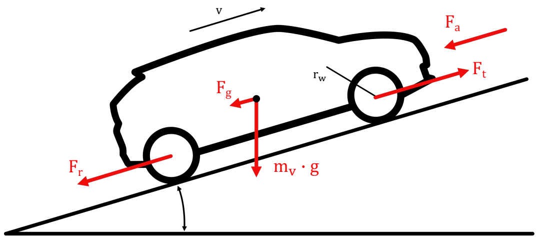

Figure 3.3: Forces acting on a vehicle in motion

they both depend on vehicle speed. In particular, their contributions can be gathered in a single polynomial expression as a function of $v(t)$ with coefficients depending on the considered vehicle and which can be practically obtained by means of a *coast-down test*.

As explained in [129], the test consists in driving the vehicle on a flat road at a certain reference speed and then starting the coast-down deceleration phase, which means the transmission shall be in neutral and the engine shall run in idle. Moreover, the brakes shall not be operated during coasting. Experimental data of measured vehicle speed are then fit with a regression curve, namely the *total-resistance curve*, which has the following form:

$$F_{cd}(t) = F_a(t) + F_r(t) = F_0 + F_1 \cdot v(t) + F_2 \cdot v^2(t) \tag{3.3}$$

where F_0 is the constant term [N], F_1 is the coefficient of the first-order term [N/(km/h)], F_2 is the coefficient of the second-order term $[\mathrm{N/(km/h)^2}]$.

The force induced by the gravitational field on the vehicle when driving on a road with a certain gradient is described by the following equation:

$$F_g(t) = m_v \cdot g \cdot \sin \alpha(t) \tag{3.4}$$

where $\alpha(t)$ is the slope angle [rad] of the road, which can be derived from the percentage slope $\alpha_{\%}(t)$ by the relationship

$$\alpha(t) = \arctan \frac{\alpha_{\%}(t)}{100} \tag{3.5}$$

Hence, the resistant force becomes:

$$F_{res}(t) = f_0 + f_1 \cdot v(t) + f_2 \cdot v^2(t) + m_v \cdot g \cdot \sin \alpha(t) \tag{3.6}$$

By substitution of Eq. (3.3), Eq. (3.4) in Eq. (3.2), the fundamental equation Eq. (3.1) can be written in the form of a non-homogeneous first-order non-linear ODE. Therefore, the acceleration and the velocity of the vehicle, which represent the output of the vehicle model, can be evaluated. Moreover, the vehicle is able to follow a given driving path thanks to a driver model. To improve the speed-following capability, the calculated vehicle speed is fed into a calibrated proportional-integral (PI) controller, that computes the accelerator and brake pedals position values.

Then, the powertrain main components, namely the engine, the electric motors, and the Automated Manual Transmission (AMT) have been modeled with Simscape mechanical libraries. More in detail, Simscape is a tool for modeling and simulating multidomain physical systems within the Simulink environment by means of physical connections [130].

3.1.2.1 Internal combustion engine

The combustion engine is modeled as a torque generator, where the requested torque input is evaluated by the supervisory controller and then saturated according to engine limitations, which depend on the temperatures of the oil and the coolant, and the engine speed. As shown in Fig. 3.4, a fuel consumption map is adopted, having as input variables the brake mean effective pressure (BMEP) and the speed of the engine, which has been generated by engine characterization at the test cell. For reasons of confidentiality, the fuel consumption has been normalized with respect to the maximum value. Moreover, an engine efficiency map, depicted in Fig. 3.5, is also implemented for the energy analyses and so the fuel consumption. Both maps are limited by the maximum torque curve (black line in bold), which depends on the engine BMEP and speed as well.

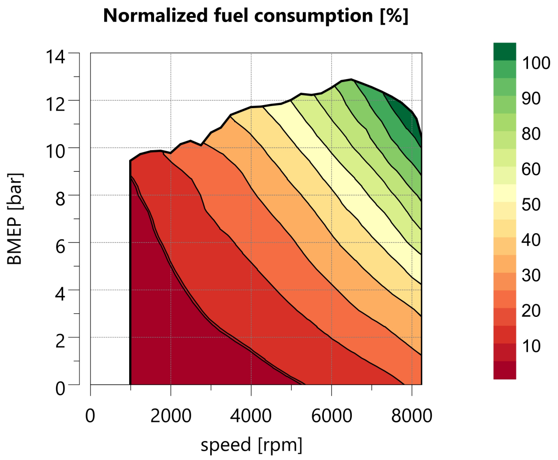

Figure 3.4: Fuel consumption map

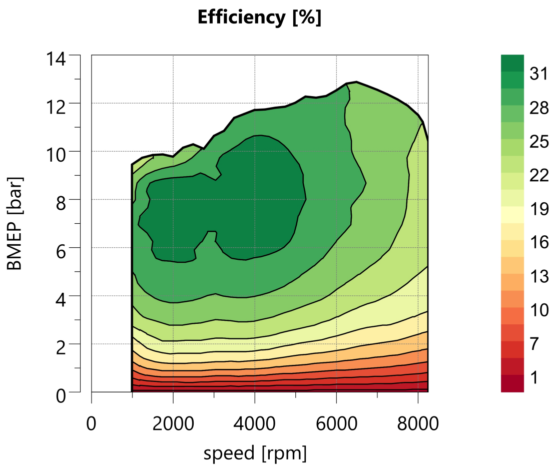

Figure 3.5: Efficiency map

3.1.2.2 Electric machine

Analogously, the electric machines, so the P1 (ISG) and the P4, have been modeled following the same approach. In particular, since all the installed motors are identical machines, a unique efficiency map accounts for energy losses occurring at the motor-inverter side, shown in Fig. 3.6.

The standard operating mode of an electric machine consists of a continuous power rating,

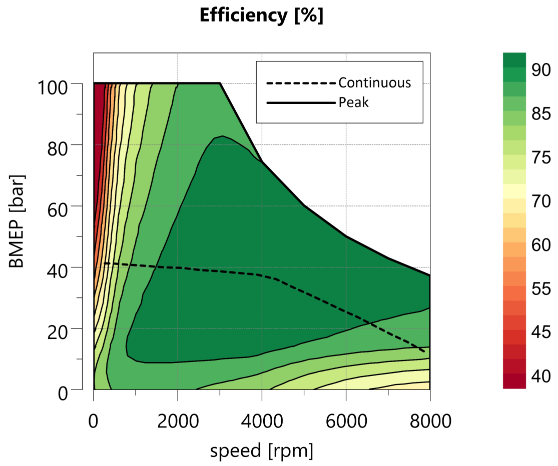

Figure 3.6: Electric machine efficiency map

which can be supported for a long period of time. In the case of high-performance requests, such a component is able to provide peak power for brief time intervals. As a consequence, two threshold curves of maximum torque can be defined, namely in *continuous* (dashed line) and *peak* (continuous line) operating modes.

The considerations previously made are still valid if the electric machine acts as a generator. Thus, the same maximum performance, with negative signs (resistant torque and power), are achieved. In fact, as a generator, the electric machine is able to convert the input mechanical energy into electrical energy, for example during regenerative braking or load point shifting. In both cases, the produced electrical energy is transferred to the battery and its charge increases. Nevertheless, it is worth pointing out that the direction of the energy flow within the electric machine affects the efficiency of the energy conversion, from mechanical to electrical (generator) and vice versa (motor), as follows:

$$P_{el} = \frac{P_{mech}}{\eta^{\alpha}(\omega,T)} = \frac{T\ \omega}{\eta^{\alpha}(\omega,T)}, \qquad \alpha = \begin{cases} 1, & T \geq 0\,(\text{motor}) \\ -1, & T < 0\,(\text{generator}) \end{cases} \tag{3.7}$$

The electric power distribution is completed with the DC/DC converter and the Integrated Power Unit (IPU), which are modeled as energy conversion efficiencies, and shown in Fig. 3.1, where the High-Voltage (red line) and the Low-Voltage buses are also depicted.

3.1.2.3 High-voltage battery

The high-voltage battery is a key component in hybrid electric vehicles, and consequently for their performance evaluation. To this aim, a control-oriented model of the battery including electrical and thermal behaviors has been developed, calibrated, and validated over experimental data in [75], and so only briefly reported hereafter. The electrical behavior of the cell has been represented by a single-polarization equivalent circuit model, also known as the first-order RC equivalent circuit model. As depicted in Fig. 3.7, the circuit model comprehends an open-circuit voltage (OCV), V_{OC}, a resistor, R_0, representing the ohmic resistance caused by the accumulation and dissipation of charge in the electrical layer. R_1 and C_1 are the activation polarization resistance and capacitance respectively, which characterize the fast transient response of the cell to a current pulse. Usually, all the mentioned parameters depend on the cell state of charge, ξ, and temperature, T, values.

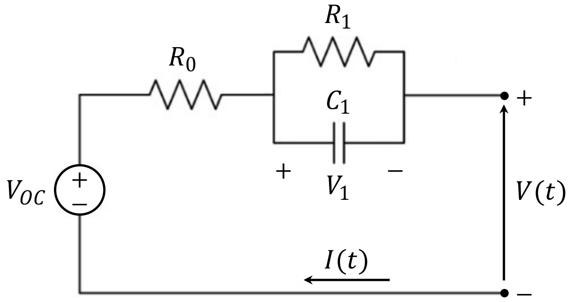

Figure 3.7: Single-polarization equivalent circuit model for cell electrical characterization

When considering a battery pack consisting of n_p parallel strings made of n_s series cells, the battery voltage V_b and current I_b can be calculated from the following system of equations:

$$\begin{cases} V_b(t) = \left(\frac{V_{OC} - R_0 \cdot I_b(t)}{n_p - V_1}\right) \cdot n_s \\ P_b(t) = V_b(t) \cdot I_b(t) \end{cases} \tag{3.8}$$

where V_1 is the voltage drop related to the RC circuit, and P_b is the battery power request, which takes into account the power requested by the EMs and the auxiliaries.

It is then possible to calculate the power losses $P_{b,loss}$ of the battery due to resistive heating as follows:

$$P_{b,loss}(t) = V_{b,int}(t) \cdot I_b(t) = \frac{n_s}{n_p} R_0 \cdot I_b^2(t) + n_s V_1 \cdot I_b(t) \tag{3.9}$$

in which $V_{b,int} = (n_s V_{OC} - V_b(t))$, from Eq. (3.8), is the internal voltage drop of the battery due to the presence of the internal resistance that causes the power dissipation $P_{b,loss}$ when the current I_b is flowing in the circuit.

Then, the battery state of charge is estimated with an Ampere-hour (Ah) integral method (also known as *Coulomb counting*) [131]. In formula:

$$\xi(t) = \xi_i - \frac{\eta_c}{C_n} \int I_b(t) dt \tag{3.10}$$

being C_n the nominal battery capacity [Ah], η_c the coulombic efficiency, and ξ_i the initial value of the state of charge.

On the other hand, since the temperature influences the battery's behavior and performance, a thermal model has been developed using a single thermal mass to reproduce the thermal behavior of the whole battery pack. In this case, contributions to the net heat flow rate are given by power losses (due to the Joule effect), air-battery convective heat exchange, and coolant-battery convective heat exchange. The latter is calculated using a simplified cooling circuit model in which the main actuators, namely the high-voltage compressor and the electric pump, have been inserted via experimentally derived characteristics respectively in the refrigerant and coolant loop of the system. Therefore, the equation for energy balance applied to the whole battery pack can be written as:

$$m_b \ c_{p,b} \ \frac{d}{dt}T(t) = P_{b,loss}(t) - \left(\dot{Q}_{air}(t) - \dot{Q}_{cool}(t)\right) \tag{3.11}$$

which gives the following equation if solved for the battery temperature T:

$$T(t) = T_i + \frac{1}{m_b} \ c_{p,b} \int \left(P_{b,loss}(t) - \dot{Q}_{air}(t) - \dot{Q}_{cool}(t)\right) dt \tag{3.12}$$

where:

$m_b, c_{p,b}$: mass and specific heat capacity [J/(kg·K)], respectively, of the battery pack;
T_i : initial battery temperature in [K], assumed to be equal to the environmental one;
$P_{b,loss}$: battery power loss in [W] due to Joule heating effect, from Eq. (3.9);
$\dot{Q}_{cool}$: cooling heat rate in [W] due to battery-coolant convective heat exchange;
$\dot{Q}_{air}$: thermal power in [W] related to the air-battery convective heat exchange.

The latter can be expressed as:

$$\dot{Q}_{air}(t) = h_a\left(v(t)\right) \cdot S_a \cdot \left(T(t) - T_{amb}\right) \tag{3.13}$$

where $h_a(v(t))$ is the convective heat transfer coefficient [W/(K·m^2)] of the surrounding air, T_{amb} is the ambient temperature, which is considered constant, and S_a is the exchange surface, i.e. the external surface of the battery pack expose to the air.

Moreover, the cooling heat rate $\dot{Q}_{cool}$ due to battery-coolant convective heat exchange can be formulated as:

$$\dot{Q}_{cool}(t) = h_c \cdot S_c \cdot \Delta T_{ml,c} \tag{3.14}$$

where h_c is the convective heat transfer coefficient of the coolant in [W/(K·m^2)], and S_c is the exchange surface where the heat exchange takes place, i.e. the internal surface of the pipelines of the cooling plate.

The term $\Delta T_{ml,c}$, used to characterize the convective heat exchange, is referred to as *logarithmic* *mean temperature difference*, and it can be written as:

$$\Delta T_{ml,c}(t) = \frac{T_{c,out} - T_{c,in}}{\ln\left(\dfrac{T - T_{c,in}}{T - T_{c,out}}\right)} \tag{3.15}$$

For the sake of simplicity, the refrigerant loop has not been modeled, so the assumption $T_{c,out} = const.$ can be made. Although experimental data confirm the weakness of this approach, the control-oriented objective of the model justifies this choice, as demonstrated by previous works [75].

Then, in order to evaluate the outlet coolant temperature, the thermal balance is applied:

$$\dot{Q}_{cool}(t) = \dot{m}_c \cdot c_c \cdot \Delta T_c(t) \tag{3.16}$$

which gives:

$$T_{c,out}(t) = T_{c,in} + \frac{\dot{Q}_{cool}(t)}{\rho_c \cdot \dot{V}_c \cdot c_c} \tag{3.17}$$

where c_c is the coolant heat specific capacity, $\dot{m}_c = \rho_c \cdot \dot{V}_c$ is the coolant mass flow rate, ρ_c is the density, and $\dot{V}_c$ is the pump volume flow, which can be considered known with good approximation while operating.

3.1.3 Controllers modeling

The simplified models of the controllers that have been implemented in the vehicle model are:

- the Engine Control Unit (ECU), which receives from the HCU the engine torque request and the start and stop command. Then, it controls the Internal Combustion Engine applying the torque limitation according to the engine characteristic and managing the idle phases;
- the Transmission Control Unit (TCU) controls the shifting phases such as the opening of the clutch, the torque reduction, the discs engagement, and the clutch closure;
- The IPUs, the DC/DC, and the ISG controllers introduce torque and power limitations, taking into account the respective efficiencies.

Then, the two software-level control unit models, which are the vehicle supervisor (HCU) and the battery control unit (BMS) are described in the next paragraphs.

3.1.3.1 Hybrid Control Unit

The prototype supervisor, named Hybrid Control Unit, coordinates the requests to the powertrain's subsystems and the respective controllers, in order to guarantee the vehicle's performance and all the safety requirements, such as:

- electric traction;
- front axle torque vectoring [1];
- four-wheel drive control;
- torque management during shifting;
- boosting function.

In particular, regarding the four-wheel drive control, the HCU calculates the driver torque request which is mapped as a function of the vehicle speed and the throttle pedal. When the latter is less than 5% and the vehicle is moving, the supervisor control interprets this condition as a negative torque request, which is actuated by electric motors operating as generators (and thus regenerative braking is performed). If the entire negative torque can not be supplied by the motors, then the mechanical brakes are actuated as well. In all the other conditions, positive torque is demanded. So, the rule-based energy management strategy, developed and presented in [128], evaluates the torque split between the ICE and the EMs depending on rules based on fixed thresholds (which have been previously calibrated).

Usually in PHEV, like the one used for this activity, the HCU is calibrated to use electric energy as a preferred source for traction. In this way, the strategy tends to discharge the battery until the lower limit (set by the manufacturer for safety reasons) is reached. Then, that limit is maintained by switching on the engine and performing load-point shift and regenerative braking. Such an approach is commonly referred to as the charge-depleting/charge-sustaining (CD/CS) approach. Since this kind of control logic is characterized by reliability and easy real-time implementation due to the low computational load required [58], it is currently the on-board standard strategy. In this case, the software of the supervisor controller has been written in MATLAB & Simulink and deployed into the dedicated rapid prototyping control unit, which is the MicroAutoBox II [132].

3.1.3.2 Battery Management System

The application software of the onboard Battery Management System (BMS) has been implemented in the Real-Time PC in the present configuration, but the Connected-HiL system is designed to integrate the corresponding hardware component seamlessly. This highly detailed model has most of the functionalities of the real software, such as:

- contactors control (for battery pre-charge);
- isolation monitoring;
- power limitation;
- system diagnostics.

---

[1] In this model the lateral dynamics of the vehicle are not modeled, thus this function is not enabled

Particular attention has been paid to the latter because error monitoring plays a vital role in preserving the safety of the vehicle's components and the passengers. Moreover, regarding the present work, the implementation of the real HCU at the HiL enables the testing of this functionality before implementing on-board any control function. Therefore, the BMS is able to recognize if threshold values for monitoring are exceeded for several important parameters, such as battery voltage, current, power, and temperature. High-voltage interlock lines and battery isolation status are monitored, as well. In case of an error, the BMS sends this information to the HCU which takes remedial action depending on the type and severity of the error. If such an action is not applied within a certain time, the BMS itself takes over control and opens the high-voltage relays. At this aim, also the battery pre-charge circuit comprehending the contactors has been implemented in the battery model.

3.1.4 Vehicle model validation

The whole vehicle model has been validated with experimental data acquired:

- during an All-Electric Range test, that consists of consecutive NEDC cycles, repeated until the battery is fully discharged and the ICE starts up. This test has been conducted on behalf of the industrial partner as a final step of the validation of the prototype vehicle [128] following the relative in force regulation EU2012/101 [133]. As it can be deduced from the typology of the test, it is then focused on the validation of the electric propulsion only;
- on a rural road drive that consists of driving the prototype vehicle in conventional mode forcing the ICE to entirely fulfill the torque request (and so neither boosting nor electric drive is allowed). In this way, the validation is not affected by the hybrid strategy but only focused on the conventional powertrain.

The results of the validations are shown in Fig. 3.8 and Fig. 3.9, respectively. The ability to correctly predict experimental data is demonstrated by the graphs, and it proves to be accurate enough for a control-oriented modeling approach.

3.2 Connected Hardware-in-the-Loop

Differently from the one presented in [127] and in [75], this simulation environment presents a layout reduced in complexity as the sole Telecommunication Control Unit (TeCU) is in charge of querying the Map Service Provider (MSP) and gatewaying the data. Moreover, in this work, an Human-Machine Interface (HMI) has been introduced to be as close to the prototype vehicle as possible. More in detail, the vehicle HMI is replicated by a tablet running an Android-based Navigator App, that allows the driver to set the desired destination and to see the suggested route based on actual traffic conditions. Meanwhile, the related navigation data are collected from the MSP and sent to the TeCU. Moreover, if the actual position of the vehicle deviates from the route

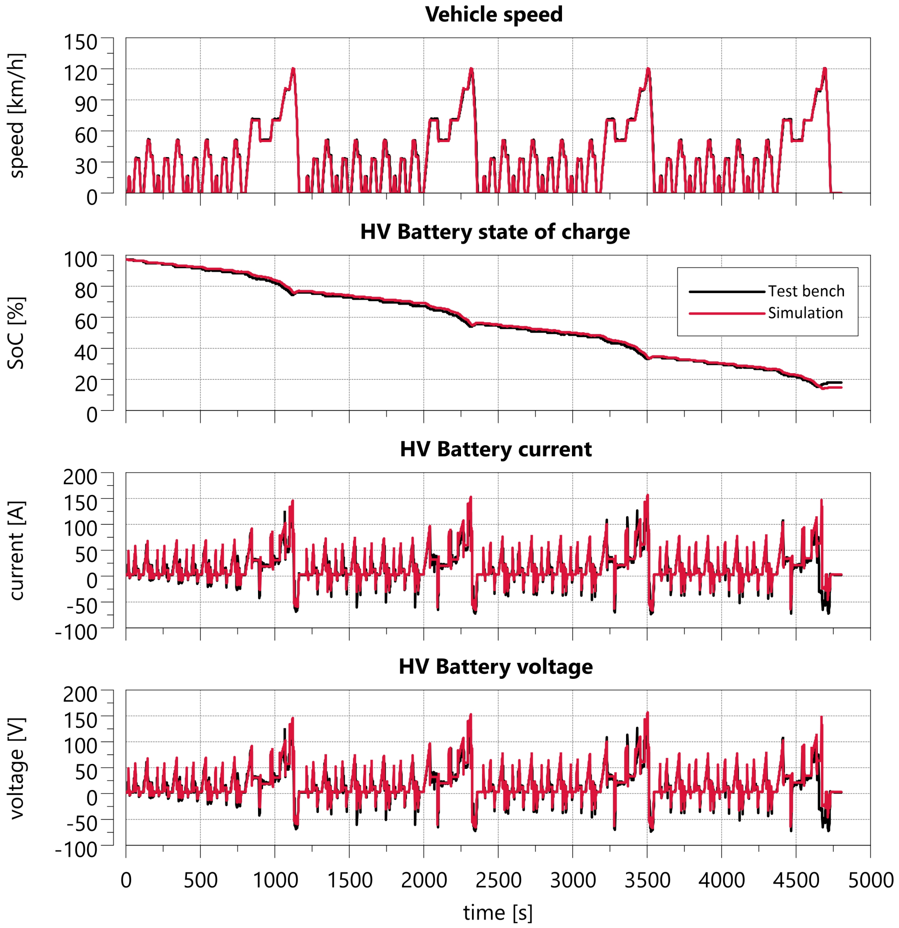

Figure 3.8: Electric powertrain validation (black line: experimental data; red line: simulation data)

proposed by the app or if the actual level of traffic changes, the app can trigger the request for a re-routing.

In this work, the focus is put on the long-range connectivity provided by the layout presented in [127]. With respect to the latter, the C-HiL has been improved and its complexity reduced. In particular, as shown by the blue boxes in Fig. 3.10, the TeCU is now in charge of both the internet service manager and the data processing, while an Android-based tablet is connected via Wi-Fi to the TeCU itself to replicate the vehicle's HMI. Furthermore, the data exchange handled by the TeCU is divided into:

- *direct-flow* ("NAV Data" label in Fig. 3.10), responsible for the transmission of the navigation data (listed in Tab. 3.1) from the MSP to the HCU;
- *back-flow* ("HMI Data" label in Fig. 3.10), for querying and transmitting the actual GPS position from the Real-Time PC to the MSP and the HMI.

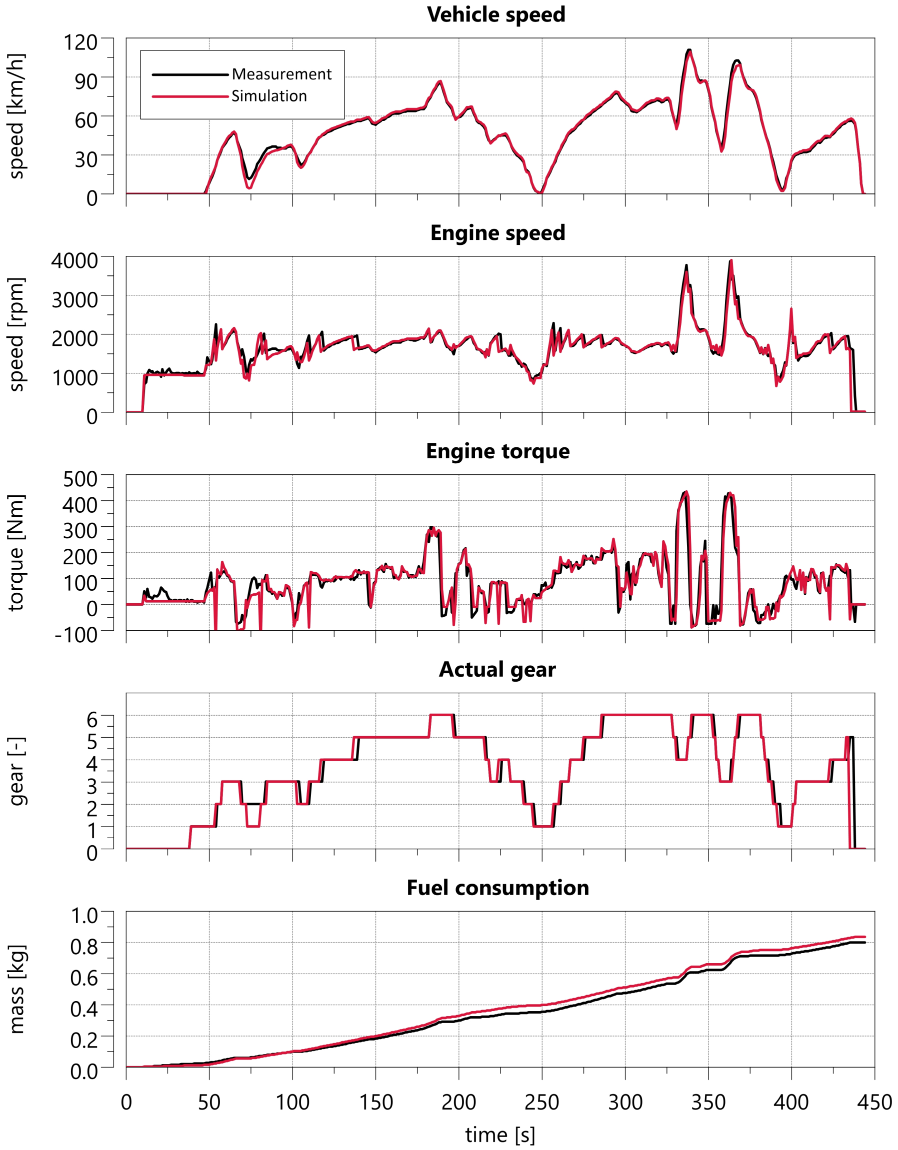

Figure 3.9: Conventional powertrain validation (black line: experimental data; red line: simulation data)

To give a proper outlook of the simulation environment, in Fig. 3.11 a photo taken during a simulation is reported, showing all the physical components of the C-HiL that are described in detail in the next paragraphs, following the workflow of the simulations.

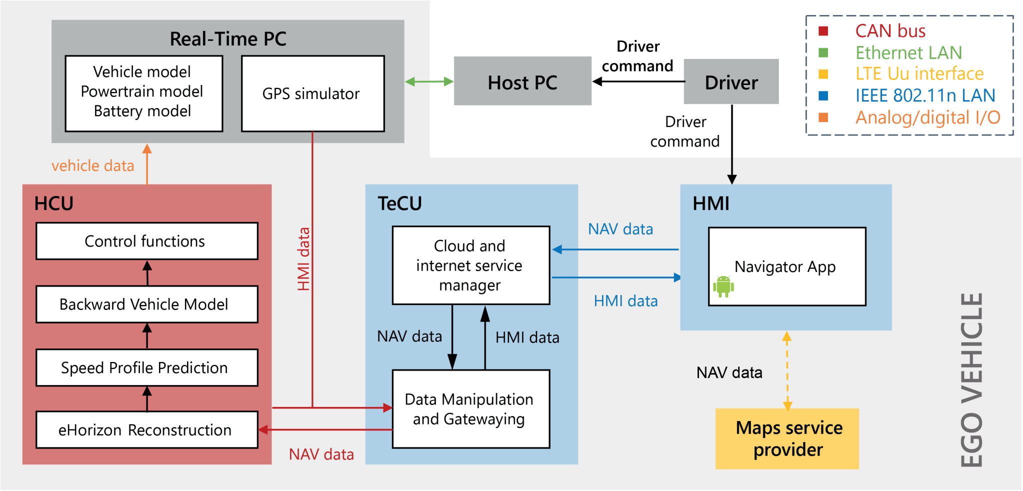

Figure 3.10: Connected HiL layout for testing predictive functions exploiting long-range connectivity

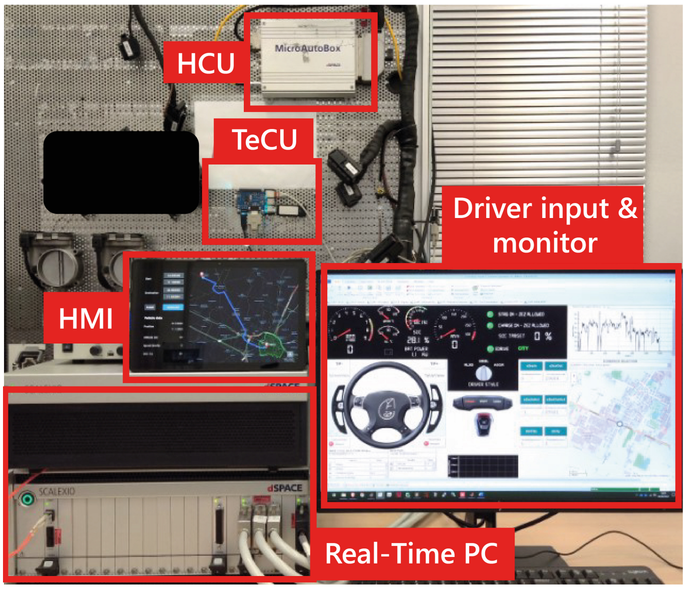

[redacted]

Figure 3.11: Connected HiL during a simulation

3.2.1 Human-Machine Interface

In the layout presented in [127], the destination had to be set directly via the Central Gateway (CG) by modifying directly on the software level, making all the process complex and prone to errors. Moreover, the original layout was not capable of re-routing and navigation data update, thus the simulated scenarios would not properly reflect the real test case. To overcome this problem, an Human-Machine Interface (HMI) Navigator App, integrating HERE SDK [134], has been developed and deployed into an Android-based tablet. In this way, several features are introduced, such as the possibility to choose the route suggestion method based on different objectives (fastest route, shortest route, etc.), directly select the destination on the touchscreen, and see the actual vehicle position moving on the map as well as the real-time traffic conditions.

So, focusing on the *direct-flow*, in order to set up the simulation, the driver first selects the desired destination directly on the HMI Navigator App, whose screenshot is represented in Fig. 3.12. The latter includes the start and destination coordinates boxes, the actual vehicle's position (blue dot), and data (coordinates, altitude, speed, and SoC in the black box on the left), and the zero-emission zone plotted as a green area. The latter has been designed by increasing the limits of the legal Limited Traffic Zone of Bologna [135] to also include the residential areas nearby. In this way, the average urban trip to reach the city center is between 2-4 kilometers and so the maneuver in pure electric is more demanding.

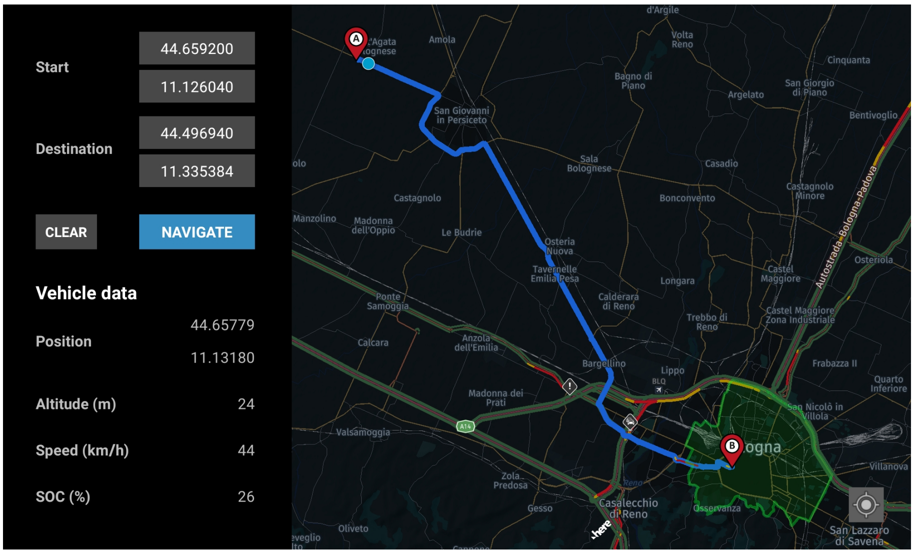

Start 44.659200 11.126040

Destination 44.496940 11.335384

Vehicle data

Position 44.65779 11.13180

Altitude (m) 24

Speed (km/h) 44

SOC (%) 26

Figure 3.12: Screenshot of the Navigator App: suggested route from point A to point B

Then, the HMI queries the MSP with the request for navigation data from the actual vehicle position (point A in Fig. 3.12) to the selected destination (point B in Fig. 3.12). This communication is allowed by the TeCu that works as a hotspot for the LTE, replicating the usual vehicle's infotainment layout where the communication is handled by the connectivity control unit, in this case the TeCU. Consequently, the MSP evaluates a proposed route according to actual traffic conditions (orange, red, and dark red lines in Fig. 3.12) and sends back the navigation data, reported in Tab. 3.1, via LTE Uu Interface to the tablet (yellow line in Fig. 3.10).

Concurrently, the HMI receives from the *back-flow* the actual vehicle position and system data and then plots it into the interface. Moreover, the Navigator App can also detect if the actual position of the vehicle is moving away from the proposed route and so triggering the so-called *re-routing* where another request is performed to the MSP to retrieve the updated navigation data. These data are then forwarded again to the TeCU following the same workflow as above.

Table 3.2: Navigation data sent by the MSP

No	Parameter	Unit	Size	Type
1	Route latitudes	deg	n+1	single
2	Route longitudes	deg	n+1	single
3	Route altitudes	m	n+1	uint16
4	Legal speed limits	m/s	n	uint8
5	Legal speed limits segments	m	n	uint16
6	ZEZ entrance/exit positions	m		uint16
7	Stop events classification	-	p	uint8
8	Traffic code classification	-	m	uint8
9	Stop events positions	m	p	uint16

3.2.2 Telecommunication control unit

The TeCU is based on a Raspberry Pi 4 computer [136], shown in Fig. 3.13a, coupled with the PiCAN2 board [137], shown in Fig. 3.13b, to manage the automotive CAN Bus standard communication. The software has been developed in Simulink by means of the MATLAB Support Package for Raspberry Pi Hardware [138], while the LTE protocol is handled by two Python scripts running in parallel.

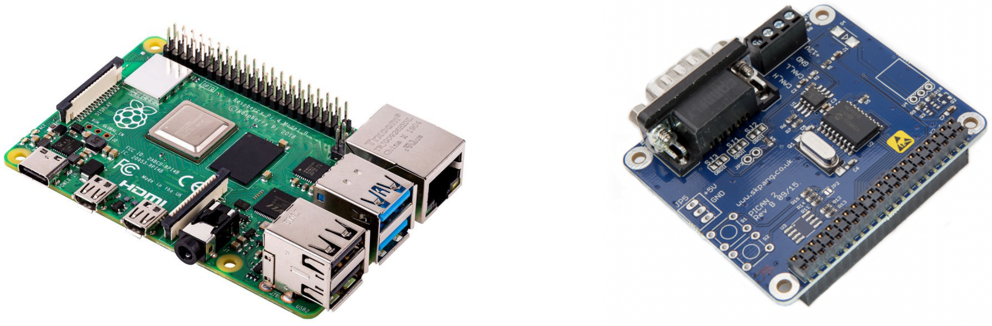

(a) Raspberry Pi 4 Model B [136]

(b) PiCAN2 Board [137]

Figure 3.13: Telecommunication control unit hardware

The TeCU is now in charge of querying the map service provider and gatewaying the data, merging the tasks of the original TeCU (described in [127]) and the CG in a single and more flexible component. In general, the TeCU is still capable of exchanging the standardized messages for the cooperative vehicular communication systems, as described in [139], which are: the Cooperative Awareness Messages (CAM), the Signal Phase and Timing (SPaT) messages, and the Decentralized Environmental Notification Messages (DENM). Nevertheless, even if these messages could include short-horizon data (such as the next traffic lights phases and timing), in this dissertation the focus is put only on the long-range communication since the merging of long- and short-horizon data is still under development.

For what concerns the communication with the MSP, and so the *direct-flow*, the TeCU receives from the HMI the navigation data listed in Tab. 3.2 via IEEE 802.11n LAN (blue line) and performs the necessary data processing to make the navigation data compliant with the HCU computational power capability. In particular, the data processing includes the removal of redundant data such as segments where both the speed limit and the slope do not change, to respect the dimensions limits listed in Tab. 3.2. Furthermore, it evaluates the ZEZ topological limits by crossing the route proposed by the MSP with the city center (green area in Fig. 3.12). Finally, it prepares and sends them via CAN bus (red line in Fig. 3.10) to the HCU itself.

Focusing on the *back-flow*, the HCU sends to the TeCU the vehicle's actual status via CAN messages, in the form of the actual state of charge of the high-voltage battery, the vehicle's speed, and the GPS position (latitude, longitude, and altitude).

Chapter 4

Predictive control strategy

In this chapter, an overview of the predictive functions' architecture is given, to explain how the navigation data are processed by the HCU (red box in Fig. 3.10). The focus is then put on the Speed Profile Prediction (SPP) algorithm developed to estimate an energetically equivalent velocity trace, related to the urban event and on the Backward Vehicle Model (BVM) that evaluates the battery energy required to fulfill the specific urban event.

Then, the RBS presented in [126] is modified into an Adaptive-RBS to increase its efficiency and then compared with the A-ECMS at the SiL on two complete Real-Driving Emissions (RDE) cycles. Consequently, analyzing the results, a Combined-RBS is finally defined to test the predictive functions at the C-HiL.

4.1 Predictive functions

The developed Predictive Functions (PF) have been implemented within the HCU according to the high-level architecture depicted in Fig. 4.1. The used nomenclatures are: driver model (DRV), space-to-time (S2T) conversion, wheels (W), motors (M), battery (B), limits (L), energy management strategies (EMS), reference SoC (REF) evaluation, equivalence factor (EF) evaluation, charge-sustaining (CS) SoC thresholds evaluation.

In general, the HCU performs the eHorizon reconstruction by picking up all the CAN messages and concatenating the values in dedicated vectors. The number of CAN messages needed for a particular route depends on the number of data and the format chosen for them.

The BVM together with the SPP represents the part of the HCU software in charge of the predictive tasks. It then takes into account the following parameters:

- *input parameter(s)*
  navigation data from the eHorizon reconstruction in the form of vectors representing the vehicle speed profile, $\mathbf{v}$, the road slope profile, $\boldsymbol{\alpha}$, and topological information regarding the

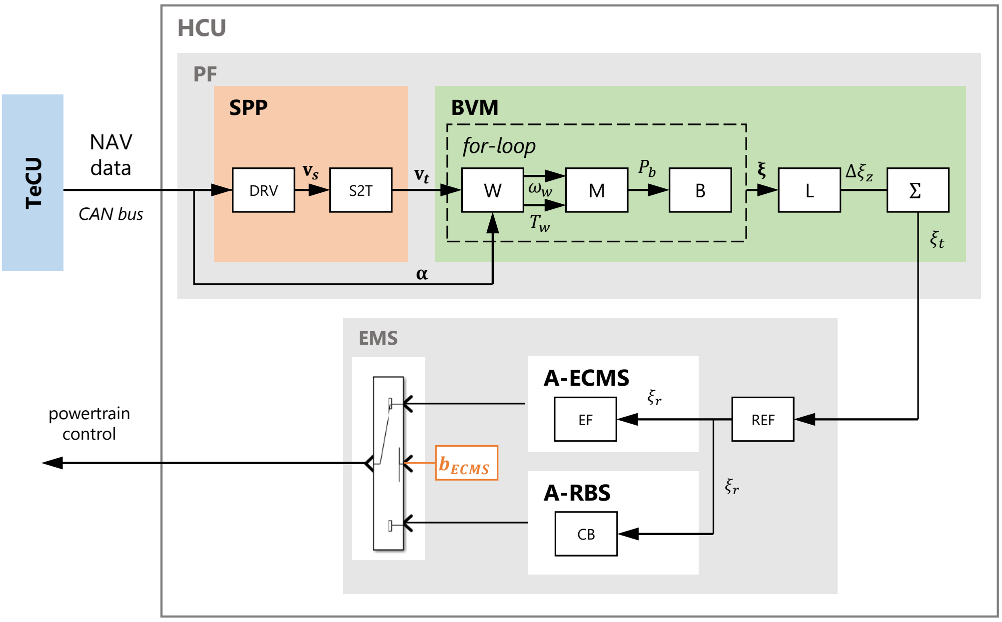

Figure 4.1: Workflow of the predictive functions for target SoC evaluation as implemented in the supervisory controller software.

zero-emission zone (distances from city entrance and exit);

- *output parameter(s)*
  target state of charge at ZEZ entrance, ξ_t, evaluated by the BVM function (Section 4.1.2);

- *state variable(s)*
  state of charge, ξ of the battery, predicted over the given urban horizon by the BVM.

In particular, the SPP algorithm (described in detail in Section 4.1.1 and in [75, 125]) calculates a space-based velocity profile that proved to be energetically equivalent to the one effectively driven. This is motivated by the fact that the aim is to evaluate the electrical energy usage of the HV battery and not to predict the exact maneuvers of the driver. Therefore, the speed profile is converted into time-domain and used by the BVM, which is described in detail in Section 4.1.2 and in [126], to predict the amount of energy to perform the ZEZ in pure electric mode, thus respecting the local legislation. Finally, the value of the SoC target becomes the input of the energy management strategies, as shown in Fig. 4.1.

4.1.1 Speed profile prediction

The application of predictive functions upon the control unit is still challenging since they are inherently dependent on future trajectories of velocity, road slope, and external disturbances, which are generally unknown for real-world drive cycles. However, with the help of the navigation data provided by the MSP, an estimation of the trajectories can be made and then used by the energy management strategy.

To do so, different approaches can be identified, which are divided into parametric and non-parametric [140]. In the first category, the driving task is modeled as a stimulus-response system, so, as a control problem where the driver's goal is to keep a safe distance from the vehicle in front or to pursue a target speed according to some imposed constraints. The second one includes algorithms based on probabilistic and artificial intelligence theories such as Artificial Neural Networks, Markov chains, or Monte Carlo methods. As reported in [140], advanced parametric models are commonly used for long-range energy management prediction, representing a valuable trade-off between reliability and ease of implementation. A remarkable algorithm for Speed Profile Prediction has been proposed by [58], which for this reason has been assumed as the reference for the one developed and tested at the MiL level in [125].

The algorithm is implemented in the simulation environment as follows:

Algorithm 1: SPP algorithm

```
begin
    nodes vector creation from navigation data
    for $j = 1 : N_S$ do
        legal speed limit and traffic code assignment
    $d = L_{trip}/(n_v \cdot c_s)$ → discretization step
    for $j = 1 : N_S$ do
        $N = (l_j - l_{j-1})/d$ → sub-segmentation
        for $i = 1 : N$ do
            next point $i$ MAS evaluation
            next point $i$ speed evaluation
        speed and space values vector assignment
    space-to-time conversion
```

The output of the algorithm are the vectors of the speed and slope trajectories, whose size is limited by the computational power of the HCU as well as the navigation data. As a consequence, their accuracy is dependent on trip segmentation, which is the result of:

1. a first segmentation that depends on the road characteristics (slope, stop events, legal speed limits) and on the traffic, so on the navigation data. This kind of segmentation is represented by N_S "nodes" in Algorithm 1. The nodes have been defined as the coordinates along the trip that correspond to the presence of a stop event or a variation in the speed limit, slope, or traffic code.

2. a second segmentation that is then applied by the algorithm to actually generate the speed trace, as shown in Fig. 4.5a (vertical black lines). In particular, a discretization step, d, is

evaluated as the ratio between the total length of the trip, L_{trip}, and the size of the output vector, n_v. Then, each segment defined by the first segmentation, with a length of $l_j - l_{j-1}$, is subdivided again into N sub-segments having a length equal to d (Algorithm 1, line 7). In this way, the density of the sub-segmentation is kept constant, since the longer is the j-th segment, the higher is the number of required sub-segments. When:

$$(l_j - l_{j-1}) < k_d \cdot d \tag{4.1}$$

i.e., the two adjacent nodes are too close to each other, a smaller discretization step is applied to have sufficient values to create the speed trace within the j-th segment. The coefficient $k_d = 4$ represents the minimum number of points required to create an acceleration-deceleration maneuver following Eq. (4.5) and Eq. (4.6). Moreover, a corrective factor c_s is applied in line 5 to take into account the additional elements required by the condition expressed by Eq. (4.1) and avoid the complete saturation of the memory. The latter is evaluated as $c_s = 1-(k_d \cdot n_c)/n_v$, where n_c is the number of segments that verify the condition expressed by Eq. (4.1). As a final remark on the second segmentation, it must be said that the discretization is dependent on the overall length of the route, so the accuracy of the speed profile could be affected for longer trips. However, this algorithm is applied only to the ZEZ, which is usually a limited event for the test cases under evaluation, and the overall accuracy is more than satisfying as proved by the results of the calibration and of the tests at the C-HiL. Moreover, the problems related to the computational power will be overcome by moving the predictive functions from the HCU to the cloud, as it will be proposed in future work.

After that, the starting values of the speed limit and traffic code are assigned to every sub-segment $i = 1, \ldots, N$ of each segment $j = 1, \ldots, N_S$ (line 4 of Algorithm 1). Consequently, for each sub-segment, the Maximum Allowed Speed (MAS) is calculated (line 7 of Algorithm 1). If a node coincides with a stop event position, then the MAS is imposed by the kind of the stop event itself. In particular, a stop event is commonly referred to as an event whose presence implies that the speed of the vehicle in that position must be partially or totally decreased. They are divided into *static*, if the breaking or stop is mandatory (e.g., bumps, stop signal), and *dynamic*, if they may not affect the current speed even if their position is known (e.g., green lights and right of ways). For the latter, a stop-over probability is introduced, as in [58], depending on traffic codes modeled by means of binomial probability and summarized in Tab. 4.1.

For the other nodes, the MAS value is affected by the traffic density, which influences the maximum speed due to the presence of the other cars and induces oscillations around that limit due to the variation of traffic flow. Thus, the MAS can be expressed as:

$$MAS = MAS_t + MAS_n \tag{4.2}$$

Table 4.1: Stop-over probability with respect to the traffic codes

Traffic code c	Traffic color [-]	Congestion [-]	Stop-over probability [%]	Code weight[1] CW
1	🔵	absent	15	0.85
2	🟠	light	40	0.60
3	🔴	medium	60	0.40
4	🟤	heavy	70	0.30

[1] the code weight and its value will be discussed in the next paragraphs.

where:

- MAS_t considers the effect related to the traffic condition, expressed in terms of colors (blue, orange, red, and dark red) and can be expressed as:

  $$MAS_t = v_{lim} \cdot CW \tag{4.3}$$

  where v_{lim} is the legal speed limit, and CW is the code weight that depends on the traffic code c.

- MAS_n replicates the effect of the driver behavior that depends on the traffic condition. In fact, the velocity often exhibits oscillations around the speed limit due to inharmonic traffic flow. As suggested by [58], to account for these oscillations, the MAS_n can be expressed as a sum of R-cosines:

  $$MAS_n = \sum_{r=1}^{R} A_r \cdot cos(2\pi f_r x) \tag{4.4}$$

  where A_r and f_r are the amplitudes and frequencies of the oscillation respectively, and R is the number of the considered cosine terms (in this case $R = 3$)

After the evaluation of MAS for each i-th point, the vehicle speed can be calculated (line 10 of Algorithm 1). Since the objective of the algorithm is to generate a speed vector, with the assumption of traveling time minimization, the driver will always try to reach the MAS, if possible. Therefore, the driver decides whether to accelerate, decelerate or keep the velocity constant depending on the actual value of the speed and on the boundary conditions of the $i+1$-th point. Thus, if the MAS has been already reached, the driver can maintain the speed or start braking. Otherwise, it starts to accelerate. For this reason, an exponential acceleration and a linear deceleration law are adopted:

$$a_{acc}(x) = a_{acc,max} \cdot k_{acc} \cdot (1 - e^{-\tau x}) \tag{4.5}$$

$$a_{dec}(x) = -a_{dec,max} \cdot k_{dec} \cdot x \tag{4.6}$$

where $a_{acc,max}$ and $a_{dec,max}$ are the maximum acceleration and deceleration that depend on vehicle performance, k_{acc} and k_{dec} are the reductive factors that consider the different driver behaviors, and τ is the time constant defining the acceleration transient.

Finally, the speed profile is converted from space to time domain by following a linear interpolation of the values to feed the Backward Vehicle Model with proper input signals (line 12 of Algorithm 1). Moreover, a stop time is assigned to each stop event depending on the traffic code and the typology of the stop event itself.

After the analysis of the algorithm, its calibration has been performed, focusing on:

- *driver-related parameters*, so k_{acc}, k_{dec}, and τ, that regards the acceleration and deceleration maneuvers described by Eq. (4.5) and Eq. (4.6), respectively. Thus, the conceived scenario is represented by a ramp-up / ramp-down cycle with a nominal speed of 50 km/h (i.e., a typical urban speed limit) and performed on a straight road;
- *traffic-related parameters*, that are CW, A_r, and f_r. To do so, the algorithm has been calibrated over three urban driving scenarios within the city of Bologna, the more representative of which is shown in Fig. 4.2.

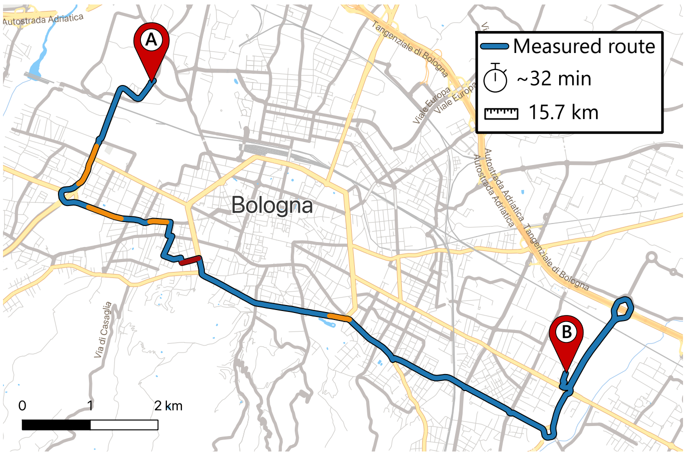

Figure 4.2: Driving scenario with different traffic codes and speed limits, within an urban area

Furthermore, as suggested by [58], the measurements have been performed to include all the possible common situations. In particular, they have been performed at different times of day to assess the influence of various traffic conditions (from the less congested road of the night to the rush hour) and on different types of urban roads, to consider as many driving conditions as possible (from the urban roads to the high-velocity ones). Since the purpose of the algorithm is to predict the amount of energy related to an urban event, the calibration and validation campaign are focused only on scenarios inside a ZEZ.

The weight of the traffic codes, the amplitudes, and the frequency of Eq. (4.4) have been determined by dividing the measured space-based velocity traces into segments and clustering them with respect to the traffic code. Then, a Fast Fourier Transform (FFT) is applied in the space domain for each traffic code cluster, as suggested in [58], obtaining a magnitude-frequency diagram. In fact, the influence of traffic congestion leads to different oscillations for each traffic code. The oscillations are intended as the variation of the vehicle speed with respect to the average value every certain number of meters, whose inverse can be seen as the space-domain frequency [m^{-1}]. By filtering the measurements, it is possible to isolate the first four space-domain frequencies and amplitudes. The first one represents the average values that are used to calculate the code weight Eq. (4.9) determining the corrected MAS value. Finally, the oscillations due to the frequencies and amplitudes going from $r = 1, \ldots, 3$ are added to the average value. For a matter of brevity, only the one related to the orange traffic color (code c=2) is reported in Fig. 4.3.

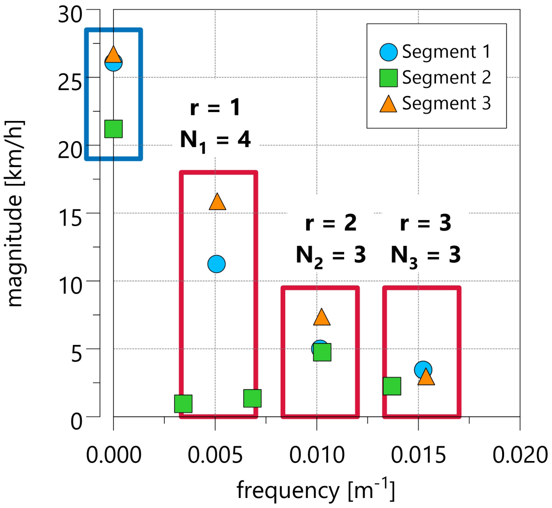

Figure 4.3: Frequency analysis with FFT for the traffic code c=2

In this case, J=3 measured speed signals have been investigated, each of them related to a certain space segmentation of length l_j. Then, the three ranges ($r = 1, \ldots, 3$) of frequencies have been identified to describe the oscillatory phenomenon with acceptable accuracy (red boxes in Fig. 4.3, where N_r is the number of points within each range). At this point, focusing on Eq. (4.4), both the frequencies and the amplitudes of each range can be expressed as arithmetic means of the relative measured values:

$$A_{c,r} = \frac{\sum_{j=1}^{J} \left(1/N_r \cdot \sum_{n=1}^{N_r} A_{n,r,j}\right) \cdot l_j}{\sum_{j=1}^{J} l_j} \tag{4.7}$$

$$f_{c,r} = \frac{\sum_{j=1}^{J} \left(1/N_r \cdot \sum_{n=1}^{N_r} f_{n,r,j}\right) \cdot l_j}{\sum_{j=1}^{J} l_j} \tag{4.8}$$

where J is the number of segments with the same traffic code c, N_r is the number of pairs of magnitudes $A_{n,r,j}$ and frequencies $f_{n,r,j}$ corresponding to the r-th range of the j-th signal. Moreover, since the amplitude A_0 of the oscillation at $f = 0$ m^{-1} (blue box in Fig. 4.3) represents the average speed on the given segments, it can be used to determine the parameter CW for each traffic code as follows:

$$CW_c = \frac{\sum_{j=1}^{J} \frac{A_{0,j}}{v_{lim,j}} \cdot l_j}{\sum_{j=1}^{J} l_j} \tag{4.9}$$

being $v_{lim,j}$ the legal speed limit for the j-th segment. In this way, according to Eq. (4.3), the static contribution to the MAS can be determined.

Afterward, two different kinds of Key Performance Indicators (KPI) have been identified to evaluate the goodness of the prediction: speed-based and energy-based KPIs. Regarding the first ones, reliable parameters for speed traces comparison are provided by [140, 141] and they can be represented by the mean absolute error (MAE) and the BIAS, both expressed in [km/h] and defined as:

$$MAE = \frac{1}{n} \sum_{i=1}^{n} |v_{p,i} - v_{r,i}| \tag{4.10}$$

$$BIAS = \frac{1}{n} \sum_{i=1}^{n} \left(v_{p,i} - v_{r,i}\right) \tag{4.11}$$

where $v_{p,i}$ and $v_{r,i}$ are respectively the predicted and the measured speed at point i, and n is the total amount of points where the differences are calculated. Moreover, since the MAE does not consider the algebraic signs of the errors, it is used to express the mean distance between the prediction and real data. Differently, the BIAS represents a good instrument to identify eventual issues related to a systematic under/overestimation of the speed.

On the other hand, energy-based KPIs suggested by SAE [142] have been assumed as references. At first, three energy components are calculated for both the predicted and the measured cycle, and they are the road load, the positive and the negative inertia, expressed as follows:

$$E_{RL} = \int_0^L F_{RL} dl = \int_0^L (F_0 + v \cdot F_1 + v^2 \cdot F_2) dl \tag{4.12}$$

$$E_{I^+} = \int_0^L F_{I^+} dl = \int_0^L (m_v \cdot a_{dec}) dl \tag{4.13}$$

$$E_{I^-} = \int_0^L F_{I^-} dl = \int_0^L (m_v \cdot a_{dec}) dl \tag{4.14}$$

where L is the total length of the route, E_{RL} represents the energy required to win rolling resistance and drag force, E_{I^+} represents the energy required by the vehicle mass m to be accelerated, and E_{I^-} represents the energy required by the vehicle mass to be decelerated. Now, three energy KPIs can be introduced in form of energy rate, where subscripts p and r are respectively referred to as the predicted and real (measured) speed profile:

$$\Delta E_{RL} = \frac{\left(E_{RL_p} - E_{RL_r}\right)}{E_{RL_r}} \cdot 100 \tag{4.15}$$

$$\Delta E_{I^+} = \frac{\left(E_{I_p^+} - E_{I_r^+}\right)}{E_{I_r^-}} \cdot 100 \tag{4.16}$$

$$\Delta E_{I^-} = \frac{\left(E_{I_p^-} - E_{I_r^-}\right)}{E_{I_r^-}} \cdot 100 \tag{4.17}$$

The results of the calibration and validation campaign are described in detail in [125]. So, for the sake of brevity, in this work, only a representative test case's validation is reported in Fig. 4.4. In this case, the scenario under test includes different traffic codes, stop events, and speed limits to consider as many conditions as possible. The numeric results of that validation are summarized in Tab. 4.2.

Table 4.2: Speed and energy KPI for the presented use case

MAE $[km/h]$	BIAS $[km/h]$	E_{RL} $[Wh]$	ΔE_{RL} [%]	E_{I^+} $[Wh]$	ΔE_{I^+} [%]	E_{I^-} $[Wh]$	ΔE_{I^-} [%]
12.4	-0.1	5	-0.4	32	-2	32	-2

In conclusion, Fig. 4.5a shows the calibrated predicted speed profile with respect to the test case presented in Fig. 4.2, alongside the legal speed limits on that route (magenta line) and the related traffic colors (filled area below the speed profile) listed in Tab. 4.1. As shown, the velocity trace is always below the limits because the CW, as expressed by Eq. (4.9), affects the MAS_t, the static component of MAS, lowering the v_{lim}, while the oscillations described by Eq. (4.4) simulate the natural speed deviation from that value.

Moreover, as shown in Fig. 4.5b and Fig. 4.5c, the speed is also reduced in correspondence to the orange and dark-red traffic codes respectively by the values reported in Tab. 4.1, showing the impact that each traffic code has on the predicted profile. Furthermore, on the x-axis, the stop events positions are plotted with the red triangles. As it can be noticed, since the stop-over probability is applied, the vehicle's speed is not always zero.

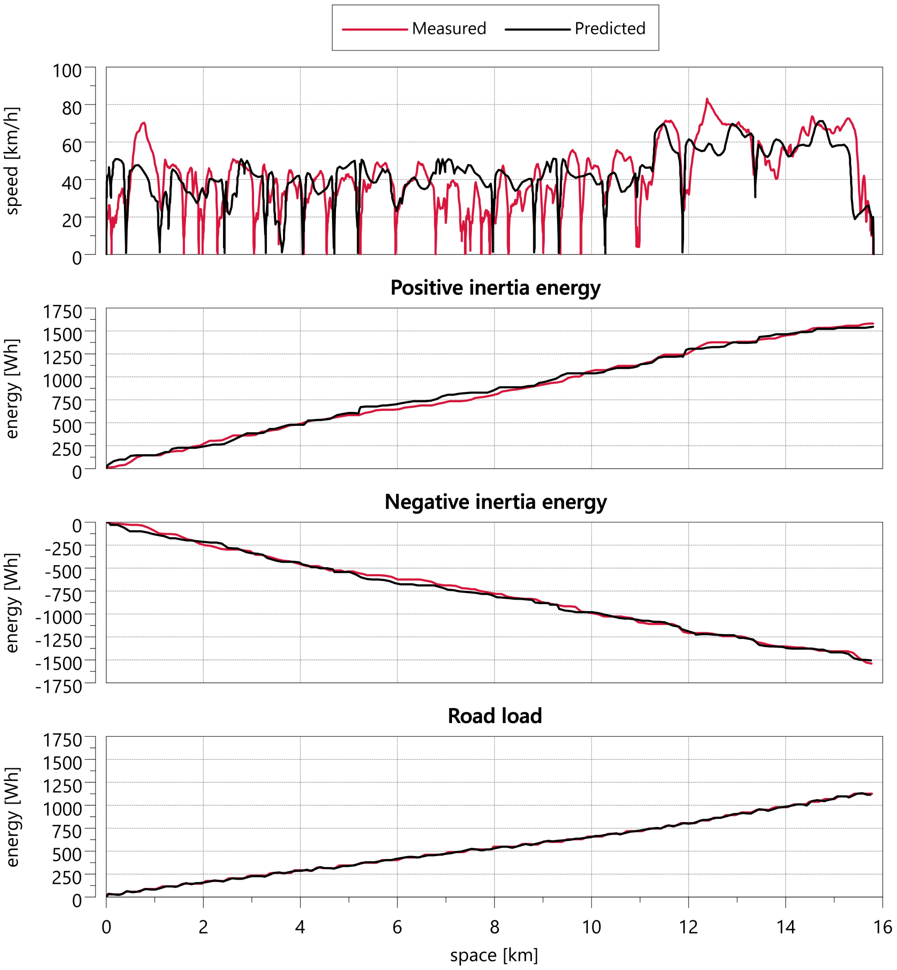

Figure 4.4: Top plot: speed profile predicted from the navigation data (black) and the measured speed on the road (red). Three bottom plots: comparison between the three energy components related to the prediction (black) and the measurements (red)

4.1.2 Backward Vehicle Model

In order to reconstruct the behavior of SoC over the given electronic horizon, the predictive functions rely on a Backward Vehicle Model (BVM) which takes the vectors of the speed, v, and the road slope, $\alpha_{\%}$, generated by the SPP for the predicted eHorizon, and it evaluates the predicted state of charge profile, ξ. The BVM is implemented in a *for-loop* block, where the number of iterations, N, is equal to the period of time required for crossing the urban area. In other words, $N = \Delta t_Z = t_{f,Z} - t_{i,Z}$. This results in a function time step equal to $t_s = 1$s that is sufficient to represent the slow dynamic of the state of charge.

The prediction is carried out by means of a quasi-static analytical model of the vehicle, developed through a backward-facing approach and based on the inverted path of the energy flow

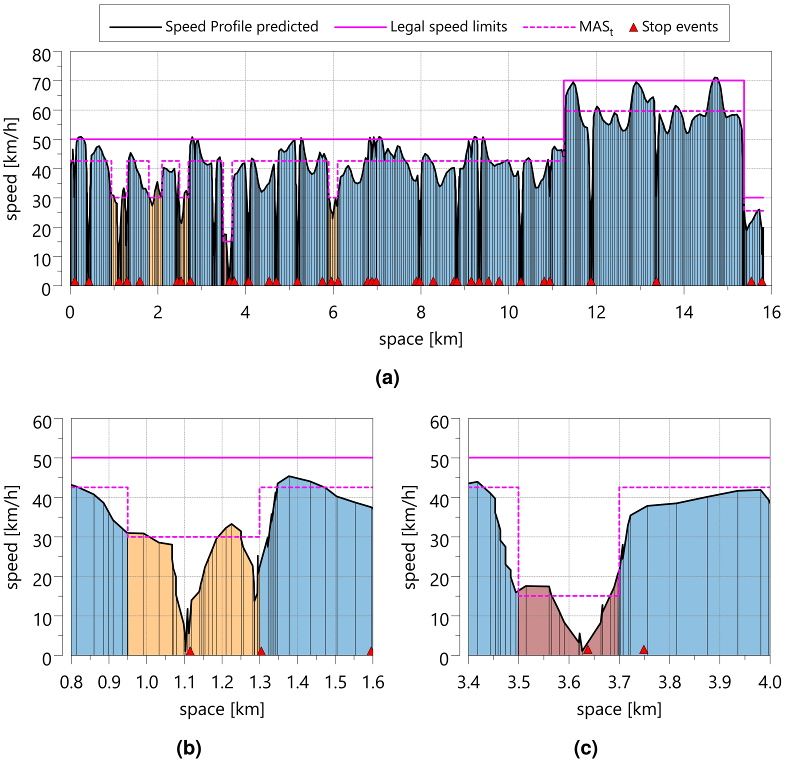

Figure 4.5: a) Speed profile predicted by the algorithm after calibration; b) detail of MAS limited by the orange traffic code; c) detail of MAS limited by the red traffic code

inside the vehicle. In this case, the source is represented by the wheels and the sinks are the energy storage devices. Here, the traction force, and consequently torque and power, are evaluated on the base of the vehicle speed and road slope, which can be considered as external disturbances acting on the dynamic system represented by the vehicle [143–145]. Thus, there is no closed-loop control on the speed, i.e., a driver model is not needed. Moreover, dynamic effects such as torque control are not inherently included. Therefore, this results in a less complex model with benefits regarding computational load [146], which is a relevant aspect to be considered for algorithm implementation inside the rapid prototyping control unit. The main equations of the Backward Vehicle Model, presented in [126], are briefly reported in the following paragraphs, while the model validation can be found in [75]. Firstly, since the vehicle dynamics analytical model only considers the longitudinal forces acting on the car, the fundamental equation for vehicle longitudinal dynamics (Eq. (3.1)) in discrete domain, i.e. for the k-th iteration of the *for-loop*, for $k = 1,\ldots,N$, can be rewritten as::

$$m_v \cdot \frac{\Delta v(k)}{\Delta t(k)} = m_v \cdot \frac{v(k) - v(k-1)}{t_s} = F_{mot}(k) - F_{res}(k) = F_r(k) \tag{4.18}$$

where $v(k) = [\mathbf{v}]_k$ is the predicted vehicle speed, and being $\Delta t(k) = t(k) - t(k-1) = t_s$. Then, considering the discrete formulation of resistance forces and inertia forces, as widely shown in literature [75], the total torque requested at the wheels can be expressed as:

$$T_r(k) = F_r(k) \cdot r_w \tag{4.19}$$

with r_w being the wheel radius.

Since the output of the BVM is the battery behavior within a zero-emission zone, where the vehicle should be driven in pure electric mode, the total torque request at the wheels is entirely provided by the electric machines Then, as already discussed in [57, 58], and reported in [126], the global electrical power request can be evaluated from Eq. (4.18) and expressed as follows:

$$P_b\left(t\right) = P_{EM}\left(t\right) + \frac{P_{aux}}{\eta_{DCDC}} \tag{4.20}$$

in which $P_{EM}\left(t\right)$ is the power requested from the electrical motors on the front axle either for traction or regenerative braking, P_{aux} is the constant power to be supplied to the low-voltage battery and the other auxiliaries, and η_{DCDC} is the efficiency of the DC\DC converter. At this point, the battery power request is modified according to power limitation maps related to charge-discharge and peak-nominal working conditions of the HV battery. These parameters are calculated by the battery electrical and thermal models, respectively, which are the same used in the vehicle's model, in Section 3.1.2. Thus, the electrical behavior of the cell has been represented by a single-polarization equivalent circuit model, also known as the first-order RC equivalent circuit model. Battery voltage V_b and current I_b can be calculated as already explained in Section 3.1.2.3. In conclusion, the battery state of charge is estimated with an Ampere-hour (Ah) integral method (also known as Coulomb counting) [131]. In formula:

$$\xi(k) = \xi_1 - \frac{\eta_c}{C_n} \sum_k I_b(k) t_s \tag{4.21}$$

being $\xi_1 = \xi(k = 1) = 95\%$. From Eq. (4.21), the net amount of SoC needed to drive the ZEZ in pure electric drive can be calculated as the difference between the maximum and minimum value of the predicted SoC profile ξ:

$$\Delta\xi_Z = max(\xi) - min(\xi) \tag{4.22}$$

Then, the target SoC value is calculated as follows:

$$\xi_t = \xi_{min,b} + \Delta\xi_Z + \xi_s \tag{4.23}$$

where $\xi_{min,b}$ is the minimum SoC to drive the vehicle in pure electric mode (in this application, it is set to 20%), ξ_s is a positive offset value that has been set to 5% to compensate for the physiological inaccuracies of the navigation data, as proved in [75]. Finally, ξ_t is the output of the model representing the minimum value of SoC to be stored in the HV battery to perform the ZEZ in pure electric, which is then forwarded to the control strategy.

4.2 Standard on-board strategies

The baseline strategies for energy and battery thermal management are presented in this section. They have been calibrated, tested, and implemented in the HCU by the industrial partner, which then represents the software developer of the entire supervisory controller. Then, the modified energy management RBS for zero-emission zones handling is introduced, as well.

4.2.1 Rule-based strategy for energy management

As previously explained, this heuristic energy management strategy, already presented in [75, 126, 127], controls the electric drive, the front axle torque vectoring, the 4WD control, the torque filling, and the boosting. Focusing on the electric drive, the RBS is based on rules depending on fixed thresholds (which have been previously calibrated). In addition to the driver torque request, parameters such as the SoC ξ, the torque at the wheels T_w, and the actual vehicle speed v are involved in the torque split factor evaluation. Eq. (4.24) represents the conditions to switch from electric to hybrid drive, while Eq. (4.25) to conditions to switch back to electric drive. Thus, the controller first discharges the battery and then keeps the state of charge around the chosen threshold. Such an approach is commonly referred to as the charge-depleting/charge-sustaining approach and is typically used for PHEVs, like the one used for this activity.

$$\begin{cases} \xi < \xi_{\min} \\ T_w > T_{\max}(n) \\ v > v_{\max} \end{cases} \tag{4.24}$$

$$\begin{cases} \xi > \xi_{\max} \\ T_w < T_{\min}(n) \\ v < v_{\min} \end{cases} \tag{4.25}$$

Moreover, if a negative torque is requested by the driver, regenerative braking occurs and the battery is recharged by the electric motors (i.e., P4), acting as generators.

Since this kind of control logic is reliable and easily real-time implementable due to the low computational burden required [57, 70, 84], it is currently the onboard standard strategy. It has been calibrated in previous activities by the industrial partner. The reliability and robustness of the rule-based energy management strategy are proven by the numerous HiL and on-road tests performed on the HCU as well as on the whole vehicle. Further details can be found in [128].

4.2.2 Adaptive rule-based strategy

The presence of constrained events, such as a ZEZ, along the route adds a boundary condition for the EMS. Without the connectivity and the information from the server, the conventional strategy works blindly, thus the driver could run into fees or traffic limitations imposed by the local municipalities. Conversely, the control strategy has to fulfill an additional objective besides fuel consumption, which is granting enough energy to drive the ZEZ in full electric drive. Then, when the ZEZ is reached by the vehicle, the strategies are bypassed, and the electric drive is forcedly switched on. Hence, the RBS is modified into an Adaptive-RBS to increase its efficiency and then compared with the A-ECMS at the SiL on two complete RDE cycles.

To do so, following the trend in literature, a blended mode leads to increased efficiency for the PHEV [147], especially if road and traffic data are accessible [148]. In fact, if the information about the ZEZ is available, thus the target SoC ξ_t can be higher than the initial SoC of the battery. In [126], the RBS has been modified to receive the navigation data as input, but it can only recharge the HV battery and then performs a conventional CS around the target, as follows:

$$\begin{cases} \xi_{min} = \xi_t \\ \xi_{max} = \xi_t + 5 \end{cases} \tag{4.26}$$

This could lead to an imbalanced comparison since the RBS has not been conceived to work in this operating condition. Thus, the control policy has been adapted to take as input the same SoC reference, ξ_r, that will be defined in Section 4.3.2 by the Eq. (25) and use it to define the new values of ξ_{max}, ξ_{min} instant by instant:

$$\begin{cases} \xi_{min}\left(d\left(t\right)\right) = \ \xi_r\left(d(t)\right) \\ \xi_{max}\left(d\left(t\right)\right) = \ \xi_r\left(d(t)\right) + 5 \end{cases} \tag{4.27}$$

4.3 Equivalent Consumption Minimization Strategy

4.3.1 Basic formulation

It is well known that the approach proposed by the ECMS allows reducing the global energy minimization problem of HEVs to a local one that can be solved instantaneously, leading to a sub-optimal control strategy. In particular, the formulation of this control policy is based on the physical equivalence between the electric energy usage of the battery and the virtual fuel consumption associated with it. Thus, the instantaneous equivalent fuel consumption to be minimized results in:

$$\dot{m}_{f,eq}(t) = \dot{m}_f(t) + \dot{m}_{f,b}(t) \tag{4.28}$$

where $\dot{m}_f$ is the effective fuel consumption referred to the engine, and $\dot{m}_{f,b}$ is the virtual fuel consumption associated with battery usage. By analogy with the engine, the latter can be expressed introducing a virtual specific fuel consumption, sfc_{eq}, giving:

$$\dot{m}_{f,b}(t) = sfc_{eq}(t) \cdot P_b(t) = \frac{s(\xi(t),t)}{Q_{lhv}} P_b(t) \tag{4.29}$$

where Q_{lhv} is the lower heating value of the fuel in [kJ/kg], $P_b(t)$ is the global electrical power request to the battery, and sfc_{eq} is considered proportional to a dimensionless equivalence factor, s.

4.3.2 Adaptive-ECMS

In [89] and more recently in [90] remarkable improvements have been obtained to make the ECMS a real-time control strategy. In particular, in the latter work, an adaptation of the equivalence factor based on feedback from SoC has been proposed. An attempt to apply this adaptive formulation of the ECMS to PHEVs is proposed in [149, 150]. As a result, the equivalence factor is expressed as:

$$s\left(\xi(t),t\right) = p\left(\xi(t),t\right) \cdot a\left(\xi(t),t\right) \tag{4.30}$$

where:

$$p\left(\xi(t),t\right) = 1 - k_p \left[\frac{\xi(t) - \left(\xi_{\max} + \xi_{\min}\right)/2}{\left(\xi_{\max} - \xi_{\min}\right)/2}\right]^n \tag{4.31}$$

$$a\left(\xi(t),t\right) = k_a\left(\xi_r(t) - \xi(t)\right) + \frac{\left(s_{k-1} + s_{k-2}\right)}{2} \tag{4.32}$$

From Eq. (4.30) it can be noticed that there are two main contributions to the adaptive formulation of the equivalence factor, s.

The first one is expressed in Eq. (4.31) and it represents a *penalty function* intended to maintain the state of charge of the battery within the range $[\xi_{\min},\xi_{\max}]$. This condition represents a local control constraint for HEV applications (where only a CS mode could be applied), while it can be considered a physical constraint in the case of a PHEV, like the considered vehicle. The definition of the penalty function is completed by the gain factor, k_p, also known as the *penalty factor*, and the polynomial coefficient, n, which can be considered as tunable parameters.

The second contribution is represented in Eq. (4.32) by an *adaptive function* that plays a vital role in the real-time implementation of the ECMS. In fact, the drawback of the offline tuning of the equivalence factor for a given drive cycle is solved by an online adaptation based on the feedback from the SoC, represented by the term $\xi_r(t) - \xi(t)$. This results in a proportional correction of s by considering an *adaptive factor*, k_a, and the difference between the reference value of the SoC, ξ_r, and the actual one. The introduced gain factor can be used for algorithm tuning, as well as the penalty factor. Since the adaptation is performed periodically every $t = k \cdot t_u$, $k = 1,2,\ldots$, the terms s_{k-1} and s_{k-2} are the values of the equivalence factor used in two previous time intervals, namely *adaptation steps*, working as an integral correction.

4.3.2.1 A-ECMS with navigation data

In case of availability of navigation data regarding the planned route, that are including a ZEZ in these test cases, the k_a has been calibrated as a 2-D map [126], presented in Fig. 4.6, based on a logarithmic approach depending on the remaining distance to the ZEZ ($\Delta d_Z(t) = d_{i,Z} - d(t)$) and the difference between the reference SoC and the actual SoC $\Delta\xi_{r,f}(t) = \xi_t - \xi_{r,f}$. Moreover, the more the vehicle gets closer to the ZEZ entrance the more the update time t_u of the adaptive factor decreases, granting more accurate control, as shown in Fig. 4.7.

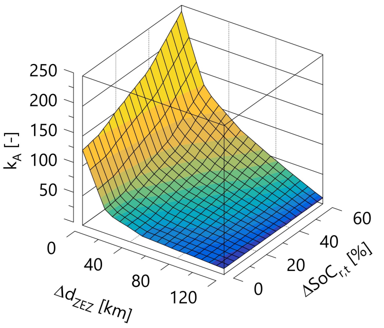

Figure 4.6: Map of the adaptive factor

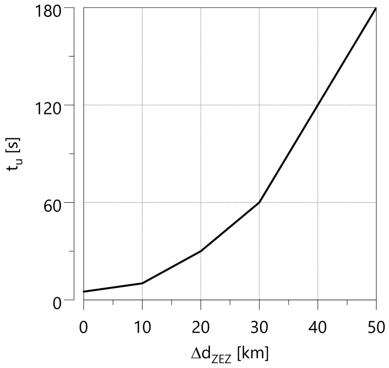

Figure 4.7: Map of the update time

In general, for a PHEV the reference SoC to be followed by the control policy can be expressed as a linear function of the total distance of the trip to gradually discharge the battery during the driving mission. Thus, neither a battery discharging nor sustaining behavior is favored, and then the resulting working mode could be referred to as charge blended. So, the general formulation for a generic drive cycle has been modified as:

$$\xi_r\left(d\left(t\right)\right) = \xi_i + \frac{\xi_f - \xi_i}{d_f - d_i}\left(d(t) - d_i\right) \tag{4.33}$$

with the following assumptions related to the ZEZ:

$$\begin{cases} t_f = t_{i,Z} \\ d(t_f) = d_f = d_{i,Z} \\ \xi(t_f) = \xi_f = \xi_{i,Z} \end{cases} \tag{4.34}$$

Where $t_{i,Z}$ is the instant of time when the vehicle reaches the ZEZ, $d_{i,Z}$ is the distance of the ZEZ from the actual position, and $\xi_{i,Z}$ is the value of the SoC at the beginning of the ZEZ.

A qualitative use case is shown in Fig. 4.8a, where a generic prediction happens in between the driving cycle (point $d_i \in [d_0, d_{f,Z}]$). In general, the first prediction occurs when the driver selects the destination on the navigator, and it is performed again every time a re-routing or changes in traffic condition occurs. Here, the CB mode is applied by the A-ECMS following the reference SoC expressed by Eq. (4.33) until the urban area is accessed at $d_f = d_{i,Z}$ reached at the instant $t = t_f$. Moreover, it is important to mention that in contrast to other formulations of the reference SoC, the global constraint $\xi_r(t_f) = \xi_{r,f} = \xi_t$ has been softened, as shown in Fig. 4.8b. The unused

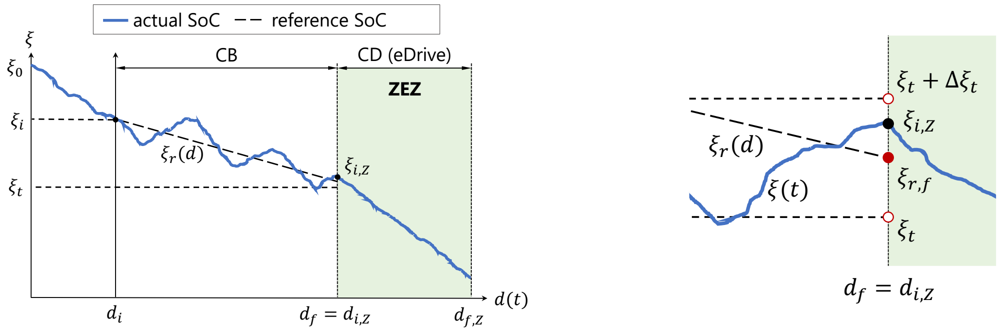

(a) Actual and reference SoC trends [126]

(b) Particular of the beginning of the ZEZ [126]

Figure 4.8: Charge Blended (CB) A-ECMS handling the ZEZ

electrical energy associated with the SoC difference $\xi_{i,Z} - \xi_t$ is justified by the more important aim of pursuing a reliable and robust energy management control strategy for handling all the ZEZ in pure-electric driving mode. Therefore, the final reference SoC value becomes the reference SoC range $[\xi_t, \xi_t + \Delta\xi_t]$ centered in $\xi_{r,f}$, with $\xi_{r,f} > \xi_t$ and $\Delta\xi_t = 5\%$.

4.4 Strategies comparison

The simulations of two RDE cycles have been performed at the SiL to compare the strategies in terms of CO_2 production, and in particular to understand if the A-RBS outperforms the conventional RBS and can be used as the new reference. Differently from the conventional RDE cycle, the two used here have been driven in the opposite direction, thus the urban event (and so the ZEZ) is located at the end of the trip. This allows the energy management strategies to prepare the battery with the proper amount of energy for the urban area. The driving cycles are represented in Fig. 4.9a and Fig. 4.9b along with the altitude profile (the 0 value is the initial vehicle position) and the ZEZ (green area).

Table 4.3: Target Soc, length of the route and of the ZEZ for each RDE

Cycle	ξ_t [%]	d_Z [km]	$d_{i,Z}$ [km]	$d_{f,Z}$ [km]
RDE 1	80	15.0	75.1	90.1
RDE 2	80	11.8	80.9	92.7

The length in km of the cycles and the urban event are listed in Tab. 4.3, where ξ_t is the target SoC calculated by the BVM, d_Z is the duration of the ZEZ, while $d_{i,Z}$ and $d_{f,Z}$ identify the start and the end of the ZEZ. The comparisons have been made starting from different values of the initial SoC ξ_i (30%, 50%, and 90%), whereas the ZEZ event remains the same and consequently the

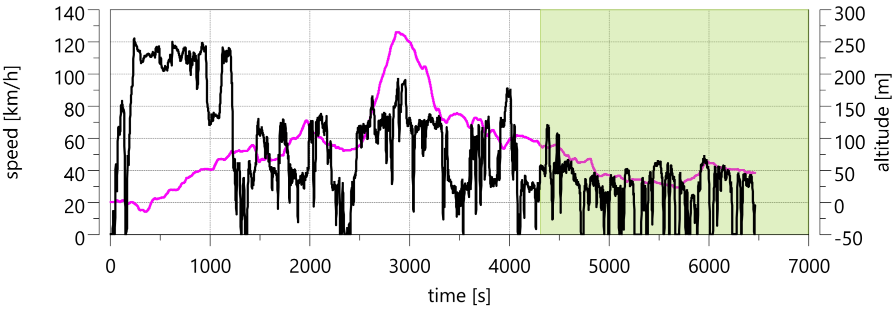

(a) RDE 1

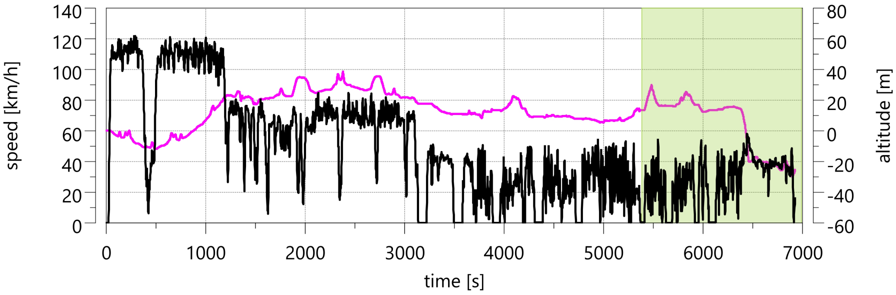

(b) RDE 2

Figure 4.9: Driving cycles (black) and altitudes (magenta) profile

target SoC. The initial values have been chosen to cover different operation modes of the strategies due to the difference between the initial SoC and the target SoC (in both test cases 80%):

- $\xi_i = 30\%$: implies a significant negative difference and so a demanding recharging phase;
- $\xi_i = 50\%$: in this case, the difference is less pronounced and so is the recharging phase;
- $\xi_i = 90\%$: here the difference is positive, as commonly happens with PHEV. This is necessary to understand if the A-RBS proposed is suitable even for a conventional CD/CS mode.

4.4.1 CO2 correction

CO_2 production has been chosen as the assessment parameter for comparing the energy consumption related to the strategies under test with respect to the reference one (namely the RBS). To make a proper comparison, a correction of CO_2 production has been proposed. In particular, the electrical energy additionally used or saved, $\Delta E = E^{AR} - E^{AE}$ (AR: A-RBS, AE: A-ECMS), at the end of the driving mission should be converted into an equivalent amount of fuel as already described in [126]. Hence, the energy correction can be:

- *negative*, meaning that more electrical energy was used by the strategy under test than the reference strategy. In this case, the assumption is that the ΔE is provided by the ICE and the

P1 is working as a generator. Thus, considering the energy balance, the mass fuel correction is expressed by:

$$\Delta m_f = \frac{\Delta E}{Q_{lhv}} \cdot \frac{1}{\bar{\eta}_{ICE} \cdot \bar{\eta}_{ISG}} \tag{4.35}$$

where Q_{lhv} is the lower heating value of the gasoline, $\bar{\eta}_{ICE}$ and $\bar{\eta}_{ISG}$ are the average efficiencies of the ICE and the ISG respectively. The instantaneous efficiency of the ICE is calculated as the ratio between the mechanical power provided by the engine and the chemical power related to the injected fuel.

- *positive*, on the contrary, if less electrical energy was used by the strategy under test. Here, the ΔE is assumed to be provided by the EMs, as the vehicle is driving in electric mode. Thus, the energy balance can be expressed as:

  $$\Delta m_f = \frac{\Delta E}{Q_{lhv}} \cdot \frac{\bar{\eta}_{ISG}}{\bar{\eta}_{ICE}} \tag{4.36}$$

  where $\bar{\eta}_{EM}$ is the average efficiency of the EMs, calculated as the ratio between the input and output power.

Finally, to evaluate the CO$_2$ production, the corrected fuel consumption $m_{f,c} = m_f + \Delta m_f$ is multiplied by a conversion factor whose value is $k_{CO_2} = 2370$ [$\mathrm{g_{CO2}/l_{fuel}}$]. The latter can be calculated as suggested by [10] from the following equation:

$$FC = \left(\frac{0.1206}{\rho_f}\right)(0.829 \cdot HC + 0.429 \cdot CO + 0.273 \cdot CO_2) \tag{4.37}$$

where $\rho_f = 0.75$ [kg/l] is the fuel density, and HC, CO, and CO$_2$ are the production of the relative chemical agents [g/km]. For the conversion factor evaluation, the conservative assumption HC=CO=0 [g/km] has been made.

4.4.2 Simulations and results

The Fig. 4.10a, Fig. 4.10c, and Fig. 4.10e show the simulation results for the RDE 1 at 30%, 50%, and 90% respectively, and likewise the Fig. 4.10b, Fig. 4.10d, and Fig. 4.10f for the RDE 2. In particular, the SoC trends for each strategy have been plotted, along with the reference SoC $\xi_r(d\,(t))$, used by both the A-RBS and the A-ECMS, expressed by Eq. (4.33). The simulation results for all the test cases are reported in Tab. 4.4 in terms of a relative percentage difference of corrected CO$_2$. The A-RBS and the A-ECMS are compared to the RBS by means of the parameters $\Delta CO_{2,\%}^{AR}$ and $\Delta CO_{2,\%}^{AE}$.

$$\Delta CO_{2,c,\%}^{AR} = \frac{\left({CO_2}^{AR} - {CO_2}^{R}\right)}{{CO_2}^{R}} \cdot 100 \tag{4.38}$$

$$\Delta CO_{2,c,\%}^{AE} = \frac{\left(CO_2{}^{AE} - CO_2{}^{R}\right)}{CO_2{}^{R}} \cdot 100 \tag{4.39}$$

where the superscript R stands for RBS, AR for A-RBS, and AE for A-ECMS. Analyzing the results listed in Tab. 4.4, for the test cases with $\xi_i = 30\%$ and $\xi_i = 50\%$, where the strategies must work in charge increasing (CI) mode (negative values of $\Delta\xi = \xi_i - \xi_t$), the A-RBS performs better than the RBS, as shown by the negative values of $\Delta CO_{2,c,\%}^{AR}$. On the other hand, if the strategies must work in the conventional CD/CS mode (positive values of $\Delta\xi$), the RBS still represents the most efficient solution. Differently, the values of $\Delta CO_{2,c,\%}^{AE}$ for the A-ECMS highlight the considerable improvements in all the test cases, confirming the results previously obtained in [126].

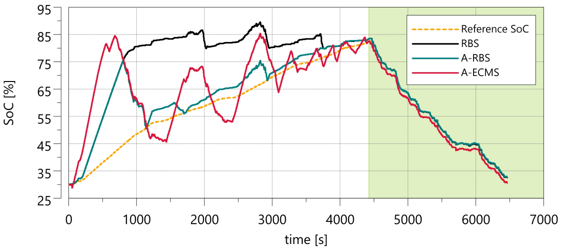

(a) TC 1: $\xi_i = 30\%$

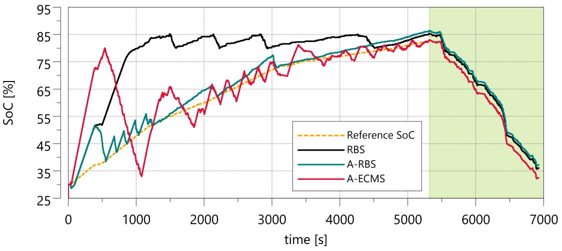

(b) TC 2: $\xi_i = 30\%$

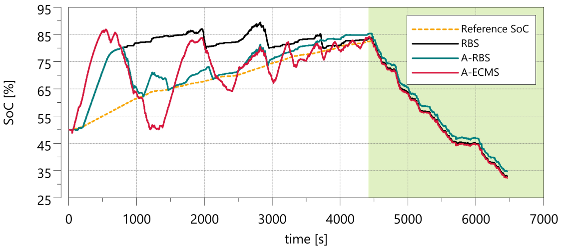

(c) TC 3: $\xi_i = 50\%$

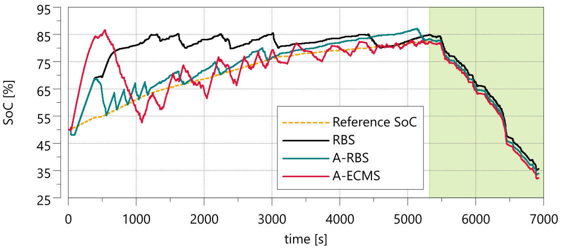

(d) TC 4: $\xi_i = 50\%$

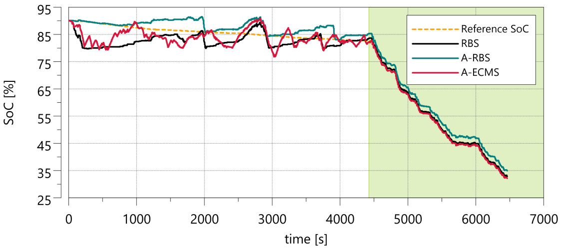

(e) TC 5: $\xi_i = 90\%$

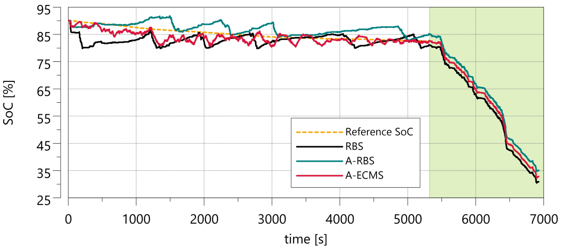

(f) TC 6: $\xi_i = 90\%$

Figure 4.10: a, b, c) RDE 1: SoC trends for each strategy approaching the ZEZ (green area) with initial SoC of 30%, 50%, and 90% respectively; d, e, f) RDE 2: SoC trends for each strategy approaching the ZEZ (green area) with initial SoC of 30%, 50%, and 90% respectively

Table 4.4: Results of the simulations in terms of CO2 production and relative errors for each test case

TC	RDE	ξ_i [%]	ξ_t [%]	$\Delta\xi$ [%]	$CO_{2,c}^{R}$ [g/km]	$CO_{2,c}^{AR}$ [g/km]	$CO_{2,c}^{AE}$ [g/km]	$\Delta CO_{2,c,\%}^{AR}$ [%]	$\Delta CO_{2,c,\%}^{AE}$ [%]
1	1	30	80	-50	319	305	268	-4.3	-16.1
2	2	30	80	-50	360	352	296	-2.2	-17.6
3	1	50	80	-30	307	295	240	-3.7	-21.7
4	2	50	80	-30	344	334	272	-3.1	-21.1
5	1	90	80	10	280	288	208	3.0	-25.4
6	2	90	80	10	312	321	230	2.8	-26.3

4.4.3 Combined rule-based strategy

In conclusion, the tests highlight that for this specific powertrain the A-RBS is more efficient only in CI, while the RBS is still better otherwise. Hence, a Combined-RBS has been identified merging the limits expressed by Eq. (4.26) and by Eq. (4.27) in Tab. 4.5.

This new strategy, defined as a combination of the RBS and the A-RBS to be the most efficient in terms of CO_2 reduction, is adopted from now on as the reference strategy and it will be tested at the C-HiL and compared to the A-ECMS to confirm the results obtained at SiL level. In Tab. 4.6 all the EMS described so far, and the relative working modes are summarized with respect to the SoC difference $\Delta\xi = \xi_t - \xi_i$.

Table 4.5: C-RBS: state of charge limits for the electric drive

	ξ_{min}	ξ_{max}
$\xi_i > \xi_t$	ξ_r	$\xi_r + 5\%$
$\xi_i < \xi_t$	$\xi_r\,(d(t))$	$\xi_r\,(d(t)) + 5\%$

Table 4.6: EMS working mode summary

	$\Delta\xi > 0$	$\Delta\xi < 0$
RBS [126]	CD/CS	CI/CS
A-RBS	CB	CB
C-RBS	CD/CS	CB
A-ECMS [126]	CB	CB

Chapter 5

Application of the control strategies

In this chapter, the C-RBS and the A-ECMS are tested at the C-HiL on a driving profile measured on-road under varying and unpredictable traffic conditions. More in detail, each test starts querying the MSP to retrieve the online navigation data in real-time for the same destination as the measured trace. Consequently, the HCU calculates the target SoC, as described in Section 4.1. Since the navigation data depends on the actual traffic conditions, they could differ from the measured data both for the proposed route and the traffic data. When the Navigator App detects that the distance between the GPS position of the vehicle and the planned route is higher than a certain threshold, it triggers a re-routing. Hence, it queries the MSP again for updated navigation data and the HCU calculates a new target SoC. In this way, the test forces the control strategies to work in conditions as near as possible to reality, validating both the predictions of the target SoC and the effectiveness of A-ECMS with respect to the C-RBS in terms of CO_2 production.

5.1 Test case scenarios

The tests have been performed on a driving profile measured onboard using MATLAB Online, and installed on a smartphone, to retrieve the actual vehicle speed, and GPS position (latitude, longitude, and altitude). To replicate a plausible and realistic scenario, the starting point has been set in the rural area near the city of Bologna, point A in Fig. Fig. 5.1a, while the destination has been set on a parking lot in the middle of the ZEZ, point B.

The measurement has been done in the afternoon of a working day to consider medium traffic congestion while maintaining a driving behavior neither aggressive nor cautious. Then, the same measured data have been set as the reference speed profile to be followed by the vehicle model and then deployed in the Real-Time PC. Finally, the tests have been conducted starting from different values of initial SoC, as for the comparison described in Section 4.4, at comparable hours of the day, to reduce the physiological variability of the traffic as much as possible. The measured driving cycle is reported in Fig. 5.2, as well as the altitude and the ZEZ.

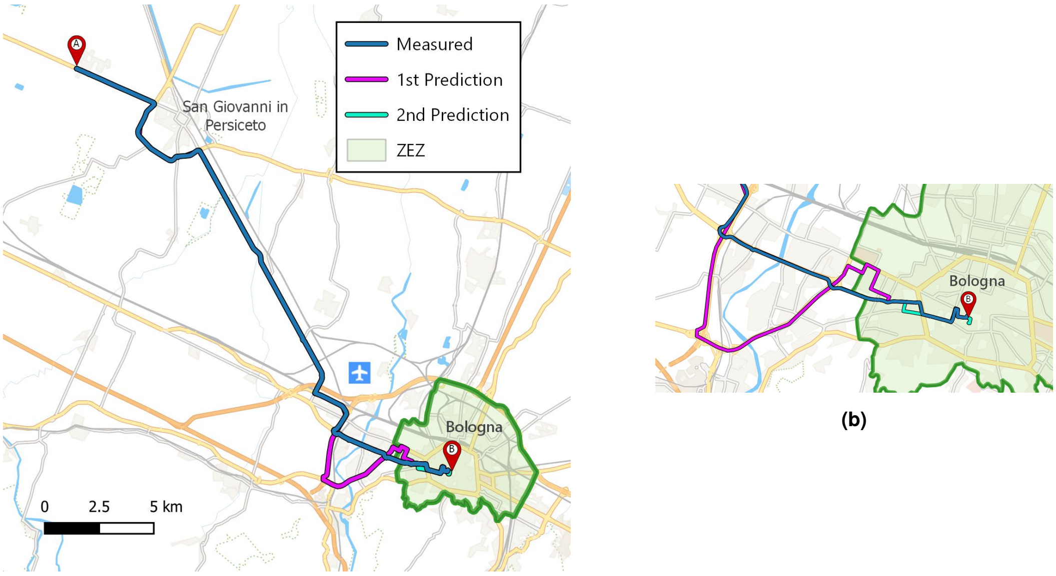

(a)

(b)

Figure 5.1: Representation of the measured route (blue line) from point A to point B and the proposed routes at each query: first one at the beginning of the test (purple line) and the second related to re-routing 1 (cyan line)

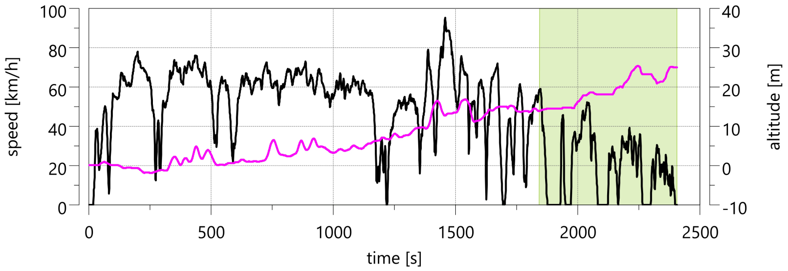

Figure 5.2: Real driving profile under test (black), altitude profile (magenta), and the ZEZ area (green)

In Tab. 5.1, the data regarding the length of the route $d_{f,Z}$, the remaining distance to the ZEZ $d_{i,Z}$, and the urban event are reported. Furthermore, in Tab. 5.2 all the test cases are summarized, along with the initial value of SoC ξ_i, and the number of re-routing n_r (excluding the first prediction that is mandatory), which occurred during the simulations.

Table 5.1: Length of the driving profile and ZEZ for the measured test case

Cycle	$\boldsymbol{d_Z}$ [km]	$d_{i,Z}$ [km]
Measured route	3.0	27.5

Table 5.2: List of all the test cases with the respective boundary conditions

TC	EMS	ξ_i [%]	n_r [-]
1	C-RBS	30	0
2	A-ECMS	30	1
3	C-RBS	50	1
4	A-ECMS	50	1
5	C-RBS	90	1
6	A-ECMS	90	0

5.2 Results and discussion

In Fig. 5.3 the results of the testing at the C-HiL have been reported. The subfigures Fig. Fig. 5.3a, Fig. 5.3c and Fig. 5.3e are referred to the simulations performed with the C-RBS, while Fig. 5.3b, Fig. 5.3d and Fig. 5.3f to the ones performed with the A-ECMS at the initial SoC value of 30%, 50%, and 90% respectively. In particular, each subfigure is divided as follows:

- *top plot*: showing the actual HV battery SoC (black line), the reference SoC (dotted line) calculated with Eq. (4.33), and the target SoC (petrol green line) calculated by the BVM with the Eq. (4.23). The latter is related to the real-time navigation data received during the simulation, so it changes when a re-routing occurs;

- *central plot*: it represents the comparison of the energy associated with each predicted speed profile with respect to the driven one (grey). The comparison is referred to the energies defined by Eq. (4.15), Eq. (4.16), and Eq. (4.17), namely the positive inertia energy (cyan), the negative inertia energy (green), and the road load (yellow). In addition, the battery consumption predicted by the BVM is also compared (orange) to the actual one. Moreover, for a matter of graphical representation, the predictions are distributed on the x-axis, whereas during the simulations they are performed at the same time once all the navigation data are received. The predictions are highlighted in each plot by means of grey boxes, but since the central plot is an enlargement of the predictions themselves the grey boxes are wider;

- *bottom plot*: the turnaround time (TAT) of the HCU, expressed in milliseconds, is reported to prove the real-time capability of these strategies. It can be noticed that the TAT is well below the maximum allowable time-step of 10ms of the HCU software for almost the duration of the test. However, the TAT presents a peak every time a prediction occurs, reaching higher values closer to the limit. This can be accepted since it occurs very few times during the cycle, and the dimensions of the vector listed in Tab. 3.2 have been chosen to avoid software overruns.

5.2.1 Energy prediction comparison

Table 5.3: Results of the tests at the C-HiL: comparison of predictions depending on the initial SoC and the meters remaining to the ZEZ event

	C-RBS (TC1)						**A-ECMS (TC2)**					
	1st prediction ($d_{i,Z}$ = 27516 m)			**2nd prediction** -			**1st prediction** ($d_{i,Z}$ = 30538 m)			**2nd prediction** ($d_{i,Z}$ = 3307 m)		
	Meas. [Wh]	Pred. [Wh]	$\Delta_{\%}$ [%]	Meas. [Wh]	Pred. [Wh]	$\Delta_{\%}$ [%]	Meas. [Wh]	Pred. [Wh]	$\Delta_{\%}$ [%]	Meas. [Wh]	Pred. [Wh]	$\Delta_{\%}$ [%]
E_{I^+}	463	449	**-3.1**	-	-	-	463	543	**17.2**	463	469	**1.2**
E_{I^-}	-456	-395	**-13.2**	-	-	-	-456	-474	**4.0**	-456	-482	**5.7**
E_{RL}	257	266	**3.2**	-	-	-	257	351	**36.3**	257	270	**5.1**
E_{batt}	855	808	**5.4**	-	-	-	836	958	**14.6**	836	782	**6.9**
	[%]	[%]	[%]	[%]	[%]	[%]	[%]	[%]	[%]	[%]	[%]	[%]
SoC	12.9	12.4	**-0.6**	-	-	-	12.9	14.7	**1.9**	12.9	12.0	**-0.8**

	C-RBS (TC3)						**A-ECMS (TC4)**					
	1st prediction ($d_{i,Z}$ = 26984 m)			**2nd prediction** ($d_{i,Z}$ = 5910 m)			**1st prediction** ($d_{i,Z}$ = 26984 m)			**2nd prediction** ($d_{i,Z}$ = 5917 m)		
	Meas. [Wh]	Pred. [Wh]	$\Delta_{\%}$ [%]	Meas. [Wh]	Pred. [Wh]	$\Delta_{\%}$ [%]	Meas. [Wh]	Pred. [Wh]	$\Delta_{\%}$ [%]	Meas. [Wh]	Pred. [Wh]	$\Delta_{\%}$ [%]
E_{I^+}	463	426	**-7.9**	463	406	**-12.3**	463	355	**-23.4**	463.1	439.9	**-8.3**
E_{I^-}	-456	-342	**-24.9**	-456	-409	**-10.2**	-456	-302	**-33.7**	-455.5	-417.6	**-5.0**
E_{RL}	257	264	**2.6**	257	265	**2.9**	257	274	**6.4**	257.4	264.9	**2.9**
E_{batt}	841	780	**7.2**	841	682	**-18.8**	839	690	**17.8**	839.4	746.5	**-11.1**
	[%]	[%]	[%]	[%]	[%]	[%]	[%]	[%]	[%]	[%]	[%]	[%]
SoC	12.9	12.0	**-0.9**	12.9	10.5	**-2.4**	12.9	10.6	**-2.3**	12.9	11.5	**-1.4**

	C-RBS (TC5)						**A-ECMS (TC6)**					
	1st prediction $d_{i,Z}$ = 26984 m			**2nd prediction** $d_{i,Z}$ = 5913 m			**1st prediction** $d_{i,Z}$ = 27539 m			**2nd prediction** -		
	Meas. [Wh]	Pred. [Wh]	$\Delta_{\%}$ [%]	Meas. [Wh]	Pred. [Wh]	$\Delta_{\%}$ [%]	Meas. [Wh]	Pred. [Wh]	$\Delta_{\%}$ [%]	Meas. [Wh]	Pred. [Wh]	$\Delta_{\%}$ [%]
E_{I^+}	463	387	**-16.5**	463.05	529.75	**14.4**	463	431	**-6.9**	-	-	-
E_{I^-}	-456	-312	**-31.4**	-455.53	-505.37	**10.9**	-456	-380	**-16.5**	-	-	-
E_{RL}	257	273	**6.1**	257.44	259.20	**0.7**	257	261	**1.4**	-	-	-
E_{batt}	837	802	**4.2**	837.12	834.15	**-0.4**	834	844	**1.2**	-	-	-
	[%]	[%]	[%]	[%]	[%]	[%]	[%]	[%]	[%]	[%]	[%]	[%]
SoC	12.9	12.3	**-0.5**	12.9	12.8	**-0.1**	12.8	13.0	**0.2**	-	-	-

In Tab. 5.3, the predicted energies E_{I^+}, E_{I^-}, E_{RL}, and E_{batt} are reported and compared to the ones related to the driven route in terms of percentage difference $\Delta_{\%}$, as in Eq. (4.12), Eq. (4.13), and Eq. (4.14). Analogously, the predicted battery energy consumption and SoC are also analyzed. Since the TC2 is the most representative test case, the related scenario is reported on the map in Fig. 5.1a and it is analyzed in detail in the following paragraph. In fact, it simulates the realistic scenario of a driver that does not follow exactly the suggestion of the navigator, independently if on purpose or not, inducing several re-routings. Focusing on it, the MSP suggests the fastest route related to the actual real-time traffic data, the purple line in Fig. 5.1a, and the HCU makes the prediction referring to that route. This leads to the first target SoC represented in Fig. 5.3b and as long as the driver follows the proposed route, the target SoC remains constant. Then, when the driver takes a different road, a re-routing occurs leading to a new query to the MSP, so updated navigation data, cyan line in Fig. 5.1b, and thus a recalculation of the target SoC, second grey box in Fig. 5.3b. Looking at the results in terms of energy in Tab. 5.3, the first prediction presents relevant errors for most of the KPIs due to the differences in the routes, and consequently a not precise target SoC calculation. After the re-routing, the driver follows the suggested route, so in this case, the energy KPIs present significantly lower errors leading to an accurate prediction. Even if there is such a considerable initial error, and the re-routing occurs close to the ZEZ ($d_{i,Z}$ = 3307 m), the initial target SoC does not change significantly after re-routing, and the EMS can grant the ZEZ in full electric. As shown in Fig. 5.1b, another re-routing occurs but this time within the ZEZ, identified also by the spike within the green area in the TAT bottom plot. Thus, the TeCU queries the MSP and retrieves the navigation data, but no prediction will be performed. In fact, at this point, the vehicle can only go in electric drive and no countermeasures can be taken by the EMS if the SoC is not sufficient enough. In general, it can be noticed that if the driver follows the proposed route (and so no re-routings occur), the energy predictions well-represent the energy necessary to perform the ZEZ in full electric drive. That is the case of TC1 and TC6, where the SoC errors are -0.6% and 0.2% respectively. For TC2, TC4, and TC5, the driver does not follow the suggested route, inducing re-routings. Even in these cases, the SoC prediction error is below 2.3%, which is covered by the offset ξ_s expressed in Eq. (4.23), and then improved after the rerouting, as well as the KPIs and the predicted battery's energy consumption. Differently, for what concerns the TC3, the relative errors increase after the re-routing, worsening the energy prediction. This was due to inaccurate values of the real-time traffic data provided by the MSP, which underestimates the congestion along the route. Even if this represents a common situation that can happen when the vehicle is driving on the road, however, the error produced is still compensated by the offset ξ_s.

5.2.2 Fuel consumption comparison

Table 5.4: Results of the tests at the C-HiL: comparison between the two strategies in terms of raw and corrected CO_2

TC	EMS	$\bar{\eta}_{ICE}$ [%]	$\bar{\eta}_{EM}$ [%]	$\bar{\eta}_{ISG}$ [%]	ξ_i [%]	ξ_f [%]	FC [l/100km]	E [Wh]	CO_2 [g/km]	$\Delta CO_{2,\%}$ [%]	ΔE [Wh]	$CO_{2,c}$ [g/km]	$\Delta CO_{2,c,\%}$ [%]
1	C-RBS	16.0	80.3	75.0	30	27.2	13.3	-139	315				
2	A-ECMS	24.3	80.9	75.6	30	29.7	10.6	-196	250	**-20.4**	57	250	**-20.4**
3	C-RBS	14.8	80.0	73.7	50	26.4	10.8	1444	256				
4	A-ECMS	23.6	80.9	75.6	50	28.3	8.4	1184	198	**-22.5**	260	189	**-26.1**
5	C-RBS	15.3	81.5	74.4	90	29.1	4.8	3902	113				
6	A-ECMS	21.4	81.2	76.1	90	31.8	4.2	3684	99	**-12.5**	218	90	**-20.1**

Then, focusing on Tab. 5.4, the C-RBS and the A-ECMS are compared in terms of corrected CO_2 production, calculated with Eq. (4.35), Eq. (4.36), and Eq. (4.37). In particular, the Tab. 5.4

reports the ICE's and electric machines' average efficiency, the fuel consumption FC, the energy consumption E, the raw CO_2, and the corrected CO_2. Similar to the comparison made in Section 4.4, the relative percentage difference has been chosen as the assessment parameter, both for the raw $\Delta CO_{2,\%}$ and corrected value $\Delta CO_{2,c,\%}$. This comparison can be considered representative since the driven profile is always the same, while the only variable parameter is the target SoC. Although, the latter varies in a limited range of a few percentage points, so it does not significantly affect the EMS. Hence, it can be noticed that for the A-ECMS the average efficiencies of the ICE and the ISG are higher, leading to lower fuel consumption and, apart from the case $\xi_i = 30\%$, a lower energy consumption. This means a reduction of raw and corrected CO_2 production, in a range of 12.5% - 22.5% and 20.1% - 26.1%, respectively. Moreover, the final values of SoC are well above the minimum SoC, $\xi_{min,b}$, proving that the ZEZ has been performed in full electric drive even if the navigation data present some normal inaccuracies, due to different proposed routes and traffic data that do not reflect exactly the current situation.

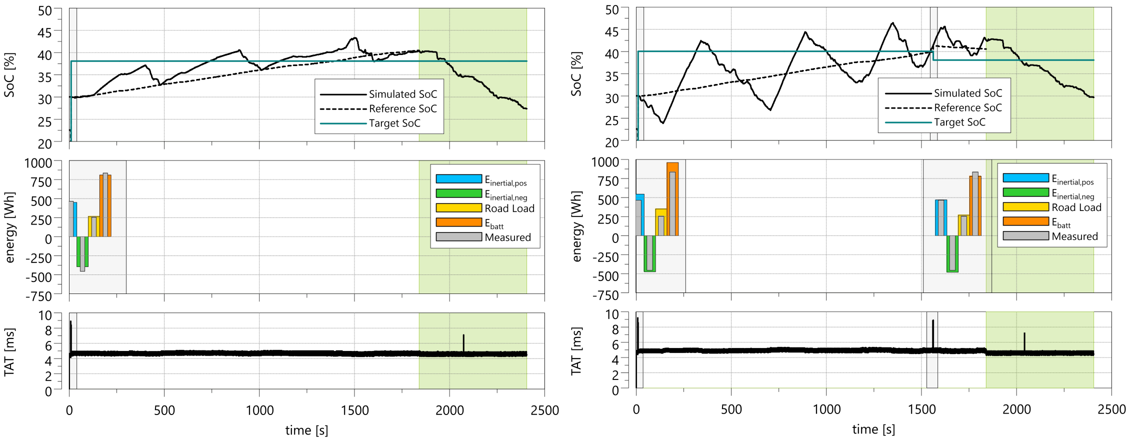

(a) TC 1: ξ_i = 30%

(b) TC 2: ξ_i = 30%

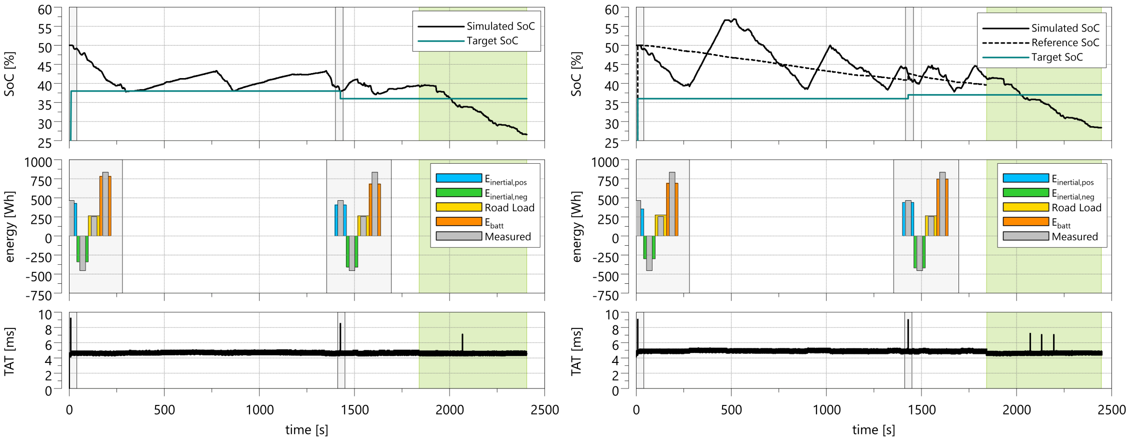

(c) TC 3: ξ_i = 50%

(d) TC 4: ξ_i = 50%

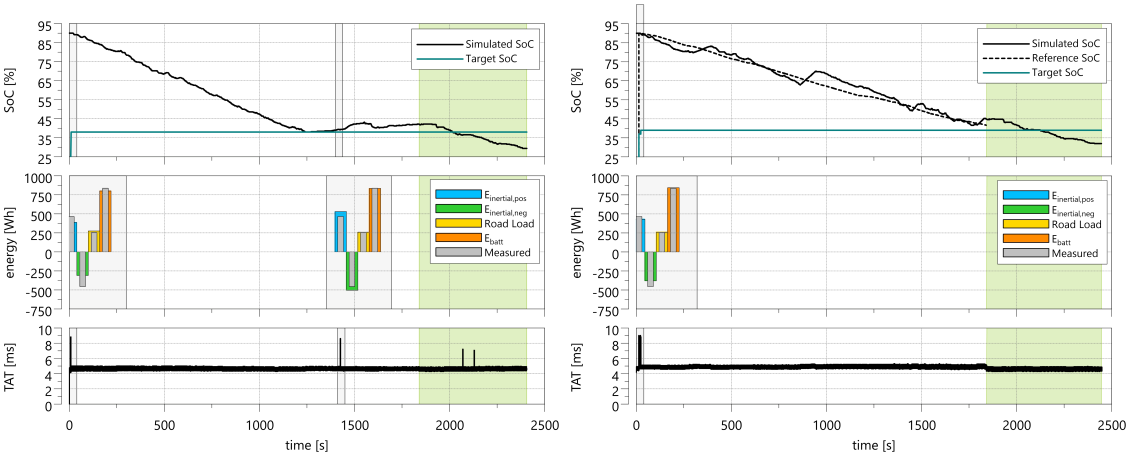

(e) TC 5: ξ_i = 90%

(f) TC 6: ξ_i = 90%

Figure 5.3: Results of the tests at the C-HiL: a) b) c) simulations performed with C-RBS at ξ_i = 30%, 50%, 90% respectively; d) e) f) simulations performed with A-ECMS at ξ_i = 30%, 50%, 90% respectively

Chapter 6

Part I - Conclusions

In this activity, a Connected Hardware-in-the-Loop system with integrated connectivity has been set up resulting in a more modular and universal tool for testing and validation of predictive electronic horizon functions. On one hand, it provides higher flexibility due to the possibility to test different types of predictive functions (both long and short horizon) and the capability of acting on each component and controller model. On the other hand, it grants higher reliability, as both the hardware and the software are the same as those implemented on the vehicle, allowing seamless functions implementation on-board once validated at the HiL. In particular, the latter is equipped with a Telecommunication Control Unit (TeCU), and a Human Machine Interface (HMI) to manage the communication with the Map Service Provider (MSP) itself, as it would be in the real vehicle, set the desired destination, and see the route suggested by the MSP. This testing platform results in a shortening of the validation process as well as a further reduction of the gap between laboratory and on-vehicle tests.

Then, a supervisory controller architecture for PHEVs based on predicted functions and an Adaptive-ECMS has been proposed to handle a Zero-Emission Zone using navigation data retrieved in real-time from the map service provider. With this information, the Speed Profile Prediction is performed to evaluate an energetically equivalent driving profile that is then fed to the BVM. The latter calculates the amount of energy necessary to drive the ZEZ in pure electric mode and forward that target SoC to the control policy. For a proper comparison, also the conventional RBS has to be modified into an A-RBS to handle the ZEZ even in situations where a Charge Increasing mode is required. Thus, the latter has been tested on two inverted RDE cycles while facing a ZEZ event. As a consequence, the test results helped to define a more efficient Combined-RBS that is finally tested on a real driving scenario measured on the road and compared to the A-ECMS at the C-HiL. Since the navigation data from the MSP are real and referred to the current traffic situation, the proposed route can differ from the driven one, leading to re-routing and consequent adaptation of the target SoC.

The results show that:

- the SPP evaluates an energetically equivalent profile with a relative error of the required battery's energy between 0.4% and 11%, which results in a variation of the target SoC between 0.1% to 2.4%. These values are compensated by the SoC offset used to calculate the target SoC, so the ZEZ in pure electric is always granted. However, the SPP prediction is strongly dependent on the accuracy of the navigation and traffic data as shown in TC3, and on the driver behavior;
- the A-ECMS outperforms the C-RBS in all the test cases in terms of fuel consumption and so corrected CO_2 production, with a reduction between 20.1% and 26.1%. Thus, the proposed predictive strategy not only grants the fully electric drive in an urban event, preventing the payment of fees but also optimizes the fuel consumption while driving outside the ZEZ;
- both strategies have been deployed into the real HCU and tested with real vehicular connectivity, proving the real-time capability and robustness of the predictive functions under different and unpredictable conditions. This has accelerated the function development laying the ground for future on-road tests.

6.1 Future works

Even if the C-HiL tests already provide positive results under challenging scenarios, further tests are required. Firstly, a scenario simulator and an improved driver model must be implemented at the C-HiL to create multiple test cases without measuring them on the road. Then, additional tests on the vehicle have to be fulfilled to definitely prove the effectiveness of the control policy. Moreover, the testing with real connectivity underlined how the SPP still presents room for improvement. On one hand, despite the good results achieved during this part of the Ph.D. research project, the validation of the SPP is limited to the scenarios under test, thus a wider and more generic campaign is needed. On the other hand, it should be enhanced with the addition of Machine Learning algorithms to adapt itself with respect to the driver's behavior preventing physiological variability. Finally, the TAT measurements show how the predictions affect the HCU, thus the next step is to transfer all the computational burden firstly to the TeCU and then to a cloud server since the information exchange does not need very low latencies.

Part II

Emissions management strategies

Chapter 7

Simulation environment

In Part I of this dissertation, the effectiveness of the energy management strategies based on navigation data has been proved by the testing at the C-HiL on a high-performance hybrid prototype vehicle. Nevertheless, this application does not aim at reducing pollutant emissions, since both the model and the strategies only focus on fuel consumption minimization. Then, in this Part II a wider analysis is performed to assess the advantages of navigation data even from the pollutants' point of view, by developing and testing an advanced model-based strategy.

With this regard, in this chapter, the vehicle's model used for the simulation is presented, with a brief description of each of the powertrain components. Then, since the focus is put on NO_x emissions, a detailed analysis of the EATS components is provided with a particular emphasis on the respective thermal model. In fact, the conversion efficiency of the components strongly depends on their temperature and on the space velocity, modeled with a map-based approach. The models' validation is then presented to underline its prediction capability for the powertrain dynamics, the fuel consumption, and the pollutants emissions.

7.1 Vehicle under test

The vehicle selected as a case study for this activity is a P2 Diesel PHEV classified as a light commercial vehicle (LCV). The chosen hybrid architecture, represented in Fig. 7.1, provides high flexibility in terms of possible operating modes and torque split strategies. The location of the EM, thanks to the separation clutch, allows performing regenerative braking as well as pure electric drive. The combination of a 9.4 kWh high-voltage (HV) battery and a 90 kW / 440 Nm electric motor ensures a significant all-electric range with a top speed that reaches 130 km/h, depending on hybrid strategy calibration. The electric power unit is paired with a 2.3-liter compression ignition engine and a 6-speed automatic transmission. The main vehicle specifications are listed in Tab. 7.1.

The operating mode between pure electric drive and hybrid drive is managed through a calibrated strategy based on vehicle speed, requested torque, and battery state of charge. Focusing

Figure 7.1: Light Commercial PHEV: powertrain layout

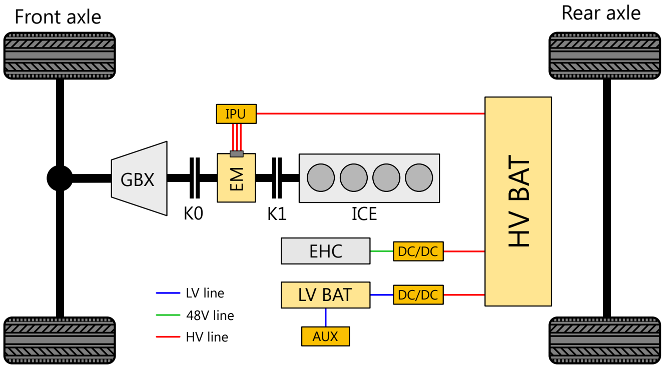

Table 7.1: Vehicle powertrain specifications

Vehicle	Curb weight	2750 kg
	Configuration	P2, front wheel drive
Engine	Type	Turbocharged Diesel
	Displacement	2.3 l
	Rated power	95 kW @ 3000 rpm
	Rated torque	380 Nm @ 2000 rpm
	Gearbox	6-DCT
Electric machine	Type	PM synchronous
	Peak power	90 kW
	Peak/continuous torque	440 / 260 Nm
	Maximum speed	6000 rpm
Battery	Type	Lithium-ion polymer
	Capacity	9.4 kWh / 25.5 Ah
	Nominal voltage	370 V

on hybrid operating mode, different configurations are possible thanks to P2 architecture: the EM can provide additional torque to support the ICE when the driver request is particularly relevant or, on the contrary, it can operate as a generator to charge the battery with the engine providing additional torque with respect to the driver request, allowing to follow the best trade-off between fuel economy and pollutant emissions. A so-called range-extender mode is also possible when the vehicle is at a standstill and the engine is running for the sole purpose of charging the battery. Hybrid strategy definition and calibration will be further discussed in Chapter 8.

7.2 Powertrain components

The vehicle has been modeled in Simulink® starting from an existing mild-hybrid P0 Diesel model relative to a light-commercial vehicle, previously developed and validated by the industrial partner. That model provides a detailed engine and EATS model, which is essential for the purposes of this activity, but does not have a high-voltage line and an electric machine in a position capable of electric drive. Thus, the model has been modified in order to have a P2 architecture with a detailed HV battery and motor model, following the same analytical approach described in Section 3.1.2. The respective components' specifications have been derived from a benchmarking activity performed by the industrial partner on a comparable vehicle. By doing so, the resulting Simulink® model represents a proof of concept and can not be validated on the prototype vehicle experimental data. Hence, the validation procedure, which will be described in Section 7.4, focuses on the vehicle's components individually and not on the whole system, such as the one done in Section 3.1.4. However, the obtained accuracy of the model is still acceptable for the purpose of this dissertation.

Focusing on the powertrain components, each of these has been modeled with the same analytical approach as in Section 3.1.2, so for a matter of brevity the detailed description is here omitted but it can be found in [151, 152]. However, a general overview of the propulsion systems is provided hereafter.

7.2.1 Internal combustion engine

For what concerns the internal combustion engine, a map-based approach has been adopted: fuel flow, exhaust gas temperature, and pollutant emissions maps allow calculating fuel consumption, turbine inlet temperature, and engine-out emissions of HC, CO, soot, and NO_x as a function of engine coolant temperature, load, and speed. All the data included in the mentioned maps have been obtained from previous activities and confidentially shared by the industrial partner. For completeness, fuel consumption, engine-out NO_x emission, and exhaust gas temperature maps have been reported in Fig. 7.2, Fig. 7.3, and Fig. 7.4 respectively.

To take into account the dependency of the maps on the engine temperature, two different maps have been evaluated by the industrial partner at the test bench: one measured when the engine has just been started, defined as *cold*, and the other measured in steady state when the coolant temperature reached its target, thus called *warm*. Focusing on the transient maneuvers, three different conditions have been identified and expressed by Eq. (7.4).

$$T_c(t) < T_{cold} \tag{7.1}$$

$$T_{cold} \leq T_c(t) < T_{warm} \tag{7.2}$$

$$T_c(t) \geq T_{warm} \tag{7.3}$$

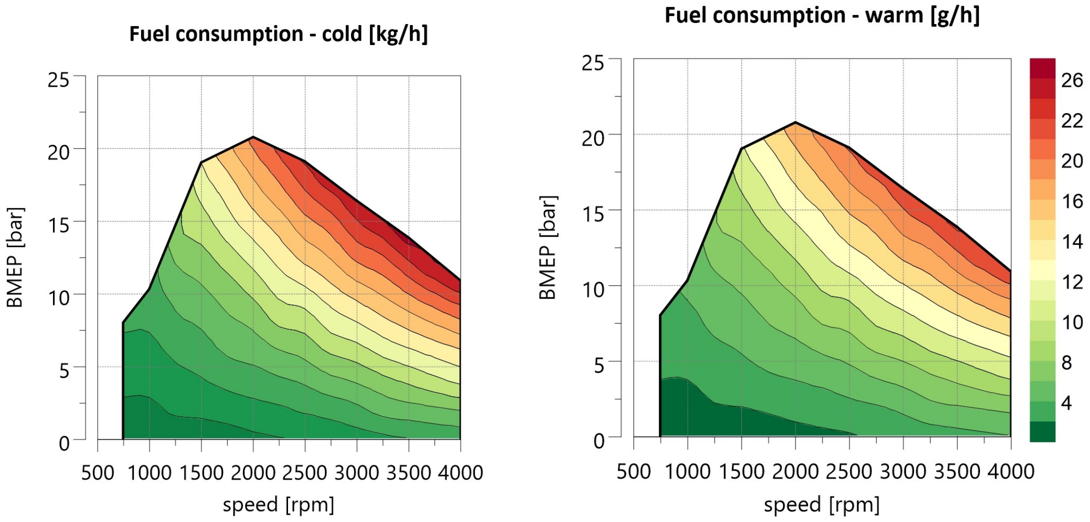

(a) (b)

Figure 7.2: *Cold* and *warm* fuel consumption maps

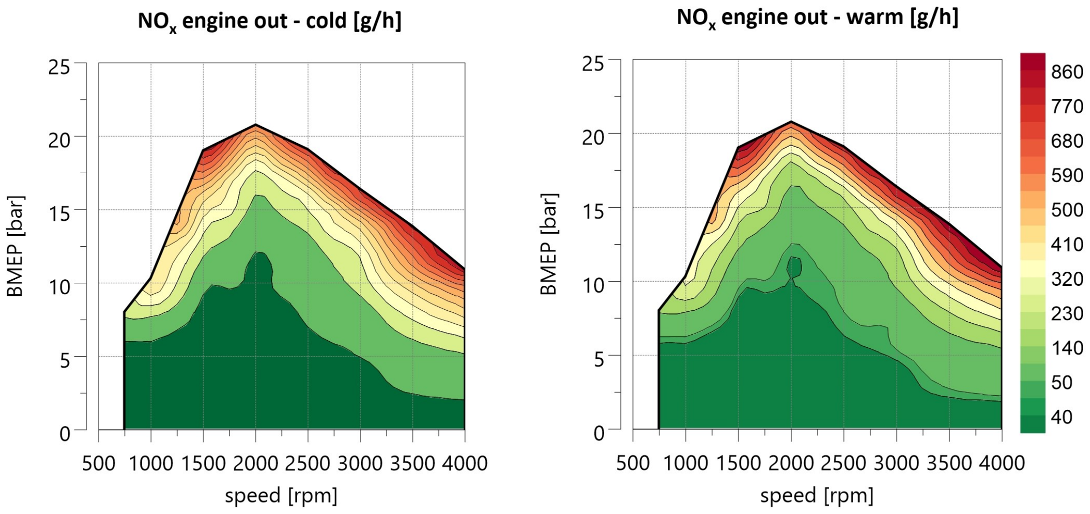

(a) (b)

Figure 7.3: *Cold* and *warm* NOx production maps

where T_c is the temperature of the coolant in °C, while T_{cold} and T_{warm} are temperature thresholds equal to 30°C and 90°C, respectively. Then, the *cold* and *warm* instantaneous values of fuel consumption, NO$_x$ and exhaust gas temperature are weighted as follows:

$$X_w = X_{cold} \cdot w_{cold} + X_{warm} \cdot w_{warm} \tag{7.4}$$

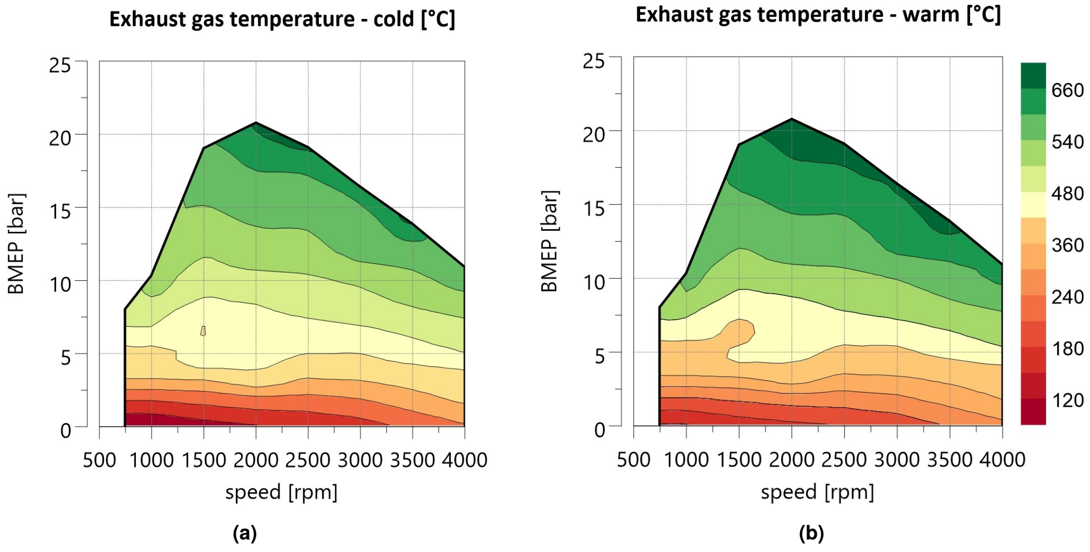

(a)

(b)

Figure 7.4: *Cold* and *warm* exhaust gas temperature maps

where X_{cold} and X_{warm} are the generic values evaluated from the maps Fig. 7.2, Fig. 7.3, and Fig. 7.4, while w_{cold} and w_{warm} are the weighting factors that depend on the conditions identified by Eq. (7.1),Eq. (7.2), and Eq. (7.3) and are summarized in Tab. 7.2.

Table 7.2: *Cold* and *warm* weighting factors

	Cold	**Warm**
Low-temperature range (Eq. (7.1))	1	0
Medium-temperature range (Eq. (7.2))	$1 - \frac{T_c(t) - T_{cold}}{T_{warm} - T_{cold}}$	$\frac{T_c(t) - T_{cold}}{T_{warm} - T_{cold}}$
High-temperature range (Eq. (7.3))	0	1

7.2.2 Electric machine

A similar map-based approach is used for the electric machine whose efficiency map is represented in Fig. 7.5, where the black lines specify the *continuous* (dashed line) and *peak* (continuous line) torque limitations while the magenta ones the *continuous* (dashed line) and *peak* (continuous line) limitations.

7.3 Exhaust after-treatment system

As introduced in Section 1, an advanced EATS is mandatory to meet the demanding targets imposed by the regulation in terms of pollutant emissions without affecting engine efficiency,

Figure 7.5: Efficiency map, power and torque limitations of the electric machine

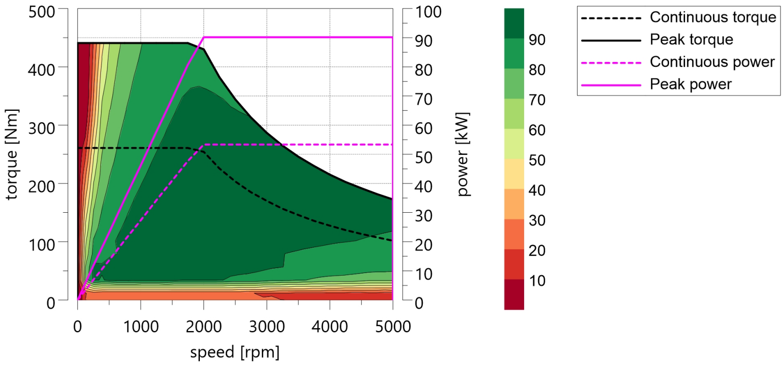

while being compliant with CO_2 emissions limits. Therefore, the modeled vehicle is equipped with a Euro 7-oriented Diesel EATS, represented in Fig. 7.6, which includes the devices listed in Tab. 7.3 with the corresponding volume V. A detailed description of each component and the respective operation methodology is provided in Section 1.3.

Table 7.3: Exhaust after-treatment components specifications

Component	**Volume [l]**
Electrical heater	-
Diesel Oxidizing Catalyst (DOC)	1.6
Low Thermal Mass Selective Catalytic Reduction (LTM-SCR) catalyst	1.2
SCR-coated Diesel Particulate Filter (SDPF)	4.0
SCR catalyst	3.5

Figure 7.6: Schematic representation of vehicle EATS architecture

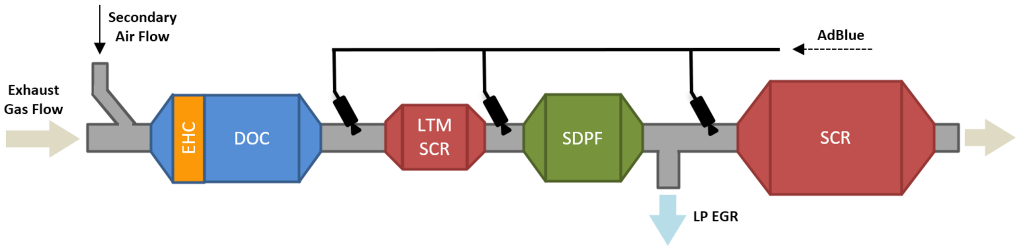

Moreover, as pointed out in Fig. 7.6, a secondary air flow is also provided since a gas flow through the heating disc is mandatory to transfer the heating power to the following devices along the exhaust line. This means that if a pre-heating phase is planned before the engine start, the air flow through the exhaust line must be provided by installing a secondary air pump upstream of the EHC. The pump is modeled by providing an additional air mass flow during pre-heating phases when the engine is not running. Then, the resulting power consumption is calculated depending on the supply voltage and air flow rate, according to the experimental data shown in Fig. 7.7, derived from secondary air pumps available on the market.

Figure 7.7: Secondary air pumps: absorbed current for different supply voltages [153]

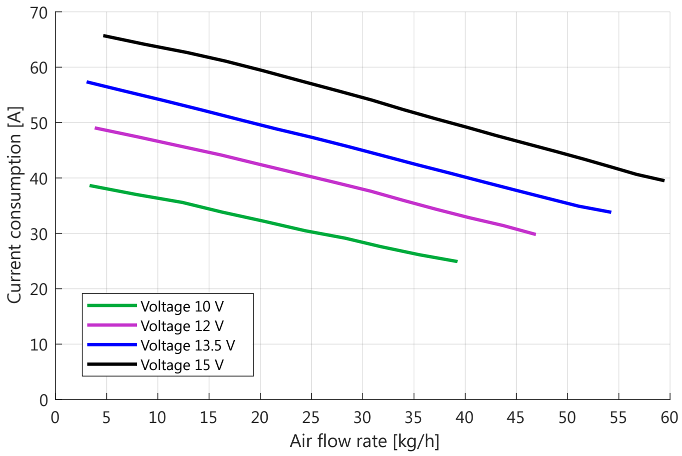

The DOC conversion efficiency maps of HC, CO, and NO depend on the volumetric flow rate and gas average temperature and allow to calculate the resulting pollutant emissions after the oxidizing reactions that take place in the DOC. Similarly, NO_x reduction performed by LTM-SCR, SDPF, and SCR is modeled for each device with a map based-approach, by first calculating NO_x conversion efficiency, which depends on gas average temperature, NO_2/NO_x ratio, and space velocity; all the mentioned maps of pollutants conversion efficiency for the different EATS devices have been obtained from experimental campaigns previously carried out by the industrial partner and the related data are confidential. Then, from the knowledge of the conversion efficiency, it is possible to obtain the amount of NH_3 that can react to reduce NO_x, and thus the amount of AdBlue® to be injected. Therefore, a comprehensive and robust EATS thermal model, which allows to correctly estimate the average temperature of each after-treatment device, is mandatory to obtain realistic results in terms of tailpipe pollutant emissions.

7.3.1 Thermal model

The thermal heat exchange with the exhaust gases is modeled for each device by dividing the physical component into a series of equivalent elementary bricks. For each of them, the contributions of conduction, radiation, external and internal convection are calculated separately using semi-empirical formulas to determine the temperature of the solid material of the brick and

Figure 7.8: Schematic representation of the thermal model with the representative temperatures and heat flows for the generic i-th brick [153]

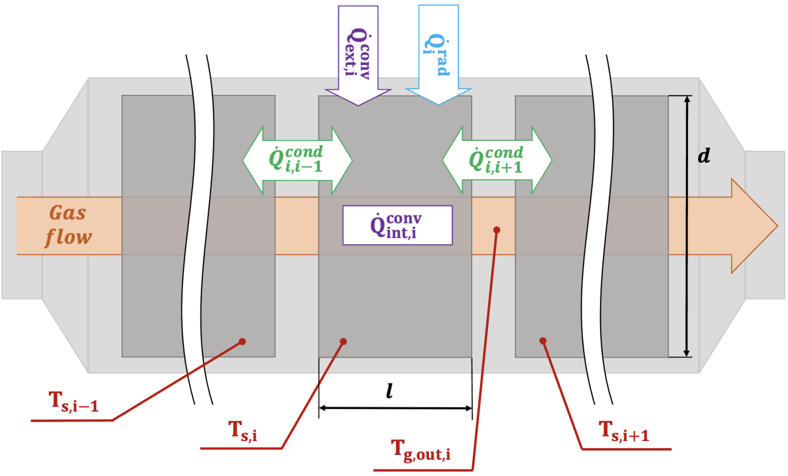

of the exhaust gas at the brick outlet. The heat exchanged by internal convection $\dot{Q}^{conv}_{int,i}$ in one simulation time-step for the single i-th brick is given by the following equation:

$$\dot{Q}^{conv}_{int,i} = h_{int} \cdot A_{int} \cdot \left(T_{g,0,i} \frac{\epsilon_s}{1 + \frac{\epsilon_s}{\epsilon_t} - \epsilon_s} - T_{s,0,i} \frac{\epsilon_t}{1 + \frac{\epsilon_t}{\epsilon_s} - \epsilon_t} \right) \tag{7.5}$$

where A_{int} is the internal brick surface in contact with the gas, $T_{g,0,i}$ and $T_{s,0,i}$ are the initial temperatures of the gas and of the solid material respectively, while the parameters ϵ_s and ϵ_t are calculated for each brick as described in [154]. Finally, h_{int} is the convective heat transfer coefficient (HTC), obtained as:

$$h_{int} = \frac{Nu \cdot \lambda_g}{d} \tag{7.6}$$

being λ_g the thermal conductivity of the considered gas, d the diameter of the cross-section, and Nu the Nusselt number, calculated as a function of Reynolds number Re according to Meisner-Sorenson relation [155]:

$$Nu = 0.077 \cdot Re^{0.769} \tag{7.7}$$

The temperature of the gas at the brick outlet $T_{g,out,i}$ at the considered simulation time-step is calculated as:

$$T_{g,out,i} = T_{g,0,i} - Nu_t \cdot \left(T_{g,0,i} \frac{\epsilon_s}{1 + \frac{\epsilon_s}{\epsilon_t} - \epsilon_s} - T_{s,0,i} \frac{\epsilon_t}{1 + \frac{\epsilon_t}{\epsilon_s} - \epsilon_t} \right) \tag{7.8}$$

where Nu_t is the corrected Nusselt number, calculated as suggested in [156] to improve the model behavior during transients. The average temperature of the solid material $\bar{T}_{s,i}$, which is used to evaluate the other types of heat exchange, is obtained through the following equation:

$$\bar{T}_{s,i} = \bar{T}_{g,i} + \epsilon_t \cdot \left(T_{s,0,i} - \bar{T}_{g,i}\right) \tag{7.9}$$

where $\bar{T}_{g,i}$ is the average temperature of the gas crossing the brick, calculated as:

$$\bar{T}_{g,i} = \frac{T_{g,0,i} + T_{s,0,i} \cdot \left(\dfrac{\epsilon_t}{\epsilon_s} - \epsilon_t\right)}{1 + \dfrac{\epsilon_t}{\epsilon_s} - \epsilon_t} \tag{7.10}$$

The heat exchanged by external convection $\dot{Q}^{conv}_{ext,i}$ between the solid material of the brick and the surrounding environment for each simulation time-step is evaluated as follows:

$$\dot{Q}^{conv}_{ext,i} = h_{ext} \cdot A_{ext} \cdot \left(T_{amb} - \bar{T}_{s,i}\right) \tag{7.11}$$

where h_{ext} and A_{ext} represent the convective HTC and the heat transfer area respectively, while T_{amb} is the ambient temperature.

The contribution of radiation for the single brick $\dot{Q}^{rad}_i$ is calculated as:

$$\dot{Q}^{rad}_i = \sigma \cdot \epsilon \cdot A_{ext} \cdot \left(T^4_{amb} - \bar{T}^4_{s,i}\right) \tag{7.12}$$

where σ is the Stefan-Boltzmann constant and ϵ is the emissivity. The heat transferred by conduction $\dot{Q}^{cond}_i$ through the bricks is obtained through the following equation:

$$\dot{Q}^{cond}_i = \frac{\lambda_s \cdot A_{cond}}{l} \cdot \left(\bar{T}_{s,i-1} - 2\bar{T}_{s,i} + \bar{T}_{s,i+1}\right) \tag{7.13}$$

where λ_s is the thermal conductivity of the solid material of the brick, A_{cond} is the contact area between the bricks and l represents the length of the considered brick. Once all the contributions are calculated, the total heat flow $\dot{Q}^{tot}_i$ for the i-th brick for one simulation time-step is defined as:

$$\dot{Q}^{tot}_i = \dot{Q}^{conv}_{int,i} + \dot{Q}^{conv}_{ext,i} + \dot{Q}^{rad}_i + \dot{Q}^{cond}_i \tag{7.14}$$

which allows calculating the final temperature $T_{s,fin,i}$ of the solid material of the brick at the end of the simulation time-step:

$$T_{s,fin,i} = T_{s,0,i} + \frac{\dot{Q}^{tot}_i}{m_s \cdot c_p} \tag{7.15}$$

being m_s the mass of the considered solid material and c_p the corresponding specific heat capacity. The base architecture of the heat transfer model is the same for each component of the exhaust line (close-coupled and under-flow pipes included), adjusting all the coefficients for each specific component and taking into consideration also the contribution of the exothermic chemical processes that may happen due to the conversion of pollutant species.

Since the attention of this activity is focused on NO_x emissions estimation, HC, CO, and soot emissions have been not taken into consideration for this analysis. Therefore, the exothermal reactions linked to the oxidation of these pollutant species, which would increase the exhaust gas temperature and thus improve the conversion efficiency of the SCR catalysts, are also conservatively neglected. Consequently, a conservative approach is adopted, and the worst case in terms of NO_x emission is considered. Focusing on NO_x reduction, the three main reactions which take place in the two SCR catalysts and in the SDPF are described by Eq. (1.21), Eq. (1.22), and Eq. (1.23) in Section 1.3.1. The "fast SCR reaction", expressed by Eq. (1.23) becomes very relevant for high values of NO_2/NO_x ratio, which happens if an oxidation catalyst is installed upstream of the SCR catalyst (as for this specific application). The overall heat generated from NO_x reduction is evaluated by considering the specific enthalpy related to each of the previous chemical reactions and the moles of reduced NO_x. More in detail, being β the ratio between NO_2 and the total NO_x mass and M_{NO_x} the molar mass of the considered species, the moles of converted NO and NO_2 are obtained from the following equations:

$$n_{NO} = (1-\beta)\cdot\frac{m_{NO_x}^{in} - m_{NO_x}^{out}}{M_{NO}} \tag{7.16}$$

$$n_{NO_2} = \beta\ \cdot\frac{m_{NO_x}^{in} - m_{NO_x}^{out}}{M_{NO_2}} \tag{7.17}$$

Then, the moles of NO and NO_2 involved in the “fast SCR” reaction are calculated as:

$$min\,(n_{NO},n_{NO_2}) = n_{NO}^{fast} = n_{NO_2}^{fast} = \frac{1}{2}n_{NH_3}^{fast} = n_{fast} \tag{7.18}$$

while the remaining moles of NO and NO_2 reacting in the “standard SCR” and “slow SCR” are:

$$n_{NO} - n_{NO}^{fast} = n_{NO}^{std} = n_{NH_3}^{std} = n_{std} \tag{7.19}$$

Finally, knowing the enthalpy of reaction h [J/mol] associated with each mole of reacting NO or NO_2, the overall heat resulting from NO_x reduction can be calculated as:

$$\dot{Q}_{exo} = \left(h_{fast}\cdot n_{fast} + h_{std}\cdot n_{std} + h_{slow}\cdot n_{slow}\right)\frac{1}{dt} \tag{7.20}$$

which is added to the total heat flow expressed by Eq. (7.14) for the mentioned EATS components.

Focusing on the heating contribution provided by the current flowing in high-resistance circuits of the EHC, located upstream of the DOC, the exhaust gas flow is rapidly heated up before proceeding along the exhaust line, allowing fast heating that is independent of engine operation and extremely focused on the target devices. In this case, the electrical heater is modeled as one single brick, following the same equations already discussed above to calculate the temperature of the exhaust gas flow at the outlet. In this case, an additional contribution to the power balance is given by the electric power employed to heat the device and then transferred to the exhaust gas flow through internal convection.

7.4 Model validation

In order to have a robust and reliable simulation tool, providing results in terms of fuel consumption and pollutant emissions that are comparable to real values, the most significant quantities involved in a hybrid electric powertrain, such as EM and ICE torque, battery current, and SoC must be simulated and compared with experimental results. Since the described model is not representing an actual existing vehicle, a comprehensive vehicle model validation would not be possible. However, the adopted models for vehicle dynamics, electric power unit, internal combustion engine, and after-treatment system have been individually validated as part of previous research activities. Accordingly, a comparison between simulated and experimental results of the most significant quantities involving ICE and EATS operation is shown in the following paragraphs.

7.4.1 Powertrain

As fully described in [151], vehicle dynamics, EM, and HV battery models were validated for an existing P2 PHEV on a WLTC performed in charge-depleting conditions, meaning that the vehicle performs the driving cycle starting with fully charged battery, which allows completing the whole test in pure electric driving mode with no engine intervention. In this regard, Fig. 7.9 shows the model's capability to accurately follow the given speed profile, validating the vehicle dynamics. Then, focusing on plot Fig. 7.10, it can be seen that the model is capable of accurately calculating EM torque and speed both in traction and generator mode, showing very good agreement with the experimental data apart from a small overestimation of the regenerative contribution which can be noticed for negative torque values. Concerning the HV battery, even though a quasi-static model is not able to fully simulate fast transient phases, current and power are simulated with good accuracy, showing an acceptable match with the measurements both for negative and positive current values. As a consequence, the simulated battery SoC trend properly reflects the experimental one, both during the charging and discharging phases.

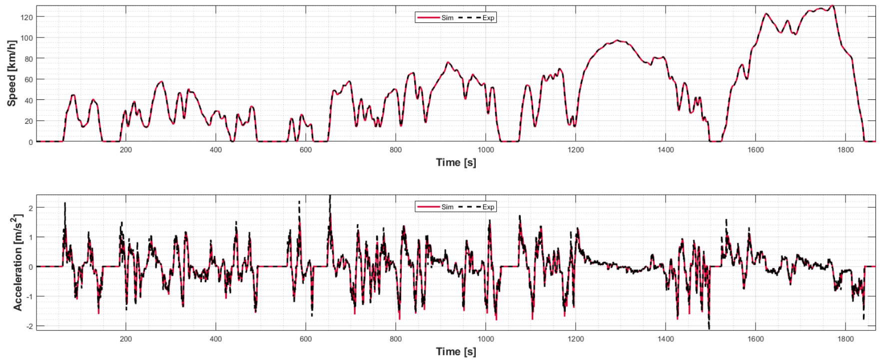

Figure 7.9: Vehicle model validation: experimental (black dashed) and simulated (red solid) results over a WLTC CD cycle

7.4.2 Exhaust after-treatment system

The map-based ICE and EATS models have been calibrated and validated by the industrial partner, comparing simulation results with measured data collected during steady-state and dynamic tests on the chassis dynamometer. Fig. 7.11a shows a good match between the simulated and the experimental trend of both ICE brake mean effective pressure (BMEP) and rotational speed. Moreover, according to the instantaneous and cumulated CO_2 profiles, even if some peaks are not perfectly captured, the transient behavior is balanced over the whole driving cycle so that the total estimated CO_2 emissions are in good agreement with the experimental values. The same applies also to raw NO_x emissions estimation Fig. 7.11b.

Concerning the EATS model, experimental data, and thus direct validation, are only available for some specific tested layouts different from the one adopted in this activity. However, a modular modeling approach was adopted, so that the same modeled blocks representing each component can be eventually combined to build several different EATS layouts depending on the specific application. This allows deriving the validation of each component as part of a specific EATS layout that has actually been tested and directly validated. For this purpose, the comparison between simulated and experimental data related to two different EATS layouts are provided in Fig. 7.12. Given the targets of this activity, the attention has been mainly focused on NO_x emission estimation and related quantities. The same considerations already made about engine-out emissions are also valid for tailpipe NO_x emissions, showing a good matching between simulated and experimental data in terms of cumulated emission, despite some inaccuracies concerning instantaneous quantities.

Focusing on the electrical heater, since experimental data were not available, a different type of validation has been proposed: output data coming from an electrical-heater validated model already available from GT-Power® libraries have been used as a reference and compared with the ones provided by the considered Simulink® model. The same input data in terms of air mass flow,

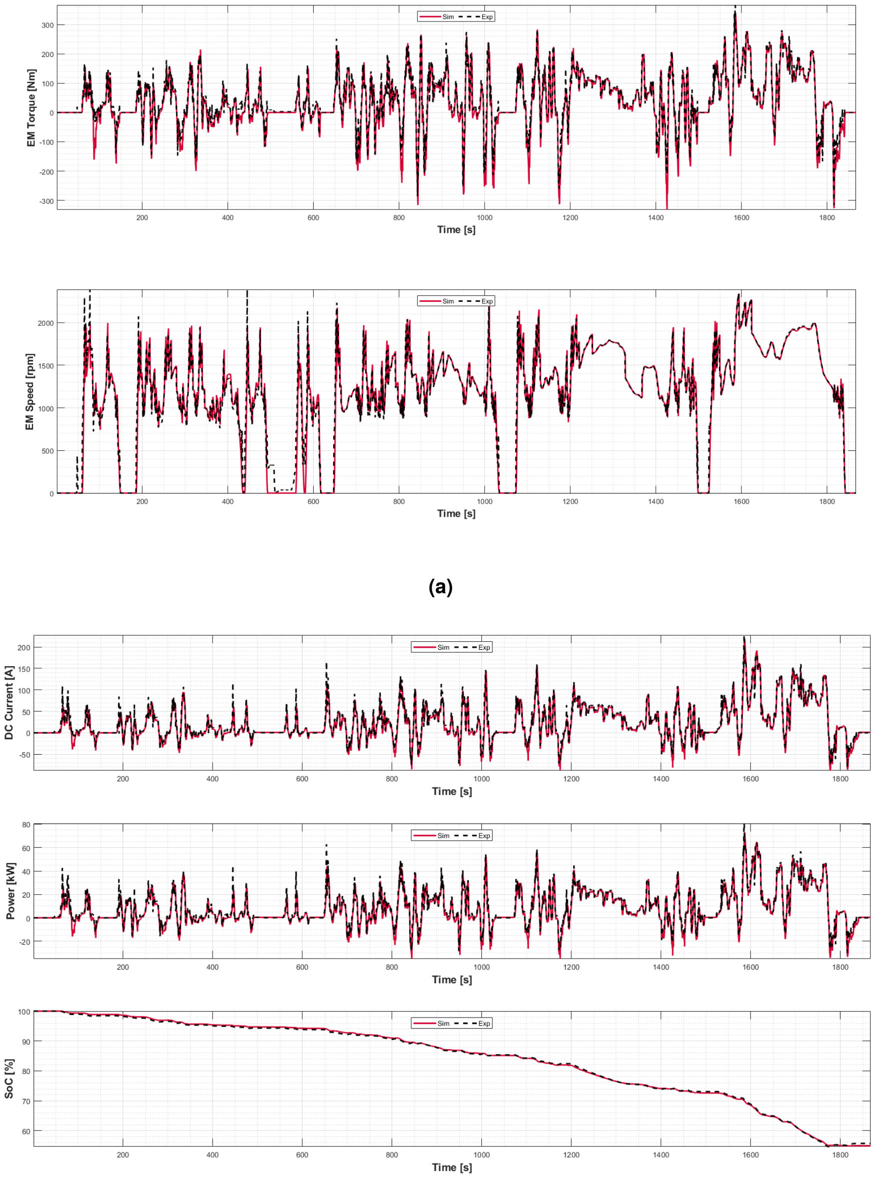

(a)

(b)

Figure 7.10: EM and HV battery model validation: experimental (black dashed) and simulated (red solid) results over a WLTC CD cycle

electrical power, and inlet temperature are supplied to both simulation platforms and exhaust gas temperature values at e-heater outlet are then compared in Fig. 7.13. Although some inaccuracies can be noticed especially during fast transients, the two sets of data follow the same general trend, which is considered acceptable within this implementation.

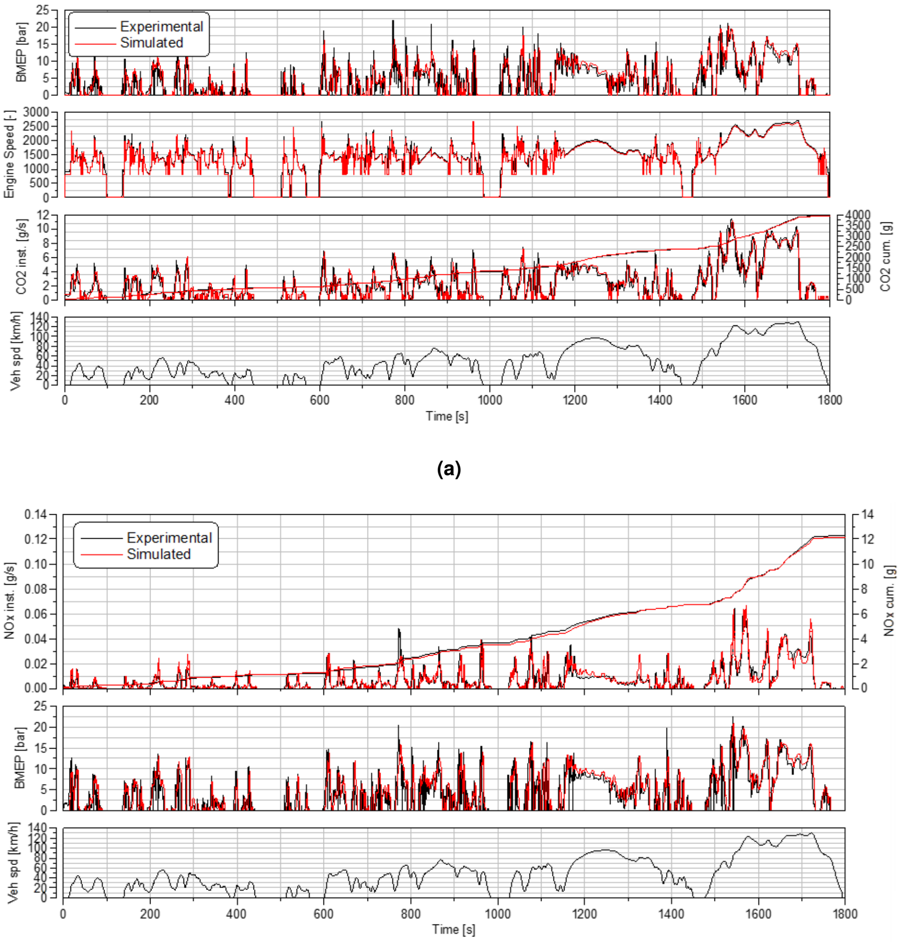

(a)

(b)

Figure 7.11: ICE model validation: experimental (black) and simulated (red) results over a WLTC

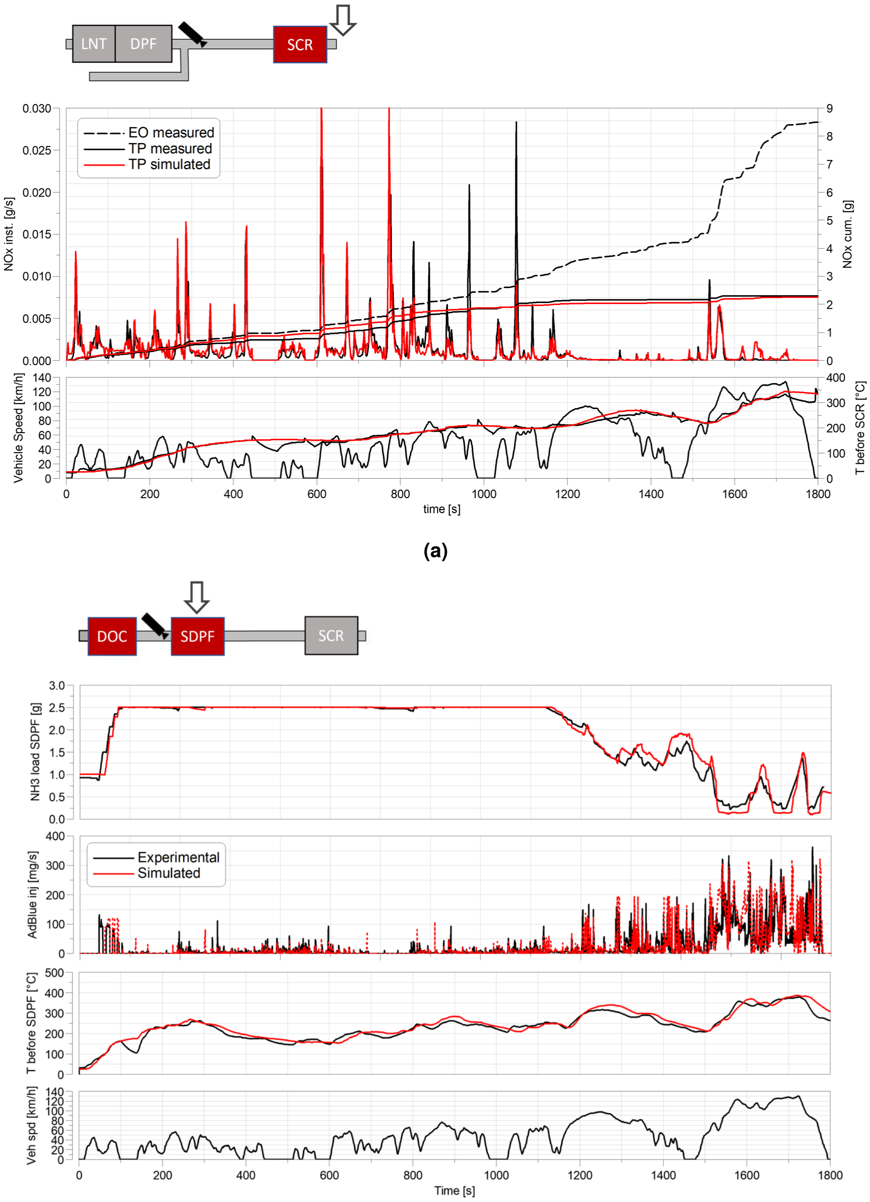

(a)

(b)

Figure 7.12: EATS components model validation: experimental (black) and simulated (red) results over a WLTC. A schematic representation of the specific tested layout and measurement location is also provided

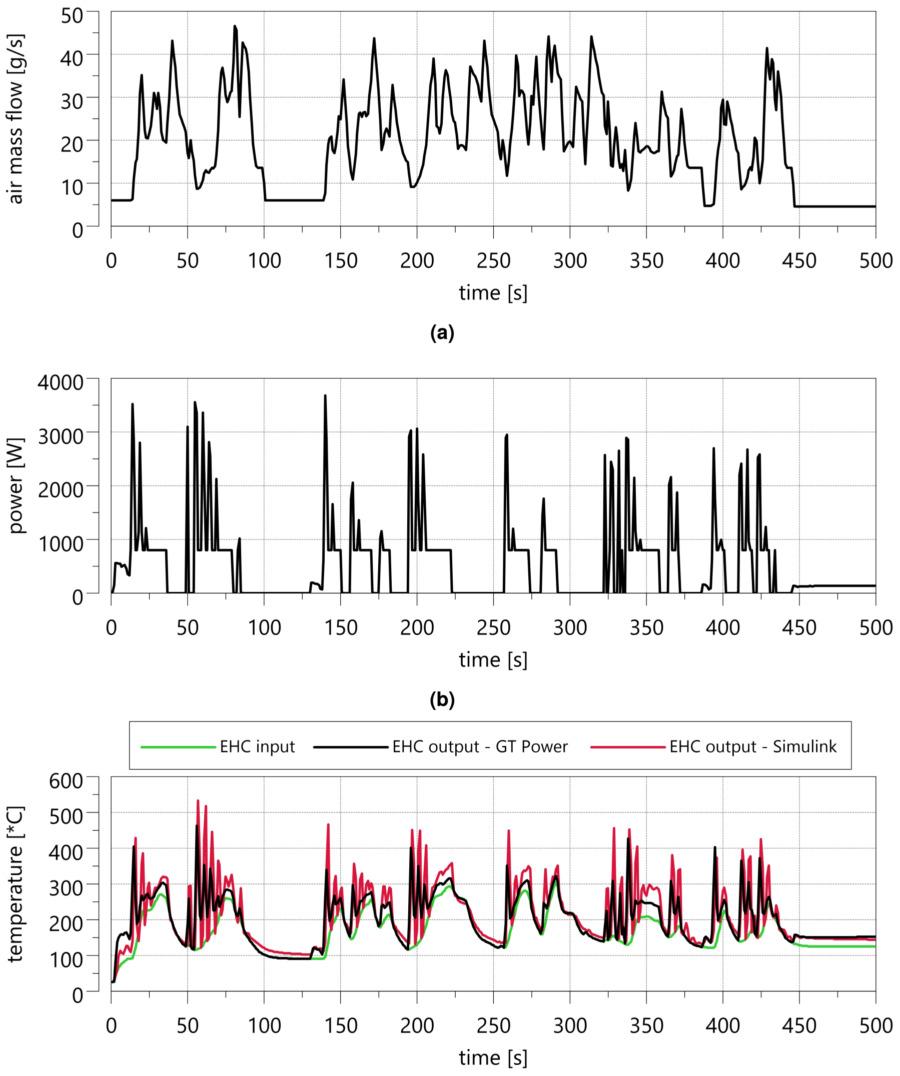

(a)

(b)

(c)

Figure 7.13: E-heater model validation: exhaust gas temperature at e-heater outlet from GT-power® (black dashed) and Simulink® (red solid) given the same input data

Chapter 8

Predictive control strategies

The development and calibration of a robust and effective control strategy is a preliminary step for the development of additional control functions involving EATS thermal management, taking advantage of the flexible hybrid architecture to reach the targets in terms of CO_2 and NO_x emissions, introduced in Section 1.2. So in this chapter, as a first step, the rule-based control strategies for the management of both hybrid powertrain and exhaust after-treatment systems are explained. In particular, the control strategy managing the driving mode and the torque split between EM and ICE is firstly investigated, followed by the description of the adopted rule-based strategy for the EHC thermal management. Then, an improved RBS has been developed and calibrated to fulfill the upcoming Euro 7 regulation by introducing model-based maps of Brake Specific Fuel Consumption (BSFC), Brake Specific NO_x ($BSNO_x$), and exhaust gas temperature.

Finally, the predictive control functions introduced in Section 4.1 have been adapted for the specific application, with a focus on the Backward Vehicle Model, in order to estimate the first engine start and consequently activate the EHC to perform a pre-heating, preventing low-efficiency operation of the EATS.

8.1 Conventional rule-based strategy

The HCU is responsible for the selection of the driving mode between full electric drive (e-drive) and hybrid drive. Thus it manages the torque split between the EM and the ICE, taking into account several parameters that will be introduced in the next paragraphs.

The selection of the driving mode relies on a set of logical conditions enabling the switch from e-drive to hybrid drive and vice-versa:

- **Vehicle speed**: E-drive is possible until actual vehicle speed is below a constant threshold which has been set to 140 km/h in compliance with EM technical specifications, allowing to perform a complete WLTC in pure electric mode. A minimum hysteresis interval of 10 km/h has been introduced to avoid instability;

- **HV battery SoC**: A constant threshold and related hysteresis have been set through a Design of Experiments (DoE) approach in order to achieve the highest reduction of CO_2 emissions. The lower limit, below which ICE is switched on, and the upper limit, above which ICE is turned off, have been varied in the interval 18-26% considering all the possible combinations, that were tested over a complete standard WLTP to evaluate equivalent CO_2 emissions. According to the results of the described analysis, graphically represented in Fig. 8.1, the selected more convenient lower and upper thresholds are 18 and 20% respectively;

- **ICE operating time**: Minimum hybrid and e-drive mode time intervals have been set to 10 and 2 seconds respectively, in order to prevent too frequent ICE and EM starts and stops that would affect vehicle drivability;

- **EM torque request** A variable torque threshold, above which e-drive is no more possible, is calculated based on available EM continuous torque, which is a function of actual motor speed. This allows to use the electric motor as much as possible keeping a minimum torque reserve for engine start phases, corresponding to the additionally available torque during motor peak operation;

- **DOC temperature**: The switch from hybrid drive to e-drive is not possible until the DOC has reached its light-off temperature, corresponding to 180°C, above which conversion efficiency reaches its maximum value. This condition has been set to promote EATS heating up after the engine cold start.

Figure 8.1: DoE analysis for SoC thresholds definition: resulting weighted CO_2 emission

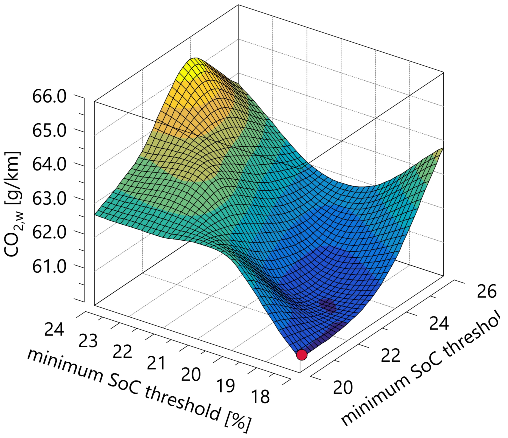

8.1.1 Torque split strategy

Focusing on the hybrid mode, the conventional hybrid strategy originally developed for this powertrain manages the torque requested by the driver favoring the usage of the internal combustion engine. In fact, as described by Eq. (8.1), the engine is responsible for the traction and the battery charging as long as the request respects the engine's limitations. Thus, the electric machine is commonly used as a generator, if these limits are satisfied, or as a motor, if some boosting is necessary.

$$\begin{cases} T_{trm,in} = \dfrac{T_w}{\tau} \\ T_{ICE} = max\left(T_{LPS} + T_{trm,in}, T_{ICE,max}\right) \\ T_{EM} = T_{trm,in} - T_{ICE} \end{cases} \tag{8.1}$$

where:

- T_{ICE} is the torque requested to the internal combustion engine;
- T_{LPS} is the amount of torque required for the load-point shift;
- $T_{trm,in}$ is the total requested torque upstream of the transmission, calculated as the ratio between the torque requested at the wheels and the actual total gear ratio τ, considering the transmission and the differential;
- T_{EM} is the torque requested to the electric machine. In particular, if the engine is able to fulfill the driver request, the EM works as a generator and $T_{EM} = -T_{LPS}$.

Moreover, the value of torque reserved for LPS, T_{LPS}, depends on the actual coolant temperature. In fact, if the catalyst heating mode is active, the LPS is limited to 16 Nm, otherwise, it is increased to 33 Nm. For a matter of completeness, both these values come from the sensibility of experienced technicians and the several activities performed by the industrial partner during the last years on the topic. However, in Section 8.1.3 the strategy proves to be compliant with the actual regulation, so it can be used as a reference.

8.1.2 Standard EHC strategy

The EHC control strategy is based on the following conditions, according to which the electrical-heater (hereafter shorten as e-heater) is activated if:

- the engine is running, meaning that the exhaust gas flow through the heating disc is not zero;
- the HV battery SoC is higher than the minimum safety threshold, which has been set to 18%;
- the exhaust gas temperature at the DOC outlet is lower than a fixed threshold equal to 200°C, which is slightly above DOC light-off temperature.

Once the e-heater is activated, the requested power is calculated based on previously calibrated maps that take into account:

- actual engine load, which is directly connected to exhaust gas temperature;
- actual engine speed, which together with engine load allows to define the actual exhaust gas flow rate;
- actual exhaust gas temperature at e-heater outlet.

More in detail, electrical power is actually provided to the e-heater if engine BMEP is lower than 12 bar and if the engine speed is lower than 2500 rpm, namely if engine-out exhaust gas temperature is below a certain threshold. Electrical power request is then calculated according to gas flow temperature at the e-heater outlet, following the trend shown in Fig. 8.2.

Figure 8.2: EHC power request as a function of exhaust gas temperature at the e-heater outlet

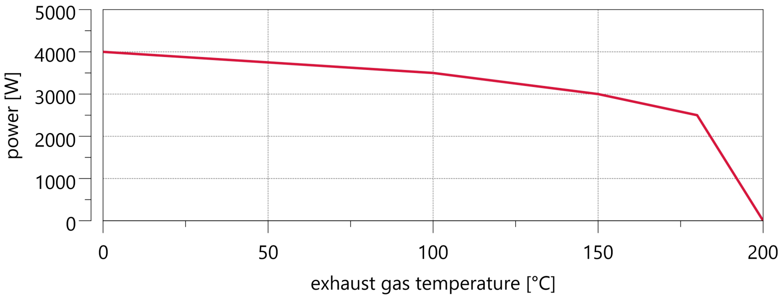

8.1.3 Performance assessment

The performance of the conventional RBS has been consequently tested following the WLTP [10], in terms of CO_2 and NO_x. The details of the procedure have been already introduced in Section 1.2.1 so will be omitted here, while only the final results are reported and summarized in Tab. 8.1.

8.2 Improved model-based strategy

Conventional rule-based strategies used to be calibrated for specific driving cycles leading to significant differences during real driving [157]. To overcome the problem, in this dissertation, a model-based torque split strategy has been developed and calibrated. In particular, the load point shift (LPS) maps have been generated with three different targets depending on ICE operating conditions:

- Moving engine operating points to higher efficiency areas;

Table 8.1: Conventional RBS performance tested with R1151 [10]

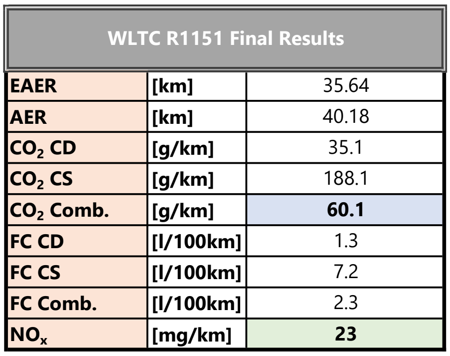

WLTC R1151 Final Results		
EAER	**[km]**	35.64
AER	**[km]**	40.18
CO_2 CD	**[g/km]**	35.1
CO_2 CS	**[g/km]**	188.1
CO_2 Comb.	**[g/km]**	**60.1**
FC CD	**[l/100km]**	1.3
FC CS	**[l/100km]**	7.2
FC Comb.	**[l/100km]**	2.3
NO_x	**[mg/km]**	**23**

- Ensuring a minimum exhaust gas temperature in order to speed up the warm-up phases and keep a high EATS conversion efficiency during standard operation;
- Limiting NO_x emission during EATS warm-up when conversion efficiency is low.

8.2.1 Torque split strategy

Since different calibrations of the LPS strategy can be adopted depending on the set targets in terms of engine efficiency and pollutant emissions, a preliminary step has been to define the targets in terms of BSFC, $BSNO_x$, and engine-out exhaust gas temperature optimal lines. Considering the opposite trends of BSFC and $BSNO_x$ with engine load variation, the respective targets must be set following a reasonable trade-off between the two trends, without focusing on a global minimization of one of the two that at the same time would strongly penalize the other. On the other hand, engine-out exhaust gas temperature target must be set to a value that allows to heat up and keep the EATS within a temperature range that ensures high conversion efficiency, without significantly affecting the BSFC.

Therefore, a DoE approach was used to calibrate the hybrid strategy by testing several configurations providing different results in terms of NO_x and CO_2 emissions. The WLTP standard test procedure [10] has been simulated to set $BSNO_x$ and exhaust temperature targets, evaluating average NO_x emission on the charge-sustaining reference cycle. This last procedure could not be used to set the BSFC target as well, since the corresponding LPS map is actually used only for the higher values of battery SoC, thus being irrelevant on a charge-sustaining cycle, as will be clarified in the next paragraphs. For this reason, an RDE cycle performed in charge-depleting mode has been considered to set the BSFC target separately from the other parameters, according to the best result achieved in terms of cumulative NO_x emission along the whole cycle. DoE parameters and resulting best configuration are listed in Tab. 8.2. In addition, Fig. 8.3 gives a graphical representation of the results obtained in terms of average NO_x and weighted CO_2 emission according to the WLTP. As expected, the lowest average NO_x emission is obtained with a low $BSNO_x$ target and a high exhaust temperature target, but still ensuring limited CO_2 emission at the same time.

Table 8.2: Definition of DoE parameters range of variation.

Parameter	**Query points**	**Definition**	**Best**
BSFC target (k_{FC})	[1 1.03 1.05 1.08 1.1]	Relative increase with respect to minimum BSFC [-]	1.05
$BSNO_x$ target (k_{NOx})	[0 0.2 0.5 1 1.2 1.5 1.8 2]	Specific engine out NO_x emission [g/kWh]	0.2
T_{exh} target (k_{T3})	[230 250 270 300 320 350 370 400]	Engine-out exhaust gas temperature [°C]	370

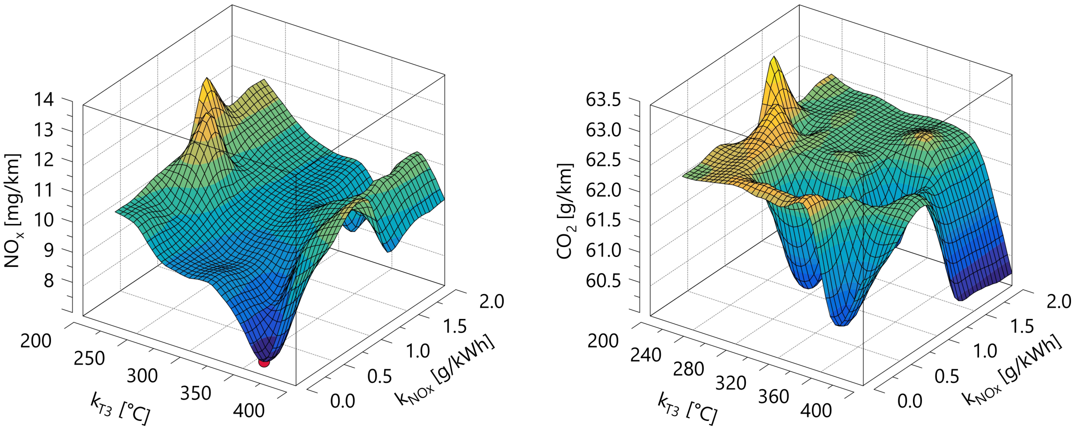

Figure 8.3: Results of DoE analysis for the definition of $BSNO_x$ and engine-out gas temperature targets: average NO_x emission (left), weighted CO_2 emission (right), and final selected configuration (red dot)

The resulting reference lines, obtained by following the mentioned targets for each engine operating condition, are shown in Fig. 8.4 and are the base for the definition of three different load point shift maps implemented in the model (Fig. 8.5):

- **Normal mode shift-down** In this situation the electric motor provides part of the driving torque request, so that the engine works at lower load. The amount of torque requested to the electric motor is calculated in order to reach the BSFC target for each given engine speed. The aim is to reduce fuel consumption by using the electric motor;
- **Cat-heating mode shift-down** Similar to the previous one, but in this case, the amount of

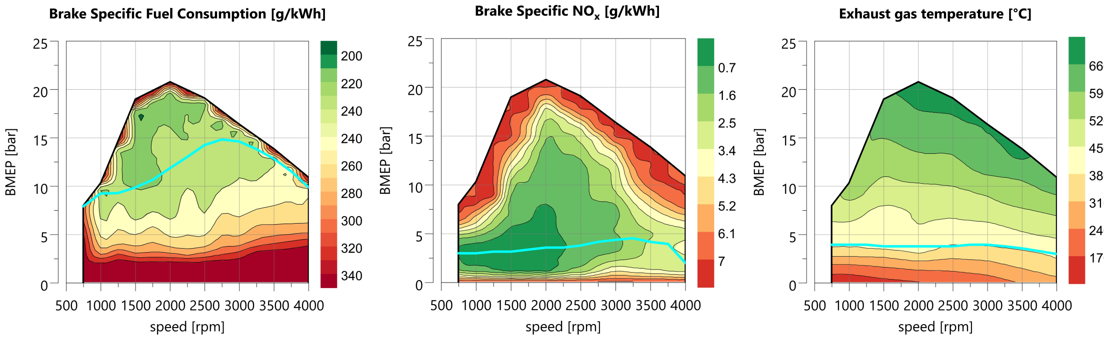

(a) **(b)** **(c)**

Figure 8.4: BSFC, BSNO$_x$, and exhaust gas temperature maps with corresponding defined targets

torque requested to the electric motor is calculated in order to reach the BSNO$_x$ target for each engine speed. The aim is to reduce NO$_x$ engine-out emissions while the EATS is cold and conversion efficiency is low;

- **Normal/Cat-heating mode shift-up** Additional torque is requested to the engine with respect to driving torque request and it is used to charge the battery. The additional torque value is calculated in order to follow the exhaust gas temperature target. The aim is to have a fast EATS heating and to keep it warm after the heating phase. In this case, the load shift map is the same for both normal and cat-heating modes.

The torque value evaluated with the LPS maps is then corrected through a multiplying factor depending on the actual battery SoC. The correction coefficients are defined together with each LPS map in order to decrease EM torque request if battery SoC is low or, on the other hand, to reduce the additional torque request to the engine if the battery is already charged (Fig. 8.5). As it can be noticed, the correction factors for cat-heating mode are defined in order to make the engine operate at higher loads with respect to normal mode, leading to a faster warm-up phase.

8.2.2 Improved EHC strategy

The standard on-board strategy for the EHC is robust, simple, and effective as demonstrated by the results obtained by the procedure and summarized in Tab. 8.1. However, it leads to undesired oscillating behavior of DOC temperature that in demanding conditions can damage the components, if not properly controlled. With this regard, a PI controller has been calibrated with a target DOC temperature of 220°C, which results in a reduction of DOC and LTM-SCR temperature oscillations while not significantly affecting the EHC energy consumption, as shown in Fig. 8.6.

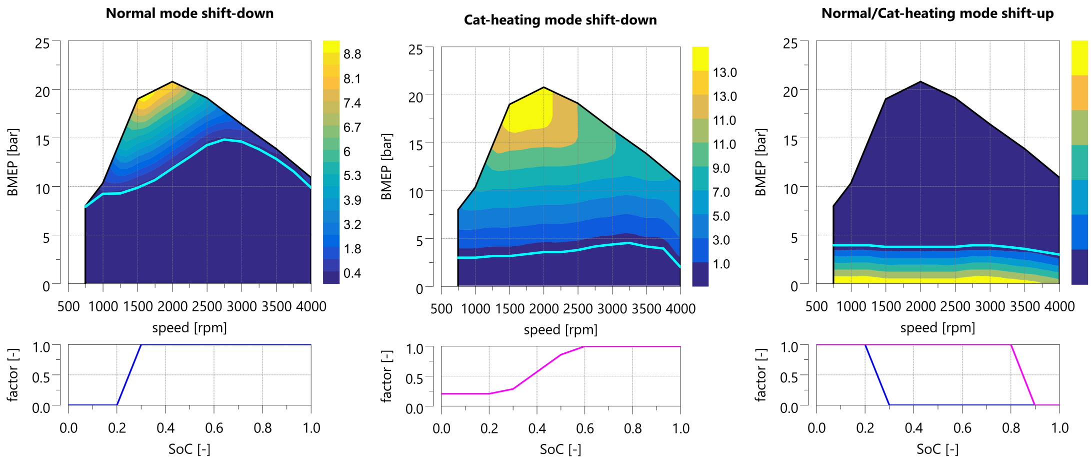

(a) (b) (c)

Figure 8.5: Load point shift maps for normal and cat-heating modes with the related SoC-based correction factors

Figure 8.6: EATS temperature and energy consumption comparison between standard and improved EHC strategy

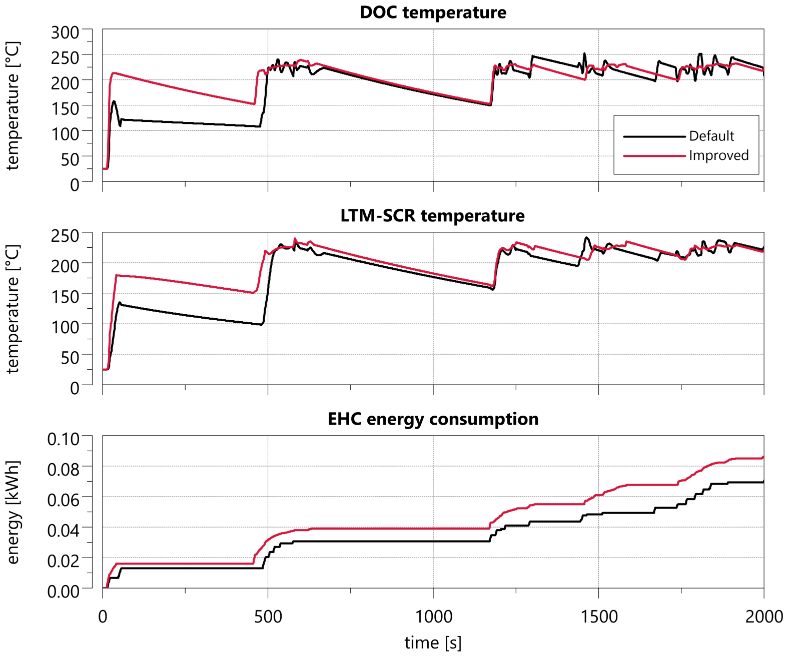

8.2.3 Performance assessment and comparison

The improved RB and EHC strategies have been tested on the WLTP as described in Section 8.1.3, obtaining the results shown in Tab. 8.3.

Table 8.3: Improved RBS performance tested with R1151 [10]

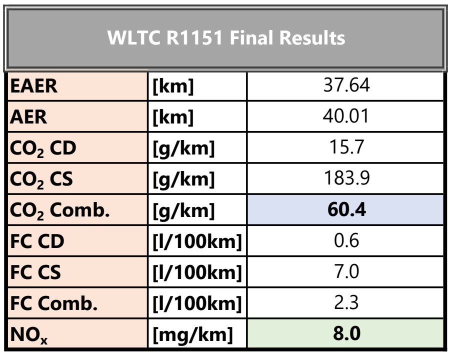

WLTC R1151 Final Results		
EAER	**[km]**	37.64
AER	**[km]**	40.01
CO_2 CD	**[g/km]**	15.7
CO_2 CS	**[g/km]**	183.9
CO_2 Comb.	**[g/km]**	**60.4**
FC CD	**[l/100km]**	0.6
FC CS	**[l/100km]**	7.0
FC Comb.	**[l/100km]**	2.3
NO_x	**[mg/km]**	**8.0**

The procedure's results show how the improved strategy reduces the NO_x emissions of 65% on the WLTC with only an increase in fuel consumption of 0.4%.

8.3 Predictive strategy

As already introduced in Chapter 1, the availability of real-time navigation data, sent to the vehicle by a map-service provider, allows the reconstruction of the future driving scenario, thus enabling the development of predictive control strategies aimed at the best results in terms of energy management and pollutant emission reduction. In particular, the knowledge of future driving conditions can be used to predict the ICE first start along the traveled route, which is a key enabler for the predictive thermal management of the EATS, allowing to perform a pre-heating phase that can be actually planned to avoid NO_x related to cold start emissions, which give a significant contribution to the total emission along the considered driving cycle.

8.3.1 Pre-heating strategy definition

A preliminary step for the development of an effective EHC control strategy is to determine the heating power needed to heat up the EATS for achieving the desired conversion efficiency. In this regard, several simulations have been performed to evaluate the effects related to different values of provided electrical power and air flow rate on DOC, LTM-SCR, SDPF, and SCR light-off time. More in detail, constant heating power, and secondary air flow rate have been provided with the engine turned off to evaluate the only effect of EHC on EATS heating dynamics. Then, the time needed to reach the light-off temperature, considered as the threshold above which the pollutants conversion efficiency of each after-treatment device reaches its maximum asymptotic value (180°C for the

DOC and 220°C for the SCR catalysts, according to the respective pollutant conversion efficiencies maps), has been evaluated for the mentioned devices. The results, graphically represented in Fig. 8.7, clearly point out that the light-off time of all the devices decreases with increasing power and air flow rate so that the same result can be achieved with different combinations of the considered parameters. It can be also noticed that the light-off temperature cannot be reached at all below a minimum threshold of secondary air flow rate and heating power, especially referring to the SCR catalyst (Fig. 8.7d). Starting from these considerations, different pre-heating strategies providing increasing heating power and secondary air flow rate have been tested to find the most convenient pre-heating strategy in terms of resulting NO_x emissions and energy consumption. As pointed out by the previous results, the light-off of the DOC (Fig. 8.7a) and especially of the LTM-SCR (Fig. 8.7b) cannot be achieved in a reasonable time for values below 2 kW and 20 kg/h of EHC power and secondary air flow rate respectively. Therefore, according to the technical specifications of secondary air pumps and EHCs available on the market for Diesel applications, a range between 2 and 4 kW for the heating power and between 20 and 55 kg/h for the secondary air flow rate has been considered for the following analysis, as summarized in Tab. 8.4.

Table 8.4: Pre-heating strategy definition: tested and final configurations

Parameter	Tested range	Final configuration
EHC power [kW]	2 - 4	4
Secondary air flow [kg/s]	20 - 55	55
Pre-heating time [s]	0 - 200	60

Each different configuration has been tested on a real-diving emissions (RDE) cycle with increasing pre-heating time. The initial state of charge (SoC) has been set to 22% arbitrarily to force ICE start along the considered driving cycle. As expected, the best results in terms of absolute NO_x cumulative emissions are achieved with the highest heating power and air flow rate. Based on this consideration, from this point on the analysis has been focused on the configurations adopting the maximum air flow rate and heating power that can be actually provided. Relative emissions are calculated as the ratio between the absolute cumulative emissions resulting from the considered pre-heating strategy and the one obtained with no pre-heating along the same driving cycle. As it can be noticed in Fig. 8.8a, the trend of NO_x reduction gets less steep as the pre-heating time increases, until reaching an asymptotic value, which is significantly higher for the lower value of EHC power due to the limited temperatures that can be reached in these conditions. On the other hand, the CO_2 trend, shown in Fig. 8.8b, is increasing with the pre-heating time, due to the higher energy consumption that is compensated by increased use of the ICE to keep the SoC above the lower threshold. In addition, a CO_2 emission reduction is observed for a limited range of pre-heating duration with respect to the base strategy with no pre-heating, despite the additional energy consumption requested in the first case. This is because, after the first start the ICE can be switched off again only when the DOC light-off is achieved, as explained in Section 8.1.

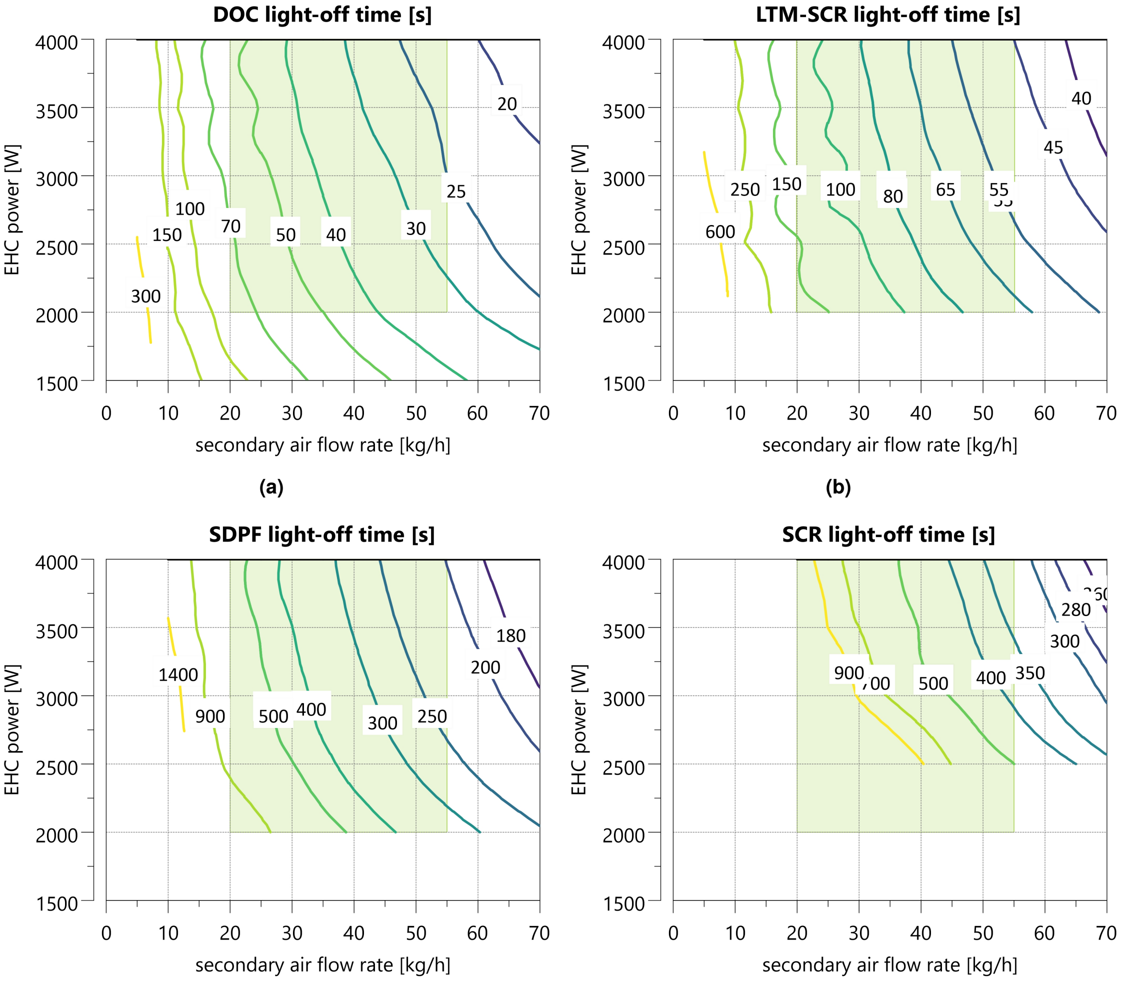

(a) (b) (c) (d)

Figure 8.7: DOC (a), LTM-SCR (b), SDPF (c), and SCR (d) light-off time as a function of secondary air flow rate and EHC power. The green area highlights the feasible range of power and secondary air flow taken into consideration for the pre-heating strategy definition

Thus, the engine is forced to run for a longer time if no pre-heating is planned, due to the lower temperature of the EATS, and this completely deletes the advantage in terms of CO_2 reduction related to the energy saved if no pre-heating takes place. Beyond this additional consideration, according to the purpose of this activity, the pre-heating duration has been set to 60 seconds, to provide a result in terms of NO_x reduction that is close to the asymptotic one but that at the same time leads to a limited CO_2 increase. In fact, for a longer pre-heating duration the gain in terms of NO_x reduction becomes less attractive considering the related cost in terms of CO_2 emission.

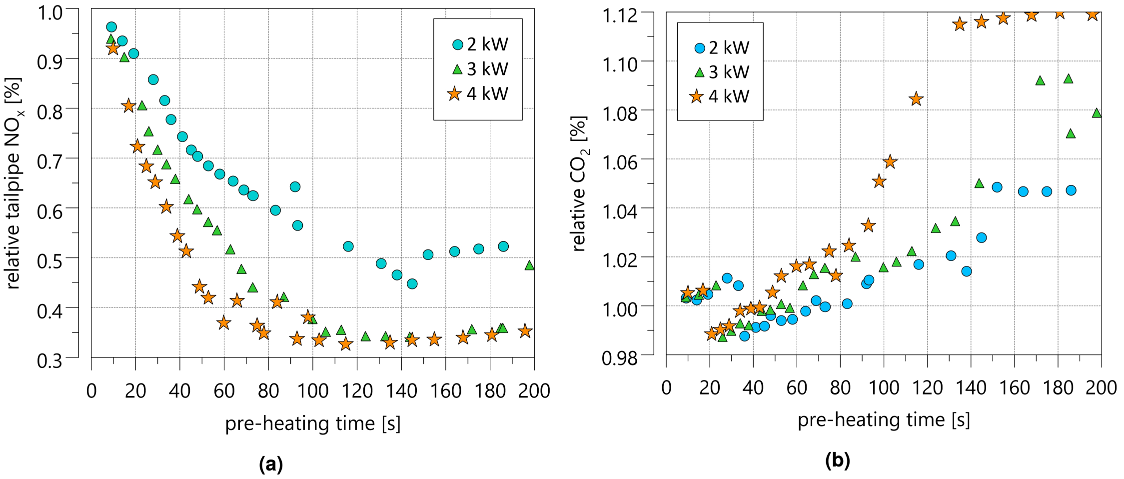

Figure 8.8: Relative tailpipe NO$_x$ (a) and CO$_2$ (b) emission for variable EHC power and pre-heating time for fixed air flow rate of 55 kg/h

8.3.2 Adaptation of the Backward Vehicle Model

Since the chosen application is a PHEV, it is reasonable to assume that in standard conditions the vehicle will start each driving cycle in full electric mode. Then, the vehicle Hybrid Control Unit (HCU) demands hybrid or pure electric drive, managing the torque split according to the calibrated rule-based strategy presented in Section 8.2. Starting from this assumption, the prediction of the engine first start is the key enabler for the development of the described EHC predictive control strategy. In this regard, the Backward Vehicle Model (BVM) introduced in Section 4.1.2 has been adapted to this specific application and implemented in the HCU to estimate the traces of all the relevant quantities, with a particular focus on the EM torque request and the HV battery SoC. Since this activity is focused on quantifying the benefits introduced by an EHC predictive function on NO$_x$ emissions reduction, navigation data, such as vehicle speed and road slope profile, which are the inputs to the BVM, are assumed to be known a priori. Due to the different powertrain layout with respect to the one described in Part I, a simplified transmission model has been added, which calculates the gear profile based on the same rule-based shifting strategy implemented in the HCU subsystem responsible for the gear shifting. Since the aim is to predict the engine first start, pure electric drive is the only driving mode considered within the prediction, so that once known the selected gear, the EM torque request can be easily derived from the total torque request, as already explained in Section 4.1.2. Starting from the power request, a simplified HV battery model allows calculating the SoC trend.

The implementation of the gearshift strategy within the BVM requires further validation of the prediction itself. To do so, a WLTC, whose speed profile is known a priori, has been used as input for the BVM for-loop algorithm. The results of the prediction are shown in Fig. 8.9.

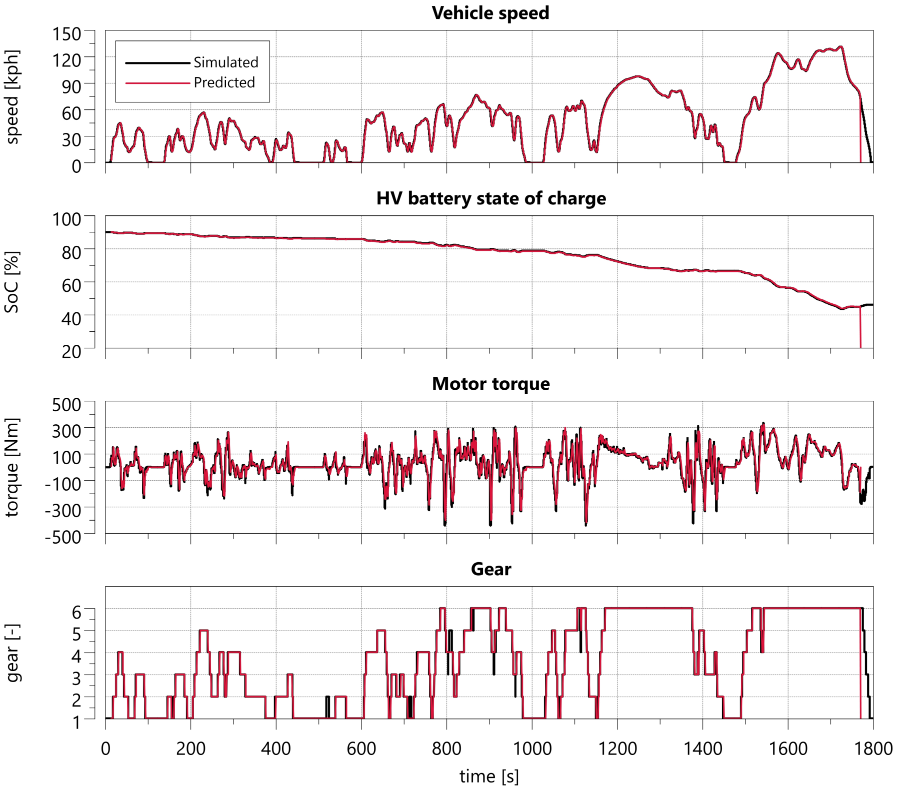

Figure 8.9: BVM validation on WLTC for the P2 architecture, with a focus on the gearshift prediction

In this case, the predicted gearshift profile accurately replicates the simulated one with some isolated exceptions that however do not significantly affect the quantities under test.

Then, the prediction of vehicle speed profile, engine torque request, and SoC trend, computed by the BVM, is the input for a dedicated function that has been developed and implemented in the HCU model to predict the engine first start, which can be derived based on the same conditions for e-drive or hybrid drive selection already implemented in the HCU and described in Section 8.1. More in detail, the output of this function is the time instant in which the engine start is expected to be requested, namely when at least one of the following conditions is true:

- predicted vehicle speed above 140 km/h;
- predicted EM torque request beyond the continuous torque available from motor specification at the considered speed;
- predicted SoC lower than 18 %.

8.3.2.1 Energy prediction and compensation

However, the so-obtained engine start prediction instant does not consider the additional energy consumption coming from the EHC and secondary air pump during the EATS pre-heating phase. This is because the pre-heating phase is planned subsequently and it is based on the ICE start prediction itself. Due to this, a significant error is introduced in the SoC trend prediction, which becomes an issue if ICE start is driven by the condition related to low SoC, leading to an inaccuracy in the engine start prediction that cannot be neglected for the purposes of this activity. For this reason, a correction has been applied to the prediction to take into account this contribution. The additional energy ΔE_{pre} needed to perform the pre-heating phase is calculated based on the requested power P_{pre} and heating time Δt_{pre} that have been previously set:

$$\Delta E_{pre} = P_{pre} \cdot \Delta t_{pre} \tag{8.2}$$

This amount of energy is then subtracted from the energy available in the HV battery to identify the correct time instant in which the SoC will drop below the selected threshold determining the ICE start request. For the sake of clarity, the top plot of Fig. 8.10 shows a comparison between the predicted SoC trajectory (not corrected) and the simulated one (resulting from the application of the predictive strategy) along the first part of an RDE urban cycle starting with very low SoC. As it can be seen, in the first 500 seconds of the cycle the two traces are almost coincident except for a slight offset due to natural inaccuracies of the predictive backward model. Then, a significant deviation between the two trends can be noticed when the pre-heating phase starts, based on the prediction itself. The additional energy request leads to a faster decrease of the actual SoC, thus causing the actual ICE start to happen in advance with respect to the prediction. Therefore, if a correction is not applied, this would lead to a shorter heating phase with respect to the planned one. Therefore, the focus is shifted to the prediction of the energy absorbed by the HV battery, shown at the bottom of Fig. 8.10: starting from the time instant corresponding to the predicted engine start (1), the amount of energy ΔE_{pre} absorbed during the pre-heating (2) is subtracted to the prediction of the total energy provided by the battery until that moment (3); finally the time instant related to the so obtained energy value corresponds to the actual ICE start if the pre-heating energy had been taken into consideration, referred to as corrected ICE start (4).

The effectiveness of the performed correction is tested over different driving cycles starting with different initial SoC values. The results, summarized in Tab. 8.5, prove that in most cases the introduced correction allows to significantly reduce the gap between predicted and actual engine start, which was the main target, even if a residual error is still present due to inevitable inaccuracies of the simplified backward model implemented in the HCU. Finally, the evaluated time instant corresponding to the predicted engine start, which is calculated by the HCU in the first few seconds of driving, is sent to the engine controller, which is responsible for the management of the EHC and the secondary air pump. Based on this information, the pre-heating phase is planned using a timer, according to the required time that has been defined in Section 8.3.1. The pre-heating

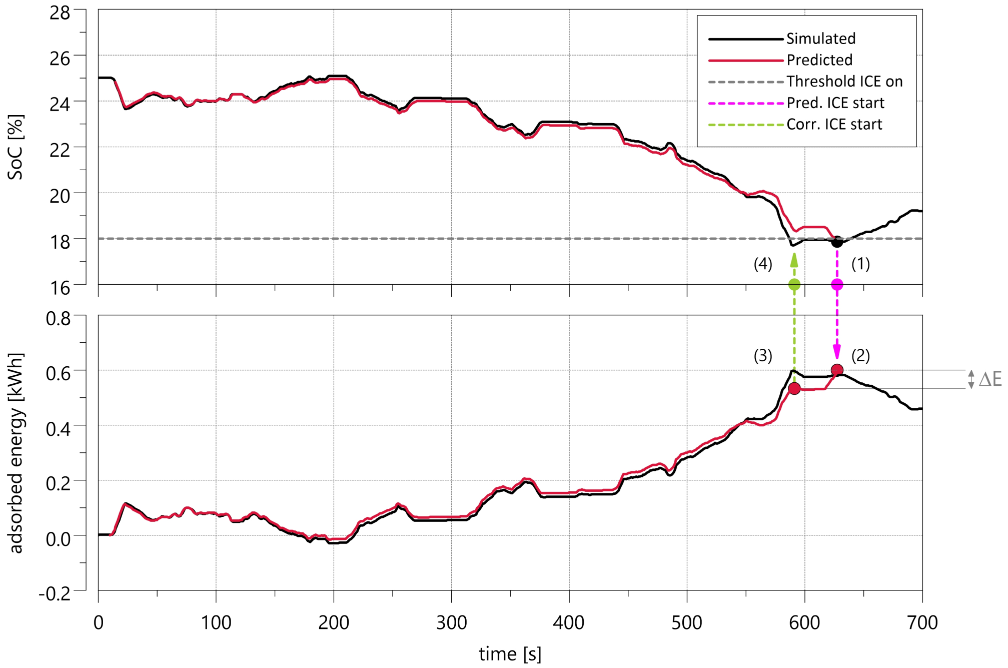

Figure 8.10: Predicted and actual HV battery state of charge (top) and corresponding adsorbed energy (bottom) along an RDE urban cycle with 25% initial SoC

phase automatically stops when the engine is switched on and from that moment the rule-based strategy manages the EHC power request by means of the PI controller, introduced in Section 8.2.2, to ensure a minimum target temperature of the exhaust gases providing the maximum conversion efficiency of the DOC and LTM-SCR.

Table 8.5: ICE start prediction testing over different driving cycles and initial HV battery SoC

Cycle	Initial SoC [%]	Predicted ICE start [s]	Corrected ICE start [s]	Actual ICE start [s]
WLTC	22	502	452	453
	25	617	672	675
	30	1416	1347	1350
RDE 1*	22	279	251	256
	25	636	599	608
	30	855	839	847
RDE 3*	22	1003	916	917
	25	1401	1341	1324
	30	2024	1956	1958

* These driving cycles will be introduced and fully described in Chapter 9.

Looking at an undesirable but still possible situation in which reliable eHorizon data were temporarily unavailable, EATS pre-heating is managed following a rule-based approach. According to this *fallback strategy*, the pre-heating starts when the SoC falls below 20%, assuming that in a short time it will decrease even more reaching the lower threshold of 18%, so that the HCU will request the engine start. However, unlike what happens considering the predictive strategy, in this case, the period between EHC activation and the engine start can significantly vary depending on the specific driving conditions; so, once the target EATS temperature is reached, then the EHC power is managed by the same PI controller that has been previously introduced, in order to keep the EATS temperature around the target until the engine start. Of course, most of the time, this strategy is far from the optimum and shows many drawbacks if compared to the predictive one: in fact, it may happen that the pre-heating gets shorter than the planned one if the SoC drops very quickly below the lower threshold, leading to higher pollutant emissions if the EATS temperature has not yet reached the target value when the engine is turned on. On the other hand, it may happen that the pre-heating gets much longer than the planned one if the power requested to the EM is low and the SoC decreases slowly, leading to significant energy waste due to the extended EHC power supply. Moreover, as a further limitation, the *fallback strategy* does not take into account ICE starts due to high torque request or high vehicle speed, being characterized by much faster dynamics that are hard to be controlled through a simple rule-based strategy that does not rely on predictive information. For the sake of brevity, and since it goes out of the scope of this dissertation, the results related to this fallback strategy are not included in the next sections.

Chapter 9

Application of the predictive strategy

In this chapter, the significant gain achieved is presented in terms of NO_x emissions reduction by considering an EHC predictive control strategy (PS), which differs from the reference RBS by the introduction of a pre-heating phase. The results have been obtained on different urban RDE cycles with different initial conditions and then analyzed in terms of emissions reduction. Moreover, considering a less demanding scenario for Euro 7, a cost analysis has been conducted to analyze the feasibility of removing a component resulting in a less complex and cheaper layout.

9.1 Test case scenarios

Table 9.1: Simulated driving cycles specifications

		RDE 1	RDE	RDE 3
Duration	[s]	2070	1770	2310
Distance	[m]	10510	12219	8467
Perc. stop	[%]	27	17.1	31.7
Max. speed	[km/h]	47.2	48.6	51.2
Avg. speed	[km/h]	25.0	30.0	19.3
Max. acc.	[m/s^2]	3.50	3.16	3.42

* The calculated average speed does not consider vehicle stops.

Different real driving scenarios have been considered to test the proposed EHC control strategy and highlight its benefits in terms of NO_x emissions reduction. In particular, three urban driving cycles, listed in Tab. 9.1, have been selected in order to provide challenging conditions from the point of view of NO_x emission, being characterized by frequent start and stop phases and, on average, by engine low load operation, which results in lower temperatures of the EATS. The vehicle speed profile and road slope of the considered driving cycles are shown in Fig. 9.1. The initial battery SoC for each simulation has been varied between 22% and 30% to force ICE start within the driving cycle. The improvement achieved thanks to the introduction of an EATS pre-heating phase based on ICE start prediction will be evaluated considering EATS components temperature profile over time and the resulting average NO_x emissions along each considered cycle. This type of test is in line with the expected Euro 7 regulations, which will consider nearly any possible driving scenario, as already introduced in Section 1.2. In this context, a comparison with the Euro 7 NO_x estimated emission limits will be provided. In particular, according to [27], two possible scenarios are considered: a less demanding "Scenario A", which would set the NO_x emissions limit to 30 mg/km, and a more demanding "Scenario B", which would lower this limit to 10 mg/km. The same ambient temperature, set to 25°C, has been considered for all the test cases, since the effect of variable environmental conditions on the resulting CO_2 and NO_x emissions has not been investigated in this work.

9.2 Results and discussion

The results in terms of tailpipe NO_x and CO_2 emissions along the three considered urban driving cycles are summarized in Fig. 9.2.

In particular, the comparison between the rule-based EHC control strategy ("EHC RBS" presented in Section 8.2.2) and the proposed predictive control strategy ("EHC PS") highlights that a significant additional reduction of average NO_x emission along the considered driving cycles is achieved thanks to the introduction of an EATS pre-heating phase. The results related to the same application with no EHC usage ("w/o EHC") are included for completeness. Focusing on Fig. 9.2c, it can be noticed that the data referred to the cases "w/o EHC" and "EHC RBS" with 28% initial SoC show an unexpected behavior, with significantly higher NO_x emissions if compared to the general trend. This is due to a very high peak in the engine-out emissions which is well managed by the PS strategy thanks to the pre-heating phase and the earlier ICE start with respect to the other two cases, in which the ICE start occurs much closer to the mentioned peak of engine-out NO_x emissions and no pre-heating takes place, thus resulting in very low EATS temperatures and conversion efficiencies.

As expected, the overall CO_2 trend is significantly increasing with decreasing initial SoC, due to a shorter e-drive range, and slightly increasing switching from the "EHC RBS" to the predictive one, which includes an EATS pre-heating phase and thus significant additional energy consumption, which is compensated by greater use of the engine to recharge the battery. On the other hand, comparing the cases without EHC and the "EHC RBS", as for the previous comparison, it would be expected higher CO_2 emissions for the "EHC RBS" due to the EHC electric consumption. However, the CO_2 trend is not the same for all the cases, which can be explained by considering the different factors that come into play. In some cases, this behavior can be simply explained by considering that the final SoC could be slightly different from one case to the other, thus leading to a higher final CO_2 emission if a higher final SoC is reached, meaning that more power has

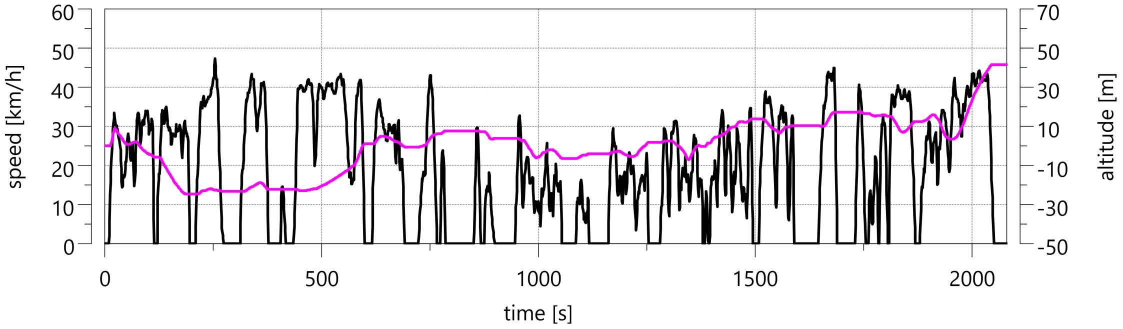

(a) RDE 1

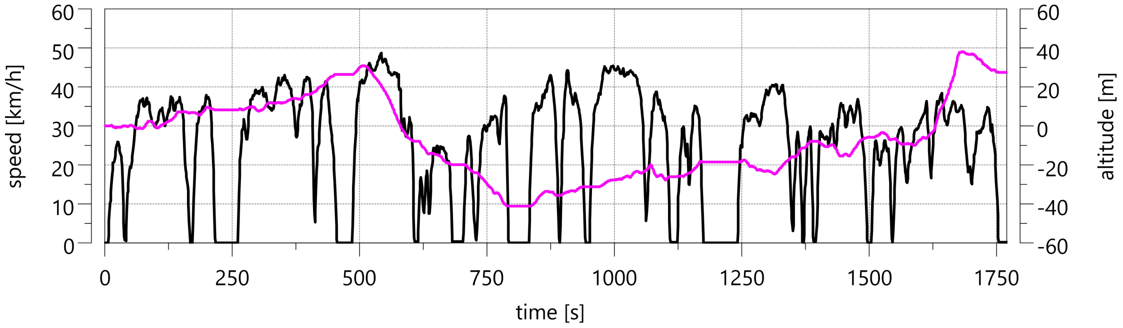

(b) RDE 2

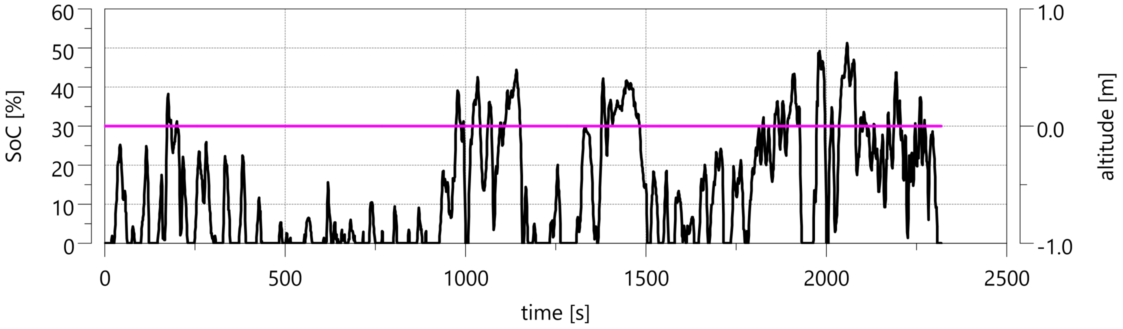

(c) RDE 3

Figure 9.1: Vehicle speed (black) and slope (magenta) profiles of the simulated urban driving cycles

been provided by the ICE, either for traction or to recharge the battery. In parallel, as described in Section 8.2, the hybrid strategy is strongly affected by EATS temperature: the ICE is forced to run until a minimum temperature of the DOC is reached, which takes a longer time if the contribution of the EHC is not considered, thus delaying the switch to the e-drive mode even if the upper SoC threshold has been already reached. Depending on the driving cycle, this could force the engine to run at inefficient operating points in which in normal conditions, namely when the cat-heating phase has been completed, it would have been switched off, leading to higher fuel consumption.

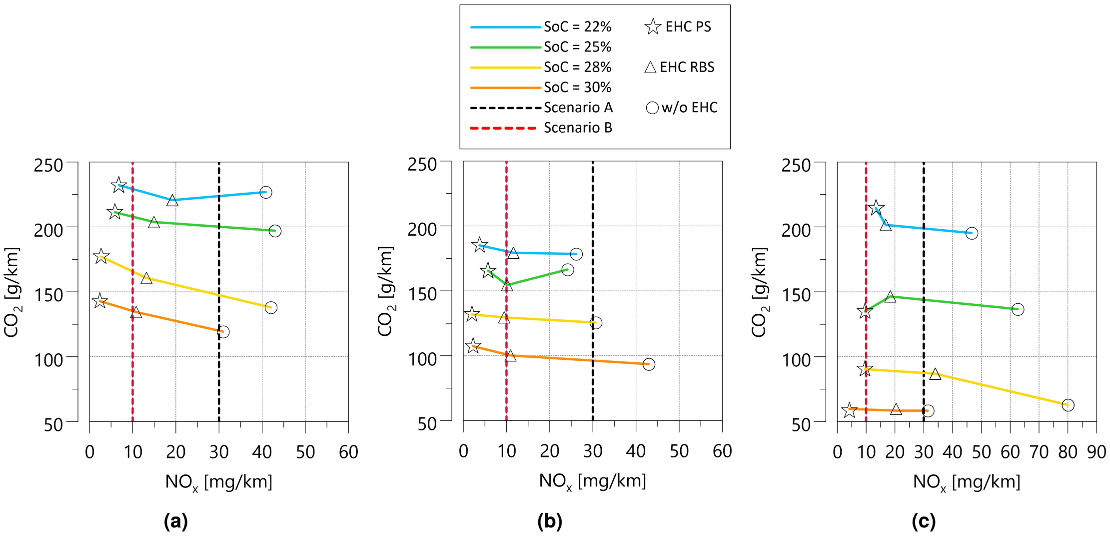

Figure 9.2: Comparison between the proposed predictive EHC strategy, the EHC rule-based strategy, and the same strategy with no EHC usage: resulting average NO_x and corresponding CO_2 emissions for different urban driving cycles with variable initial SoC (SoCinit)

Moreover, the EATS temperature has an impact on the choice of the LPS maps to be used as well as shown in Fig. 8.5: when the EATS temperature is above the lower threshold, the LPS map used for the torque split during EM boosting is set to operate the engine following the target BSFC; during cat-heating, a different LPS map is used, with the aim of limiting engine-out NO_x emission by reducing the engine load, which, on the other hand, results in higher BSFC due to lower engine efficiency. These considerations, combined with the previous ones related to the final SoC values and the presence of some specific maneuvers reflecting the randomness of the cycle, fully explain the different behaviors of the considered cases in terms of CO_2 emissions. For the sake of brevity, and since it goes outside the scope of this dissertation, the values of the final SoC and average BSFC for all the cases have not been included in this work. To highlight the benefits in terms of NO_x emissions reduction given by the introduction of an EATS pre-heating phase based on engine start prediction, the attention is now focused on the comparison between the RBS and PS. Three cases among those simulated are deeper analyzed in the following section as representative of possible different situations that can be encountered, based on all the observed cases:

- **Case 1**: RDE 1 urban cycle with 25% initial SoC;

- **Case 3**: RDE 3 urban cycle with 25% initial SoC;

- **Case 3**: RDE 3 urban cycle with 30% initial SoC.

9.2.1 Case 1

In this case, the first ICE start is determined by the minimum SoC condition, and it is correctly predicted by the HCU (Fig. 9.3 and Fig. 9.4), allowing to perform the planned pre-heating phase. The exhaust gas temperature profiles at LTM-SCR, SDPF, and SCR outlet obtained with the two different strategies are shown in Fig. 9.5, together with EHC requested power and the resulting tailpipe NO_x emissions. It can be noticed that almost 60% of the total NO_x is emitted within 200 seconds after the first ICE start. Therefore, the gain obtained with the introduction of a pre-heating phase is significant, allowing to heat up in advance the SCR catalysts and reduce the average tailpipe NO_x emissions along the driving cycle by more than 50%, from 15.1 mg/km to 5.9 mg/km, although engine-out emissions are almost the same.

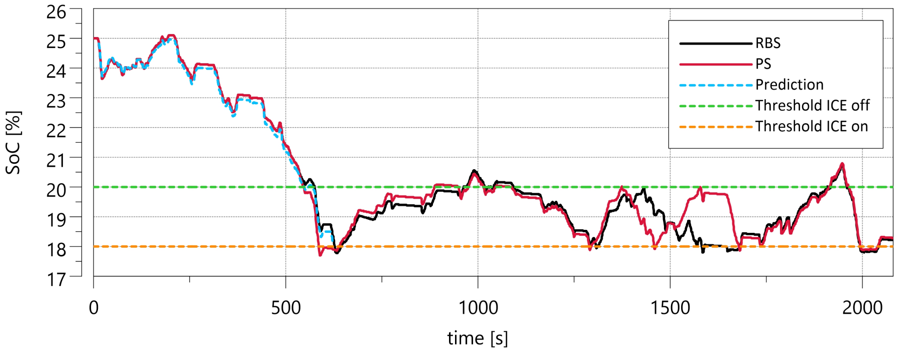

Figure 9.3: Case 1: comparison of SoC traces for rule-based (black) and predictive (red) EHC control strategies; cyan dashed line shows the SoC trace prediction. Lower and upper SoC thresholds below and above which ICE is turned on or off respectively are shown as well

9.2.2 Case 2

As for case 1, the first ICE start is determined by the SoC-related condition and it is correctly predicted by the HCU, as shown in Fig. 9.6 and Fig. 9.7. However, despite the pre-heating phase, a higher NO_x emission is observed for the predictive strategy during the first ICE start, as pointed out by Fig. 9.8: in this case, immediately after the ICE start, there is accidentally a peak in the driver torque request (Fig. 9.7). This results in a peak of engine-out NO_x emissions and therefore higher tailpipe emissions with respect to the case in which the rule-based strategy is applied, despite the higher EATS temperature and conversion efficiency provided by the EHC predictive strategy. Anyway, the pre-heating phase, thanks to the higher temperature reached by the SDPF and the SCR catalyst, in particular, allows to limit NO_x tailpipe emission for the last part of the cycle, thus compensating for the higher emission resulting from the first ICE start. Consequently, the average NO_x emission along the whole driving cycle results still 47% lower for the predictive approach (9.7 mg/km with respect to 18.5 mg/km resulting from the "EHC RBS"), showing

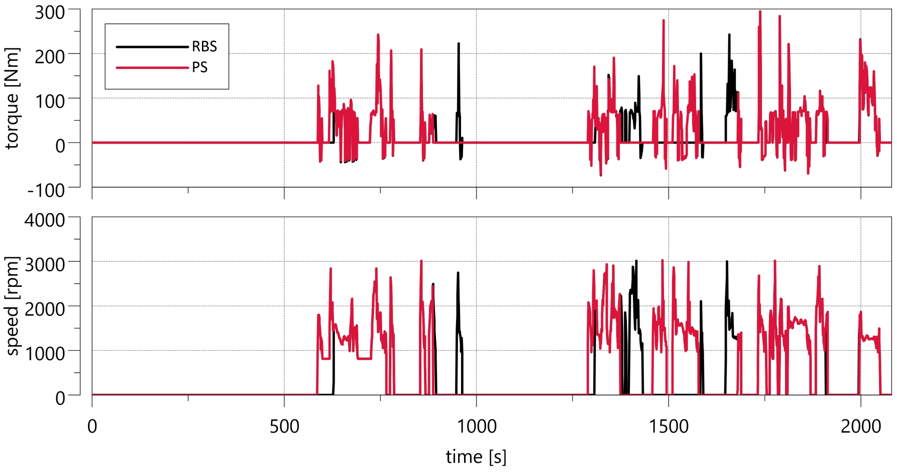

Figure 9.4: Case 1: comparison of ICE speed and torque for rule-based (black) and predictive (red) EHC control strategies

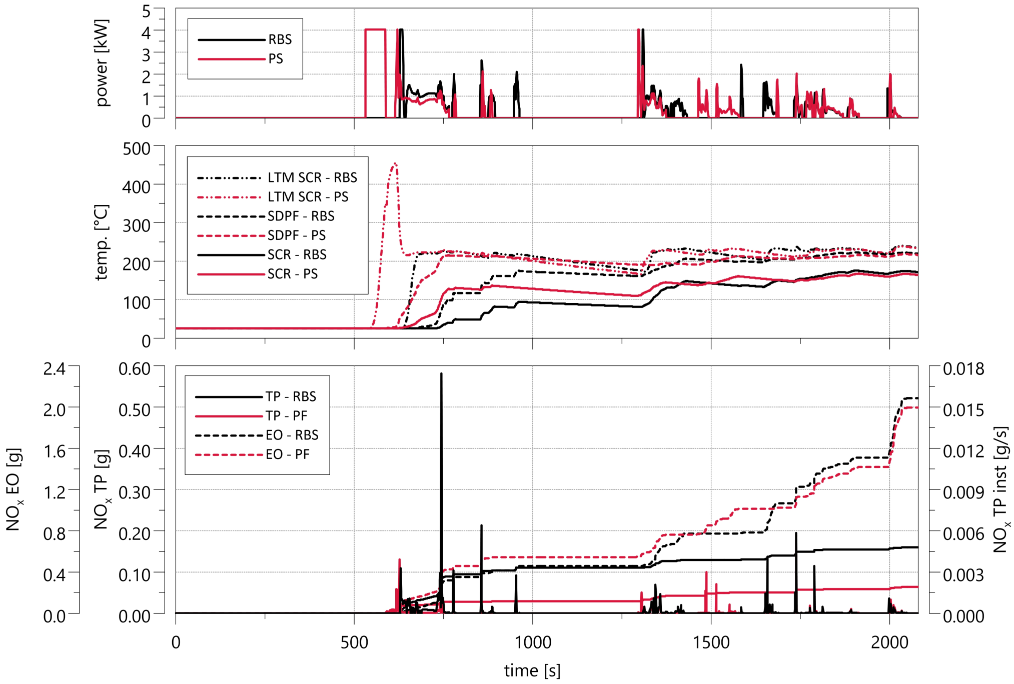

Figure 9.5: Case 1: exhaust temperatures at LTM-SCR, SDPF, and SCR outlet for rule-based (black) and predictive (red) EHC control strategies and corresponding EHC adsorbed power; on the bottom, tailpipe NO_x emission for the two considered EHC control strategies; EO: engine out, TO: tailpipe out

the effectiveness of this strategy in limiting the final tailpipe emissions, despite the much more demanding situations that may be realistically encountered and thus higher engine-out emissions. The same considerations can justify the similar trend of NO_x reduction shown by the test case performed on the same driving cycle but with 22% initial SoC.

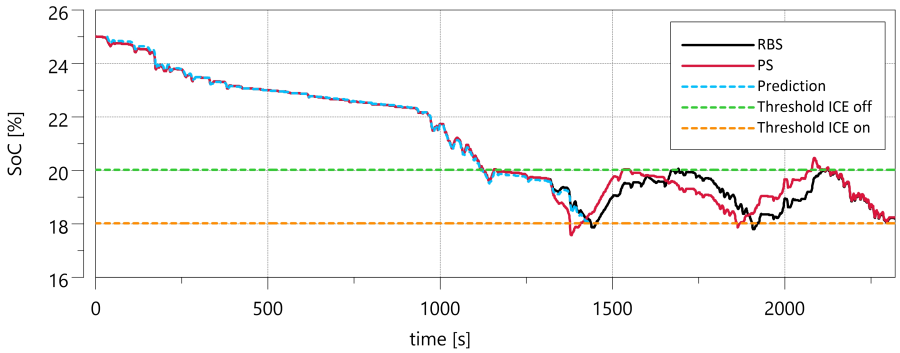

Figure 9.6: Case 2: comparison of SoC traces for rule-based (black) and predictive (red) EHC control strategies; cyan dashed line shows the SoC trace prediction. Lower and upper SoC thresholds below and above which ICE is turned on or off respectively are shown as well

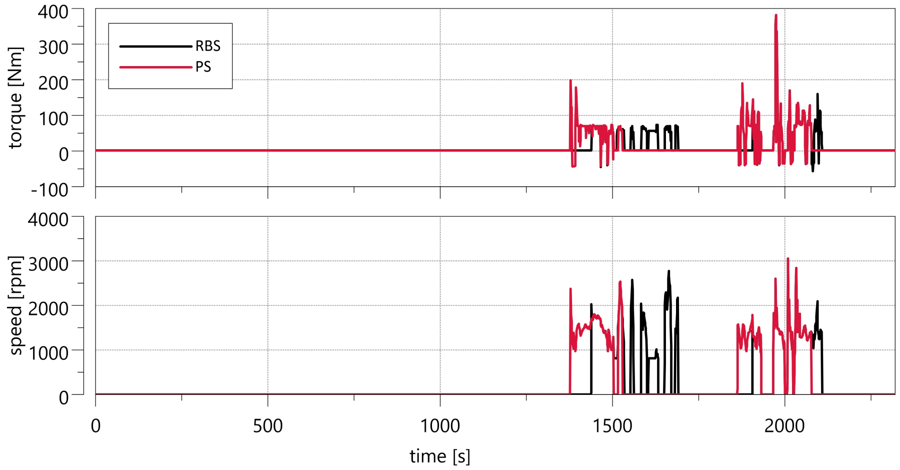

Figure 9.7: Case 2: comparison of ICE speed and torque for rule-based (black) and predictive (red) EHC control strategies

9.2.3 Case 3

In this case, the first ICE start is determined by the condition related to the EM torque limit and it is correctly predicted by the HCU, as proven by Fig. 9.9, which compares the actual and predicted trend of EM torque request together with the corresponding EM torque limits in the

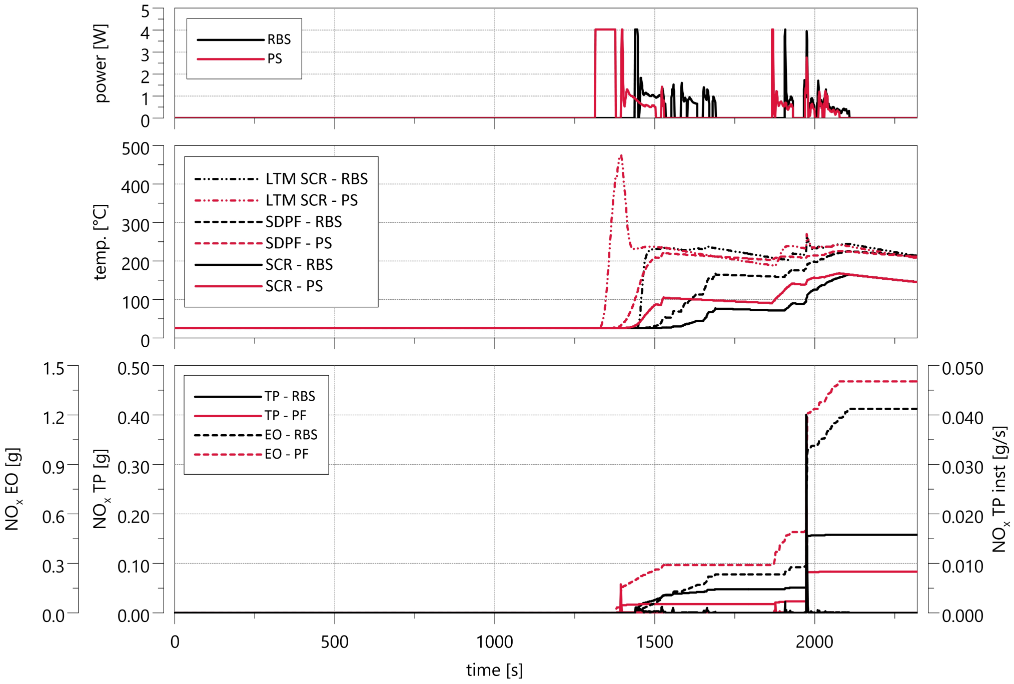

Figure 9.8: Case 2: exhaust temperatures at LTM-SCR, SDPF, and SCR outlet for rule-based (black) and predictive (red) EHC control strategies and corresponding EHC adsorbed power; on the bottom, tailpipe NO$_x$ emission for the two considered EHC control strategies; EO: engine out, TO: tailpipe out

last 500 seconds of the considered driving cycle. As for the other cases, the higher temperature reached by the EATS thanks to the planned pre-heating phase allows to strongly reduce NO$_x$ emissions due to ICE first start (Fig. 9.11), which in this case are responsible for almost 70% of the final tailpipe emissions. Therefore, due to the high impact of ICE first start on the total emissions, a very significant percentage reduction, which is close to 80%, in the average tailpipe NO$_x$ emission is observed, moving from 20.4 mg/km for the "EHC RBS" to 4.3 mg/km for the "EHC PS".

9.3 Vehicle decontenting

Considering the less demanding Euro 7 scenario, referred to as "Scenario A" [27], the significant margin between the very low NO$_x$ emissions obtained by implementing an EHC predictive function and the limit imposed by the regulation (30 mg/km), paves the way to a simplification of the EATS layout to limit the related costs: part of the gain in terms of NO$_x$ emission reduction can be converted into a cost saving that results from a vehicle decontenting process. In this respect, the same rule-based and predictive control strategies have been applied to a simplified EATS layout without LTM-SCR. This layout modification is consistent with the implementation of an improved

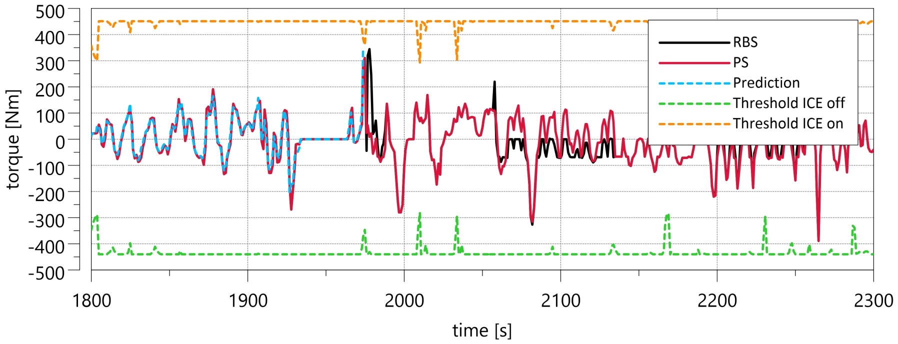

Figure 9.9: Case 3: EM torque for rule-based (black) and predictive (red) EHC control strategies in the last 500 seconds of the considered driving cycle; cyan dashed line shows EM torque prediction

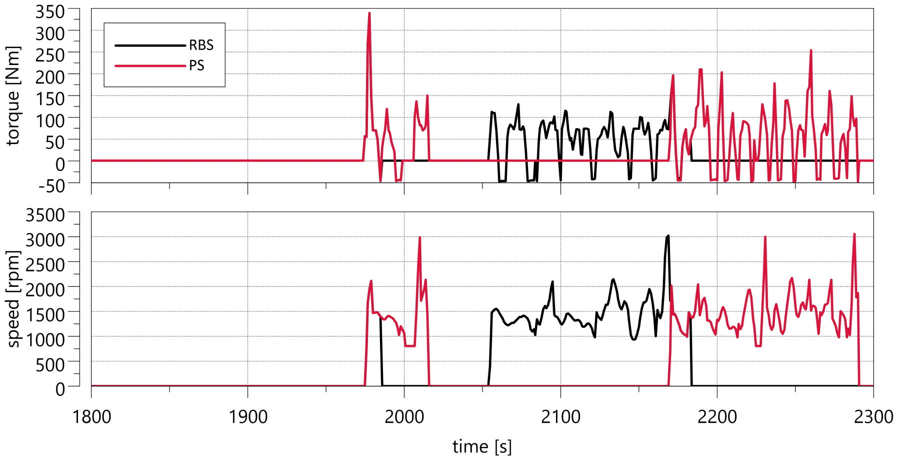

Figure 9.10: Case 3: ICE speed and torque for rule-based (black) and predictive (red) EHC control strategies

EATS thermal management strategy: the introduction of an electrical heater and especially of a pre-heating phase based on engine start prediction, allows to significantly speed up the heating of all EATS devices, thus making the installation of an additional SCR with reduced thermal inertia (LTM-SCR) less incisive from the point of view of limiting cold start tailpipe emissions. Moreover, the LTM-SCR removal results in a faster light-off of the SDPF and SCR catalyst, which will be installed closer to the DOC. The results, represented in Fig. 9.12, show that the average NO_x emissions, obtained performing the same simulations over RDE 1 (Fig. 9.12a) and RDE 3 (Fig. 9.12b) urban cycles, are still below the considered limit for all the test cases if the predictive EHC control strategy is applied. The removal of the LTM-SCR has a positive impact on the total cost of the EATS, which has been quantified by estimating the likely cost of each after-treatment device included in the exhaust line, according to the analysis carried out in [158]. As a final result, the implementation of the proposed predictive EHC control strategy allows to save approximately

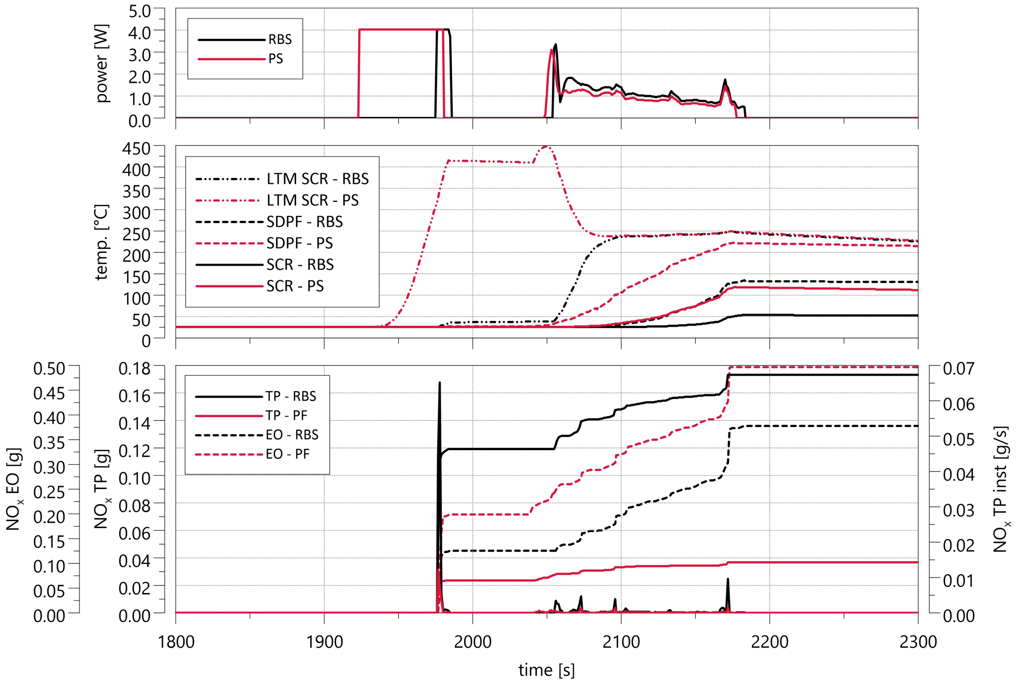

Figure 9.11: Case 3: exhaust temperature at LTM-SCR, SDPF, and SCR outlet for rule-based (black) and predictive (red) EHC control strategies and corresponding EHC adsorbed power in the last 500 seconds of the considered driving cycle; on the bottom, tailpipe NOx emission for the two considered EHC control strategies; EO: engine out, TO: tailpipe out

between the 12% and 13% of the EATS total manufacturing cost.

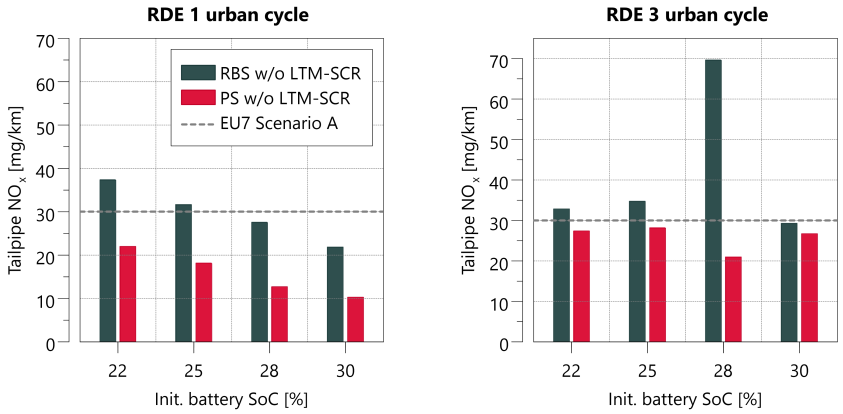

(a) **(b)**

Figure 9.12: Average tailpipe NO$_x$ emission on RDE 1 cycle (a) and RDE 3 cycle (b) resulting from the rule-based strategy applied to the complete EATS layout, including LTM-SCR, and from the predictive strategy applied to a simplified EATS layout with no LTM-SCR

Chapter 10

Part II - Conclusions

The present activity has been focused on the development of a predictive EHC control function for a Diesel PHEV equipped with a state-of-the-art EATS. For this purpose, a comprehensive Simulink® model representative of the vehicle under study has been considered. As a first step, several simulations have been performed to evaluate the effect of EHC heating power and secondary air flow rate on the light-off time of the considered EATS components. Based on this analysis, the most convenient EATS heating strategy has been defined, aimed to minimize tailpipe NO_x emissions with limited additional energy consumption. In particular, constant power of 4 kW has been provided to the EHC with a constant secondary air flow rate of 55 kg/h for the whole duration of the pre-heating phase, which has been set to 60 seconds. A dedicated EHC control function has been implemented in the vehicle HCU to manage the planned EATS pre-heating phase based on ICE first start prediction. The proposed predictive control strategy has been tested on different urban driving scenarios, and the results discussed in Section 9.2, highlight that:

- the introduction of a pre-heating phase allows to speed-up EATS warm-up and improve NO_x conversion efficiency of LTM-SCR, SDPF, and SCR catalysts during engine cold start, always reducing the average NO_x emission over all the considered driving cycles with respect to the base EHC strategy, despite random events that may occur;
- the average NO_x emission achieved with the proposed predictive control strategy is reduced by more than 50% if compared to the base EHC strategy, except for a few cases that have been commented in Section 9.2.2. Depending on the considered driving conditions, the NO_x emission reduction can reach values around 70% for some of the considered cases;
- the EATS pre-heating phase requires additional energy to be provided to EHC, which is compensated by greater use of the engine to recharge the battery, thus resulting in increased CO_2 emissions, which range from 1% to 10% with a single case that exceeds the 30%. This percentage increase is related to the specific driving conditions since the impact of the pre-heating strongly depends on the total amount of emitted CO_2 and also on the engine

operating conditions along the considered cycle, that could be influenced by a different SoC trend and EATS temperature, as highlighted in Section 9.2. Further research should be done to limit this significant cycle dependence;

- considering the foreseen future limits introduced by the Euro 7 proposal [27], the described EATS equipped with an EHC would be able to meet the NO_x emission target for LCVs even without the introduction of a predictive strategy if the less demanding "Scenario A" is considered, which will set the actual limit to 30 mg/km. Nevertheless, the improvement in NO_x emissions control enabled by the implementation of a predictive EHC control function would allow being compliant with the regulation in most of the considered cases even if this limit were lowered to 10 mg/km, according to the most stringent situation referred to as "Scenario B";
- thanks to the implementation of the proposed EHC predictive control strategy, the average tailpipe NO_x emissions can still be kept below the limit imposed by the less demanding Euro 7 scenario even considering a simplified EATS layout without LTM-SCR, thus allowing to reduce the corresponding EATS manufacturing cost.

10.1 Future works

Besides these promising results, which show the potential of including an EATS pre-heating based on ICE start prediction, the tests described in Section 9 highlight that the final result may be strongly affected by the randomness of the occurring driving conditions. This issue must be solved in order to reach the robustness required in view of a real-world application of the proposed control strategy. Based on all these considerations, the developed predictive control strategy can be definitely considered a successful proof of concept to be used as a starting point for further improvements. In this respect, future research will be focused on developing a probabilistic approach that would evaluate ICE start probability within each road segment composing the complete driving cycle, rather than the exact time instant in which it should happen. This would help to solve the problem related to inevitable prediction inaccuracies and resulting random errors that may affect the final result, thus improving the robustness of the developed control strategy in view of HiL (Hardware-in-the-Loop) simulation and real-world application. In addition, further analysis could be performed by extending the temperature range of the considered test cases to evaluate the gain introduced by the predictive control strategy when very low ambient temperatures are considered. Finally, an important step would be to integrate the developed control function with additional predictive control strategies focused on energy management, in order to achieve the best results in terms of efficiency and pollutant emissions at the same time.

Chapter 11

Conclusions

In a global context where pollutant emissions and urban mobility lead to stringent regulations, hybrid electric vehicles became a well-established technology to face the problems of the transportation sector. At the same time, the spreading of novel technologies, such as advanced driving assistance systems (ADAS), and the availability of data from the surrounding environment (vehicle-to-everything) are paving the way to the concept of smart mobility. In fact, it can be intended as a new way of organizing mobility, with important social and cultural implications especially in urban contexts, while creating a connected ecosystem, where data sharing between vehicles and infrastructures can help improving the quality of the urban environment. An example of that is the introduction of Zero-Emissions Zones by the local administration to forbid the use of conventional engines within an urban area. However, the more the systems become complex the more their testing and validation require advanced testing facilities to comply with the shortening of the time-to-market.

In this challenging surrounding, the objective of this dissertation is to highlight the additional contribution brought by vehicular connectivity, in terms of CO_2 and pollutant emissions reduction, especially within an urban center.

With this aim, an innovative validation platform has been developed to test predictive control functions bridging the gap between the simulation and the on-road tests. The simulation environment consists of a Hardware-in-the-Loop enhanced with a Telecommunication Control Unit (TeCU) specifically developed to enable long- and short-horizon data exchange, using the same technologies usually available on the vehicles. Moreover, a Human-Machine Interface (HMI), based on a tablet running an Android-based Navigator App, has been introduced to allow the driver to set the desired destination and to see the suggested route based on actual traffic conditions. As additional feature, the Navigator App can update the navigation data if a re-routing or changes in traffic conditions are detected, as it would be in a real vehicle.

Then, Part I of the dissertation is focused on the development and testing of a supervisory controller for a high-performance PHEV based on predicted functions and an Adaptive-ECMS. This has been proposed to handle a Zero-Emission Zone using navigation data retrieved in real-time from the map service provider. With this information, a Speed Profile Prediction is performed to evaluate an energetically equivalent driving profile that is then fed to the BVM. The latter calculates the amount of energy necessary to drive the ZEZ in pure electric mode and forward that target SoC to the control policy. The A-ECMS is finally tested on a real driving scenario measured on the road and compared to an adapted rule-based strategy at the C-HiL. Since the navigation data from the MSP are real and referred to the current traffic situation, the proposed route can differ from the driven one, leading to re-routing and consequent adaptation of the target SoC, reflecting a common situation during everyday driving. The testing campaign shows how the supervisory controller not only grants the fully electric drive in an urban event, preventing the payment of fees, but also optimizes the fuel consumption while driving outside the ZEZ. Moreover, the strategy has been deployed into the real HCU and tested with real vehicular connectivity, proving the real-time capability and robustness of the predictive functions under different and unpredictable conditions. This has accelerated the function development laying the ground for future on-road tests. The main quantitative results of this part of the Ph.D. activity have been presented and discussed in detail in Chapter 6, at the end of Part I.

On the other hand, Part II of the dissertation concentrates on the plausible benefits of navigation data to reduce localized pollutant emissions, acting especially on cold-start maneuvers whose weight will increase with the introduction of Euro 7 real-driving emissions procedure. In this case, the vehicle under test is a Light Commercial Diesel PHEV equipped with a state-of-the-art exhaust after-treatment system (EATS) that has been modeled and validated.

More in detail, thanks to the knowledge of future driving scenarios provided by vehicular connectivity, engine first start can be predicted and therefore an EATS pre-heating phase can be planned using an Electrically Heated Catalyst. In this regard, the model has been consequently adapted by means of a secondary air pump, and then the ideal combination of electrical power and air mass flow has been defined finding the best trade-off between energy consumption and time to reach the light-off temperature. In addition, an improved Rule-Based Strategy, developed with a model-based approach, has been introduced and tested on the WLTP resulting in a cycle-independent strategy calibration. Consequently, the predictive thermal management strategy has been tested on different urban cycles representative of the Euro 7 testing procedure. Although the pre-heating introduction implies an additional energy request which results in increased fuel consumption, the results show that the final NO_x emission over a complete driving cycle can be significantly reduced compared to the base EHC strategy. Moreover, this would allow to comply with the scenarios introduced by the Euro 7 regulation proposal, while enabling the adoption of a simplified EATS architecture resulting in reduced manufacturing costs. Also in this case, for the sake of clarity, the main results related to this part of the Ph.D. activity have been analyzed in detail in Chapter 10, at the end of Part II.

In conclusion, it can be asserted that the Ph.D. course has been translated into a significant experience in control function development and testing with a specific focus on the advantages of using vehicular connectivity to answer the market demand for more sustainable and intelligent mobility.

Bibliography

[1] M. Pesaresi, M. Melchiorri, A. Siragusa, and T. Kemper, "Atlas of the Human Planet 2016. Mapping Human Presence on Earth with the Global Human Settlement Layer," *EUR 28116 EN*, p. 137, 2016. doi: 10.2788/889483.

[2] H. Ritchie and M. Roser, "Urbanization," *Our World in Data*, 2018. [Online]. Available: https://ourworldindata.org/urbanization.

[3] H. Ritchie and M. Roser. "CO_2 and Greenhouse Gas Emissions," Our World in Data. (May 2017), [Online]. Available: https://ourworldindata.org/co2-and-other-greenhouse-gas-emissions (visited on 04/27/2020).

[4] European Environment Agency. "Air quality statistics." (Jul. 7, 2022), [Online]. Available: https://www.eea.europa.eu/data-and-maps/dashboards/air-quality-statistics (visited on 07/07/2022).

[5] L. Ntziachristos, G. Mellios, D. Tsokolis, M. Keller, *et al.*, "In-use vs. type-approval fuel consumption of current passenger cars in europe," *Energy Policy*, vol. 67, pp. 403–411, Apr. 1, 2014, ISSN 0301-4215. doi: 10.1016/j.enpol.2013.12.013.

[6] I. C. on Clean Transportation, "Real-driving emissions test procedure for exhaust gas pollutant emissions of cars and light commercial vehicles in europe," Policy Update. [Online]. Available: https://theicct.org/publication/real-driving-emissions-test-procedure-for-exhaust-gas-pollutant-emissions-of-cars-and-light-commercial-vehicles-in-europe/ (visited on 07/07/2022).

[7] J. Mueller and Y. Le Petit. "Low-emission zones are a success - but they must now move to zero-emission mobility," European Federation for Transport and Environment AISBL. (), [Online]. Available: https://www.transportenvironment.org/sites/te/files/publications/2019_09_Briefing_LEZ-ZEZ_final.pdf.

[8] International Council on Clean Transportation, "CO2 emission standards for passenger cars and light-commercial vehicles in the european union," Policy Update, Jan. 2019, p. 9. [Online]. Available: https://theicct.org/sites/default/files/publications/EU-LCV-CO2-2030_ICCTupdate_20190123.pdf.

[9] X. Mosquet, A. Dinger, G. Xu, M. Andersen, *et al.*, "The Electric Car Tipping Point," Boston Consulting Group (BCG), 2018. [Online]. Available: https://www.bcg.com/publications/2018/electric-car-tipping-point.

[10] *Commission regulation (EU) 2017/1151 of 1 june 2017 supplementing regulation (EC) no 715/2007 of the european parliament and of the council on type-approval of motor vehicles with respect to emissions from light passenger and commercial vehicles (euro 5 and euro 6) and on access to vehicle repair and maintenance information, amending directive 2007/46/EC of the european parliament and of the council, commission regulation (EC) no 692/2008 and commission regulation (EU) no 1230/2012 and repealing commission regulation (EC) no 692/2008*, Jul. 7, 2017. [Online]. Available: http://data.europa.eu/eli/reg/2017/1151/oj/eng (visited on 05/21/2021).

[11] Jan Dornoff, Uwe Tietge, and Peter Mock, “On the way to "real-world" CO2 values: The european passenger car market in its first year after introducing the WLTP,” International Council on Clean Transportation, May 2020. [Online]. Available: https://theicct.org/publication/on-the-way-to-real-world-co2-values-the-european-passenger-car-market-in-its-first-year-after-introducing-the-wltp/.

[12] A. Dimaratos, Z. Toumasatos, S. Doulgeris, G. Triantafyllopoulos, *et al.*, “Assessment of CO2 and NOx emissions of one diesel and one bi-fuel gasoline/CNG euro 6 vehicles during real-world driving and laboratory testing,” *Frontiers in Mechanical Engineering*, vol. 5, 2019, ISSN 2297-3079. doi: 10.3389/fmech.2019.00062.

[13] G. Triantafyllopoulos, A. Dimaratos, L. Ntziachristos, Y. Bernard, *et al.*, “A study on the CO2 and NOx emissions performance of euro 6 diesel vehicles under various chassis dynamometer and on-road conditions including latest regulatory provisions,” *Science of The Total Environment*, vol. 666, pp. 337–346, May 20, 2019, ISSN 0048-9697. doi: 10.1016/j.scitotenv.2019.02.144.

[14] *Regulation (EC) 443/2009 of the european parliament and of the council of 23 april 2009 setting emission performance standards for new passenger cars as part of the community's integrated approach to reduce CO 2 emissions from light-duty vehicles (text with EEA relevance)*, Apr. 23, 2009. [Online]. Available: http://data.europa.eu/eli/reg/2009/443/oj/eng.

[15] *Regulation (EU) 2019/631 of the european parliament and of the council of 17 april 2019 setting CO2 emission performance standards for new passenger cars and for new light commercial vehicles, and repealing regulations (EC) no 443/2009 and (EU) no 510/2011 (text with EEA relevance.)* Apr. 25, 2019. [Online]. Available: http://data.europa.eu/eli/reg/2019/631/oj/eng.

[16] *40 CFR 86.1869-12 - CO_2 credits for off-cycle CO_2 reducing technologies.* Jul. 2021. [Online]. Available: https://www.ecfr.gov/current/title-40/chapter-I/subchapter-C/part-86/subpart-S/section-86.1869-12.

[17] *GB 18352.6-2016 - limits and measurement methods for emissions from light-duty vehicles (CHINA 6)*, Aug. 2016. [Online]. Available: https://www.chinesestandard.net/PDF.aspx/GB18352.6-2016.

[18] *Commission implementing regulation (EU) no 725/2011 of 25 july 2011 establishing a procedure for the approval and certification of innovative technologies for reducing CO 2 emissions from passenger cars pursuant to regulation (EC) no 443/2009 of the european parliament and of the council text with EEA relevance*, Jul. 26, 2011. [Online]. Available: http://data.europa.eu/eli/reg_impl/2011/725/oj/eng.

[19] U. Tietge, Peter Mock, and Jan Dornoff, "Overview and evaluation of eco-innovations in european passenger car CO2 standards," International Council on Clean Transportation, Brussels, Belgium, Briefing, Jul. 2018, pp. 1–11. [Online]. Available: https://theicct.org/publications/eco-innovations-european-passenger-car-co2-standards (visited on 12/28/2021).

[20] *Communication from the commission to the council and the european parliament 6 results of the review of the community strategy to reduce CO2 emissions from passenger cars and light-commercial vehicles {SEC(2007) 60} {SEC(2007) 61}*, 2007. [Online]. Available: https://eur-lex.europa.eu/legal-content/EN/TXT/?uri=celex%3A52007DC0019 (visited on 07/15/2022).

[21] O. US EPA. "Criteria air pollutants." (Apr. 9, 2014), [Online]. Available: https://www.epa.gov/criteria-air-pollutants (visited on 07/18/2022).

[22] J. A. Harrington and R. C. Shishu, "A single-cylinder engine study of the effects of fuel type, fuel stoichiometry, and hydrogen-to-carbon ratio on CO, NO, and HC exhaust emissions," presented at the National Automobile Engineering Meeting, Feb. 1, 1973, p. 730 476. doi: 10.4271/730476.

[23] J. Kasab and A. Strzelec, *Automotive Emissions Regulations and Exhaust Aftertreatment Systems*. SAE International, Aug. 31, 2020, ISBN 978-0-7680-9955-3. doi: 10.4271/9780768099560.

[24] G. A. Lavoie, J. B. Heywood, and J. C. Keck, "Experimental and theoretical study of nitric oxide formation in internal combustion engines," *Combustion Science and Technology*, vol. 1, no. 4, pp. 313–326, Feb. 1, 1970, ISSN 0010-2202. doi: 10.1080/00102206908952211.

[25] "EU: Light-duty: Emissions | transport policy." (), [Online]. Available: https://www.transportpolicy.net/standard/eu-light-duty-emissions/ (visited on 07/18/2022).

[26] "Commission regulation (EU) no 459/2012 of 29 may 2012 amending regulation (EC) no 715/2007 of the european parliament and of the council and commission regulation (EC) no 692/2008 as regards emissions from light passenger and commercial vehicles (euro 6)text with EEA relevance," May 2012, p. 9.

[27] Z. Samaras, S. Hausberger, and D. G. Mellios, "Preliminary findings on possible euro 7 emission limits for LD and HD vehicles," Online AGVES Meeting, Oct. 2020.

[28] ACEA, *ACEA proposal for euro 7*, Jul. 2021. [Online]. Available: https://www.acea.auto/files/ACEA_proposal_for_Euro7.pdf (visited on 07/23/2022).

[29] N. Hooftman, M. Messagie, J. Van Mierlo, and T. Coosemans, "A review of the european passenger car regulations – real driving emissions vs local air quality," *Renewable and Sustainable Energy Reviews*, vol. 86, pp. 1–21, Apr. 2018, ISSN 13640321. doi: 10.1016/j.rser.2018.01.012.

[30] B. Degraeuwe and M. Weiss, "Does the new european driving cycle (NEDC) really fail to capture the NOX emissions of diesel cars in europe?" *Environmental Pollution*, vol. 222, pp. 234–241, Mar. 1, 2017, ISSN 0269-7491. doi: 10.1016/j.envpol.2016.12.050.

[31] "Commission regulation (EU) 2018/1832 of 5 november 2018 amending directive 2007/46/EC of the european parliament and of the council, commission regulation (EC) no 692/2008 and commission regulation (EU) 2017/1151 for the purpose of improving the emission type approval tests and procedures for light passenger and commercial vehicles, including those for in-service conformity and real-driving emissions and introducing devices for monitoring the consumption of fuel and electric energy (text with EEA relevance.),"

32018R1832, Nov. 27, 2018, Legislative Body: COM, GROW. [Online]. Available: http://data.europa.eu/eli/reg/2018/1832/oj/eng (visited on 05/21/2021).

[32] A. Joshi, "Review of Vehicle Engine Efficiency and Emissions," en, Apr. 2021, pp. 2021–01–0575. doi: 10.4271/2021-01-0575.

[33] W. A. Cannon, E. F. Hill, and C. E. Welling, "SINGLE CYLINDER ENGINE TESTS OF OXIDATION CATALYSTS," presented at the Pre-1964 SAE Technical Papers, Jan. 1, 1957, p. 570 280. doi: 10.4271/570280.

[34] G. J. Nebel and R. W. Bishop, "CATALYTIC OXIDATION OF AUTOMOBILE EXHAUST GASES- an evaluation of the houdry catalyst," presented at the Pre-1964 SAE Technical Papers, Jan. 1, 1959, p. 590 224. doi: 10.4271/590224.

[35] M. Keenan, "Exhaust emissions control: 60 years of innovation and development," presented at the 13th International Conference on Engines & Vehicles, Sep. 4, 2017, pp. 2017–24–0120. doi: 10.4271/2017-24-0120.

[36] "Denoxtronic from bosch," Bosch Auto Parts. (), [Online]. Available: https://www.boschautoparts.com/en/w/denoxtronic-from-bosch (visited on 08/04/2022).

[37] M. V. Twigg, "Roles of catalytic oxidation in control of vehicle exhaust emissions," *Catalysis Today*, vol. 117, no. 4, pp. 407–418, Oct. 15, 2006, ISSN 0920-5861. doi: 10.1016/j.cattod.2006.06.044.

[38] N. R. Collins and M. V. Twigg, "Three-way catalyst emissions control technologies for spark-ignition engines—recent trends and future developments," *Topics in Catalysis*, vol. 42, no. 1, pp. 323–332, May 1, 2007, ISSN 1572-9028. doi: 10.1007/s11244-007-0199-6.

[39] John Heywood, *Internal Combustion Engine Fundamentals*, 2nd ed. McGraw-Hill Education, Apr. 10, 2018, ISBN 978-1-260-11610-6. [Online]. Available: https://www.mheducation.com/highered/product/internal-combustion-engine-fundamentals-2e-heywood/9781260116106.html.

[40] W. Bögner, M. Krämer, B. Krutzsch, S. Pischinger, *et al.*, "Removal of nitrogen oxides from the exhaust of a lean-tune gasoline engine," *Applied Catalysis B: Environmental*, vol. 7, no. 1, pp. 153–171, Dec. 7, 1995, ISSN 0926-3373. doi: 10.1016/0926-3373(95)00035-6.

[41] J. Klimstra, "Catalytic converters for natural gas fueled engines—a measurement and control problem," presented at the 1987 SAE International Fall Fuels and Lubricants Meeting and Exhibition, Nov. 1, 1987, p. 872 165. doi: 10.4271/872165.

[42] K. Hirata, N. Masaki, H. Ueno, and H. Akagawa, "Development of urea-SCR system for heavy-duty commercial vehicles," presented at the SAE 2005 World Congress & Exhibition, Apr. 11, 2005, pp. 2005–01–1860. doi: 10.4271/2005-01-1860.

[43] W. Liu, *Hybrid electric vehicle system modeling and control* (Automotive series), 2nd edition. John Wiley & Sons, 2017, 1 p., ISBN 978-1-119-27894-8.

[44] C. Mi and M. A. Masrur, *Hybrid Electric Vehicles: Principles and Applications with Practical Perspectives*. John Wiley & Sons, 2017, 597 pp., ISBN 978-1-118-97056-0.

[45] M. A. Hannan, F. A. Azidin, and A. Mohamed, "Hybrid electric vehicles and their challenges: A review," *Renewable and Sustainable Energy Reviews*, vol. 29, pp. 135–150, 2014, ISSN 1364-0321. doi: 10.1016/j.rser.2013.08.097.

[46] K. V. Singh, H. O. Bansal, and D. Singh, “A comprehensive review on hybrid electric vehicles: Architectures and components,” *J. Mod. Transport.*, vol. 27, no. 2, pp. 77–107, 2019, ISSN 2196-0577. doi: 10.1007/s40534-019-0184-3.

[47] C. Ress, A. Etemad, D. Kuck, and J. Requejo, “Electronic horizon - providing digital map data for adas applications,” *Proceedings of the 2nd International Workshop on Intelligent Vehicle Control Systems - Volume 1: IVCS, (ICINCO 2008)*, INSTICC, vol. 1, SciTePress, 2008, pp. 40–49, ISBN 978-989-8111-34-0. doi: 10.5220/0001508000400049.

[48] C. Ress, D. Balzer, A. Bracht, S. Durekovic, *et al.*, “ADASIS Protocol for advanced in-vehicle applications,” 2008. [Online]. Available: https://www.researchgate.net/publication/228880192_Adasis_protocol_for_advanced_in-vehicle_applications.

[49] ADASIS. “New advanced driver assistance systems specification provides impactful and more accurate features to support automated driving.” (2020), [Online]. Available: https://adasis.org/2020/11/26/new-advanced-driver-assistance-systems-specification-provides-impactful-and-more-accurate-features-to-support-automated-driving/.

[50] I. Campero-Jurado, J. Q. Gomez, O. D. Vargas-Buitrón, F. R. Trejo-Macotela, *et al.*, “Embedded system based on IoT and V2X for Smart Cities,” *International Journal of Combinatorial Optimization Problems and Informatics*, vol. 10, no. 3, pp. 50–58, 2019, ISSN 2007-1558.

[51] R. Shrestha, S. Y. Nam, R. Bajracharya, and S. Kim, “Evolution of V2X Communication and Integration of Blockchain for Security Enhancements,” *Electronics*, vol. 9, no. 9, p. 1338, 2020. doi: 10.3390/electronics9091338.

[52] F. Outay, F. Kamoun, F. Kaisser, D. Alterri, *et al.*, “V2V and V2I Communications for Traffic Safety and CO_2 Emission Reduction: A Performance Evaluation,” *Procedia Computer Science*, vol. 151, pp. 353–360, 2019, ISSN 1877-0509. doi: 10.1016/j.procs.2019.04.049.

[53] W. He, H. Li, X. Zhi, X. Li, *et al.*, “Overview of V2V and V2I Wireless Communication for Cooperative Vehicle Infrastructure Systems,” *2019 IEEE 4th Advanced Information Technology, Electronic and Automation Control Conference (IAEAC)*, vol. 1, 2019, pp. 127–134. doi: 10.1109/IAEAC47372.2019.8997786.

[54] K. Kiela, V. Barzdenas, M. Jurgo, V. Macaitis, *et al.*, “Review of V2X–IoT Standards and Frameworks for ITS Applications,” *Applied Sciences*, vol. 10, no. 12, p. 4314, 2020, ISSN 2076-3417. doi: 10.3390/app10124314.

[55] European Commission, *European Urban Mobility: Policy Context*. Publications Office of the European Union, 2017, ISBN 978-92-79-57527-3. doi: 10.2832/827766.

[56] ETSI, “Technical Specification Group Services and System Aspects,” Technical Report 3GPP TS 33.185 V14.1.0, 2020. [Online]. Available: https://portal.3gpp.org/desktopmodules/Specifications/SpecificationDetails.aspx?specificationId=3618.

[57] L. Guzzella and A. Sciarretta, *Vehicle Propulsion Systems: Introduction to Modeling and Optimization*, 3rd ed. Springer International Publishing, 2013, ISBN 978-3-642-35912-5. doi: 10.1007/978-3-642-35913-2.

[58] T. J. Böhme and B. Frank, *Hybrid Systems, Optimal Control and Hybrid Vehicles: Theory, Methods and Applications* (Advances in Industrial Control Series). Springer International Publishing, 2017, ISBN 978-3-319-51315-7. doi: 10.1007/978-3-319-51317-1.

[59] P. Caratozzolo, M. Serra, and J. Riera, “Energy management strategies for hybrid electric vehicles,” *IEEE International Electric Machines and Drives Conference, 2003. IEMDC’03.*, vol. 1, 2003, pp. 241–248. doi: 10.1109/IEMDC.2003.1211270.

[60] X. He, M. Parten, and T. Maxwell, “Energy Management Strategies for a Hybrid Electric Vehicle,” *2005 IEEE Vehicle Power and Propulsion Conference*, 2005, pp. 536–540. doi: 10.1109/VPPC.2005.1554610.

[61] J. Gonder and T. Markel, “Energy Management Strategies for Plug-In Hybrid Electric Vehicles,” SAE Technical Paper 2007-01-0290, 2007. doi: 10.4271/2007-01-0290.

[62] M. F. M. Sabri, K. A. Danapalasingam, and M. F. Rahmat, “A review on hybrid electric vehicles architecture and energy management strategies,” *Renewable and Sustainable Energy Reviews*, vol. 53, pp. 1433–1442, 2016, ISSN 1364-0321. doi: 10.1016/j.rser.2015.09.036.

[63] P. Pisu and G. Rizzoni, “A Comparative Study Of Supervisory Control Strategies for Hybrid Electric Vehicles,” *IEEE Transactions on Control Systems Technology*, vol. 15, no. 3, pp. 506–518, 2007, ISSN 1558-0865. doi: 10.1109/TCST.2007.894649.

[64] L. Serrao, S. Onori, and G. Rizzoni, “A Comparative Analysis of Energy Management Strategies for Hybrid Electric Vehicles,” *Journal of Dynamic Systems, Measurement, and Control*, vol. 133, no. 3, 2011, ISSN 0022-0434. doi: 10.1115/1.4003267.

[65] A. Ali and D. Söffker, “Towards Optimal Power Management of Hybrid Electric Vehicles in Real-Time: A Review on Methods, Challenges, and State-Of-The-Art Solutions,” *Energies*, vol. 11, no. 3, p. 476, 2018, ISSN 1996-1073. doi: 10.3390/en11030476.

[66] P. Zhang, F. Yan, and C. Du, “A comprehensive analysis of energy management strategies for hybrid electric vehicles based on bibliometrics,” *Renewable and Sustainable Energy Reviews*, vol. 48, pp. 88–104, 2015, ISSN 1364-0321. doi: 10.1016/j.rser.2015.03.093.

[67] F. Zhang, L. Wang, S. Coskun, H. Pang, *et al.*, “Energy Management Strategies for Hybrid Electric Vehicles: Review, Classification, Comparison, and Outlook,” *Energies*, vol. 13, no. 13, p. 3352, 2020. doi: 10.3390/en13133352.

[68] N. J. Schouten, M. A. Salman, and N. A. Kheir, “Energy management strategies for parallel hybrid vehicles using fuzzy logic,” *Control Engineering Practice*, Automotive Systems, vol. 11, no. 2, pp. 171–177, 2003, ISSN 0967-0661. doi: 10.1016/S0967-0661(02)00072-2.

[69] V. Navale and T. C. Havens, “Fuzzy logic controller for energy management of power split hybrid electrical vehicle transmission,” *2014 IEEE International Conference on Fuzzy Systems (FUZZ-IEEE)*, 2014, pp. 940–947. doi: 10.1109/FUZZ-IEEE.2014.6891785.

[70] T. Hofman, M. Steinbuch, R. Druten, and A. Serrarens, “Rule-based energy management strategies for hybrid vehicles,” *International Journal of Electric and Hybrid Vehicles*, vol. 1, 2007. doi: 10.1504/IJEHV.2007.014448.

[71] T. Hofman, M. Steinbuch, R. M. van Druten, and A. F. A. Serrarens, “Rule-Based Energy Management Strategies For Hybrid Vehicle Drivetrains: A Fundamental Approach In Reducing Computation Time,” *IFAC Proceedings Volumes*, 4th IFAC Symposium on Mechatronic Systems, vol. 39, no. 16, pp. 740–745, 2006, ISSN 1474-6670. doi: 10.3182/20060912-3-DE-2911.00128.

[72] D. Bianchi, L. Rolando, L. Serrao, S. Onori, *et al.*, "A Rule-Based Strategy for a Series/Parallel Hybrid Electric Vehicle: An Approach Based on Dynamic Programming," *ASME 2010 Dynamic Systems and Control Conference, Volume 1*, 2010, pp. 507–514, ISBN 978-0-7918-441 7-5978-0-7918-3884-6. doi: 10.1115/DSCC2010-4233.

[73] T. J. Boehme, M. Schori, H. Rabba, and M. Schultalbers, "Analytical Calibration of Map-Based Energy Managements of Parallel Hybrid Vehicles," SAE Technical Paper 2014-01-1902, 2014. doi: 10.4271/2014-01-1902.

[74] S. Onori, L. Serrao, and G. Rizzoni, *Hybrid Electric Vehicles - Energy Managament Strategies* (SpringerBriefs in Electrical and Computer Engineering). Springer London, 2016, ISBN 978-1-4471-6779-2978-1-4471-6781-5. doi: 10.1007/978-1-4471-6781-5.

[75] A. Capancioni, "Development of predictive energy management strategies for hybrid electric vehicles supported by connectivity," Doctoral Thesis, Alma Mater Studiorum - Università di Bologna, Mar. 30, 2022. doi: 10.48676/unibo/amsdottorato/10044. [Online]. Available: http://amsdottorato.unibo.it/10044/.

[76] R. Bellman, "On the Theory of Dynamic Programming," *Proc Natl Acad Sci U S A*, vol. 38, no. 8, pp. 716–719, 1952, ISSN 0027-8424. doi: OntheTheoryofDynamicProgramming.

[77] R. Bellman, "The theory of dynamic programming," *Bull. Amer. Math. Soc.*, vol. 60, no. 6, pp. 503–516, 1954, ISSN 0002-9904. doi: 10.1090/S0002-9904-1954-09848-8.

[78] R. Bellman, "Dynamic Programming," *Science*, vol. 153, no. 3731, pp. 34–37, 1966. doi: 10.1126/science.153.3731.34.

[79] Y. Huang, H. Wang, A. Khajepour, H. He, *et al.*, "Model predictive control power management strategies for HEVs: A review," *Journal of Power Sources*, vol. 341, pp. 91–106, 2017, ISSN 03787753. doi: 10.1016/j.jpowsour.2016.11.106.

[80] L. Serrao, S. Onori, and G. Rizzoni, "ECMS as a realization of Pontryagin's minimum principle for HEV control," *2009 American Control Conference*, 2009, pp. 3964–3969. doi: 10.1109/ACC.2009.5160628.

[81] G. Paganelli, "Conception et commande d'une chaîne de traction pour véhicule hybride parallèle thermique et électrique," Doctoral thesis, Université de Valenciennes et du Hainaut-Cambrésis, Valenciennes, 1999.

[82] G. Paganelli, G. Ercole, A. Brahma, Y. Guezennec, *et al.*, "General supervisory control policy for the energy optimization of charge-sustaining hybrid electric vehicles," *JSAE Review*, vol. 22, pp. 511–518, 2001. doi: 10.1016/S0389-4304(01)00138-2.

[83] G. Paganelli, S. Delprat, T. Guerra, J. Rimaux, *et al.*, "Equivalent consumption minimization strategy for parallel hybrid powertrains," *Vehicular Technology Conference. IEEE 55th Vehicular Technology Conference. VTC Spring 2002 (Cat. No.02CH37367)*, vol. 4, 2002, pp. 2076–2081. doi: 10.1109/VTC.2002.1002989.

[84] F. R. Salmasi, "Control Strategies for Hybrid Electric Vehicles: Evolution, Classification, Comparison, and Future Trends," *IEEE Transactions on Vehicular Technology*, vol. 56, no. 5, pp. 2393–2404, 2007. doi: 10.1109/TVT.2007.899933.

[85] G. Rizzoni and S. Onori, "Energy Management of Hybrid Electric Vehicles: 15 years of development at the Ohio State University," *Oil Gas Sci. Technol. – Rev. IFP Energies nouvelles*, vol. 70, no. 1, pp. 41–54, 2015. doi: 10.2516/ogst/2014006.

[86] G. Paganelli, S. Delprat, T.-M. Guerra, J. Rimaux, *et al.*, "Equivalent consumption minimization strategy for parallel hybrid powertrains," *IEEE 55th Vehicular Technology Conference*, vol. 4, 2002, pp. 2076–2081, ISBN 978-0-7803-7484-3. doi: 10.1109/VTC.2002.1002989.

[87] A. Cerofolini, "Optimal Supervisory Control of Hybrid Vehicles," Doctoral thesis, University of Bologna, 2014. doi: 10.6092/unibo/amsdottorato/6357.

[88] D. E. Kirk, *Optimal Control Theory: An Introduction*. Courier Corporation, 2017, ISBN 978-0-486-43484-1.

[89] C. Musardo, G. Rizzoni, Y. Guezennec, and B. Staccia, "A-ECMS: An adaptive algorithm for hybrid electric vehicle energy management," *European Journal of Control*, vol. 11, no. 4, pp. 509–524, Jan. 1, 2005, ISSN 0947-3580. doi: 10.3166/ejc.11.509-524.

[90] S. Onori, L. Serrao, and G. Rizzoni, "Adaptive equivalent consumption minimization strategy for hybrid electric vehicles," presented at the ASME 2010 Dynamic Systems and Control Conference, American Society of Mechanical Engineers Digital Collection, Jan. 25, 2011, pp. 499–505. doi: 10.1115/DSCC2010-4211.

[91] Y. Yu, J. Jiang, P. Wang, J. Li, *et al.*, "A-EMCS for PHEV based on real-time driving cycle prediction and personalized travel characteristics," *MBE*, vol. 17, no. 6, pp. 6310–6341, 2020. doi: 10.3934/mbe.2020333.

[92] Z. Lei, D. Qin, L. Hou, J. Peng, *et al.*, "An adaptive equivalent consumption minimization strategy for plug-in hybrid electric vehicles based on traffic information," *Energy*, vol. 190, p. 116 409, 2020. doi: 10.1016/j.energy.2019.116409.

[93] D. Chen, Y. Kim, and A. G. Stefanopoulou, "Predictive Equivalent Consumption Minimization Strategy With Segmented Traffic Information," *IEEE Transactions on Vehicular Technology*, vol. 69, no. 12, pp. 14 377–14 390, 2020. doi: 10.1109/TVT.2020.3034552.

[94] C. Sun, F. Sun, and H. He, "Investigating adaptive-ECMS with velocity forecast ability for hybrid electric vehicles," *Applied Energy*, vol. 185, pp. 1644–1653, 2017. doi: 10.1016/j.apenergy.2016.02.026.

[95] J. Soldo, B. Skugor, and J. Deur, "Optimal Energy Management Control of a Parallel Plug-In Hybrid Electric Vehicle in the Presence of Low Emission Zones," SAE Technical Paper 2019-01-1215, 2019. doi: 10.4271/2019-01-1215.

[96] J. Gao, G. Tian, A. Sorniotti, A. E. Karci, *et al.*, "Review of thermal management of catalytic converters to decrease engine emissions during cold start and warm up," *Applied Thermal Engineering*, vol. 147, pp. 177–187, Jan. 25, 2019, ISSN 1359-4311. doi: 10.1016/j.applthermaleng.2018.10.037.

[97] D. B. Gosala, A. K. Ramesh, C. M. Allen, M. C. Joshi, *et al.*, "Diesel engine aftertreatment warm-up through early exhaust valve opening and internal exhaust gas recirculation during idle operation," *International Journal of Engine Research*, vol. 19, no. 7, pp. 758–773, Sep. 1, 2018, Publisher: SAGE Publications, ISSN 1468-0874. doi: 10.1177/1468087417730240.

[98] T. Nüesch, A. Cerofolini, G. Mancini, N. Cavina, *et al.*, "Equivalent consumption minimization strategy for the control of real driving NOx emissions of a diesel hybrid electric vehicle," *Energies*, vol. 7, no. 5, pp. 3148–3178, May 2014. doi: 10.3390/en7053148.

[99] F. Millo, A. Zanelli, L. Rolando, and R. Fuso, “Development of a comprehensive model for the concurrent minimization of CO2 and NOx emissions of a 48v mild-hybrid diesel car,” *SAE International Journal of Electrified Vehicles*, vol. 10, no. 2, Apr. 9, 2021, Number: 14-10-02-0014, ISSN 2691-3747,2691-3755. doi: 10.4271/14-10-02-0014.

[100] L. Tribioli and G. Bella, “Reduction of particulate emissions in diesel hybrid electric vehicles with a PMP-based control strategy,” *Energy Procedia*, ATI 2018 - 73rd Conference of the Italian Thermal Machines Engineering Association, vol. 148, pp. 994–1001, Aug. 1, 2018, ISSN 1876-6102. doi: 10.1016/j.egypro.2018.08.062.

[101] A. Simon, P. Michel, D. Nelson-Gruel, Y. Chamaillard, *et al.*, “Gasoline-HEV equivalent consumption and pollutant minimization strategy,” *2015 IEEE Vehicle Power and Propulsion Conference (VPPC)*, Oct. 2015, pp. 1–6. doi: 10.1109/VPPC.2015.7352956.

[102] M. Villani, A. Shiledar, T. Zhao, C. Lana, *et al.*, “Optimal energy management strategy for energy efficiency improvement and pollutant emissions mitigation in a range-extender electric vehicle,” presented at the SAE Technical Papers, ISSN: 0148-7191 Issue: 2021, 2021. doi: 10.4271/2021-24-0103.

[103] J. Kuchly, D. Nelson-Gruel, A. Charlet, A. Simon, *et al.*, “Forecasting ECMS for hybrid electric vehicles,” *IFAC-PapersOnLine*, 21st IFAC World Congress, vol. 53, no. 2, pp. 14 154–14 160, Jan. 1, 2020, ISSN 2405-8963. doi: 10.1016/j.ifacol.2020.12.1027.

[104] F. Xu and T. Shen, “A traffic-in-loop simulation system for validation of emission control strategy in diesel engine,” presented at the Proceedings - 2018 IEEE Industrial Cyber-Physical Systems, ICPS 2018, 2018, pp. 85–90, ISBN 978-1-5386-6531-2. doi: 10.1109/ICPHYS.2018.8387642.

[105] A. Guille des Buttes, B. Jeanneret, A. Kéromnès, L. Le Moyne, *et al.*, “Energy management strategy to reduce pollutant emissions during the catalyst light-off of parallel hybrid vehicles,” *Applied Energy*, vol. 266, p. 114 866, May 15, 2020, ISSN 0306-2619. doi: 10.1016/j.apenergy.2020.114866.

[106] M. Hopka, D. Upadhyay, and M. V. Nieuwstadt, “Smart DPF regenerations - a case study of a connected powertrain function,” vol. SAE Int. J. Adv. & Curr. Prac. in Mobility, no. 1, pp. 762–770, 2019. doi: 10.4271/2019-01-0316.

[107] G. Caramia, N. Cavina, D. Moro, S. Patassa, *et al.*, “Predictive nox emission control of a diesel-hev for co2 and urea consumption reduction,” *AIP Conference Proceedings*, vol. 2191, no. 1, p. 020 035, Dec. 17, 2019, publisher: American Institute of Physics, ISSN 0094-243X. doi: 10.1063/1.5138768.

[108] A. Hassdenteufel, E. Schünemann, V. Neubert, and A. Hirchenhein, “Gasoline powertrain solutions with ultra low tailpipe emissions,” *Transportation Engineering*, vol. 8, p. 100 109, Jun. 2022, ISSN 2666691X. doi: 10.1016/j.treng.2022.100109.

[109] J. Hofstetter, P. Boucharel, F. Atzler, and G. Wachtmeister, “Fuel consumption and emission reduction for hybrid electric vehicles with electrically heated catalyst,” *SAE International Journal of Advances and Current Practices in Mobility*, vol. 3, no. 1, pp. 702–714, Jun. 30, 2020, ISSN 2641-9637,2641-9645. doi: 10.4271/2020-37-0017.

[110] J. Gao, G. Tian, and A. Sorniotti, “On the emission reduction through the application of an electrically heated catalyst to a diesel vehicle,” *Energy Science & Engineering*, vol. 7, no. 6, pp. 2383–2397, 2019, ISSN 2050-0505. doi: 10.1002/ese3.416.

[111] B. Bargman, S. Jang, J. Kramer, I. Soliman, *et al.*, “Effects of electrically preheating catalysts on reducing high-power cold-start emissions,” SAE Technical Paper, Warrendale, PA, SAE Technical Paper 2021-01-0572, Apr. 6, 2021, ISSN: 0148-7191, 2688-3627. doi: 10.4271/2021-01-0572.

[112] M. R. Hamedi, O. Doustdar, A. Tsolakis, and J. Hartland, “Energy-efficient heating strategies of diesel oxidation catalyst for low emissions vehicles,” en, *Energy*, vol. 230, p. 120 819, Sep. 2021, [Online; accessed 2021-12-16], ISSN 03605442. doi: 10.1016/j.energy.2021.120819.

[113] A. García, J. Monsalve-Serrano, R. Lago Sari, and S. Martinez-Boggio, “Energy assessment of an electrically heated catalyst in a hybrid rcci truck,” en, *Energy*, vol. 238, p. 121 681, Jan. 1, 2022, [Online; accessed 2021-12-06], ISSN 0360-5442. doi: 10.1016/j.energy.2021.121681.

[114] V. Schallhart, H. Berthold, E. Klemm, and L. Moeltner, “Light-off support for mobile denox systems,” en, *Chemie Ingenieur Technik*, vol. 93, no. 5, pp. 814–818, 2021, ISSN 1522-2640. doi: 10.1002/cite.202000212.

[115] W. Wachenfeld and H. Winner, “The release of autonomous vehicles,” *Autonomous Driving: Technical, Legal and Social Aspects*, M. Maurer, J. C. Gerdes, B. Lenz, and H. Winner, Eds. Berlin, Heidelberg: Springer Berlin Heidelberg, 2016, pp. 425–449, ISBN 978-3-662-48847-8. doi: 10.1007/978-3-662-48847-8_21.

[116] M. Tideman and M. van Noort, “A simulation tool suite for developing connected vehicle systems,” *Intelligent Vehicles Symposium (IV)*, Gold Coast City, Australia: IEEE, Jun. 2013, pp. 713–718, ISBN 978-1-4673-2755-8978-1-4673-2754-1. doi: 10.1109/IVS.2013.6629551.

[117] M. Aramrattana, T. Larsson, J. Jansson, and A. Nåbo, “A simulation framework for cooperative intelligent transport systems testing and evaluation,” *Transportation Research Part F: Traffic Psychology and Behaviour*, vol. 61, pp. 268–280, Feb. 2019, ISSN 13698478. doi: 10.1016/j.trf.2017.08.004.

[118] F. Xu and T. Shen, “Look-ahead prediction-based real-time optimal energy management for connected HEVs,” *IEEE Transactions on Vehicular Technology*, vol. 69, no. 3, pp. 2537–2551, Mar. 2020, ISSN 0018-9545,1939-9359. doi: 10.1109/TVT.2020.2965163.

[119] T. Grahle and M. Tonne, “Regeneration of the particulate filter by using navigation data,” *MTZ Worldwide*, vol. 77, no. 1, pp. 16–21, Jan. 2016. doi: 10.1007/s38313-015-0078-7.

[120] M. Menarini, P. Marrancone, G. Cecchini, A. Bazzi, *et al.*, “TRUDI: Testing environment for vehicular applications running with devices in the loop,” *International Conference on Connected Vehicles and Expo*, Graz, Austria: IEEE, Nov. 2019, pp. 1–6, ISBN 978-1-72810-142 -2. doi: 10.1109/ICCVE45908.2019.8965152.

[121] Z. Szendrei, N. Varga, and L. Bokor, “A SUMO-based hardware-in-the-loop v2x simulation framework for testing and rapid prototyping of cooperative vehicular applications,” *Vehicle and Automotive Engineering 2*, ser. Lecture Notes in Mechanical Engineering, K. Jármai and B. Bollò, Eds., VAE 2018: Springer, Cham, 2018, pp. 426–440, ISBN 978-3-319-75677-6.

[122] S. Y. Gelbal, S. Tamilarasan, M. R. Cantas, L. Guvenc, *et al.*, “A connected and autonomous vehicle hardware-in-the-loop simulator for developing automated driving algorithms,” *2017 IEEE International Conference on Systems, Man and Cybernetics (SMC)*, Banff, Canada: IEEE, Oct. 2017, pp. 3397–3402, ISBN 978-1-5386-1645-1. doi: 10.1109/SMC.2017.8123155.

[123] Y. Shao, M. A. M. Zulkefli, Z. Sun, and P. Huang, “Evaluating connected and autonomous vehicles using a hardware-in-the-loop testbed and a living lab,” *Transportation Research Part C: Emerging Technologies*, vol. 102, pp. 121–135, May 2019, ISSN 0968090X. doi: 10.1016/j.trc.2019.03.010.

[124] Y. Kim, S. Tay, J. Guanetti, F. Borrelli, *et al.*, “Hardware-in-the-loop for connected automated vehicles testing in real traffic,” *21st International Conference on Intelligent Transportation Systems*, Maui, HI: IEEE, 2018, pp. 2878–2883. doi: 10.1109/ITSC.2018.8569753.

[125] M. Boccolini, “Development of a speed profile prediction algorithm based on navigation data for energy management optimization,” Master Thesis, University of Bologna, Apr. 6, 2021. [Online]. Available: https://amslaurea.unibo.it/22543/.

[126] A. Capancioni, L. Brunelli, N. Cavina, and A. Perazzo, “Development of adaptive-ECMS and predictive functions for plug-in HEVs to handle zero-emission zones using navigation data,” SAE International, Warrendale, PA, SAE Technical Paper 2021-24-0105, Sep. 5, 2021, ISSN: 0148-7191, 2688-3627. doi: 10.4271/2021-24-0105.

[127] L. Brunelli, A. Capancioni, P. Gonnella, R. Casadio, *et al.*, “A hybrid vehicle hardware-in-the-loop system with integrated connectivity for ehorizon functions validation,” *IEEE Transactions on Vehicular Technology*, vol. 70, no. 5, pp. 4340–4352, May 2021, Conference Name: IEEE Transactions on Vehicular Technology, ISSN 1939-9359. doi: 10.1109/TVT.2021.3073807.

[128] R. Parenti, S. Mazzetti, F. Belletti, F.-W. Speckens, *et al.*, “Will the 95g/km limit affect fun and emotion? the lamborghini answer,” *24th Aachener Kolloquium Automobile and Engine Technology*, Aachen, Germany, 2015.

[129] “ISO 10521-1:2006 - Road vehicles — Road load — Part 1: Determination under reference atmospheric conditions,” 2006, p. 30. [Online]. Available: https://www.iso.org/standard/37533.html.

[130] *Simscape*, it. [Online]. Available: https://it.mathworks.com/products/simscape.html (visited on 09/04/2022).

[131] Rui Xiong and Weixiang Shen, *Advanced Battery Management Technologies for Electric Vehicles* (Automotive Series), en-us. Wiley, 2019, ISBN 978-1-119-48164-5. [Online]. Available: https://www.wiley.com/en-us/Advanced+Battery+Management+Technologies+for+Electric+Vehicles-p-9781119481645.

[132] “MicroAutoBox II.” (), [Online]. Available: https://www.dspace.com/en/inc/home/products/hw/micautob/microautobox2.cfm (visited on 09/02/2022).

[133] European Commission, *Regulation No 101 of the Economic Commission for Europe of the United Nations (UN/ECE) — Uniform provisions concerning the approval of passenger cars powered by an internal combustion engine only, or powered by a hybrid electric power train with regard to the measurement of the emission of carbon dioxide and fuel consumption and/or the measurement of electric energy consumption and electric range, and of categories M1 and N1 vehicles powered by an electric power train only with regard to the measurement of electric energy consumption and electric range*, Regulation (EU) 2012/101, 2012. [Online]. Available: https://eur-lex.europa.eu/legal-content/IT/TXT/?uri=CELEX%3A42012X0526%2801%29.

[134] “HERE SDK: Online, offline and global maps for iOS and android | HERE.” (Apr. 6, 2022), [Online]. Available: https://developer.here.com/products/here-sdk (visited on 04/06/2022).

[135] “Zona a traffico limitato (ztl).” (), [Online]. Available: https://www.comune.bologna.it/servizi-informazioni/zona-traffico-limitato-ztl (visited on 09/29/2022).

[136] R. P. Ltd. “Raspberry pi 4 model b,” Raspberry Pi. (), [Online]. Available: https://www.raspberrypi.com/products/raspberry-pi-4-model-b/ (visited on 09/20/2022).

[137] “PiCAN2 CAN-bus board for raspberry pi 2-3,” SK Pang Electronics Ltd. (), [Online]. Available: https://www.skpang.co.uk/products/pican2-can-bus-board-for-raspberry-pi-2-3 (visited on 09/20/2022).

[138] “MATLAB support package for raspberry pi hardware documentation - MathWorks italia.” (), [Online]. Available: https://it.mathworks.com/help/supportpkg/raspberrypiio/ (visited on 09/20/2022).

[139] J. Santa, F. Pereñíguez, A. Moragón, and A. F. Skarmeta, “Experimental evaluation of cam and denm messaging services in vehicular communications,” *Transportation Research Part C: Emerging Technologies*, vol. 46, pp. 98–120, 2014, ISSN 0968-090X. doi: https://doi.org/10.1016/j.trc.2014.05.006.

[140] S. Lefèvre, C. Sun, R. Bajcsy, and C. Laugier, “Comparison of parametric and non-parametric approaches for vehicle speed prediction,” *2014 American Control Conference*, ISSN: 2378-5861, Jun. 2014, pp. 3494–3499. doi: 10.1109/ACC.2014.6858871.

[141] K. Liu, Z. Asher, X. Gong, M. Huang, *et al.*, “Vehicle velocity prediction and energy management strategy part 1: Deterministic and stochastic vehicle velocity prediction using machine learning,” SAE International, Warrendale, PA, SAE Technical Paper 2019-01-1051, Apr. 2, 2019, ISSN: 0148-7191, 2688-3627. doi: 10.4271/2019-01-1051.

[142] S. T. Standard, *J2951: Drive quality evaluation for chassis dynamometer testing - SAE international*. [Online]. Available: https://www.sae.org/standards/content/j2951_201401/ (visited on 09/06/2021).

[143] R. Trigui, E. Vinot, and B. Jeanneret, “Backward modeling and energy management optimization of a two-clutches series-parallel HEV for efficiency assessment,” *IFAC Proceedings Volumes*, 8th Power Plant and Power System Control Symposium, vol. 45, no. 21, pp. 422–427, Jan. 1, 2012, Number: 21, ISSN 1474-6670. doi: 10.3182/20120902-4-FR-2032.00075.

[144] T. Hofman and D. van Leeuwen, “Analysis of modeling and simulation methodologies for vehicular propulsion systems,” *2009 IEEE Vehicle Power and Propulsion Conference*, ISSN: 1938-8756, Sep. 2009, pp. 1619–1626. doi: 10.1109/VPPC.2009.5289633.

[145] Lekshmi S. and Lal Priya P.s., “Mathematical modeling of electric vehicles - a survey,” *Control Engineering Practice*, vol. 92, p. 104 138, Nov. 1, 2019, ISSN 0967-0661. doi: 10.1016/j.conengprac.2019.104138.

[146] G. Mohan, F. Assadian, and S. Longo, “Comparative analysis of forward-facing models vs backwardfacing models in powertrain component sizing,” *IET Hybrid and Electric Vehicles Conference 2013 (HEVC 2013)*, Nov. 2013, pp. 1–6. doi: 10.1049/cp.2013.1920.

[147] Z. Lei, D. Qin, P. Zhao, J. Li, *et al.*, “A real-time blended energy management strategy of plug-in hybrid electric vehicles considering driving conditions,” *Journal of Cleaner Production*, vol. 252, p. 119 735, Apr. 10, 2020, ISSN 0959-6526. doi: 10.1016/j.jclepro.2019.119735.

[148] B. V. Padmarajan, A. McGordon, and P. A. Jennings, “Blended rule-based energy management for PHEV: System structure and strategy,” *IEEE Transactions on Vehicular Technology*, vol. 65, no. 10, pp. 8757–8762, Oct. 2016, ISSN 1939-9359. doi: 10.1109/TVT.2015.2504510.

[149] N. Cavina, G. Caramia, S. Patassa, and M. Caggiano, “Predictive energy management strategies for hybrid electric vehicles: Fuel economy improvement and battery capacity sensitivity analysis,” presented at the WCX World Congress Experience, Apr. 3, 2018, pp. 2018–01–0998. doi: 10.4271/2018-01-0998.

[150] G. Caramia, N. Cavina, M. Caggiano, S. Patassa, *et al.*, “Battery state of charge management strategies for a real-time controller of a plug-in hybrid electric vehicle,” en, *Energy Procedia*, ATI 2018 - 73rd Conference of the Italian Thermal Machines Engineering Association, vol. 148, pp. 258–265, Aug. 1, 2018, [Online; accessed 2022-03-05], ISSN 1876-6102. doi: 10.1016/j.egypro.2018.08.076.

[151] G. Di Pierro, “Development of an integrated experimental and numerical methodology for the performance analysis of multiple hybrid electric architectures over different driving cycles,” Doctoral Thesis, Politecnico di Torino, Torino, Jun. 2020. [Online]. Available: https://iris.polito.it/handle/11583/2843980.

[152] S. Canè, “Development of a Predictive Control Function for a Plug-in Hybrid Electric Vehicle with Electrically-heated Catalyst,” Master Thesis, University of Bologna, Oct. 2021. [Online]. Available: https://amslaurea.unibo.it/24073/.

[153] S. Canè, L. Brunelli, S. Gallian, A. Perazzo, *et al.*, “Performance assessment of a predictive pre-heating strategy for a hybrid electric vehicle equipped with an electrically heated catalyst,” *Applied Thermal Engineering*, p. 119 341, Sep. 24, 2022, ISSN 1359-4311. doi: 10.1016/j.applthermaleng.2022.119341.

[154] A. Lubeski, “Real-time catalytic converter temperature estimator in the powertrain controller,” SAE International, Warrendale, PA, SAE Technical Paper 2000-01-0651, Mar. 6, 2000, ISSN: 0148-7191, 2688-3627. doi: 10.4271/2000-01-0651.

[155] S. Meisner and S. C. Sorenson, “Computer simulation of intake and exhaust manifold flow and heat transfer,” SAE International, Warrendale, PA, SAE Technical Paper 860242, May 1, 1986, ISSN: 0148-7191, 2688-3627. doi: 10.4271/860242.

[156] P. J. Shayler, D. J. Hayden, and T. Ma, “Exhaust system heat transfer and catalytic converter performance,” SAE International, Warrendale, PA, SAE Technical Paper 1999-01-0453, Mar. 1, 1999, ISSN: 0148-7191, 2688-3627. doi: 10.4271/1999-01-0453.

[157] “Real-world usage of plug-in hybrid vehicles in europe: A 2022 update on fuel consumption, electric driving, and CO2 emissions,” International Council on Clean Transportation. (), [Online]. Available: https://theicct.org/publication/real-world-phev-use-jun22/ (visited on 10/10/2022).

[158] T. Dallmann, F. Posada, and A. Bandivadekar, “Costs of emission reduction technologies for diesel engines used in non-road vehicles and equipment,” International Council on Clean Transportation, 2018. [Online]. Available: https://theicct.org/wp-content/uploads/2021/06/Non_Road_Emission_Control_20180711.pdf (visited on 10/10/2022).